The role of nuclear physics in supernovae and the evolution of neutron stars

Neutrino Opacities, Equation of State, Transport Coefficients, and Dark Matter Production

Ermal Rrapaj

A dissertation
submitted in partial fulfillment of the
requirements for the degree of

Doctor of Philosophy

University of Washington

2016

Reading Committee:
Sanjay Reddy, Chair
Martin Savage
Emily Levesque

Program authorized to offer degree
Physics

University of Washington

Abstract

The role of nuclear physics in supernovae and the evolution of neutron stars

Neutrino Opacities, Equation of State, Transport Coefficients, and Dark Matter Production

Ermal Rrapaj

Sanjay Reddy, Chair
Martin Savage
Emily Levesque

A massive star, of at least eight solar masses, end their life cycle in a sudden, catastrophic collapse under its own gravity. In a thousandth of a second, it can shrink from thousands of kilometers across to a ball of ultra-condensed matter just a few kilometers across. Ultimately, it all ends in a cataclysmic explosion known as a supernova, and for a few short weeks it burns as brightly as several billion suns, briefly outshining the star's entire home galaxy. The visible light of a supernova, though, represents only about 1% of the released energy, the vast majority being in the form of ultraviolet light, x-rays, gamma rays and, especially neutrinos. In the first chapter of work, I study neutrino - nucleon interactions and their role in the nucleosynthesis of heavy elements. Another key ingredient is the equation of state, which relates the thermodynamic properties of these extreme environments to the micro physics of nuclear interactions, explored in the second chapter. As a supernova cools, a new neutron star is born. The thermal, electric properties and the shear viscosity of this object are analyzed in terms of a newly discovered interaction, among electrons and neutrons, in the third chapter. Given the enormous amount of energy released during the explosion, I study the possibility of producing light massive particles, candidates for what is commonly called dark matter, in the last chapter of this work. I find that supernovae are ideal environments where the interplay of all forces in nature can be observed, nuclear forces playing a paramount role.

Contents

List of Figures

Introduction

ὁ δὲ ἀνεξέταστος βίος οὐ βιωτὸς ἀνθρώπῳ (The unexamined life is not worth living.)

Socrates' trial, excerpt from Plato's 'Apology'

From Stars to Neutron Stars

Accretion, fusion, and collapse

Needless to say, stars are fascinating objects. The creation and evolution of a star is rather complicated process involving a plethora of physical phenomena. Here, I will provide a very brief and schematic time-line of the life of stars, and the consequent explosion, which when extremely violent is known as supernova, and the birth of neutron stars.

A star begins its life as a cloud of dust and gas, primarily hydrogen, known as a nebula. Gravity causes the dust to clump together in a process called accretion which leads to the formation of the proto-star. As more and more matter moves inward towards the core of the star, its temperature, pressure and density increase. When a critical temperature is reached, nuclear fusion begins and a star is born. However, when the critical temperature is not reached, it can become a brown dwarf, or dead star, and never attains star status.

A typical star like our own sun, which is technically classified as a yellow dwarf star, is fueled by nuclear fusion, the conversion of hydrogen into helium. The nucleus of a helium atom actually weighs only 99.3% as much as the two protons and two neutrons that go to make it up, the remaining 0.7% being released as heat and energy. This very small fraction, essentially due to the extent to which the strong nuclear force is able to overcome the electrical repulsion, turns out to be critical in determining the life-cycle of stars and the development of the variety of atoms we see in the universe around us.

The sun's own gravity traps and squeezes this ultra-hot gas into a confined space, thus generating enough heat for the fusion reaction to take place. The process remains in equilibrium as long as it retains enough fuel to create this heat- and light-producing outward energy which counteracts the inward pressure of its gravity, remaining in quasi-hydrostatic equilibrium. This period is known as the main sequence of the star.

Already about 4.5 - 5 billion years old, when the sun's hydrogen fuel starts to run out, its main sequence comes to an end, and it starts to cool down and collapse under its own gravity. However, energy from the collapse then heats up the core even more, until it is hot enough to start burning helium and, under the extra heat of the helium burning, its outer layers expand briefly, for the "short" time scale of a 100 million years, into a massive red giant star.

As the star runs out of fuel, the outer layers blow off completely and the core settles down into a white dwarf star - a small cinder about the size of the earth composed mainly of carbon and oxygen. Over a very long stretch of time, white dwarfs will eventually fade into black dwarfs, and this is the ultimate fate of about 97% of stars in our galaxy. The matter which makes up white and black dwarfs is largely composed of, and

supported by, electron-degenerate matter, in which the Pauli pressure of electrons is the last resort the star has to counterbalance the inward gravitational pull. However, here we are interested in that tiny fraction of stars that very massive.

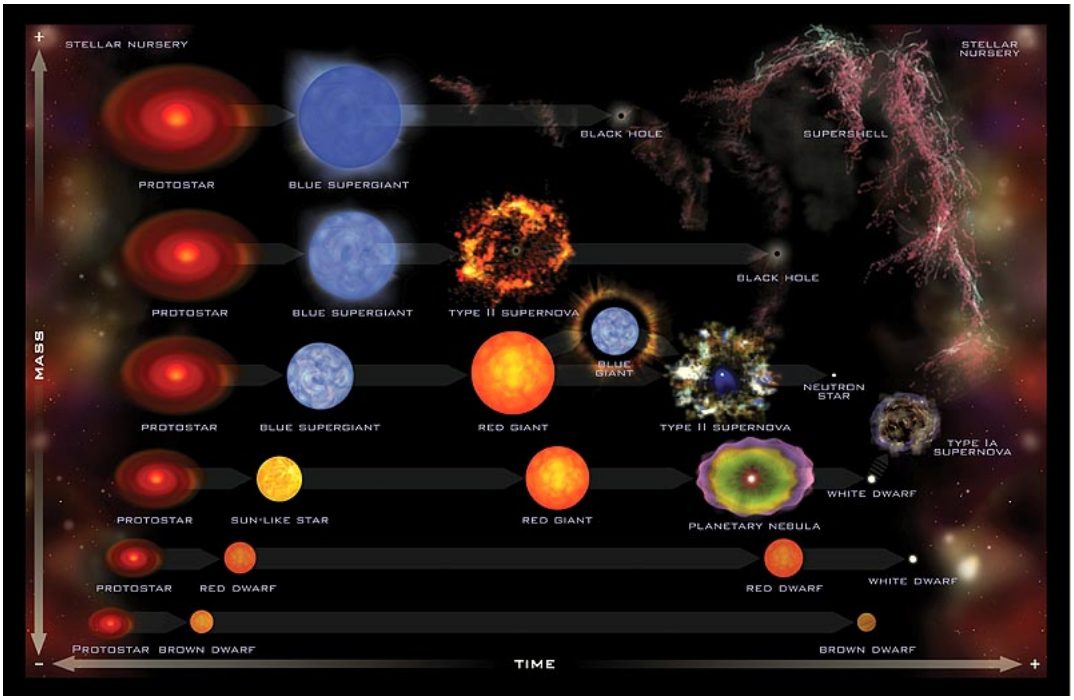

Figure 1: A Summary of Stellar Evolution The evolution of isolated stars depends on their masses. The higher the mass, the shorter the lifetime. Stars less massive than about 8 solar masses can eject enough mass to become white dwarfs. High-mass stars can produce Type II supernovae and become neutron stars or black holes. Source: Chandra X-ray Center [5]

A star significantly larger than our sun is hotter and burns up its fuel more quickly and generally has a shorter but more dramatic life. A star of ten solar masses, for example, would burn fuel at about a thousand times the rate of the sun, and would exhaust its hydrogen fuel in less than 100 million years.

Larger stars can reach higher temperatures that are sufficient to fuse even helium. The helium then becomes the raw fuel, and it goes on to release ever higher levels of energy as it is fused into carbon and oxygen, while the outer layer of hydrogen actually cools and expands significantly in the star's red giant phase.

Even larger stars continue in further rounds of nuclear fusion, each of successively increased violence and shorter duration, as carbon fuses into neon, neon into magnesium and oxygen, then to silicon and finally iron. Thus, a larger star continues though a chain of transmutations to progressively heavier nuclei. Eventually, a star of sufficient initial mass becomes a red super-giant, which has a core layered like an onion, with a broad shell of hydrogen on the outside, surrounding a shell of helium, and then successively denser shells of carbon, then neon, then oxygen, then silicon, and finally a core of white-hot iron.

The iron in the star's core is very resistant to further fusing and this is the final element produced by the chain of fusion reactions. At this stage, the heat from nuclear fusion is no longer sufficient to support the star against its own crushing gravity and it will suddenly and catastrophically collapse. The final collapse of a massive star under its own gravity happens incredibly quickly: in a thousandth of a second it can shrink from thousands of kilometers across to a ball of ultra-condensed matter just a few kilometers across.

This rapid collapse results in a massive rebound when the core reaches nuclear saturation density, resulting in ultra-hot shock-waves which are imparted to the rest of the star. The star ultimately ends its life in a cataclysmic explosion known as a supernova, and for a few short weeks it burns as brightly as several billion suns, briefly outshining the star's entire home galaxy. The Crab Nebula was recorded by Chinese astronomers in the year 1054 as visible to the naked eye for several months, even in the daytime, and bright enough to read by at night, despite its being about 6,500 light years away. The visible light of a supernova, though, represents only about 1% of the released energy, the vast majority being in the form of ultraviolet light, x-rays, gamma rays and, especially neutrinos.

Indeed, we will focus on the paramount role this extremely light and weakly interacting particles play in the supernova explosion and the production of heavy elements in our first chapter.

The conditions in the blast of a supernova allow for elements heavier than iron to be created, such as radioactive versions of aluminum, titanium, etc. In the process of its explosion, a supernova blows out into space a nebula of debris containing a mix of all of the naturally-occurring elements, in proportions which agree closely with those calculated to exist on earth. The variety of atoms in the dusty cloud from which our solar system were formed 4.5 billion years ago were essentially the ashes of generations of earlier stars having run through their entire life-cycles. Supernovas are therefore ultimately responsible for providing a good part of mix of atoms on Earth, and the building blocks of the chemistry of life. In this respect, we are composed of "stardust".

The ultra-dense remnant of the imploding core has become known as a neutron star, as its electrons and protons are crushed together in the huge gravity to form neutrons. A neutron star is typically between 1.4 and 2 times as massive as our own sun, but is squeezed into a volume only about 7 to 20 kilometers in diameter, and so has an extremely high density. The gravitational pull of a small, dense neutron star is much greater than that around a normal star of many times its size. In fact, the gravitational force on a massively dense neutron star is about a million million times fiercer than on the Earth, and a projectile would need to attain almost half the speed of light in order to escape its gravity. So, general relativity is needed to understand the structure of this object. For instance, clocks on a neutron star would run 10 - 20% slower than those on Earth, and any path of light from its surface would be so strongly curved that, viewed from afar, part of the back of the neutron star would be visible as well.

For neutron stars, Pauli pressure is not sufficient, and nuclear interactions are the primary source that balances the effects of gravity, making the star stable. Thus, understanding nuclear forces is paramount, if we hope to understand these stars. And, given the high density of these environments, the nuclear physics at play should be the same as the one we can probe with nuclear experiments here on earth.

In the second chapter, we try to understand, and constrain the nuclear equation of stable of both supernovae and neutron stars. Because neutron stars retain the angular momentum of the original much larger star, but have a much smaller moments of inertia, they usually rotate at very high angular speed, as fast as several hundred times per second in a newly formed neutron star. In some cases, their intense magnetic fields sweep regular pulses of radio waves across the universe, for which they are known as pulsars. We know of about 2,000 neutron stars in our own Milky Way galaxy, the majority of which were detected as radio pulsars.

Interestingly, the same nuclear interactions which provide stability for these stars, also effect the cooling, and spin down of these stars as we demonstrate in the third chapter.

We conclude this dissertation in chapter four by exploring scenarios in which supernovae can emit light dark matter particles and constrain these extensions to the standard by model by analyzing their effect on the thermodynamic evolution of the explosion.

As we will show, much is yet to be discovered, as the field of nuclear astrophysics is relativity young, and only in the last decades have we started to tackle this interplay of all physical forces and such diverse timescales

with the numerical precision that advances in computational technology allow us. Despite being daunting, this endeavor is inextricably thrilling. While the contribution a lifetime can give is small, the examined universe is definitely worth living in!

Nuclear Interactions

What holds us together

Nuclear interactions are responsible for the binding of protons and neutrons in nuclei, ultimately causing the vast diversity of chemical elements found in nature. Also known as the 'strong' force, the nuclear force is about 10^6 stronger than the chemical binding between atoms in a molecule. Unlike other familiar forces, such as gravity or electromagnetic interactions , this interaction is extremely short range, of the order of a femtometer (10^{-15} m).

After the discovery of the neutron in 1932 [6] , the picture of the nucleus made up of protons and neutrons came into existence. The strong repulsive Coulomb force between protons at such short distances, needs to compensated by a new force to make the nucleus stable. Thus, the concept of the nuclear force is naturally introduced. The first theory for this force is due to the physicist Hideki Yukawa in 1935 [7]. This first model consists of force carriers, called mesons. The number of discovered mesons grew quickly in the 1960's and the one-boson-exchange model was established as a quantitatively successful way of describing this new interaction.

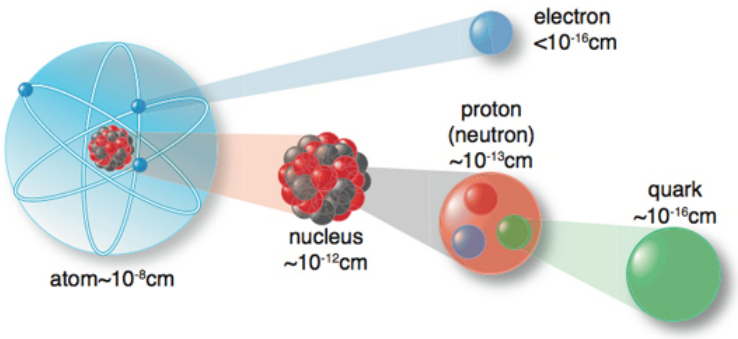

Figure 2: Nuclear interactions cover a wide range of very small scales.

Source: 'Universe and multiverse, part 3', Gerald Cleaver. [8]

In the early 1970's the fundamental theory of quantum chromo dynamics (QCD) was discovered [9]. Based on QCD, mesons and nucleons are not elementary particles, but composites made up of quarks and gluons. The inherent non perturbative nature of QCD, together with the counterintuitive dependence on energy scales (strong at low energy and weak at high energy, contrary to Coulomb forces or gravity), makes it a formidable task to explain nuclear interactions across the wide energy range required to cover both quarks and gluons and the residual force between nucleons and mesons. As fig. 2 illustrates, the scale range under consideration spans at least four orders of magnitude!

Currently, the most promising method is to compute quark interactions by brute computational power, by discretization of time and space, known as lattice QCD. Unfortunately, we are far away from using this tool to explain all the nuclei found in nature.

Luckily, during the same time period, the algorithmic approach of Effective Field Theory (EFT) was applied to low energy QCD. Steven Weinberg, the first proposer of this approach, wrote down the most general Lagrangian consistent with the symmetries of low energy QCD. In particular, the so-called chiral symmetry is spontaneously broken. This should lead to the existence of massless particles based on the Goldstone theorem which are the pions. Massless particles should respect this symmetry, which means that their intrinsic spin and angular momentum are either parallel or anti-parallel. However, chiral symmetry is only approximate and pions have light masses. In comparison to quarks and gluons, the interaction between pions and nucleons is weak, making perturbative calculations feasible. The natural small parameter for expanding this effective theory is the momentum exchange over the 'chiral symmetry breaking scale'. Nowadays, this is scheme is commonly referred to as Chiral Effective Field Theory (χEFT), and it allows for a systematic treatment of nuclear many body forces in a single hierarchy.

In this work, subsection 1.4.1 in chapter 1 is dedicated to a proper explanation of CH-PT, from the realization of the chiral symmetry in QCD, the algorithmic treatment of effective theories, up to the systematic organization of nuclear many forces in this formalism.

Despite, its appealing systematics, χEFT is far from being fully developed and some of the open issues are mentioned throughout the first chapter. At present, there are about 3000 known nuclei and in experiments various isotopes can be created making the number of possible nuclei to be studied easily double. Trying to explain medium and large nuclei with χEFT becomes very expensive computationally. Thus, alternative treatments have come to help. These are mean field models (relativistic or not) that fall into the category of Energy Density Functionals (EDF). EDF theory has been successfully applied to condensed matter physics and chemistry, based on the foundations laid by the work of Walter Kohn. Indeed, density functional theory (DFT), the general framework used to develop EDF, was put on firm theoretical ground from the two Hohenberg–Kohn theorems (H-K) [10].

The first H–K theorem demonstrates that the ground state properties of a many-electron system are uniquely determined by an electron density that depends on only 3 spatial coordinates. It lays the groundwork for reducing the many-body problem of N electrons with 3N spatial coordinates to 3 spatial coordinates, through the use of functionals of the electron density. This theorem can be extended to the time-dependent domain to develop time-dependent density functional theory (TDDFT), which can be used to describe excited states. The second H–K theorem defines an energy functional for the system and proves that the correct ground state electron density minimizes this energy functional.

Within the framework of Kohn–Sham DFT (KS DFT), the intractable many-body problem of interacting electrons in a static external potential is reduced to a tractable problem of non-interacting electrons moving in an effective potential. The effective potential includes the external potential and the effects of the Coulomb interactions between the electrons, e.g., the exchange and correlation interactions. Modeling the latter two interactions becomes the difficulty within KS DFT. The simplest approximation is the local-density approximation (LDA), which assumes that the exchange - correlation energy functional in DFT depends only on the density at each point in space.

In nuclear theory, this approach has been widely used to model interactions among nuclei in heavy isotopes and infinite matter calculations, within the LDA approximation. In sections 2.3.1 and 2.3.2 mean field models are described in detail.

In this work, Ch-PT, EDF and other approximations to nuclear forces are used in order to properly explain the extreme physical phenomena of supernovae explosions and neutron star properties.

Seeing how interactions at the level of subatomic particles affect stellar phenomena, how the 'tiny' and the 'huge' are interrelated, is very intriguing and exciting!

Chapter 1

Charged - current reactions in supernovae

1.1 Introduction

When a very massive star, at least 8 solar masses, reaches the end of its life-cycle it core-collapses through a type II supernova to form either a proto-neutron star (PNS) or a black hole (BH) [11], [12]. Most of its gravitational binding energy, roughly about 3×10^{53} erg, is emitted in the form of neutrinos of all flavors in a period of several tens of seconds. Given the enormous amount of energy these particles carry, they are expected to play a vital role in the thermodynamical evolution of the explosion mechanism. At the present, the time delayed neutrino heating mechanism [13] is commonly assumed to be the leading candidate in powering the supernova explosion. Once it sets in, the neutrino 'stream' from the core of the PNS drives the subsequent mass outflow in a process referred to as neutrino-driven wind [14]. This site has a potential for the nucleosynthesis of elements heavier than iron [15] through the rapid capture of free neutrons from the nuclei in the ejecta (r-process). Analytic [16], parametric [17], and steady state wind models [18, 19] have shown that neutrino driven winds are capable of producing both light and heavy r-process elements under certain conditions. Specifically, provided the ejecta have short dynamical time scales of the order of few milliseconds, high entropy per baryon (above 150 k_B/nucleon) and low electron fraction ($Y_e < 0.5$) the r-process can be successful in producing heavy and rare isotopes. While hydrodynamical simulations have found the short timescales to be within reach [20], they fail to produce the high entropy needed [21]. Under these circumstances, it is commonly believed that only elements up to $Z = 50$ can be produced. However, so far we have not considered the role the electron fraction of the ejecta plays in the nucleosynthesis. As various studies have found [22], [23], the outcome of the neutrino - driven wind is particularly sensitive to this parameter, which, in turn, is set by the competition of neutrino absorption by neutrons and anti-neutrino absorptions by protons and their reverse reactions:

$$\begin{aligned} \nu_e + n &\leftrightarrow p + e^- \\ \overline{\nu}_e + p &\leftrightarrow n + e^+ \end{aligned} \tag{1.1}$$

The rates of these reactions are dependent upon the luminosity and spectral differences of the electron neutrinos and anti-neutrinos.

Deep in the PNS, neutrinos are in thermal and chemical equilibrium with matter due to the extremely high densities the core can reach. However, proceeding further out towards the surface, the density and temperature drop quickly and neutrinos decouple [19]. Subsequently, neutrinos can be thought of as free streaming. The region where the decoupling occurs is commonly referred to as neutrino sphere and charged current rates in this region, being absorption processes, allow us to understand neutrino spectra. As μ and τ flavors interact

primarily through neutral current reactions they decouple early in their path to the surface. The electron flavor reflects the composition of matter with ν_e being the last to decouple. The longer neutrinos exchange energy with the nuclear medium, the more energy they deposit in the environment and, consequently, the average energy of the neutrino flux lowers with the increase of the radius of the neutrino sphere.

Thus, the expected spectra is, $\epsilon_{\nu_{\mu,\tau}} > \epsilon_{\overline{\nu}_e} > \epsilon_{\nu_e}$ [24], with $\epsilon = \langle E^2 \rangle / \langle E \rangle$. Despite, the $\overline{\nu}_e$ average spectra being higher than ν_e, the difference needed to obtain neutron rich ejecta is $\epsilon_{\overline{\nu}_e} - \epsilon_{\nu_e} > 4(m_n - m_p)$, assuming comparable luminosities [16],[25],[26].

From recent developments in numerical simulations and Boltzmann neutrino transport codes, it is possible to relate the spectra of the neutrinos in the high density part of the star ($\rho \approx 10^{12} - 10^{14}\ g\ cm^{-3}$) to the photosynthesis in the ejecta (its electron fraction). It has been established that charged current reactions, described by eq. 1.1 are paramount in determining the neutrino spectra, and the spectral differences between ν_e and $\overline{\nu}_e$ persist, impacting the composition of the matter outflow [27],[28], [29].

Due to matter degeneracy, strong and electromagnetic correlations, and multi particle excitations of nuclear matter, even at supra nuclear densities, have been found to be important in calculating neutrino rates [30, 31, 32, 33]. In particular, supernova and PNS simulations that incorporate some of these improvements to the free gas neutrino interaction rates have found both temporal and spectral modifications of the neutrino emission [34],[35], [36], [37]. For instance, inclusion of mean field effects in PNS cooling simulations, results in changes in the electron fraction in the neutrino driven wind (NDW) [28]. As already emphasized, the nucleosynthesis ([17], [22],[23]) and neutrino oscillations outside the neutrino sphere are impacted [38], [39].

In every simulation the rates are approximated, with mean field effects being the dominant one. An in depth analysis of various mean field treatments of the equation of state, and how they compare to ab-inito calculations from χEFT is given in chapter 2.

Here, we discuss our improvements on neutrino rates by performing an ab-inito treatment of the nuclear medium and understanding its impact on charged current reactions. In Sec. 1.2 the kinematics of charged-current reactions is described with an emphasis on nucleon dispersion relations. The nucleon dispersion relation and the composition of matter in the neutrino-sphere are calculated in Sec. 1.3, where also the NN interactions used are discussed and the validity of the HF approximation for the relevant conditions is assessed. In Sec. 1.6 the neutrino-absorption rates using the HF self-energies are calculated and compared to results obtained in earlier work. Sec. 1.10 discusses the implications of the new findings and identify areas where improvements are necessary. Throughout these sections, natural units are employed: $\hbar = 1$, the speed of light $c = 1$ and the Boltzmann constant $k_B = 1$. Energy and temperature are measured in MeV, and the density is measured in units of nucleons per fm^3.

1.2 Kinematics of the reaction

The tree level Feynman diagrams relevant for the process at hand are given in fig. 1.13. To understand the role nuclear interactions play in the neutrino cross section, we start by delineating the kinematics of these processes. As the neutrino energy in the neutrino sphere is comparable to the typical energy and momentum of nucleons in the hot and dense plasma in this region, kinematic restrictions are paramount in determining the average neutrino and anti-neutrino energies. Due to strong electron degeneracy, the final-state blocking of the ν_e absorption rate becomes relevant when the neutrino energy is equal to or less than the electron Fermi energy. On the other hand, $\bar{\nu}_e$ absorption is associated with emission of e^+, for which there are practically no final space effects since there are few positrons in hot and dense nuclear matter which is close to β equilibrium (the chemical potential of an anti-particle is the negative of that of the particle, in other words, there is no Pauli blocking of final states for positrons). However, this reaction requires a neutrino energy large enough to

overcome the energy difference between the proton in the initial state and the neutron plus positron energy in the final state. These constraints are depicted in Fig. 1.1, where for illustration, energy and momentum conservation for an incoming neutrino of energy E_ν = 24 MeV are depicted. Assuming an ambient temperature of T = 8 MeV, this is the typical neutrino energy to be expected. For a better understanding of the ambient condition of the neutrino sphere, the reactions described here, need to be included in numerical simulations and neutrinos need to be traced through their 'escape' from the star. As described later, the improved neutrino opactities are expected to have nonlinear effects by shifting the locations and, thus, properties of the neutrino and anti-neutrino spheres. To give a numerical understanding of nuclear many body implications, fiducial values of temperature and density are used in this work.

The axis of abscissas is the magnitude of the momentum transferred to the nucleons, $\vec{q} = \vec{k}_\nu - \vec{k}_e$, where $\vec{k}_\nu$ and $\vec{k}_e$ are the ν_e ($\bar{\nu}_e$) and final state e^- (e^+) lepton momenta, respectively. The axis of ordinates is the final-state lepton energy E_e. The shaded area enclosed by the solid black lines is the region allowed by lepton kinematics.

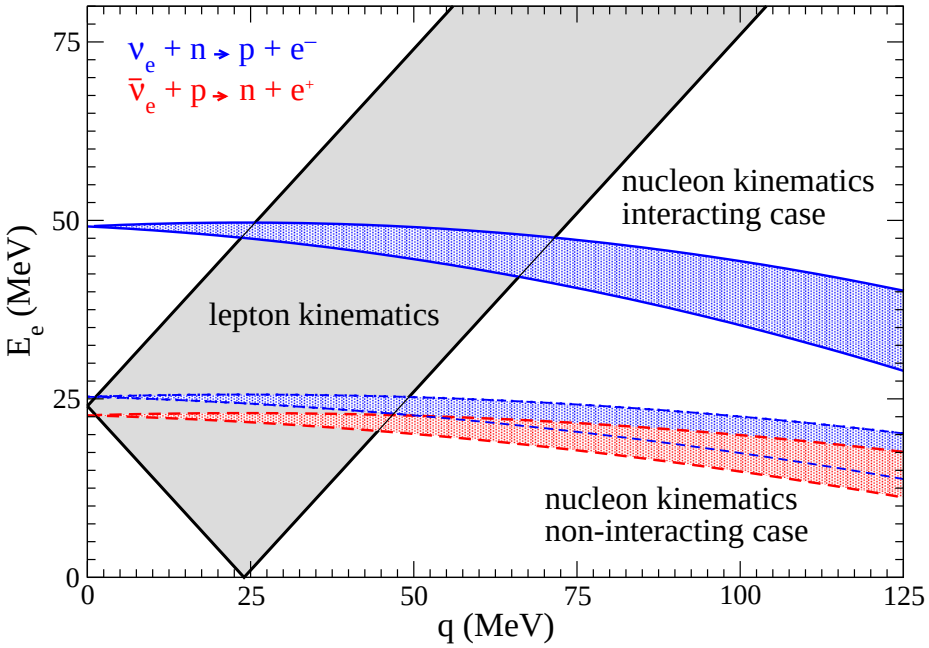

Figure 1.1: Energy and momentum constraints on the charged-current reactions for conditions discussed in the text. Reactions are possible when the allowed region for lepton kinematics, shown by the shaded region enclosed by the black lines, overlaps the allowed region for nucleon kinematics, shown by the regions enclosed by blue and red lines corresponding to the ν_e and $\bar{\nu}_e$ reactions, respectively. The region enclosed by the solid blue lines includes the nuclear self-energy difference for the transition $n \to p$ associated with the ν_e reaction, and regions enclosed by the dashed lines are for non-interacting nucleons. The $p \to n$ transition associated with the $\bar{\nu}_e$ reaction, for conditions depicted here, is kinematically forbidden, as there is no overlap with the leptonic kinematics region,when nucleon self-energy corrections are included.

The charged current-reaction can proceed when the allowed regions for nucleon and lepton kinematics

overlap. Energy and momentum constraints imposed by the nucleons for the $\nu_e + n \to e^- + p$ and $\bar{\nu}_e + p \to e^+ + n$ reactions are shown by the regions enclosed by the dashed blue and red curves, respectively. For the ν_e reaction, the blue region is defined by the equation $E_n(|\vec{k}\,|) - E_p(|\vec{k} + \vec{q}\,|) = -\omega$, and for the $\bar{\nu}_e$ reaction the red region is defined by $E_p(|\vec{k}\,|) - E_n(|\vec{k} + \vec{q}\,|) = -\omega$, where $\omega = E_\nu - E_e$ is the energy transferred to the nucleons. When nuclear interactions are neglected, the neutron and proton single-particle energies are given by $E_n(|\vec{k}\,|) = M_n + k^2/2M_n$ and $E_p(|\vec{k}\,|) = M_p + k^2/2M_p$, respectively. In this case, the allowed kinematic region for the ν_e and $\bar{\nu}_e$ are similar and the small difference arises solely due to the small neutron-proton mass difference.

In an interacting system, the single-particle energy of a nucleon is given by

$$E_{i=n,p}(|\vec{k}\,|) = M_i + \frac{k^2}{2M_i} + \Sigma_i(k) \equiv \varepsilon_i(k) + M_i\,, \tag{1.2}$$

where $\Sigma_i(k)$ is the momentum-, density-, and temperature-dependent self-energy. In general, this quantity is also energy dependent. In this study it is treated at Hartree-Fock (HF) level in many perturbation theory, for which no energy dependency arises. At the densities $\rho \simeq 10^{11} - 10^{13}$ g/cm^3 and temperatures $T \simeq 3 - 10$ MeV of interest in the neutrino-sphere, matter is very neutron-rich with an electron fraction Y_e of only a few percent (note that charge neutrality requires the proton fraction $Y_p = Y_e$). Due to this large asymmetry, the proton and neutron self-energies are not equal, $\Sigma_n(k) \neq \Sigma_p(k)$. Both neutron and proton energies are shifted downwards by the nuclear interaction at the densities and temperatures encountered in the neutrino-sphere, i.e., $\Sigma_i < 0$, because NN interactions are on average attractive at the relevant low momenta ($k < 200$ MeV). However, the energy shift is much larger for the protons and $\Sigma_n - \Sigma_p > 0$ because of the denser neutron background and the additional attraction in the neutron-proton interaction. This energy difference is related to the potential part of the nuclear symmetry energy — in neutron-rich matter it costs nuclear interaction energy to convert protons to neutrons, and there is an energy gain resulting from the conversion of neutrons to protons. The resulting change in the reaction Q value modifies the relative ν_e and $\bar{\nu}_e$ absorption rates as described below.

In Fig. 1.1 the allowed nucleon kinematic regions due to the inclusion of self- energy modification of the nucleons dispersion relation is shown by solid lines (using the same color legend). The Q value for the reaction at $q = 0$ is the energy shift $\Sigma_n(k) - \Sigma_p(k) \simeq 30$ MeV which is much larger than the rest mass difference $M_n - M_p = 1.3$ MeV. This large energy gain associated with $n \to p$ conversion shifts the outgoing electron energy to larger values and the overlap region between lepton and nucleon kinematic regions is enhanced. Further, the higher Q value also helps overcome the Pauli blocking in the final state for the degenerate electrons with $\mu_e/T \gtrsim 3 - 10$. In contrast, the $\bar{\nu}_e$ reaction is now kinematically forbidden because the $\bar{\nu}_e$ energy $E_\nu = 24$ MeV is insufficient to overcome the energy threshold $\simeq 30$ MeV to convert protons to neutrons.

This indicates rather distinct ν_e and $\overline{\nu}_e$ spectra, in sharp contrast with what one would expect when nuclear interactions are completely neglected. In the next section, we treat nucleon dispersion relations arising from many body effects.

1.3 Nucleon single-particle energies in the neutrino-sphere

Nucleon dispersion relations are modified in a hot and dense medium due to nuclear interactions. In this section, we calculate these modifications using realistic nuclear interactions in the HF approximation. In the HF, long-range correlations due to bound states in the particle-particle channel, polarization effects in the particle-hole channel, and Pauli-blocking of intermediate states are neglected. As we discuss later, this restricts us to high temperatures and the relatively low densities characteristic of the supernova neutrino-sphere. The self-consistent HF self-energy $\Sigma_{\rm HF}$ is defined through the Feynman diagrams shown in Fig. 1.2. We calculate

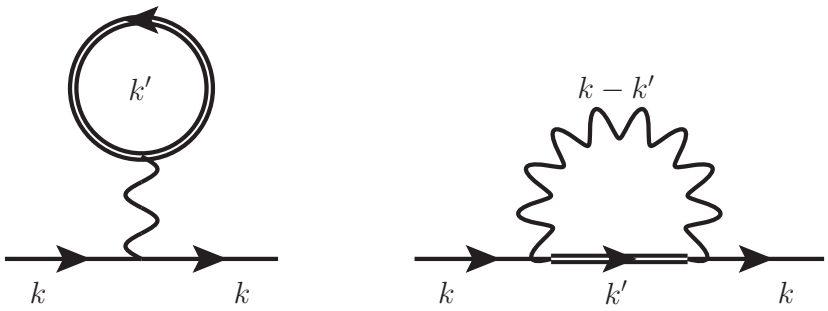

Figure 1.2: Feynman diagrams depicting the self-consistent HF self-energy. The double lines are the dressed nucleon propagators and wavy lines represent the NN interaction.

$\Sigma_{\rm HF}$ using the finite-temperature imaginary-time formalism for non-relativistic fermion propagators:

$$\begin{aligned} G_{\vec{k}}(i\omega_n) =& \frac{1}{i\omega_n - \xi(\vec{k})} \\ \omega_n =& 2(n+1)\pi T \end{aligned} \tag{1.3}$$

and find the standard expression

$$\Sigma_{\rm HF}(\vec{k}) = \sum\!\!\!\!\!\!\int \frac{d^4k'}{(2\pi)^4} \frac{\overline{V}(\frac{\vec{k}-\vec{k}'}{2}, \frac{\vec{k}-\vec{k}'}{2})}{i\nu_{k'} - \xi(\vec{k}')} = \int \frac{d^3k'}{(2\pi)^3} \overline{V}\left(\frac{\vec{k}-\vec{k}'}{2}, \frac{\vec{k}-\vec{k}'}{2}\right) f(\xi(\vec{k}'))\,, \tag{1.4}$$

where $\xi(\vec{k}') = \varepsilon(\vec{k}') - \mu = k'^2/2M + \Sigma(k') - \mu$ is the single-particle energy measured with respect to the non-relativistic chemical potential (the rest mass of the nucleon has been subtracted). The overline indicates that the potential matrix is antisymmetrized under particle exchange. The first argument is the relative momentun of the system of the two initial nucleons, and the second one is the respective for the outgoing nucleons. So, both contributions in Fig. 1.2 (the Hartree contribution on the left and the Fock contribution on the right) are contained in the single expression above. More details on the matrix element can be found in section 1.4.

The sum over Matsubara frequencies is performed to obtain the Fermi distribution function $f(\xi(k'))$ using the following identity:

$$\begin{aligned} T\sum_n F\big(k^0 = i(2n+1)\pi T\big) =& -\sum_a \mathrm{Res}_{z=a}\big[F(z) \times \frac{1}{2}\tanh(\frac{z}{2T})\big] \\ =& \sum_a \mathrm{Res}_{z=a}\big[F(z) \times \big(f(z) - \frac{1}{2}\big)\big] \\ \equiv& \sum_a \mathrm{Res}_{z=a}\big[F(z)\ f(z)\big] + \text{vacuum} \end{aligned} \tag{1.5}$$

The contribution from 1/2 in eq. 1.5 is due to the vacuum (which persists even when $T = 0$ and $\mu = 0$) and is neglected for matter calculations. a is the singular point of the function $F(z)$. In eq. 1.4, the nucleon propagator plays the role of this function and the self-energy is the singular point.

Since in this work we calculate the self-energy only at HF level in many body perturbation, we will drop the HF suffix, which from this point forward is implied.

For pure neutron matter the self-energy can be written as

$$\Sigma_n(\vec{k}) = \frac{1}{2\pi}\int_0^\infty k'^2 dk' \int_{-1}^1 d\cos\theta_{k'}\, f(\xi(\vec{k}')) \sum_{l,S,J} (2J+1)\Big\langle |(\vec{k}-\vec{k}')/2| \left|\overline{V}^{J1}_{llS}\right| |(\vec{k}-\vec{k}')/2| \Big\rangle\,, \tag{1.6}$$

where $\theta_{k'}$ is the angle between $\vec{k}'$ and $\vec{k}$. The self-consistent solution to Eq. (1.6) can be obtained by iteration. To simplify notation we set $p = |\frac{1}{2}(\vec{k} - \vec{k}')|$ in the following. In asymmetric matter, containing neutrons and protons we obtain the following coupled equations:

$$\Sigma_{m_t}(\vec{k}) = \frac{1}{2\pi}\int_0^\infty k'^2 dk' \int_{-1}^{1} d\cos\theta_{k'} \sum_{l,S,J,T,m'_t} (2J+1)\,|\mathcal{C}^{T\,m_t+m'_t}_{\frac{1}{2}\,m_t\,\frac{1}{2}\,m'_t}|^2\,\langle p|\overline{V}^{JT}_{llS}|p\rangle\, f(\varepsilon_{m'_t}(\vec{k}') - \mu_{m'_t}), \tag{1.7}$$

where m_t and m'_t label the isospin of the external and intermediate-state nucleon, respectively.

1.4 Nuclear potential matrix

We use a spherical decomposition to represent the anti-symmetrized potential in a partial-wave basis:

$$\langle \vec{p} S m_s T|\overline{V}|\vec{p}\,' S m'_s T\rangle = (4\pi)^2 \sum_{l,m,l',m',J,M} i^{l'-l}\, Y_l^m(\hat{p}) Y_{l'}^{m'*}(\hat{p}\,') C^{JM}_{lmSm_s} C^{JM}_{l'm'Sm'_s} \langle p|V^{JT}_{ll'S}|p'\rangle (1-(-1)^{l+S+T})\,, \tag{1.8}$$

where $\vec{p}$ and $\vec{p}\,'$ are relative momenta and $\overline{V} \equiv V(1-P_{12}) = V(1-(-1)^{l+S+T})$, with P_{12} the particle-exchange operator. The other symbols appearing in Eq. (1.8) have standard meaning: l, S, J and T are the relative orbital angular momentum, spin, total angular momentum and total isospin quantum numbers of the nucleon pair, and the projections of $\vec{S}$ and $\vec{l}$ onto the z-axis are given by the quantum numbers m_s and m, respectively.

We employed two approaches for the nuclear matrix element, chiral perturbation theory and the pseudo potential which are described respectively in subsections 1.4.1 and 1.4.2.

1.4.1 Potential from χEFT

As is well known, strong interactions are described by quantum chromodynamics (QCD). In this theory, the fundamental degrees of freedom are quarks, the matter constituents, and gluons, the force (interaction) carriers. Their interactions are characterized by non-Abelian gauge field theory with color SU(3) as the underlying gauge group. This non-abelian nature has immense consequences for the strength and nature (repulsive or attractive) of the interaction at various energy scales (inter - particle distances). For instance, in contrast to the familiar electromagnetic interaction, nuclear forces are rather weak at large momentum transfer ("asymptotic freedom"), and very strong at low energies leading to confinement of the quarks into colorless objects, the hadrons. In nuclear astrophysics, hadrons and their interactions are our focus. The residual strong interactions, the nuclear forces, between the hadrons, the building blocks of stars, govern the stability of very compact object against gravitational attraction and impact thermodynamical reactions, as well.

Nuclear physics at the low energies (from a QCD point of view), can be considered in analogy to Vander-Waals forces between neutral molecules. Thus, an efficient approach to tackle it is developed in terms of an effective theory for which nucleons are the relevant degrees of freedom and the pions are the force carries. Contact terms (short distaces) are required by (chiral) symmetry and incorporate the effects from high energy physics on low energy theory.

In order for this theory to be qualitatively and quantitatively successful, there must be a clear separation of (energy) scales, in the range of which all low energy symmetries are taken into consideration in the development of the effective Lagrangian. Quoting the essence of this algorithmic approach of 'theory making' in the words of Weinberg [40]:

"If one writes down the most general possible Lagrangian, including all terms consistent with assumed symmetry principles, and then calculates matrix elements with this Lagrangian to any given order of perturbation

theory, the result will simply be the most general possible S-matrix consistent with analyticity, perturbative unitarity, cluster decomposition, and the assumed symmetry principles."

The necessary steps of this algorithm can be summarized as follows:

1. Identification of soft and hard scales, and the appropriate degrees of freedom
2. Identification of all the relevant symmetries of the low energy theory (and if or how they are broken)
3. Construct the most general Lagrangian with the given degrees of freedom that respects the symmetries found (and respective symmetry breaking patterns)
4. Design an organizational scheme that can distinguish between more and less relevant terms (a low momentum expansion)
5. Using the low-momentum expansion calculate the Feynman diagrams for a given physical quantity up to the accuracy needed

And as already mentioned, chiral symmetry is almost exact in the low energy spectrum of QCD.

Chiral Symmetry in QCD

The QCD Lagrangian in terms of the quarks:

$$\mathcal{L}_{\text{QCD}} = \overline{q}(i\gamma^{\mu}\mathcal{D}_{\mu} - M)q - \frac{1}{4}\mathcal{G}_{\mu\nu,a}\mathcal{G}_{a}^{\mu\nu} \tag{1.9}$$

where, M is the mass matrix in flavor space and the covariant derivative is given by,

$$\mathcal{D}^{\mu} = \partial_{\mu} - ig\frac{\lambda_a}{2}A_{\mu,a} \tag{1.10}$$

and the gluon strength tensor:

$$\mathcal{G}_{\mu\nu,a} = \partial_{[\mu}A_{\nu]_{-},a} + gf_{abc}A_{\mu b}A_{\nu,c} \tag{1.11}$$

As per usual notation, q are the quark fields, A are the gluon fields, g is the coupling constant and f_{abc} are the structure constants of the lie algebra, while λ are the familiar Gell-Mann matrices [41].

Given the very small masses of up and down quarks [42] with respect to the other quarks, it is of practical interest to study the Lagrangian of only these two flavors in the limit of vanishing masses. In this limit, right and left handed quarks rotate independently in phase space. The respective projection operators are defined as:

$$\begin{aligned} P_{L,R} &= \frac{1}{2}(1 \pm \gamma_5) \\ q_{L,R} &= P_{L,R}q \end{aligned} \tag{1.12}$$

and the Lagrangian can be written as:

$$\mathcal{L}_{QCD}^{M=0} = \overline{q}_R i\gamma^{\mu}\mathcal{D}_{\mu}q_R + \overline{q}_L i\gamma^{\mu}\mathcal{D}_{\mu}q_L - \frac{1}{4}\mathcal{G}_{\mu\nu,a}\mathcal{G}_{a}^{\mu\nu} \tag{1.13}$$

Γ	1	γ^μ	$\sigma^{\mu\nu}$	γ_5	$\gamma^\mu\gamma_5$
$\gamma^0\Gamma\gamma^0$	1	γ^μ	$\sigma^{\mu\nu}$	$-\gamma_5$	$-\gamma^\mu\gamma_5$

Table 1.1: Parity transformation of Dirac matrices

Since left and right handed quarks don't mix, a new symmetry arises, $SU(2)_R \otimes SU(2)_L$, which is what we call chiral symmetry. Based on Noether's theorem, the following currents are conserved:

$$\begin{aligned} R_i^\mu &= \overline{q}_R \frac{\tau_i}{2} q_R, \ \partial_\mu R_i^\mu = 0 \\ L_i^\mu &= \overline{q}_L \frac{\tau_i}{2} q_L, \ \partial_\mu L_i^\mu = 0 \end{aligned} \tag{1.14}$$

These vector and axial currents are constructed as follows:

$$\begin{aligned} V_i^\mu &= R_i^\mu + L_i^\mu = \overline{q} \frac{\tau_i}{2} q \\ A_i^\mu &= R_i^\mu - L_i^\mu = \overline{q}\gamma_5 \frac{\tau_i}{2} q \end{aligned} \tag{1.15}$$

which are even and odd under parity transformation.

Specifically, under parity, a quark field transforms as follows:

$$q_f(t,\vec{x}) \xrightarrow{P} \gamma^0 q_f(t,-\vec{x}) \Longrightarrow \Gamma \xrightarrow{P} \gamma^0\Gamma\gamma^0 \tag{1.16}$$

The transformation for the bilinear operator Γ was derived by requiring Lagrangian invariance. The transformation of Dirac matrices is given in table 1.1. From eq. 1.15 and this table, one can deduce the claimed the properties of axial and vector currents.

For completeness, one should mention that the full symmetry structure of this Lagrangian should be $U(2) \times U(2) = SU(2)_R \otimes SU(2)_L \otimes U(1)_V \otimes U(1)_A$. $U(1)_V$ is the vector current, and $U(1)_A$ is the axial current.

In general, there are three main ways a symmetry of the Lagrangian is broken, and in the case of chiral symmetry all these are present.

1. A symmetry can be explicitly broken by a term; in the case of QCD, the mass term mixes left and right quarks, but due to the small values of these masses of the quarks under consideration, with respect to other scales in QCD, this is a 'soft' breaking. An additional source of soft explicit breaking is due to electromagnetic interactions among quarks.

2. The measure of the quantum path integral does not respect the symmetry; this is the case of $U(1)_A$, and such breaking is usually called anomalous. In other words, a classical symmetry is broken at the quantum level (scale).

3. The ground state of the system does not respect the symmetry, this is the familiar spontaneous symmetry breaking. In this regard, pions would be pseudo Goldstone bosons.

Spontaneous Symmetry Breaking

A continuous symmetry is considered spontaneously broken when it is a symmetry of the Lagrangian, and respected at the quantum level, but not realized in the ground state of the system.

As already mentioned, in the low energy of the QCD spectrum, quarks are confined within hadrons and mesons. While, based on the existence of both axial and vector current we would expect the ground state to show both types of symmetries, it is only parity even and the vacuum expectation value (vev) can be characterized by a non-vanishing di-quark condensate $\langle \overline{q}q \rangle$. This feature, [43], is not necessary for chiral symmetry breaking, but it is sufficient for our purpose here.

The light masses of the odd $\{\pi^{\pm}, \pi^0\}$ mesons are in agreement with them being considered pseudo Goldstone bosons. If there was no explicit symmetry breaking, pions would be massless. However, since the explicit breaking scale, at the level of a couple of MeV (up and down quark masses), is much lower than the spontaneous breaking scale of about 140 MeV, it is still very useful to think of these parity odd mesons as Goldstone bosons with masses added to the effective action.

By its very definition, an effective theory must be bounded by an energy range where it's predictions are valid. The high energy scale at which χEFT breaks down, which is commonly denoted by Λ_χ. The first meson of the non-Goldstone type to appear is the ρ meson and shows up as a resonance in p - wave π π scattering. Thus, the mass of this meson can be used as a simple estimate of the chiral breaking scale, $\Lambda_\chi \sim M_\rho \approx 770$ MeV. By expanding in terms of momentum exchange between nucleons divided by the hard energy scale Λ_χ, χEFT is a practical way to construct the nuclear potential order by order in a perturbative expansion.

Chiral Perturbation Expansion

The formalism for the construction of the Lagrangian was put in place by Callan, Coleman, Wess, and Zumino (CCWZ), by working on non-linear realizations of the chiral symmetry [44],[45]. Since the interaction of the Goldstone bosons must vanish in the zero momentum transfer limit, all pion couplings must be associated by the presence of derivatives or pion masses. Thus, the expansion in powers in Q/Λ_χ allows for a systematic organization of the relevant terms. This is, in simple terms, is chiral perturbation theory (χPT).

The effective Lagrangian can be formal written as,

$$\mathcal{L}_{eff} = \mathcal{L}_{\pi\pi} + \mathcal{L}_{\pi N} + \mathcal{L}_{NN} + ... \tag{1.17}$$

Here, both baryons and mesons are incorporated in the effective Lagrangian. In leading order (LO), the πN Lagrangian has been derived by Gasser et al [46]:

$$\mathcal{L}^{(1)}_{\pi N} = \overline{\Psi}(i\gamma^\mu \mathcal{D}_\mu - M_N + \frac{g_A}{2}\gamma^\mu\gamma_5 u_\mu)\Psi \tag{1.18}$$

where, Ψ in the baryon field, g_A is the effective low energy axial coupling, and,

$$\begin{aligned} \mathcal{D}_\mu =& \partial_\mu + \Gamma_\mu, \\ \Gamma_\mu =& \frac{1}{2}[\xi^\dagger, \partial_\mu \xi]_+, \;\; u_\mu = i[\xi^\dagger, \partial_\mu \xi]_- \\ \xi =& \sqrt{U}, \;\; U = \exp(i\vec{\tau}\cdot\vec{\pi}/f_\pi) \end{aligned} \tag{1.19}$$

$\vec{\tau}$ are the Pauli matrices, and f_π is the pion decay constant.

By expanding in pion fields, the leading order relativistic Lagrangian is,

$$\mathcal{L}^{(1)}_{\pi N} = \overline{\Psi}(i\gamma^\mu\partial_\mu - M_N - \frac{1}{4f_\pi^2}\gamma^\mu\vec{\tau}\cdot(\vec{\pi}\times\partial_\mu\vec{\pi}) - \frac{g_A}{2f_\pi}\gamma^\mu\gamma_5\vec{\tau}\cdot\partial_\mu + ...)\Psi \tag{1.20}$$

However, the relativistic treatment of baryons leads to problems. The time-derivative of a relativistic baryon field generates a factor $E \approx M_N$, which is not small compared to the chiral-symmetry breaking scale ($M/\Lambda_\chi \approx 1$).

Also, the nucleon mass does not vanish in the chiral limit. Thus, the one-to-one correspondence between the expansion in pion loops, on the one hand, and the expansion in terms of small external momenta and pion masses, on the other side, is destroyed [46, 47, 48]. A solution has been put forth by Jenkins and Manohar [49] using the heavy quark formalism developed by Georgi [50].

Power counting of the interactions between nuclei in χPT is a very complicated problem; while in the pion sector, naive dimensional analysis of Feynman diagrams proves to be a useful tool, in the nucleon sector it fails. Contrary to the interaction between Goldstone bosons (the pion sector), nucleons interact with each other in the limit of vanishingly small momenta and quark masses. Chiral symmetry does not constrain few-nucleon operators in the effective Lagrangian which contains derivative-less terms. In fact, the interaction between the nucleons at low energy is particularly strong. Shallow bound states such as the deuteron, triton etc. represent non-perturbative phenomena that cannot be described in perturbation theory. Weinberg, attributed the failure of perturbation theory to diagrams containing purely nucleonic intermediate states. He proposed to treat the nucleon mass as a separate hard scale according to the rule:

$$M_N \sim \frac{\Lambda_\chi^2}{Q} \gg \Lambda_\chi$$

where, Q is the typical momentum exchange bewteen nucleons, which should be comparable to the pion mass. The resulting power is what is commonly called as Weinberg power counting [51, 52, 53]. However, while this power counting works well for two nucleon forces, there are problems with higher number of nucleons [54, 55].

Before displaying the organization of many forces based on Weinberg's prescription, it is worth mentioning that power counting in the nucleon sector is far from a resolved issue. There are alternative approaches that have been developed since the pioneering work of Weinberg. The approach due to Kaplan, Savage and Wise (KSW) [56, 57] represents a generalization of the pionless EFT , which works well for very low energy processes, to perturbatively include diagrams with exchange of one or more pions. The scaling of the contact interactions is assumed to be the same as in pionless EFT. In contrast to pionless EFT, the pion mass is treated as a soft scale with $Q \sim m_\pi \sim a^{-1}$, where a is the nucleon - nucleon scattering length. Compact analytic expressions for the scattering amplitude are a particulalry nice feature of the KSW approach.

Appart from the regulation of the pion loops in the diagrammatic expansion of the potential order by order, there is an addition complication in that the nuclear potential has to be able to reproduce the nucleon scattering phase shifts measured in laboratory experiments. The connection between potential and scattering data is achieved through the Lippmann–Schwinger (LS) equation [58]:

$$T_l(p_1, p_2; k^2) = V(p_1, p_2) + 2M \int_0^\infty \frac{V_l(p_1, q) T(q, p_@, k^2)}{k^2 - q^2 + i\epsilon}$$

and the on-shell scattering matrix $T(p_1, p_2; k^2)$ can be described in terms in spherical basis in terms of the scattering phase shifts, $\delta_l(k)$:

$$T_l(k, k; k^2) = -\frac{2k}{\pi} \sin(\delta_l(k)) e^{i\delta_l(k)}$$

The converge of the KSW expansion was tested and found to fail in the spin-triplet channels [59, 60, 61]. While the power counting approach due to Weinberg allows for a nonperturbative resummation of the 1π-exchange potential, as mentioned previously there are complications that come with this treatment. Contrary to the KSW approach, the leading NN potential is non-renormalizable in the traditional sense (iterations of the LS equation generate divergent terms with structures that are not included in the original potential). To make matters worse, currently, resummation of the 1π-exchange potential in the LS equation can only be carried out numerically. This makes it impossible to use regularization prescriptions such as dimensional regularization

which avoids the appearance of hard scales. Most of the available calculations employ various forms of cut-off regularization (Λ), with the cut-off being kept finite. In theory there should not be any dependence on the cut-off, and taking it to be very large should not give rise to any problems. In practice the contrary is seen, with potentials obtained by employing cut-offs in the range 400 MeV $\lesssim \Lambda \lesssim$ 500 MeV being more perturbative than potentials with higher cut-off values. An additional reason for using lower cut-off potentials is to obtain better convergence in the many body perturbative calculations as discussed in subsection 2.2.3 in chapter 2. The interaction we are using in our calculation, from Ref. [62], is at N^3LO from the fig. 1.3 and the high momentum cut-off chosen Λ = 500 MeV. When we discuss the equation of state in the next chapter we employ a wider range of cut-offs. Finally, we are ready to give a systematic expansion of nucleon forces in χPT:

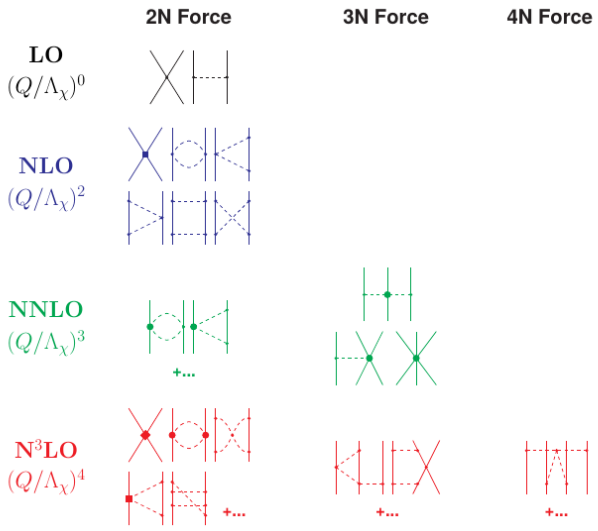

Figure 1.3: Figure taken from [55]. Hierarchy of nuclear forces in Weinberg power counting. Solid lines represent nucleons and dashed lines pions. Small dots, large solid dots, solid squares, and solid diamonds denote vertices of index $\triangle$= 0, 1, 2, and 4, respectively.

1.4.2 Pseudo Potential

In the second approach we define and use the pseudo-potential. As already mentioned, in the HF calculation, the N^{3}LO potential is treated in the Born approximation. In contrast, the pseudo-potential defined by the relation

$$\langle p|V_{llSJ}^{pseudo}|p\rangle = -\frac{\delta_{lSJ}(p)}{pM}\,, \tag{1.21}$$

is constructed from the measured nucleon-nucleon phase shifts $\delta_{lSJ}(p)$ in laboratory conditions, and should be viewed as including a re-summation of the ladder diagrams in the particle-particle channel. It is also known to correctly predict the energy shift in a system containing Fermions interacting strongly with a heavy impurity and is known in the context of condensed matter physics as Fumi's theorem [63].

1.5 Comparison with Virial Calculations

At low densities and high temperatures, where the neutron fugacity satisfies $z_n = e^{\mu_n/T} \ll 1$, the virial expansion provides a model-independent benchmark [64, 65]. This allows us to assess the validity of the HF

approximation at densities characteristic of the neutrino-sphere. First, we analyze the HF predictions for the energy per particle in pure neutron matter in the density range $n_B = 0.001 - 0.02$ fm^{-3} and temperature range $T = 5 - 10$ MeV. The particle number and energy density in HF in pure neutron matter are:

$$\begin{aligned} n &= 2 \int \frac{dk^3}{(2\pi)^3} f(\xi(\vec{k}))\,, \\ \mathcal{E} &= 2 \int \frac{dk^3}{(2\pi)^3} \left(\varepsilon(\vec{k}) - \frac{1}{2}\Sigma_n(\vec{k})\right) f(\xi(\vec{k}))\,. \end{aligned} \tag{1.22}$$

In the following we show that the pseudo-potential when used in the HF approximation reproduces the energy shift predicted by the virial expansion which is known to be exact in the limit of low density and high temperature. In the virial expansion, two-body interactions are included through the second virial coefficient b_2, which is directly related to scattering phase shifts and is given by

$$b_2 = \frac{1}{\pi\sqrt{2}\,T} \int_0^\infty d\epsilon\, e^{-\epsilon/2T} \sum_{lSJ} (2J+1)\delta_{lSJ}(\epsilon) - 2^{-5/2}\,, \tag{1.23}$$

where $\epsilon = p^2/2m$ is the kinetic energy and the sum is over allowed partial waves. The number density n and the energy density $\mathcal{E}$ are calculated in terms of the b_2 coefficient and are given by [65]

$$\begin{aligned} n &= \frac{2}{\lambda^3}(z_n + 2z_n^2 b_2)\,, \\ \mathcal{E} &= \frac{3T}{\lambda^3}\left[z_n + z_n^2\left(b_2 - \frac{2}{3}T b_2'\right)\right], \end{aligned} \tag{1.24}$$

where $b_2' = db_2/dT$.

A detailed study of low-density hot matter in the virial expansion is presented in Refs. [64, 65]. Here we consider neutron matter and use the second virial coefficient computed in Ref. [65] to compare with the results obtained using the chiral NN potential and the pseudo-potential in the HF approximation. Results for $T = 8$ MeV are displayed in Fig. 1.4, which shows the change in the energy per particle due to NN interactions. At very low densities (with corresponding fugacities $z < 0.25$), the virial equation of state is well reproduced at the HF level when the pseudo-potential is used, in agreement with previous statistical-mechanics consistency checks [66, 67]. At the breakdown scale of the virial expansion $e^{\mu/T} \sim 0.5$, the pseudo-potential predicts additional attraction over the virial equation of state due to using full Fermi-Dirac distribution functions. On the other hand, the chiral NN potential when used in the HF approximation significantly underestimates the strength of the attractive mean field at low densities and therefore provides a conservative upper bound on the energy per particle at temperatures and densities beyond the scope of the virial expansion. Higher-order perturbative contributions from chiral NN interactions are attractive and could lead to a narrower uncertainty band for the energy per particle. We omit contributions from three-neutron forces, which are small at these low densities.

A comparison between the second-order virial calculation and the HF calculation of matter with a finite proton fraction $Y_p = n_p/(n_p + n_n)$, where n_n and n_p are the neutron and proton densities, is complicated by the presence of the deuteron bound state. The HF description solely in terms of neutrons and protons will fail at low temperature and density when there is a large abundance of deuterons and light nuclei. However, on general grounds we expect the abundance of weakly bound states such as the deuteron to decrease rapidly with increasing temperature and density. The second-order virial calculation provides a correct description of deuterons at low density and moderate temperature, but it does not capture the physics relevant to the dissolution of weakly bound states with increasing density. Finite-density effects due to Pauli blocking of

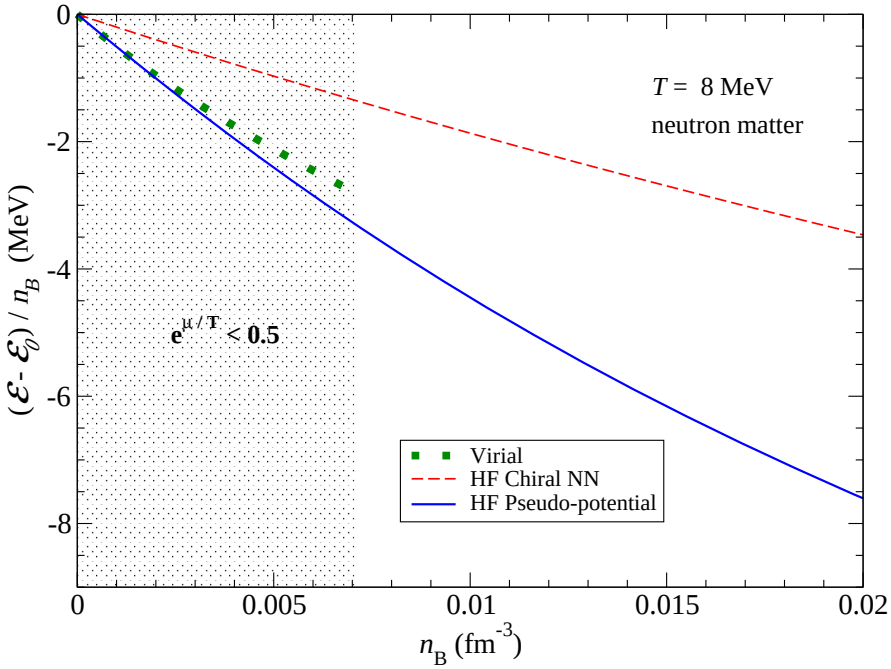

Figure 1.4: Change in the energy per particle of neutron matter from NN interactions in the Hartree-Fock (HF) approximation. Results for both the chiral NN potential and the pseudo-potential are shown and compared to the model-independent virial equation of state [65]. The shaded area denotes the density region in which the fugacity $z < 0.5$.

intermediate states in the T-matrix and modifications to the nucleon propagators alter the scattering in the medium at low momentum. Recent calculations have shown that this leads to a decrease in the binding energy of light nuclei [68]. These results indicate that the deuteron abundance is suppressed for $n_B \gtrsim 0.005$ fm^{-3} [68, 69, 70] even at relatively low temperatures. Since the typical densities encountered in the neutrino-sphere are larger, especially during the proto-neutron star phase, in the following we will neglect the deuteron pole and calculate the nucleon self-energies in the HF approximation using both the chiral NN potential and the pseudo-potential.

To assess the importance of the deuteron pole in neutron-proton scattering, we study its contribution in the second-order virial calculation. Since the contributions to the second virial coefficient from the bound state denoted by b^{d} and the scattering continuum denoted by b^{s} can be calculated separately [64], the ratio

$$r = \frac{b^{\mathrm{s}}}{b^{\mathrm{s}} + b^{\mathrm{d}}}\,, \tag{1.25}$$

is a measure of the relative importance of the scattering continuum. In the virial calculation r is independent of density and increases rapidly with temperature as shown in Fig. 1.5. At the physical value of the deuteron binding energy the contribution from the scattering continuum is about 70% at T = 8 MeV. Medium effects mentioned earlier reduce the deuteron binding energy, and although such changes to B_d are beyond the scope of the virial expansion, it is still useful to explore how the ratio r changes for smaller values of B_d.

The red-dashed curve in Fig. 1.5 was obtained by setting B_d = 1 MeV and shows how dramatically the deuteron contribution decreases with B_d. Model calculations of the reduction in the deuteron binding energy

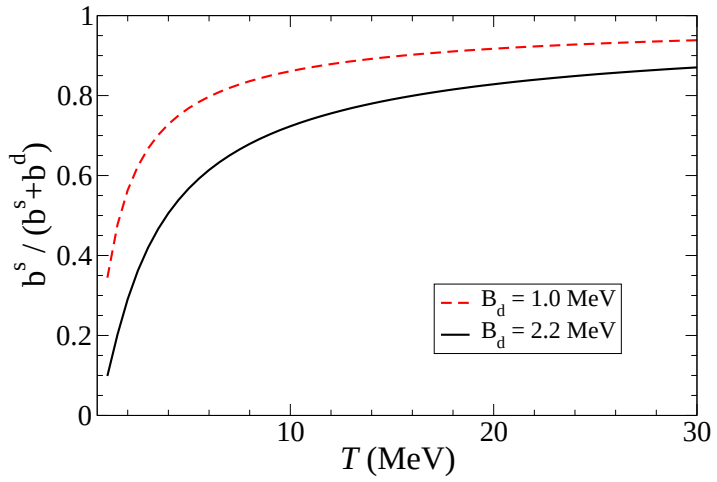

Figure 1.5: The relative importance of the scattering continuum contribution to the second virial coefficient (normalized with respect to the sum of bound- and scattering-state contributions). Results assuming a free-space deuteron binding energy and a medium-reduced binding energy of $B_d = 1.0\,\mathrm{MeV}$ are shown.

predict $B_d < 1$ MeV for $n_B > 0.005$ fm^{-3} for typical temperatures in the range $T = 5 - 10$ MeV [69].

The neutron-proton scattering phase shift at low energies in the $^3S_1$ channel is dominated by the deuteron bound state and by Levinson's theorem is set equal to π at zero momentum. This complicates the definition of the pseudo-potential that is to be used in the Born approximation since the potential constructed does not explicitly include these negative energy states. This in principle restricts the use of the pseudo-potential to large temperatures where we expect the deuteron abundances to be small. To assess the importance of the low-momentum behavior of the $^3S_1$ phase shifts we have modified them by hand. The modified potential mimics the low-momentum behavior expected for a resonance close to zero energy and asymptotically matches the original values of the $^3S_1$ phase shift at high momenta. We show both the original and modified versions of the $^3S_1$ phase shifts in Fig. 1.6. In Fig. 1.7 the pseudo potential for all isospin channels with and without the modification of the $^3S_1$ phase shift. To make a comparison between the HF and viral results for hot matter containing protons we consider neutron-rich matter at temperature $T = 8\,\mathrm{MeV}$ and determine the proton fraction in charge-neutral matter in beta-equilibrium for baryon densities in the range $n_B = 0.0001 - 0.02\,\mathrm{fm}^{-3}$. We solve for the proton and neutron single-particle energies self-consistently and use them to obtain the proton and neutron densities given by

$$n_i = \frac{1}{\pi^2}\int_0^\infty p^2 dp \frac{1}{e^{(p^2/2M_i + \Sigma_i(p) - \mu_i)/T} + 1}\,. \tag{1.26}$$

Attractive interactions between neutrons and protons increase the proton fraction Y_p relative to the non-interacting case as is evident from Fig. 1.8, which shows the proton fraction as a function of the density from different treatments of nuclear interactions. At the lower densities where the virial expansion is reliable, the HF pseudo-potential matches its predictions well. The HF calculation with the chiral potential underestimates the attraction between neutrons and protons and predicts lower values of Y_p.

Since the deuteron pole is a nonperturbative characteristic of nuclear interactions, many body calculation at HF level does not provide a reliable treatment of the neutron-proton $^3S_1$ channel, which is nonetheless included in defining the pseudo-potential. We study how the results are affected when the low-energy $^3S_1$ phase shifts are modified. The alteration is designed to replace the bound state by a scattering resonance at low momentum

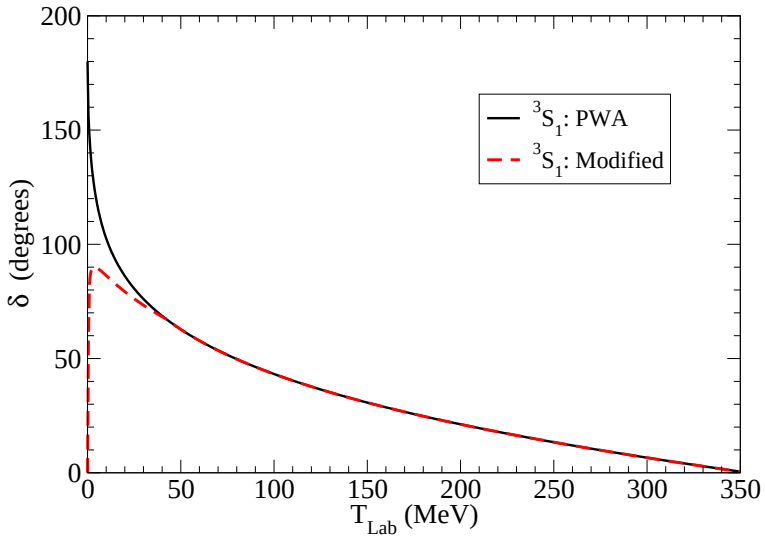

Figure 1.6: ${}^3S_1$ phase shift as a function of laboratory energy $T_{\rm lab}$ from the Nijmegen partial-wave analysis (PWA) [71] as well as those used in the modified pseudo-potential.

and to asymptotically match with the experimental values of the phase shifts at high momenta. By using the original and altered phase shifts in this channel a theoretical band for the prediction of the HF pseudo-potential approach can be provided as shown in Fig. 1.8 and in all future plots where the pseudo-potential results are shown.

The ambient conditions encountered in the neutrino-sphere span densities and temperatures in the range $n_B = 0.001 - 0.05\,\mathrm{fm}^{-3}$ and $T = 3 - 8$ MeV. To study the nuclear medium effects, we choose baryon density $n_B = 0.02\,\mathrm{fm}^{-3}$ and temperature $T = 8\,\mathrm{MeV}$ to compare with earlier results obtained in Ref. [72]. For these conditions the pseudo-potential predicts a proton fraction of $Y_p = 0.049$ (modified pseudo-potential: $Y_p = 0.038$), while for the HF chiral NN potential $Y_p = 0.019$. The neutron and proton momentum-dependent single-particle energies associated with mean-field effects from the nuclear pseudo-potential are shown with filled circles and squares in Fig. 1.9, and qualitatively similar results were found for the chiral NN potential and modified pseudo-potential. For convenience in calculating the charged-current reaction rates described later in the text, we parametrize the momentum dependence of the single-particle energies with an effective mass plus energy shift:

$$\varepsilon(k) = \frac{k^2}{2M} + \Sigma(k) \simeq \frac{k^2}{2M^*} - U\,, \tag{1.27}$$

where U is momentum independent. To demonstrate that the quadratic form in Eq. (1.27) provides a good description, we display in Fig. 1.9 the single-particle energies computed for the pseudo-potential (points) and quadratic fit (curves). The results for the proton and neutron effective masses and energy shifts are presented in Table 1.2. The Hartree-Fock energy from the chiral NN potential is considerably smaller for both protons and neutrons than those obtained using the pseudo-potential. The pseudo-potential predictions are also higher than those obtained in the relativistic mean-field (RMF) models employed in recent astrophysical simulations [72, 73]. Simple RMF models such as the GM3 model from Ref. [74] provide a fair description of symmetric nuclei but fail to reproduce ab-initio neutron matter calculations and are therefore not suitable for asymmetric

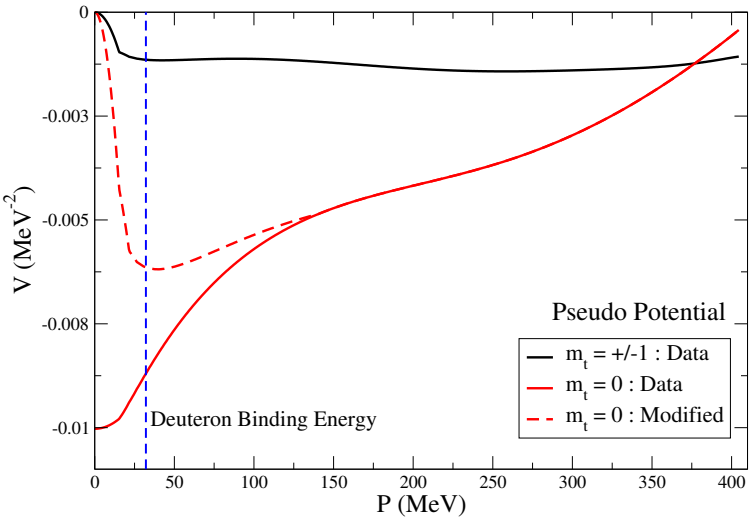

Figure 1.7: The pseudo-potential as a function of the momentum exchange from the Nijmegen partial-wave analysis (PWA) [71]. m_t is the isospin channel of the interaction. The red dashed line is due to the modified $^3S_1$ phase shift. The blue dashed line in the momentum exchange corresponding to the deuteron binding momentum ($p \approx \sqrt{\mathrm{B_d}\ M_n/2} \approx 32.2$ MeV)

matter calculations. In contrast, a new class of RMF models, such as the IUFSU model from Ref. [75], that are constructed to simultaneously provide a good description of nuclear masses, neutron skin measurements, and match ab-initio calculations of pure neutron matter predict larger energy shifts and are closer in magnitude to those obtained using the HF pseudo-potential approach.

Model	Y_p	M_n^*/M_n	M_p^*/M_p	U_n	U_p	ΔU
HF Pseudo-potential	4.9%	0.65	0.42	22	55	33
HF Pseudo-potential (mod)	3.8%	0.78	0.57	18	42	23
HF Chiral N^{3}LO Λ = 500 MeV	1.9%	0.94	0.90	7	10	3
RMF: GM3	2.5%	0.96	0.96	14	23	9
RMF: IUFSU	4.0%	0.94	0.94	31	52	21
RMF: DD2	4.2%	0.92	0.92	9	25	16

Table 1.2: The Hartree-Fock (HF) effective masses M^* and energy shifts U (in units of MeV) for protons and neutrons in beta equilibrium at $n_B = 0.02\,\mathrm{fm}^{-3}$ and temperature $T = 8\,\mathrm{MeV}$. The difference in proton and neutron mean-field shifts is given by $\Delta U = U_p - U_n$, and the proton fraction is denoted by Y_p. Results for both the pseudo-potential and its modified (mod) version are compared to those from the chiral NN interaction and RMF models [72, 76].

In Fig. 1.10 we show the difference in the neutron and proton self-energies for the chiral NN potential and the pseudo-potential. The momentum dependence is also quite different for these two cases. While the effective masses of proton and neutron quasi-particles are similar and close to bare masses when chiral NN interactions are treated in the HF approximation, the implicit iteration of NN interactions in the pseudo-potential results in proton and neutron effective masses that are quite different from each other and much smaller than the free-space masses. The density dependence of self-energy shifts and nucleon effective masses are shown in Figures 1.11 and 1.12 respectively. As discussed earlier, the band for the pseudo-potential represents the variation expected

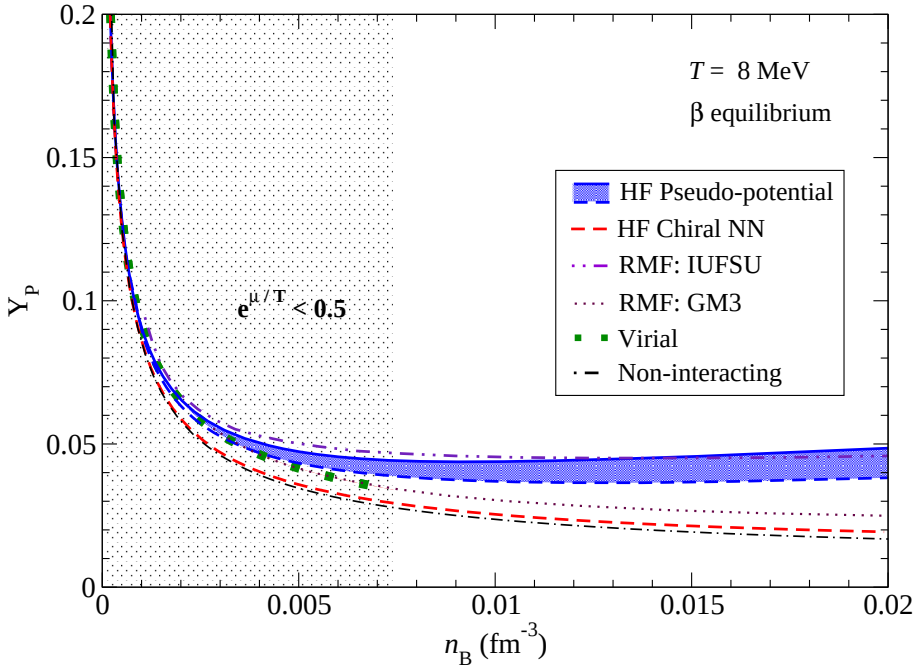

Figure 1.8: The proton fraction Y_p as a function of density for matter in beta-equilibrium at temperature $T = 8$ MeV. Results for the chiral NN potential and the pseudo-potential in the Hartree-Fock (HF) approximation are shown. The shaded Y_p band is enclosed by solid and dashed lines resulting from the pseudo-potential and modified pseudo-potential calculations, respectively. The region between the HF chiral and HF pseudo-potential band should be considered as a conservative uncertainty range. In addition, we compare to the model-independent virial equation of state [65] as well as the predictions from relativistic mean-field (RMF) theory [72]. The shaded area denotes the density region in which the fugacity $z < 0.5$.

for different treatments of the low-momentum behavior of the potential in the deuteron channel. The rapid increase in $\Delta U = U_n - U_p$ and a similarly rapid decrease in the nucleon effective masses obtained in the HF pseudo-potential approach are quite intriguing. Although the HF pseudo-potential approach is well motivated at these low densities and high temperatures as discussed earlier, these predictions for the self-energies are surprisingly large and have to be tested with explicit higher-order calculations in the many-body expansion. For now, it would be reasonable to suppose that the range spanned by the predictions of the HF chiral and HF pseudo-potential approaches represents our current uncertainty associated with non-perturbative effects. Using this as a representative range we discuss in the following section how the energy shifts and effective masses influence the neutrino/anti-neutrino mean free paths at the temperatures and densities of relevance to the neutrino-sphere.

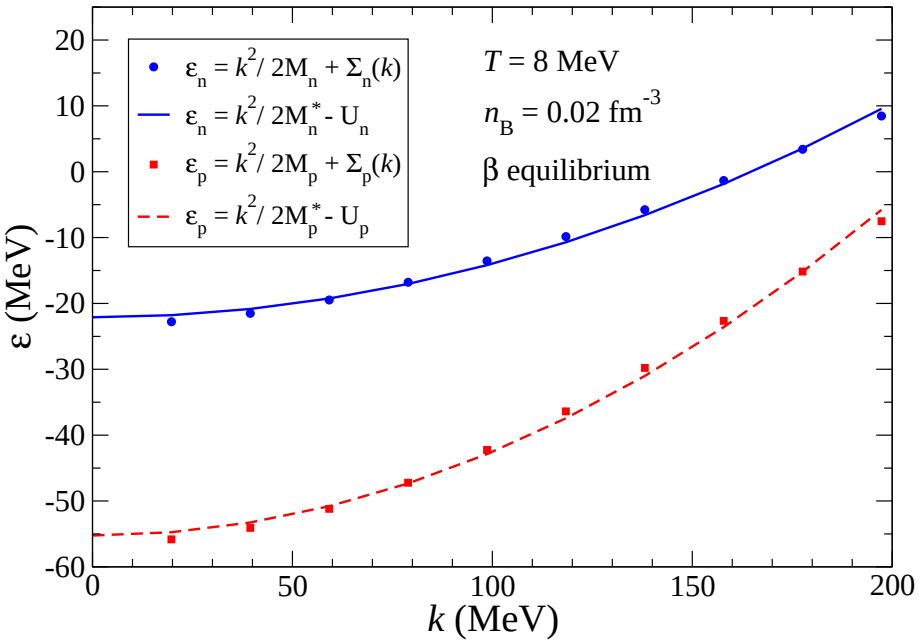

Figure 1.9: Momentum dependence of the neutron and proton single-particle energies in hot (T = 8 MeV) and dense (n_B = 0.02 fm^{-3}) beta-equilibrated nuclear matter calculated in the HF approximation from the pseudo-potential. The solid and dashed lines are parametrized fits, with the form given in Eq. (1.27), of the non-relativistic dispersion relations for protons and neutrons respectively.

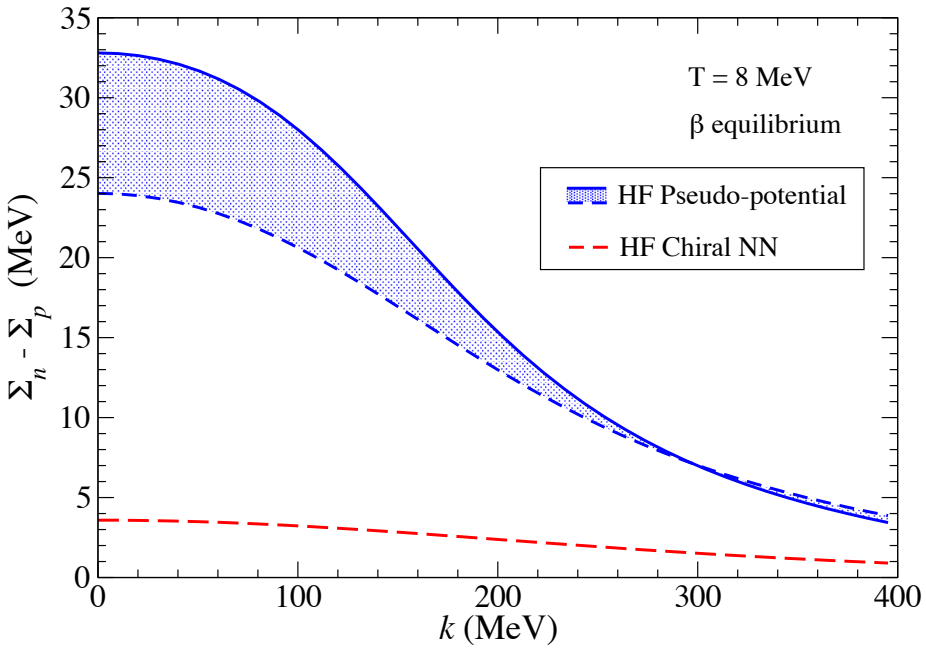

Figure 1.10: Difference in the momentum-dependent self-energies of neutrons and protons in the HF approximation for beta-equilibrated matter at $n_B = 0.02\,\mathrm{fm}^{-3}$ and temperature $T = 8\,\mathrm{MeV}$. Results for the chiral NN potential and pseudo-potential are shown.

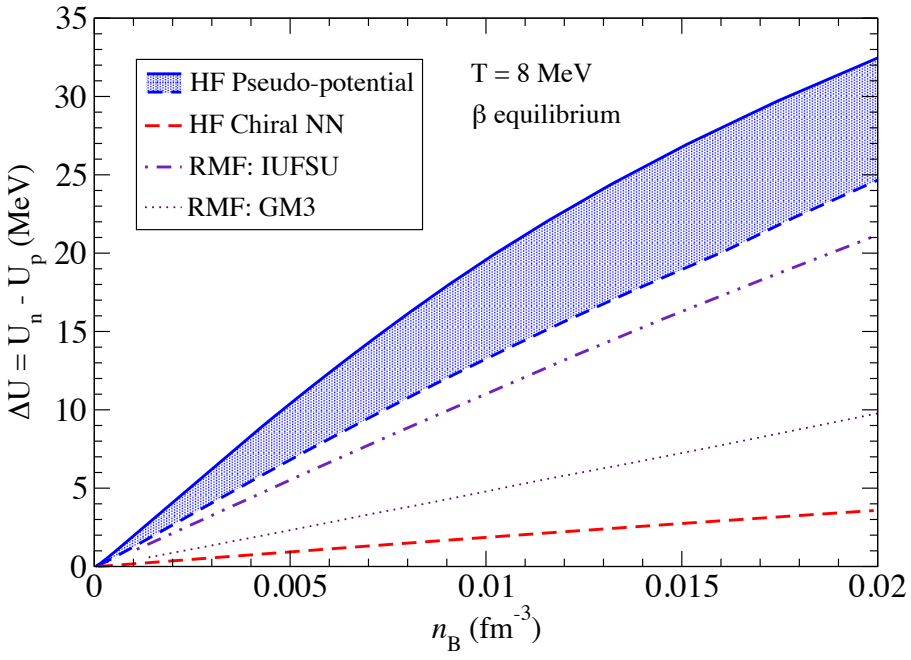

Figure 1.11: Difference in the HF proton and neutron energy shifts U, defined in Eq. (1.27), as a function of the density. The results from the pseudo-potential and chiral NN interaction are compared to those from RMF models [72].

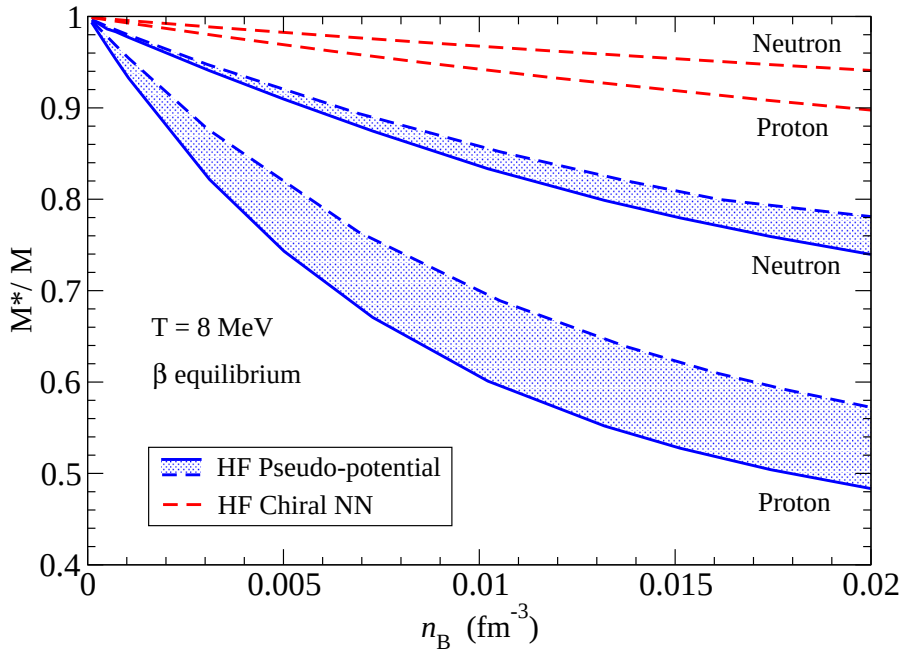

Figure 1.12: Proton and neutron effective masses M^*/M in the HF approximation as a function of the density for the pseudo-potential and chiral NN interaction.

1.6 Neutrino charged current cross section

The differential cross-section for the reaction $\nu_e + n \to e^- + p$ follows from Fermi's golden rule and is given by

$$\frac{d\sigma}{V} = \frac{2}{(2\pi)^5} \int d^3p_n\, d^3p_e\, d^3p_p\; \mathcal{W}_{fi}\; \delta^{(4)}(p_{\nu_e} + p_n - p_e - p_p) f_n(\xi_n)(1 - f_e(\xi_e))(1 - f_p(\xi_p))\,, \tag{1.28}$$

where $f(\xi)$ and E are the Fermi distribution functions and energies of the particles, and

$$\mathcal{W}_{fi} = \frac{\langle|\mathcal{M}|^2\rangle}{2^4 E_n E_p E_e E_{\nu_e}} \tag{1.29}$$

is the transition probability. $\langle|M|^2\rangle$ is the squared matrix element (corresponding to the diagram in Fig. 1.13), averaged over initial spin states and summed over the final spin states. For the reaction $\bar{\nu}_e + p \to e^+ + n$ one obtains a similar expression but with the replacement: $n \leftrightarrow p$, $e^- \to e^+$, and $\nu_e \to \bar{\nu}_e$. To simplify notation, we label the incoming neutrino as particle 1 with four-momentum $p_1 = (E_1, \vec{p}_1)$, the incoming baryon as particle 2 with four-momentum $p_2 = (E_2, \vec{p}_2)$, and the outgoing lepton and baryon by the particle labels 3 and 4, with four-momenta $p_3 = (E_3, \vec{p}_3)$ and $p_4 = (E_4, \vec{p}_4)$, respectively.

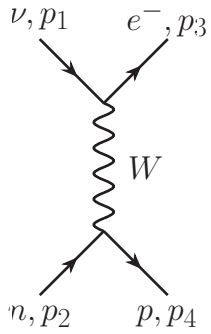

Figure 1.13: Tree-level scattering amplitude for the process $\nu_e + n \to e^- + p$.

In the non-relativistic limit, retaining only terms independent of the nucleon velocity, Eq. (2.39) simplifies to

$$\frac{1}{V}\frac{d^2\sigma}{d\cos\theta\, dE_3} = \frac{G_F^2 \cos^2\theta_C}{4\pi^2} |\vec{p}_3|\, E_3\, (1 - f_3(\xi_3))\Big[(1 + \cos\theta) S_\tau(q_0, q) + g_A^2 (3 - \cos\theta) S_{\sigma\tau}(q_0, q)\Big]\,, \tag{1.30}$$

where $g_A = 1.26$ is the nucleon axial charge, θ is the angle between the initial-state neutrino and the final-state lepton, and θ_C is the Cabibbo angle. $S_\tau(q_0, q)$ and $S_{\sigma\tau}(q_0, q)$ are the response functions associated with the Fermi and Gamow-Teller operators, respectively [72]. The energy transfer to the nuclear medium is $q_0 = E_1 - E_3$, and the magnitude of the momentum transfer to the medium is $q^2 = E_1^2 + E_3^2 - 2E_1E_3\cos\theta_{13}$, because for the leptons $|\vec{p}_1| = E_1$ and $|\vec{p}_3| = E_3$. In general, the response functions $S_\tau(q_0, q)$ and $S_{\sigma\tau}(q_0, q)$ are different because of isospin and spin-isospin dependent correlations in the medium [77, 36]. However, in the HF approximation $S_\tau(q_0, q) = S_{\sigma\tau}(q_0, q) = S_{\rm F}(q_0, q)$ where

$$S_{\rm F}(q_0, q) = \frac{1}{2\pi^2} \int d^3p_2 \delta(q_0 + E_2 - E_4) f(E_2)(1 - f(E_4))\,, \tag{1.31}$$

is the response function for a non-interacting Fermi gas, and follows directly from Eq. (2.39). The effects of interactions are included in Eq. (1.31) by using the HF self-energies for neutrons and protons calculated in Sec. 1.3. We use the quadratic form defined by Eq. (1.27):

$$E_2 = M_2 + \frac{p_2^2}{M_2^*} - U_2 \quad \text{and} \quad E_4 = M_4 + \frac{p_4^2}{M_4^*} - U_4\,, \tag{1.32}$$

where M_2, M_4 are the physical masses, M_2^*, M_4^* are the effective masses, and U_2, U_4 are the momentum-independent interaction-energy shifts of the initial- and final-state nucleon, respectively. It is also straightforward to include in the nucleon currents corrections due to weak magnetism of order $|\vec{p}|/M$. To do so, we explicitly calculate the square of the matrix element appearing in Eq. (1.29) for the Fermi weak interaction Lagrangian

$$\mathcal{L} = \frac{G_F}{2\sqrt{2}}\,\bar{\psi}_4(g_V\gamma_\mu + ig_M\,\frac{\sigma_{\mu\nu}q^\nu}{M} - g_A\gamma_\mu\gamma_5)\psi_2\cdot\bar{e}_3(\gamma^\mu-\gamma^\mu\gamma^5)\nu_1\,, \tag{1.33}$$

where the ψ's are the nucleon spinors and e and ν are the final-state lepton and initial-state neutrino spinors. The nucleon current has a vector component with $g_V = 1$, an axial-vector component with $g_A = 1.26$, and a Pauli component that incorporates weak magnetism with $g_M = 3.71$ [78]. The differential cross-section per unit volume can be written as

$$\frac{d\sigma(E_1)}{V\,d\Omega dE_3} = E_3^2\,(1-f_3(E_3))\int\frac{d^3p_2}{(2\pi)^3}\,\mathcal{W}_{\rm fi}\,\delta(E_1+E_2-E_3-E_4)f_2(E_2)(1-f_4(E_4))\,. \tag{1.34}$$

1.7 Transition rate including weak magnetism for non-relativistic nucleons

In this section the expressions for the transition rate $\mathcal{W}_{fi}$ including the contribution from weak magnetism are derived. We shall consider thermal neutrinos with energy $E_\nu \simeq T$ and calculate $\mathcal{W}_{fi}$ to linear order in T/M where M in the the average nucleon mass. The expressions are derived for neutrinos, and analogous expression for anti-neutrinos are obtained by the substitution $\{g_V, g_M\} \to \{-g_V, -g_M\}$.

The transition rate

$$\mathcal{W}_{fi} = \frac{\langle|\mathcal{M}|^2\rangle}{2^4E_1E_2E_3E_4}\,, \tag{1.35}$$

where

$$\begin{aligned}\langle|\mathcal{M}|^2\rangle &= \frac{1}{8}\,G_F^2\,\mathrm{Tr}\Big[\,\gamma^\mu(1-\gamma^5)\,\not{p}_1\,\gamma^\nu(1-\gamma^5)\,\not{p}_3\,\Big]\\ &\quad\times\mathrm{Tr}\Big\{\Big[\,\gamma_\mu(g_V-g_A\gamma^5)+ig_M\frac{\sigma_{\mu\alpha}q^\alpha}{M}\,\Big](\not{p}_2+M_2)\Big[\,\gamma_\nu(g_V-g_A\gamma^5)-ig_M\frac{\sigma_{\nu\alpha}q^\alpha}{M}\,\Big](\not{p}_4+M_4)\Big\}\\ &\equiv 8\,G_F^2(\langle|\mathcal{M}|^2\rangle^{VA}+\langle|\mathcal{M}|^2\rangle^{VAM}+\langle|\mathcal{M}|^2\rangle^{M})\,.\end{aligned} \tag{1.36}$$

is the square of the matrix element summed over final-state spins and averaged over initial-state spins for the interaction in Eq. (1.33). Here, the vector-axial part is given by

$$\langle|\mathcal{M}|^2\rangle^{VA} = (g_A-g_V)^2\;(p_1\cdot p_4)(p_2\cdot p_3)+(g_A+g_V)^2\;(p_1\cdot p_2)(p_3\cdot p_4)+(g_A^2-g_V^2)\;M_2M_4\;(p_1\cdot p_3)\;, \tag{1.37}$$

the mixed term is given by

$$\begin{aligned}\langle|\mathcal{M}|^2\rangle^{VAM} = -\frac{g_M}{M}\Big\{&\;(p_1\cdot q)\Big[\;(2g_A-g_V)M_4(p_2\cdot p_3)+(2g_A+g_V)M_2(p_3\cdot p_4)\;\Big]+(p_4\cdot q)g_VM_2(p_1\cdot p_3)\\ &-(p_2\cdot q)g_VM_4(p_1\cdot p_3)-(p_3\cdot q)\Big[\;2(g_A+g_V)M_4(p_1\cdot p_2)-(2g_A-g_V)M_2(p_1\cdot p_4)\;\Big]\;\Big\}\,,\end{aligned} \tag{1.38}$$

and the contribution due to weak magnetism is given by

$$\langle|\mathcal{M}|^2\rangle^M = \frac{g_M^2}{M^2}\Big\{ (p_1\cdot q)\Big[(p_2\cdot q)(p_3\cdot p_4) - (M_2M_4 + p_2\cdot p_4)(p_3\cdot q) + (p_2\cdot p_3)(p_4\cdot q)\Big] + (p_3\cdot q)\Big[(p_1\cdot p_4)(p_2\cdot q) + (p_1\cdot p_2)(p_4\cdot q)\ \Big] - q^2\Big[(p_1\cdot p_3)(M_2M_4 - p_2\cdot p_4) + 2\Big[(p_1\cdot p_4)(p_2\cdot p_3) + (p_1\cdot p_2)(p_3\cdot p_4)\ \Big]\ \Big]\Big\}. \tag{1.39}$$

Setting $q^\mu = p_1^\mu - p_3^\mu$, these results confirm eqs. (11) and (12) in Ref. [79].

At this stage only the electron and neutrino masses have been neglected because they are small compared to the thermal energies of the lepton $E_1 \simeq |\vec{p}_1| \sim T$ and $E_3 \simeq |\vec{p}_3| \sim T$. In addition, for the typical ambient conditions we consider here, nucleons are non-relativistic and non-degenerate thus $|\vec{p}_2| \sim \sqrt{MT}$ and $|\vec{p}_4| \sim \sqrt{MT}$. Since the nucleon mass is large compared to the temperature it is useful to define the following expansion parameters

$$\begin{pmatrix} \{\chi_1,\ \chi_3,\ \chi_0\} \\ \{v_2,\ v_4,\ \chi_q\} \end{pmatrix} \equiv \begin{pmatrix} \{E_1/M,\ E_3/M,\ q_0/M\} \\ \{|\vec{p}_2|/M,\ |\vec{p}_4|/M,\ |\vec{q}|/M\} \end{pmatrix} \sim \begin{pmatrix} T/M \\ \sqrt{T/M} \end{pmatrix} \tag{1.40}$$

where elements in the first row are parametrical of order T/M and elements in the second row are order $\sqrt{T/M}$. Using energy-momentum conservation, $p_4^\mu = p_1^\mu + p_2^\mu - p_3^\mu$ and expanding to linear order in T/M:

$$\begin{aligned} \mathcal{W}_{fi} \approx \frac{G_F^2}{2} \times \Big\{ & \Big[g_V^2(1+\eta_{13}) + g_A^2(3-\eta_{13})\Big] && \mathcal{O}(1) \\ & + \Big[2\ g_M g_A \chi_q\ (\eta_{1q} - \eta_{3q}) - (g_A^2 + g_V^2) v_2 (\eta_{12} + \eta_{23})\Big] && \mathcal{O}(\sqrt{\frac{T}{M}}) \\ & + \Big[\frac{1}{2}\Big[\ (g_A + g_V)^2\chi_1 - (g_A - g_V)^2\chi_3\ \Big](1-\eta_{13}) + (g_A^2 + g_V^2) v_2^2 \eta_{12}\eta_{23} \\ & \quad + 2\ g_M g_A v_2 \chi_q\ (\eta_{12}\eta_{3q} - \eta_{1q}\eta_{23}) + g_M^2 {\chi_q}^2 (1 - \eta_{1q}\eta_{3q})\Big]\Big\} && \mathcal{O}(\frac{T}{M}) \end{aligned}$$

where the first line contains terms of $\mathcal{O}(1)$, the second line contain terms of $\mathcal{O}(\sqrt{T/M})$ and the third and fourth lines contains terms of $\mathcal{O}(T/M)$. The angles between three vectors $\vec{p}_i$ and $\vec{p}_j$ is denoted by η_{ij} and the angle between $\vec{p}_i$ and $\vec{q}$ is denoted by η_{iq}.

1.8 The differential absorption rates

The differential absorption rates for neutrinos and anti-neutrinos are shown in Fig. 1.14. The rates are shown as a function of the energy of the outgoing lepton (e^- for $\nu_e + n \to p + e^-$ or e^+ for $\bar{\nu}_e + p \to n + e^+$) and for an incoming neutrino energy of 24 MeV which is the mean thermal energy $E_\nu \sim 3T = 24$ MeV at the ambient temperature of $T = 8$ MeV. The trends seen in the figure can be understood on the basis of our earlier discussion of reaction kinematics in Sec. 1.2, where it was shown that the interaction-energy shifts in neutron-rich matter enhance the rate for ν_e absorption and suppress the $\bar{\nu}_e$ rate. Further, since the energy shifts are larger and the effective masses are smaller for the pseudo-potential, charged-current rates calculated using the pseudo-potential show larger differences than with the chiral NN potential in the Born approximation.

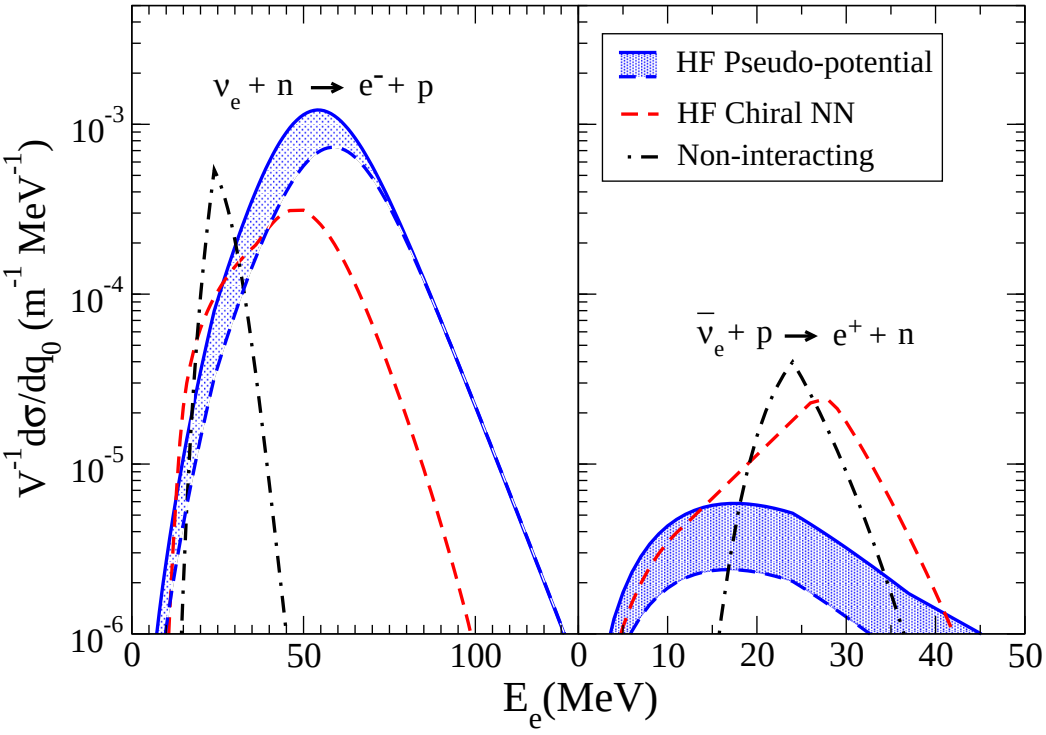

Figure 1.14: Effect of the in-medium neutron (proton) dispersion relation on the differential cross-section for (anti-)neutrino absorption as a function of the outgoing lepton energy E_e. We consider an incoming neutrino energy $E_\nu = 24$ MeV and matter in beta equilibrium at a density $n_B = 0.02$ fm^{-3} and temperature $T = 8$ MeV, including weak magnetism and leading $|\vec{p}|/M$ corrections. The chiral NN interaction and pseudo-potential are both used in the HF approximation. This provides a range for the theoretical uncertainty due to the many-body treatment, which can be improved by performing higher-order calculations.

1.9 Neutrino mean free path

The inverse neutrino mean free path for the absorption reactions mentioned, $\lambda_\nu^{-1}(E_\nu) = v_{\rm rel}\sigma/V$, where $v_{\rm rel} = c$ is the relative velocity for relativistic neutrinos, can be calculated by numerical integration of the differential cross-section defined in Eq. (1.34). The results shown in Fig. 1.15 follow the trends expected from the results for the differential cross-section. The difference between neutrino and anti-neutrino mean free paths is enhanced by the difference between the neutron and proton self-energies, and is larger for the case where the HF self-energy was obtained using the pseudo-potential. Our range for the mean free paths should be compared with those obtained in Refs. [73, 72]. We refer to Fig. 1 in Ref. [73] and Figs. 2 and 3 in Ref. [72] where similar results were obtained using a phenomenological RMF model. Our results are qualitatively similar to those obtained earlier, but important quantitative differences exist. The $\nu_e + n \rightarrow e^- + p$ rate is enhanced by almost a factor of 7 relative to the non-interacting case for $E_\nu = 24$ MeV and the $\bar{\nu}_e + p \rightarrow e^+ + n$ rate is suppressed by a larger factor $\simeq 30$. Under these conditions, neutral current scattering $\bar{\nu}_e + N \rightarrow \bar{\nu}_e + N$ and the inverse bremsstrahlung process $\bar{\nu}_e + \nu_e + N + N \rightarrow N + N$, where N can be either a neutron or a proton, can be expected

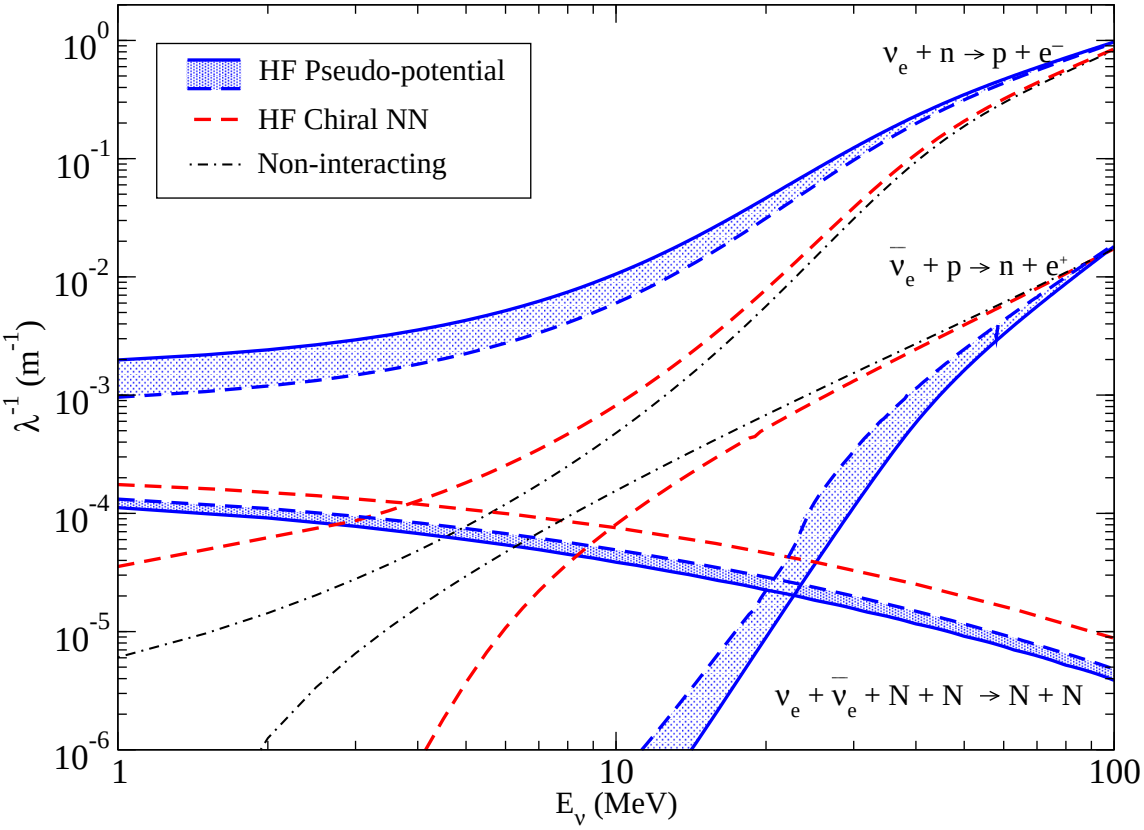

Figure 1.15: Effect of the in-medium neutron (proton) dispersion relation on the (anti-)neutrino absorption mean free path in beta-equilibrated matter at density $n_B = 0.02$ fm^{-3} and temperature $T = 8$ MeV. The chiral NN potential and pseudo-potential are both used in HF approximation. This provides a conservative range for the theoretical uncertainty due to the many-body treatment, which can be improved by performing higher-order calculations. Also shown is the mean free path for the neutrino-pair absorption process.

to be more important. For energy exchange, the latter absorption process will be more relevant and is shown in Fig. 1.15. Its rate is given by [80]

$$\lambda^{-1}_{\rm Brems}(\omega_1) = 2\pi\, G_F^2\, n_B \int \frac{d^3\vec{k}_2}{(2\pi)^3}\,(3-\cos\theta) f_2 S_A(\omega_1+\omega_2)\ , \tag{1.41}$$

where $\vec{k}_2$ is the momentum of the neutrino, ω_1 and ω_2 are the energies of the anti-neutrino and neutrino, respectively, θ is the scattering angle, and f_2 is the occupation number of the neutrinos. We use the axial response function $S_A(\omega)$ from Ref. [81] and assume a Maxwell-Boltzmann distribution at temperature T for the neutrinos. The inverse mean free path due to the neutrino-pair absorption obtained using the chiral NN potential is shown in red, and results obtained using the full T-matrix potential (corresponding to our pseudo-potential for the self-energy calculations) is shown in blue using consistently the electron fractions and effective masses given in Table 1.2.

1.10 Conclusions

In this study we have presented a calculation of the HF self-energy of protons and neutrons in the hot neutron-rich matter encountered in the neutrino-sphere of supernovae and used them to calculate the charged-current neutrino and anti-neutrino mean free paths. The mean free paths were found to be quite sensitive to the nucleon dispersion relation, especially to the difference in the energy shifts experienced by neutrons and protons in hot and relatively low-density neutron-rich matter. The difference between the results obtained using a chiral N^3LO potential and the pseudo-potential is large and indicates that non-perturbative effects in the particle-particle channel, which are approximately included in the pseudo-potential, are important. A desirable feature of the HF pseudo-potential approach is that it reproduces the predictions of the virial calculation for the energy shifts which are exact in the low-density, high-temperature limit. However, the reader should not assume the results obtained by the pseudo-potential at the densities and temperatures comparable to the ones displayed in Figs. 1.14 and 1.15 to be the definitive answer. Instead, it would be prudent to treat the entire region between the HF chiral potential and pseudo-potential as a theoretical band, which needs to be further improved by higher-order many-body calculations. Indeed, the chiral potential used in this study reproduces the NN phase shifts, and thus the difference found should not be attributed to a failure of the effective theory. To obtain the phase shifts, the LS equation must be used, while the pseudo potential is what one would obtain if only the first term in the Born series expansion was kept (hence the pseudo potential can be directly expressed from scattering data). If the chiral potential is used in many-body higher-order diagrams (beyond just HF), one would expect the result to be closer to the pseudo potential band. The uncertainty associated with not including the deuteron bound state contribution consistently in the HF pseudo-potential approach was studied by altering the low-momentum $^3S_1$ phase shift to mimic the behavior expected from a low-energy resonance. This error was found to be relatively small in comparison at the relevant temperatures and densities. Although the RMF model predictions are roughly consistent with the theoretical band it should be noted that they are constrained by fitting to the properties of nuclei, which are largely determined by the behavior at nuclear saturation density and small isospin asymmetry and zero temperature. The error introduced by their extrapolation to low density, large isospin asymmetry and high temperature can be large.

At temperatures lower than those considered in the present work, the importance of Pauli blocking precludes the use of the pseudo-potential, and an alternative strategy would be to employ an in-medium T-matrix as an effective interaction. This framework treats on equal footing quasi particle energy shifts from the nuclear mean field and Pauli blocking in intermediate states, both of which tend to suppress the role of the strongly attractive components of the nuclear interaction. Consequently, we can expect that the large energy shifts reported in the present study should be reduced in this regime, while at higher temperatures the in-medium T-matrix and pseudo-potential results could be expected to match quantitatively.

The larger difference between neutrino and anti-neutrino rates compared to the predictions of the RMF models will have an impact on supernova nucleosynthesis. To quantitatively gauge its importance it will be necessary to incorporate these new rates into supernova and PNS simulations and predict the resulting neutrino spectra. Qualitatively, we can anticipate a larger $\delta\epsilon$ that would favor smaller Y_e in the neutrino-driven wind compared to the predictions in Ref. [72] based on the RMF models. Simulations that incorporate our current results will be able to ascertain if the change in $\delta\epsilon$ is large enough to favor conditions for a robust r-process in the standard supernova neutrino-driven wind scenario. In addition, our calculations of neutrino cross sections were performed in the impulse approximation. Here we neglect vertex corrections (screening) and finite lifetime effects (damping), which arise because the weak interaction amplitude involving different nucleons in the system will interfere. These effects were studied within the purview of the RMF model in Ref. [72] and were found not to have as large of an effect as the corrections due to energy shifts because the typical energy and momentum transfer were large compared to characteristic scales associated with temporal and spatial correlations, respectively.

Nonetheless, these effects, which are known to be important in the study of neutral-current reactions, warrant further investigation. They can be systematically studied using chiral EFT interactions within self-consistent Green's functions where both particle-particle and particle-hole diagrams in the response function are partially re-summed. At the high densities and temperatures chosen for this study, alpha particles and light clusters are disfavored. However, for a better understanding of a wider range of ambient conditions encountered in the neutrino-sphere, the role of these micro-physical effects will need to be investigated and incorporated in proto-neutron star simulations, which will be explored in future work.

Chapter 2

Equation of State in Supernovae and Neutron Stars

2.1 Introduction

Astrophysical phenomena such as core collapse supernovae and binary neutron star mergers, including the accompanying gravitational wave production and heavy-element nucleosynthesis in the matter outflow, are sensitive to the thermodynamics of isospin-asymmetric nuclear matter across many orders of magnitude in the nuclear density. In contrast to the hot ambient conditions characterizing these astrophysical environments, the structure and evolution of neutron stars are largely governed by the properties of cold and dense neutron-rich matter. Efforts are underway to combine astrophysical observations of neutron star properties [82, 83, 84, 85, 86], terrestrial laboratory experiments of finite nuclei and hot/compressed nuclear matter [87, 88], and microscopic many-body theory [89, 90, 91, 92, 93, 94] to construct a more complete picture of the nuclear equation of state (EoS) across the range of conditions probed in supernovae and neutron star merger simulations.

The equation of state was briefly mentioned in the previous chapter and here we delve into the details of constructing it from mean field models and microscopic interactions, as well.

Traditionally mean field models, based on either Skyrme phenomenology [95] or relativistic mean field (RMF) theory [96, 97], have been the method of choice for constructing nuclear equations of state for numerical astrophysics simulations. This is primarily due to the computational simplicity of such models and the possibility to have semi - analytical expressions for the various thermodynamic quantities of interest. The energy scales probed are much below the regime where a perturbative treatment based on QCD, the fundamental theory of strong interactions, is feasible. Non-perturbative lattice QCD simulations may in principle overcome such difficulty, but at present multi-nucleon simulations are beyond the reach of modern supercomputers, although extracting a nucleon-nucleon interaction from lattice data is a topic of intense current research (see e.g., [98, 99, 100, 101, 102, 103, 104, 105, 106, 107, 108, 109]). An alternative is to construct a low-energy theory of strongly interacting matter, chiral effective field theory [40, 62, 110, 55], which has already had many successes in the description of nuclear structure and reactions of light and medium-mass nuclei [111, 112, 113, 114, 54, 115, 116, 117, 118, 119, 120], as well as nucleonic matter at zero temperature [121, 122, 123, 124, 125, 126, 127, 128, 92, 129]. In recent years nuclear thermodynamics [130, 131, 132, 133, 134] from chiral effective field theory has been successful at describing the homogeneous phases of symmetric and asymmetric matter (including the equilibrium mixed liquid-gas phase) up to densities $n \simeq 2n_0$, where $n_0 = 0.16\,\mathrm{fm}^{-3}$ is the saturation density of nuclear matter, and temperatures up to $T \simeq 25\,\mathrm{MeV}$. However, the construction of an equation of state for direct use in astrophysical simulations is still in progress, since the description of nuclear matter at larger densities

and temperatures is currently outside the scope of many-body perturbation theory with coarse-resolution chiral nuclear potentials. Here phenomenological mean field models can be used to extend the description, provided they match onto the low-energy theory.

In this work we analyze both Skyrme and RMF models for consistency with chiral nuclear thermodynamics. That is, we explore what conditions are required for mean field models [135, 136, 137] fit to the zero-temperature equation of state to be also consistent with the finite-temperature equation of state and transport properties of nuclear matter. In particular we will show that it is possible to find both (i) non-relativistic (i.e., Skyrme-type) as well as (ii) relativistic mean field models (RMF) that produce a thermodynamic equation of state for both pure neutron matter (PNM) and symmetric nuclear matter (SNM) compatible with many-body perturbation theory (MBPT) calculations employing chiral two- and three-nucleon interactions. Such models are also compatible with recent experimental constraints on nuclear matter properties [88], and their use in astrophysical simulations may therefore serve as an accurate substitute for the more computationally demanding microscopic chiral equations of state. In section 2.2 we compare MBPT calculations at both second- and third-order to non-perturbative quantum Monte Carlo calculations at zero temperature to assess uncertainties coming from neglected correlations in the perturbative treatment. This analysis is used in Section 2.3 to identify mean-field models for the zero-temperature equation of state compatible with results obtained from a coarse-resolution ($\Lambda = 414\,\mathrm{MeV}$) chiral interaction at next-to-next-to-next-to-leading order ($\mathrm{N^3LO}$) [138]. We then analyze the consistency of mean field models with chiral nuclear thermodynamics in section 2.3.4 as well as nuclear single-particle properties in Section 2.3.5 that affect the charged-current weak reactions in proto-neutron stars which we treated in chapter 1.

2.2 Ab initio uncertainty estimates on microscopic EOS models

In the present section we analyze the theoretical uncertainties from many-body perturbation theory in computing the ground state energy of symmetric nuclear matter and neutron matter. As a nonperturbative benchmark we employ quantum Monte Carlo techniques. The goal is to identify the nuclear force models and density regimes where microscopic many-body calculations can impose the strictest constraints on phenomenological mean field models. One may already anticipate that interactions with low-momentum regulators would perform qualitatively better in this regard, especially in neutron matter, however our goal here is to have a quantitative understanding of these errors for a relevant set of potentials.

2.2.1 Many body perturbation theory

Perturbative Expansion

The ground state of the system is given by the expectation value of the Hamiltonian (obtained from χPT, etc) with respect to the ground state of the interacting system:

$$E = \langle \mathcal{H}_0 \rangle + \langle \mathcal{V}_{NN} \rangle + \langle \mathcal{V}_{3N} \rangle + ... \tag{2.1}$$

where,

$$\langle A \rangle \equiv \frac{\langle \Psi^{(0)} | A | \Psi^{(0)} \rangle}{\langle \Psi^{(0)} | \Psi^{(0)} \rangle} \tag{2.2}$$

But, in order to know the ground state wavefunction of the interacting system $|\Psi^{(0)}\rangle$, one needs to solve the Schrödinger equation, which is not possible in general. Alternatively, we wish to express the energy in terms

of the ground state of the non-interacting system $|\Phi^{(0)}\rangle$. The connection between these states is given by the Gell-Mann and the Low theorem [139]:

$$|\Psi^{(0)}\rangle = \hat{U}(0, \pm\infty)|\Phi^{(0)}\rangle \tag{2.3}$$

The states in the equation above are within the interaction picture, $|\Psi(t)\rangle = e^{-i\mathcal{H}(t-t_0)}|\Psi(t-t_0)\rangle$. The relationship between the operator in the Heisenberg picture and the interaction picture is given by:

$$\mathcal{A}_I \equiv e^{i\mathcal{H}_0 t}\mathcal{A}e^{-i\mathcal{H}t} \tag{2.4}$$

and the time evolution equation for $\hat{U}$ is,

$$\begin{aligned} i\frac{\partial}{\partial t}\hat{U} &= \mathcal{V}_I\hat{U} \\ \hat{U}(t_0, t_0) &= 1 \end{aligned} \tag{2.5}$$

and $\mathcal{V}_I$ is the potential in the interaction picture. The formal solution of this equation is,

$$\hat{U}(t, t_0) = \sum_{\nu=0}^{\infty} \frac{(-i)^\nu}{\nu!} \int_{t_0}^{t} dt_1 ... \int_{t_0}^{t} dt_\nu e^{-\epsilon(|t_1|+...|t_\nu|)}\mathcal{T}[\mathcal{V}_I(t_1)...\mathcal{V}_I(t_\nu)] \tag{2.6}$$

where $\mathcal{T}[...]$ denotes the time ordered product of (fermionic) operators. By combining eq. 2.2, the Gell-Mann and Low theorem and eq. 2.6 the expectation value of an operator can be expressed as a perturbative expansion in terms of the non-interacting ground state and the interacting Hamiltonian:

$$\frac{\langle\Psi^{(0)}|A(t)|\Psi^{(0)}\rangle}{\langle\Psi^{(0)}|\Psi^{(0)}\rangle} = \frac{1}{\langle\Phi^{(0)}|\hat{U}(t, t_0,)|\Phi^{(0)}\rangle}\langle\Phi^{(0)}|\sum_{\nu=0}^{\infty} \frac{(-i)^\nu}{\nu!} \int_{t_0}^{t} dt_1 ... \int_{t_0}^{t} dt_\nu e^{-\epsilon(|t_1|+...|t_\nu|)}\mathcal{T}[\mathcal{V}_I(t_1)...\mathcal{V}_I(t_\nu)A_I(t)]|\Phi^{(0)}\rangle \tag{2.7}$$

What is left to do is to perform the expectation value of a time ordered product of operators in the non-interacting ground state. This is accomplished by means of Wick's theorem, in other words, the ground state average of the time ordered product is equal to the sum of the fully contracted versions of this sequence [140]. The only non-vanishing contractions are those of operators with their adjoints, which result in the free propagator of the single particle.

Finite Temperature Formalism

Although, the comparison with quantum Monte Carlo (QMC) calculations is performed at zero temperature, later in this chapter, many body perturbation theory will be used at finite temperature. Thus, here we give a brief description of the formalism. At finite temperature, we work in the grand canonical potential of the system:

$$\mathcal{K} = \mathcal{H}_0 - \mu\mathcal{N} + \mathcal{V}_{NN} + \mathcal{V}_{3N} + ... \tag{2.8}$$

where, $\mathcal{N} = \int d^3x\hat{\Psi}^\dagger(\vec{x})\hat{\Psi}(\vec{x})$ is the number density operator, and μ is the chemical potential. The statistical ensemble is characterized by the statistical operator $\hat{\varrho}$:

$$\hat{\varrho} = \mathcal{Z}^{-1}e^{-\beta\mathcal{K}} \tag{2.9}$$

where, $\beta = T^{-1}$ is the inverse temperature and $\mathcal{Z} = \mathrm{Tr}e^{-\beta\mathcal{K}}$ is the grand partition function. The basic quantity from which all physical observables are derived in the grand canonical potential density Ω:

$$\Omega = -\frac{1}{\beta V}\ln\mathcal{Z} \tag{2.10}$$

The single particle propagator is in imaginary time formalism as described in section 1.3. As calculations are performed, relevant references for the respective details are provided throughout the rest of this chapter. To be precise, the Gell-Mann and Low theorem gives the connection for the state $|\Psi^{(0)}\rangle$ that develops adiabatically from $|\Phi^{(0)}\rangle$, as the interaction is switched on. This is not always the same as the ground-state of the interacting system, which might not have a perturbation series in terms of the interaction. An example of such a scenario is a perfect Fermi gas in a uniform magnetic field (see pages 61,254,289 in [141]). This gives rise to a subtle difference between many-body perturbation at finite temperature versus zero temperature. For finite temperature calculations, there are so-called anomalous diagrams in many-body perturbation which have no counterpart for T= 0. These diagrams contain a momentum integral over both a 'hole' and a 'particle' degree of freedom, given by the Fermi distributions $f(k)$ and $1-f(k)$, respectively. For zero temperature, where instead of Fermi distributions we have Heavyside step functions, the range of such an integral is zero. The zero temperature limit of the free energy per particle is the true ground state of the interacting system, while the ground state calculated in the zero temperature formalism is the one obtained by evolving the system adiabatically. Luckily, for spherically symmetric Fermi surfaces and interactions that are invariant under rotations,the T= 0 always gives the same result as zero temperature calculations. This result is a theorem due to Kohn, Luttinger and Ward [142, 143]. Contributions from anomalous diagrams are included in this work. For a list of all many-body diagrams used at finite temperature, see [134]. And, the last technique to be explained before results can be analyzed is Monte Carlo.

2.2.2 Monte Carlo Method

The quantum Monte Carlo calculations presented here are based on the recently developed configuration interaction Monte Carlo (CIMC) method [144, 145, 92]. Projection QMC methods like CIMC are based on filtering out an eigenstate $|\Psi_0\rangle$ of the Hamiltonian H by repeated application of the propagator $\mathcal{P} = e^{-\Delta\tau(H-E_T)}$ on an initial state $|\Psi_I\rangle$:

$$|\Psi_0\rangle = \lim_{N_\tau\to\infty} \mathcal{P}^{N_\tau}|\Psi_I\rangle. \tag{2.11}$$

Here, N_τ is the number of imaginary time steps, E_T is an energy shift used to keep the norm of the wave function approximately constant, and $\Delta\tau$ is a finite step in 'imaginary' time: $\Delta\tau = i\Delta t$. The state $|\Psi_0\rangle$ is the eigenstate with the lowest eigenvalue within the subset of states having non-zero overlaps with $|\Psi_I\rangle$. The application of the propagator is carried out stochastically.

The main difference between the CIMC method and traditional continuum projection Monte Carlo methods is that in the CIMC method this stochastic projection is performed in Fock space (i.e., the basis is provided by the Slater determinants that can be constructed from a finite set of single particle (sp) basis states), as opposed to in coordinate space. As a result, non-local Hamiltonians do not pose any technical problems. In this work, we use the sp basis given by eigenstates of momentum and the z components of spin and isospin. A finite sp basis is chosen by imposing a "basis cutoff" $k_{\max}$ and convergence is checked by performing a sequence of calculations with increasingly larger values of the cutoff. This same sp basis is then employed to perform many-body perturbation theory calculations at both 2nd and 3rd order (see e.g., Ref. [146]).

In order for a stochastic sampling to be feasible, the matrix elements of the propagator, $\mathcal{P}$, need to be positive semi-definite. For nucleons interacting with realistic interactions this condition is never fulfilled due to the presence of repulsive contributions, giving rise to the so-called sign problem. In CIMC we circumvent this by using a coupled-cluster double (CCD) wavefunction to restrict the random walk in a sub-sector of the full many-body Hilbert space where the positivity of the propagator is guaranteed (for details see Appendix A.1 and Ref. [145]). This introduces a systematic bias in the calculation (see Appendix A.1 for an attempt to estimate its effects), but nevertheless the final energy eigenvalue E_0^{FN} is guaranteed to be an upper bound of the true ground state energy E_0.

The formalism is fully compatible with the use of a three-body interaction in the Hamiltonian (eg. in the same way as these are dealt with in CC-theory [128]), however in order to have more control on the fixed-node procedure the explicit inclusion of triplet correlations in the coupled cluster wavefunction has to be accounted for. Presently this poses strong limitations on the size of the sp basis that can be handled, making it difficult to reach convergence with respect to $k_{\max}$. An alternative approach based on cancellation techniques (see e.g., Ref. [147, 148, 149]), which may allow one to neglect explicit three-body correlations, is currently being explored.

2.2.3 Results

In this study of the convergence of MBPT we will use four different chiral NN interactions: the NNLO$_{opt}$ from Ekström et al. [150], the two low-momentum cutoff interactions from Coraggio et al. [138] at N^{3}LO with cutoffs of Λ = 414 MeV and Λ = 450 MeV and finally a version of the N^{3}LO interaction with a Λ = 500 MeV cutoff from Entem and Machleidt [62, 55] where the N^{3}LO contact terms have been refitted using the same regulator for all partial waves.

Calculations at constant density are performed by first choosing the number of particles in the system N and the target density n. The size L of the box is then given by $L = (N/n)^{1/3}$. In the present simulations the number of particles is fixed at the closed shell $N = 14$, and all of the results are converged with respect to the single-particle momentum cutoff $k_{\max}$, and we find that values of $k_{\max}$ slightly higher than the cutoff Λ in the regulating function of the chiral potentials is needed for convergence (this is in good agreement with the findings in Ref. [92]). We have carefully examined the dependence on the system size and found that $N = 14$ provides reliable estimates at the low densities we are interested in, a more detailed discussion is provided in Appendix A.2. Furthermore, all the perturbative calculations are performed by including corrections to the nucleon self-energy at the Hartree-Fock level, in other words by performing normal ordering with respect to the Hartree-Fock state (for additional details see e.g., Ref. [146]). More detailed comparisons to results obtained using a free-particle spectrum can be found in Appendix A.3.

Pure Neutron Matter EOS

We first concentrate on the equation of state of pure neutron matter, shown in Fig. 2.1, for both perturbative methods and the nonperturbative CIMC method employing chiral two-body forces. The first qualitative observation that can be made is that the NNLO result lies consistently outside the N^{3}LO band obtained by cutoff variation. However, as noted in Refs. [91, 151, 152] this variation may not be a reliable estimate of the spread in predictions at a given order in the chiral expansion. From the inset in Fig. 2.1 we observe that three-body interactions are needed for a quantitative study for densities $n \gtrsim 0.06$ fm^{-3}. In the present section we focus on NN forces only, and consequently this is the highest density where we may draw rigorous conclusions.

Evaluating the convergence of the perturbative calculations in Fig. 2.1, we see that in PNM the third-order contributions are generally sufficient to bring the MBPT results very close to those from the non-perturbative CIMC, indicating a good convergence pattern for MBPT for all four interactions considered, regardless of the regularization cutoff. To estimate the errors corresponding to the perturbative convergence, we consider in Fig. 2.2 the relative difference between the CIMC results and the energies obtained at different orders in perturbation theory. We observe that the interactions split into two groups with N^{3}LO Λ = 414 and Λ = 450 deviating from CIMC by $\approx 2-3\%$ at second order and the NNLO$_{opt}$ and N^{3}LO Λ = 500 interactions that have deviations of $6-8\%$. For all interactions the third-order calculations are compatible with CIMC for all densities apart from NNLO$_{opt}$, which at the highest densities has a small deviation of $\approx 1-2\%$.

One can study the effect of the bias coming from the fixed-node procedure by adding to the wavefunction

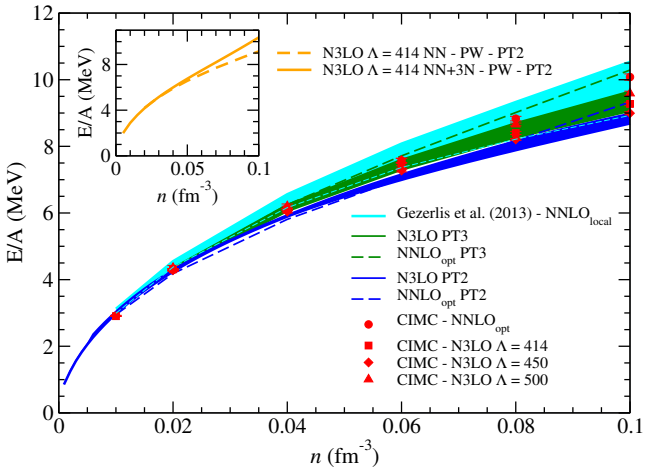

Figure 2.1: Energy per particle of pure neutron matter as a function of density from different chiral interactions at NNLO and N^{3}LO. Results at second-order (PT2) and third-order (PT3) in perturbation theory are shown together with those from configuration interaction Monte Carlo (CIMC) and auxiliary field diffusion Monte Carlo [124]. The inset shows the results at second-order in MBPT for the N^{3}LO Λ = 414 interaction with and without three-nucleon forces.

a non-zero overlap with all states in the Hilbert space (triplet and higher order irreducible correlations) and checking the differences in the final estimate for the energy. In the case of PNM and for all four interactions this procedure gives results compatible with the energies obtained by employing the CCD wavefunction, which indicates that this source of systematic error is under control (a more detailed study of this systematic error is presented in Appendix A.1).

Before concluding this section we comment on the low density regime of neutron matter, which due to the large neutron-neutron scattering length ($a_{nn} \sim -19$ fm) is very close to that of a non-perturbative unitary Fermi gas. From the results in Fig. 2.2 we may draw the (wrong) conclusion that at low densities ($n \lesssim 0.02$ fm^{-3}) the perturbative calculations converge faster, with the second-order results at $n \approx 0.02$ fm^{-3} almost compatible with CIMC. This is however an artifact coming from the fact that the second-order predictions change from too attractive at high density to too repulsive at low ones, that is, the relative difference with CIMC changes sign at low densities (as is evident from Fig. 2.2). This is then in agreement with the expectation that at sufficiently low densities the convergence of MBPT breaks down.

Symmetric Nuclear Matter (SNM)

We now focus on the results for symmetric nuclear matter, shown in Fig. 2.3, that have been computed using A = 28 nucleons. In contrast to the neutron matter equation of state in the last section, here the various chiral two-nucleon forces give rise to larger variations. As a result the energy per particle from the NNLO interaction is now contained in the N^{3}LO band, which is mostly due to the N^{3}LO 500 results that are consistently less attractive than the rest for intermediate to high densities. Reaching low densities with this high-cutoff interaction is computationally more demanding, and since we already observed a lack of convergence in the simpler case of neutron matter, we will discuss in the following only the remaining three interactions. Another interesting feature apparent from the data (and compatible with earlier findings by Coraggio et al. [138]) is that at intermediate to high densities the third-order perturbative correction is negligible. To better understand this behavior we plot in Fig. 2.4 the ratio between third- and second-order perturbative corrections

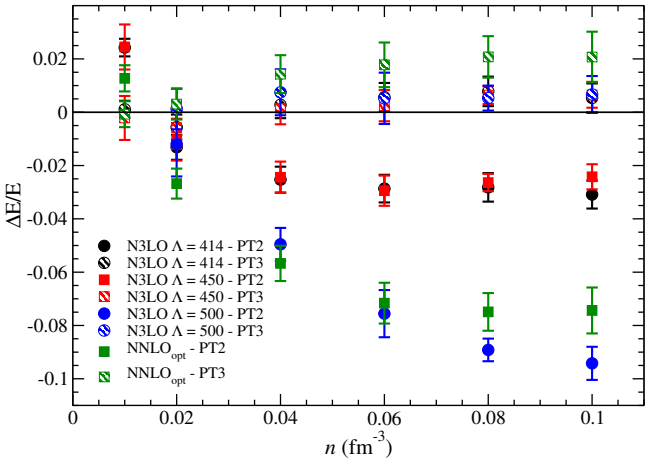

Figure 2.2: Relative differences in energies obtained at different orders in perturbation theory with respect to the corresponding CIMC result for pure neutron matter. Notation same as in Fig. 2.1.

in both neutron and symmetric nuclear matter. We see that the third-order correction slowly changes sign around the empirical saturation density, giving an artificially small correction to the energy per particle.

If we were to evaluate the perturbativeness of the calculation by only comparing the magnitudes of the contributions at different orders in perturbation theory (see e.g., Fig. 2.4), we might draw the counterintuitive (and wrong) conclusion that the convergence pattern in SNM is much better than in PNM. That this is not the case can be understood by noticing that if the third-order calculation is already converged then the CCD wavefunction used in the fixed node procedure would be the exact ground state, but if that were the case then the third-order perturbative results and the ones predicted by CIMC should be on top of each other, which is not the case.

Another way to see this is to exploit the freedom in CIMC to tune the guiding wavefunction by truncating contributions beyond a given number of particle-hole excitations. The second-order energies contain information about 2p-2h excitations above the Hartree-Fock ground state, so any important effects coming from higher orders cannot be recovered in this low truncation of the MBPT expansion. We tested the NNLO$_{opt}$ interaction at $n = 0.08$ fm^{-3} in both PNM and SNM and found that in the first case in order to recover the full CIMC results we have to allow up to 6p-6h contributions in the guiding wavefunction (with the 4p-4h truncation lying just outside the error bands) while for the latter case up to 12p-12h states are needed to reproduce the non-truncated CIMC result. Similar observations hold for the N^{3}LO $\Lambda = 414$ interaction that is used in subsequent sections of the paper, with 4h-4p being converged in PNM and 10p-10h for SNM. This observation is again in strong favor for enhanced non-perturbative features in the symmetric nuclear matter case, even for an interaction with a low-momentum cutoff.

We conclude that it may be misleading to evaluate the convergence of second-order calculations using only the magnitude of the next order as guidance (or equivalently using Padé extrapolations), especially in regimes where the third-order contributions are changing sign and are thus artificially small. Without the fourth-order results it is then difficult to judge convergence within MBPT itself and comparison with non-perturbative methods are important.

Fig. 2.5 displays the difference between the second- and third-order perturbative results for the symmetric matter equation of state and that obtained from CIMC. Recall that the main systematic error in the Monte Carlo calculations, the fixed-node error, is thought to be much more severe in this system especially at low

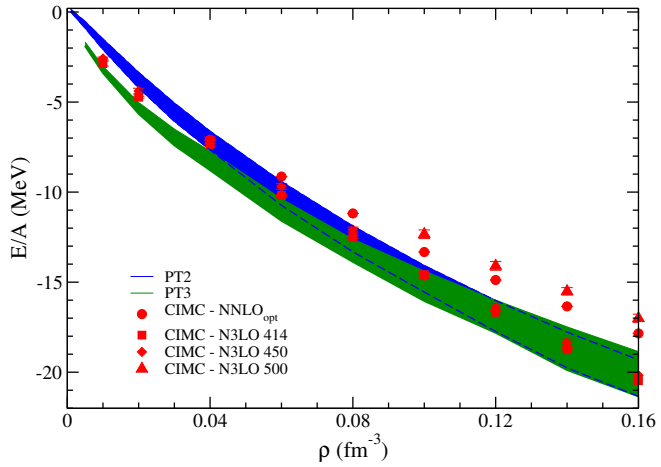

Figure 2.3: Same as in Fig. 2.1, except for symmetric nuclear matter. The NNLO$_{opt}$ results now are contained in the N^{3}LO bands.

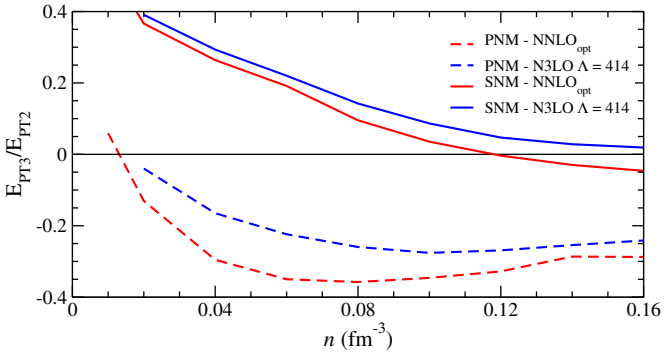

Figure 2.4: Ratio of the third-order correction to the second-order one in PNM (dashed lines) and SNM (full lines) for NNLO$_{opt}$ (red) and N^{3}LO $\Lambda = 414$ (blue).

densities due to the appearance of bound states that are extremely difficult to capture explicitly in the coupled-cluster ansatz for the guiding wavefunction. One of the appealing properties of the CIMC method however is that it is guaranteed to give an upper bound to the energy. As was mentioned above, by looking at the relative variations in Fig. 2.5 one can get the impression that second-order calculations provide as good (or better) estimates of the energy than those obtained at third order in the density range $0.04 - 0.10$ fm^{-3}. This is a well known feature of asymptotic expansions (see e.g., Ref. [153]) like the one employed in MBPT (which does not involve any small parameter), where one finds in fact that the smallest error achievable (without employing re-summations) is obtained by truncating the series at an optimal order N^* which may indeed be very small. However, given the present large uncertainties, no conclusive statement can be made.

A more rigorous statement can be made instead for lower densities $n =< 0.04$ fm^{-3} by using the upper bound nature of CIMC energies: in the low density regime the errors introduced by stopping the perturbative expansion at second order are larger than $\approx 20\%$. One should be cautious about any statement on properties of nuclear matter in this regime, such as the spinodal instability region, coming from second-order MBPT. In order to have more control in that region, comparisons to higher-order results are therefore needed before a better understanding of non-perturbative physics is achieved. In the intermediate-density regime, both second

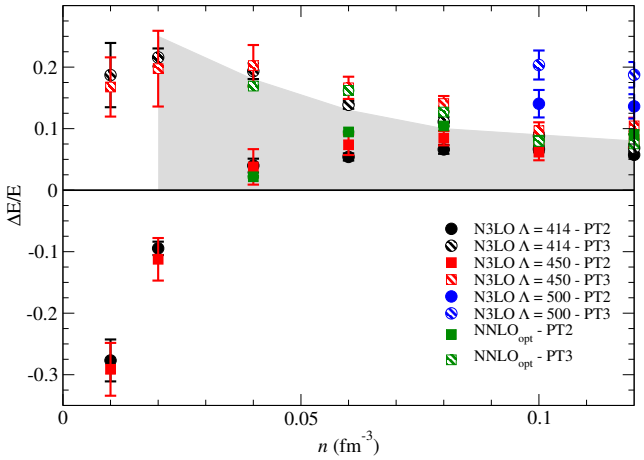

Figure 2.5: Relative deviations of energies obtained at different orders in perturbation theory with respect to the corresponding CIMC result for symmetric nuclear matter. The gray band is a qualitative estimate of the uncertainties in the fixed-node approximation (see text for the details).

and third-order calculations of the ground state energy are very similar to each other and on average $7-10\%$ more bound than CIMC results. Due to the lack of control on the fixed-node errors, this would be the most reliable error band we can attribute to perturbation theory, but due to its qualitative nature it will not be used to discriminate among the various mean field models in subsequent sections. We note however that this estimate is consistent with the findings of Hagen et al. [128] in which the NNLO$_{opt}$ interaction resulted in a difference between CCD and MBPT at second order of $\approx 12\%$ at $n = 0.06$ fm^{-3} to $\approx 8\%$ around saturation density.

2.3 EoS from Mean Field Models

In the previous section we found that the two coarse-resolution chiral interactions at N^{3}LO with cutoffs Λ = 414 and 450 MeV have good perturbative properties in PNM and SNM, with average errors on the order of $\Delta E/E \approx 2-3\%$ for the former and $\Delta E/E \approx 8-10\%$ for the latter in the vicinity of nuclear matter saturation density. In addition, as shown in fig. 2.1, for densities up to $0.05-0.06$ fm^{-3}, the contribution to the energy per particle from 3N forces is negligible and the error estimates from our analysis can be used quantitatively to select mean field models that are consistent with second-order MBPT calculations at low densities. In the following we will adopt the most perturbative N^{3}LO 414 interaction including both NN and 3N forces.

In astrophysical simulations of core-collapse supernovae and neutron star mergers, equations of state based on mean field models have been used for more than three decades. They provide a practical way of describing the physical properties of dense matter while being computationally inexpensive, thus allowing for the fast generation of data needed for simulations. Among these models those derived from Skyrme interactions are widely used for the description of both nuclei and infinite matter, with a prominent example being that of Lattimer and Swesty [95].

2.3.1 Skyrme density functionals

The Skyrme force was first introduced by Skyrme ([154]) as an effective force for nuclear HF calculations. Its widespread application started with the revival by Vautherin and Brink [155], [156].

Motivation of the Skyrme functional

Traditional nuclear theories start from nucleons and two-body interactions between them as basic building blocks. The interaction is determined from an analysis of nucleon-nucleon scattering, with the aim of having a microscopic description of the correlated nuclear state. The most formally clear way of expressing the construction of an effective interaction is to write the fully correlated state as a unitary transformation of some mean field state:

$$|\Psi\rangle = \hat{U}|\Phi\rangle \tag{2.12}$$

At the lowest level, this transformation is composed of from exponentiated two body correlations:

$$\hat{U} = \exp i \sum c_{abcd} \hat{a}_a^\dagger \hat{a}_b^\dagger \hat{a}_c \hat{a}_d \tag{2.13}$$

where, $(\hat{a}^\dagger, \hat{a})$ are Fermion creation and annihilation operators. The energy expectation value is given as:

$$E = \langle\Psi|\hat{H}|\Psi\rangle = \langle\Phi|\hat{U}^\dagger \hat{H} \hat{U}|\Phi\rangle = \langle\Phi|\hat{H}_{eff}|\Phi\rangle \tag{2.14}$$

Note that the expectation value of $\hat{H}_{eff}$ is well defined only with respect to mean-field states $|\Phi\rangle$. This places restrictions on the 'legitimate' Hilbert space, which are best handled by variational methods.

The most general potential energy becomes,

$$E_{pot} = \int d^3x d^3x' d^3y d^3y' n(\vec{x}, \vec{x}') K(\vec{x}, \vec{x}', \vec{y}, \vec{y}') n(\vec{y}, \vec{y}') \tag{2.15}$$

where $n(\vec{x}, \vec{x}')$ is the one - body density matrix, $K(\vec{x}, \vec{x}', \vec{y}, \vec{y}')$ is the integral kernel which represent interactions. The one - body density can be expanded in $|\vec{x} - \vec{x}'|^n$ around $\overline{\vec{x}} = (\vec{x} + \vec{x}')/2$ as follows,

$$n(\vec{x}, \vec{x}') \approx n(\overline{\vec{x}}) + i(\vec{x} - \vec{x}') \cdot \vec{j}(\overline{\vec{x}}) + \frac{1}{2}|\vec{x} - \vec{x}'|^2 (\tau - \frac{1}{4} \triangle n(\overline{\vec{x}})) \tag{2.16}$$

where $(n, \vec{j}, \tau)$ are the local density, local current, and kinetic energy density,

$$\begin{aligned} n &= 2 \int \frac{d^3k}{(2\pi\hbar)^3} f(k) \\ \tau &= 2 \int \frac{d^3k}{(2\pi\hbar)^3} k^2 f(k) \\ \vec{j} &= \int \frac{d^3k}{(2\pi\hbar)^3} \vec{k} \times \sum_{s,s'} \langle s|\vec{\sigma}|s'\rangle \; f(k) \end{aligned} \tag{2.17}$$

and σ is the Pauli matrix for used for spin projection; f is the Fermi distribution. An expansion of K with respect to $(\vec{x} - \vec{x}')$ yields gradient terms proportional to $\triangle n(\overline{\vec{x}})$ in the effective functional. As is apparent from this expansion, this is a low energy or momentum expansion, which puts even more constraints on the allowed mean-field states (the spatial structure should be sufficiently smooth).

Thus, density functional theory provides the conceptually, and technically, easiest way to derive an energy density functional. This is the local density approximation (LDA) [157].

When one considers nuclei all these constraints are very relevant, while for unpolarized (time reversal invariant) uniform matter, by construction, there are no density gradients or currents and the general expression

for the energy density functional is given by

$$\begin{aligned}\mathcal{E} &= \sum_{q=n,p}\frac{1}{2M_q}\tau_q + \frac{1}{4}t_0\Big[(2+x_0)n^2 \\ &- (1+2x_0)\sum_{q=n,p}n_q^2\Big] + \frac{1}{8}\Big[a\tau n + 2b\sum_{q=n,p}n_q\tau_q\Big] \\ &+ \frac{1}{24}t_3 n^{\alpha}\Big[(2+x_3)n^2 - (1+2x_3)\sum_{q=n,p}n_q^2\Big], \end{aligned} \tag{2.18}$$

The energy density is given at HF level, and the Skyrme interactions are usually constrained by the properties of finite nuclei close to the valley of stability. The predictive power of Skyrme models however is difficult to assess away from the region in parameter space where it has been fitted. The astrophysical environments mentioned above span a wide range of densities, from a rarefied gas to dense matter possibly 2-5 times that of normal nuclei, and neutrons represent the vast majority of the nuclear composition. Moreover, these environments are characterized by high temperatures that can reach up to $T = 50\,\mathrm{MeV}$ [158]. The reliability of effective Skyrme interactions to accurately cover this range of parameter space based on fits to terrestrial nuclei is an open question.

A first consistency check can be carried out using experimentally extracted constraints for nuclear matter properties. In Ref. [88] Dutra et al. have benchmarked a set of 240 Skyrme parametrizations against a set of 11 infinite matter constraints. Only 16 parametrizations were shown to meet all of these constraints. Due to the wide range of conditions encountered in supernovae simulations, a careful calibration of the models also in conditions that are difficult to achieve in terrestrial experiments is therefore important. Recent developments in both many-body techniques and nuclear forces allow the equation of state of PNM to be relatively well constrained at low densities. Using these results, together with properties of double-magic nuclei [159], Brown and Schwenk [135] have refitted from the consistent models in Ref. [88] a selected smaller set of six "best fit" Skyrme models: SKT1, SKT2, SKT3, SKa25s20, Ska35s20, Sv-sym32. In Ref. [135] two slightly different parameter sets for these interactions have been obtained by requiring a particular value for the effective mass ($m^*/m = 0.9$ or 1.0) in neutron matter at the density $n = 0.10\ \mathrm{fm}^{-3}$.

In this work we will consider all of these final 12 parametrizations. For mean field Skyrme models, theoretical uncertainties can be estimated through a careful extraction of the correlation matrix for the parameters entering the functionals [160, 161, 162]. In recent years important efforts have been devoted by the UNEDF collaboration to construct Skyrme parametrizations with reliable error quantifications; for this reason we have also considered the parametrizations UNEDF0 [163], UNEDF1 [164] and UNEDF2 [165]. For the other parametrizations there are no publicly available parameter correlations that can be used to study uncertainties and propagation of systematic errors. It is important to realize however that detailed error extrapolations in complicated simulations (like those for core–collapse supernovae) poses major technical challenges and therefore parametrizations whose central values are already close to the expected ones are to be preferred. In this work, we therefore focus on constraining mean field models from the low-density microscopic equation of state and study their properties at saturation density as described by Table 2.1 assuming negligible errors in the parameters. However, we would like to stress the need for a detailed study of parametric uncertainties, which is outside the scope of this study. Such analysis would be greatly facilitated if new parametrizations would be published together with their parameter's covariance matrix informations.

2.3.2 Relativistic mean field models

In the past decades, Walecka et al [166] have shown that ground-state properties of nuclear matter, and of doubly magic nuclei, can be described within a mean-field approximation to a relativistic quantum-field

theory of nucleons, in which the strong interactions are produced by the exchange of massive mesons. With few adjustable parameters this model is able to reproduce the binding energy and the density of nuclear matter as well as the density profiles and the spin-orbit splitting in doubly magic spherical nuclei [167], [168], [169] (the parameters are fit to match these properties). Recent astrophysical simulations also employ relativistic mean field models of the nuclear equation of state.

Relativistic Lagrangian

The Lagrangian density is given by, $\mathcal{L} = \mathcal{L}_0 + \mathcal{L}_{int}$,

$$\begin{aligned}
\mathcal{L}_0 =& \overline{\Psi}(i\gamma^\mu\partial_\mu - M)\Psi + \frac{1}{2}(\partial_\mu\phi\partial^\mu\phi - m_s^2\phi^2) \\
&+ \frac{1}{2}m_v^2 V_\mu V^\mu - \frac{1}{4}F_{\mu\nu}F^{\mu\nu} + \frac{1}{2}m_b^2\vec{b}_\mu\cdot\vec{b}^\mu - \frac{1}{4}V_{\mu\nu}V^{\mu\nu} - \frac{1}{4}\vec{b}_{\mu\nu}\cdot\vec{b}^{\mu\nu}, \\
\mathcal{L}_{int} =& \overline{\Psi}\Big[g_s\phi - \gamma^\mu(g_V V_\mu + \frac{g_b}{2}\vec{\tau}\cdot\vec{b}_\mu + \frac{e}{2}(1+\tau_3)A_\mu)\Big]\Psi \\
&- \frac{\kappa}{3!}(g_s\phi)^3 - \frac{\lambda}{4!}(g_s\phi)^4 + \frac{\zeta}{4!}(g_V^2 V_\mu V^\mu)^2 \\
&+ \Lambda_V(g_V^2 V_\mu V^\mu)(g_b^2\vec{b}_\mu\cdot\vec{b}^\mu)
\end{aligned} \tag{2.19}$$

and, $\Psi = \begin{pmatrix}\Psi_p \\ \Psi_n\end{pmatrix}$. The various tensor fields are defined as follows,

$$\begin{aligned}
F_{\mu\nu} =& \partial_\mu A_\nu - \partial_\nu A_\mu \\
V_{\mu\nu} =& \partial_\mu V_\nu - \partial_\nu V_\mu \\
\vec{b}_{\mu\nu} =& \partial_\mu\vec{b}_\nu - \partial_\nu\vec{b}_\mu
\end{aligned} \tag{2.20}$$

Each of the Yukawa couplings are responsible different types of interaction: scalar - isoscalar ϕ meson is responsible for the intermediate range attraction, vector - isoscalar V^μ is responsible for short range repulsion, and for isospin differences the vector - isovector $\vec{b}^\mu$ is used. The inclusion of isoscalar self - interactions is to soften the equation of state of symmetric matter, and the mixed isoscalar - isovector coupling is to change the density dependence of the symmetry energy [169].

Mean Field Approximation

By using Lagrange's equation of motion, the equations for the meson fields are

$$\begin{aligned}
(\partial_\mu\partial^\mu + m_s^2)\phi =& g_s\overline{\Psi}\Psi - \frac{\kappa}{2}g_s^3\phi^2 - \frac{\lambda}{3!}g_s^4\phi^3, \\
\partial_\mu V^{\mu\nu} + m_V^2 V^\nu =& g_V\overline{\Psi}\gamma^\nu\Psi - \frac{\zeta}{3!}g_V^4(V_\mu V^\mu)V^\nu - 2\Lambda_V(g_b\vec{b}_\mu\cdot\vec{b}^\mu)g_V^2 V^\nu, \\
\partial_\mu\vec{b}^{\mu\nu} + m_b^2\vec{b}^\nu =& g_b\overline{\Psi}(\frac{\tau}{2}\gamma^\nu)\Psi - 2\Lambda_V(g_V^2 V_\mu V^\mu)g_b\vec{b}^\nu
\end{aligned} \tag{2.21}$$

Similarly, the equation of motion for the baryon fields, the modified Dirac equation, is,

$$\Big[\gamma^\mu(i\partial_\mu - g_V V_\mu - \frac{g_b}{2}\vec{\tau}\cdot\vec{b}_\mu) - (M_t - g_x\phi)\Big]\Psi_t = 0 \tag{2.22}$$

where the index t refers to the isospin. Since these relativistic Lagrangian is applied near nuclear saturation density, the meson field operators are replaced by their expectation values, and can be regarded as classical

condensed fields (mean field background) where the baryons move. In practice, the only 'quantum' behavior is the treatment of the nucleons in the presence of scalar and vector potentials created by the meson condensates.

For uniform, spherically symmetric matter this implies,

$$\begin{aligned}
\langle \phi(x) \rangle &= \phi_0 \\
\langle V^\mu(x) \rangle &= g^{\mu 0} V_0 \\
\langle b_i^\mu(x) \rangle &= g^{\mu 0} \delta_{i3} b_0 \\
\langle A^\mu(x) \rangle &= g^{\mu 0} A_0
\end{aligned} \tag{2.23}$$

Energy density in RMF

The energy-momentum tensor is defined as:

$$T_{\mu\nu} = -g_{\mu\nu}\mathcal{L} + \frac{\partial \Psi}{\partial x^\nu} \frac{\partial \mathcal{L}}{\partial \frac{\partial \Psi}{\partial x_\mu}} \tag{2.24}$$

And, assuming uniform matter to be a perfect fluid,

$$T_{\mu\nu} = (\mathcal{E} + P) u_\mu u_\nu - P g_{\mu\nu} \tag{2.25}$$

where $\mathcal{E}$ is the energy density, P is the pressure, and u_μ is the four-velocity of the fluid. by applying mean field approximation, the general expression for the energy density functional in terms of nucleon Ψ, scalar ϕ, vector V_μ, and vector isovector b_μ fields is given by

$$\begin{aligned}
\mathcal{E} &= \sum_{s,t} \int \frac{d^3k}{(2\pi)^3} \sqrt{k^2 + (M_t - g_S\phi_0)^2} (f_{s,t} + \overline{f}_{s,t}) \\
&+ \frac{1}{2} m_s^2 \phi_0^2 + \frac{\kappa}{3!} (g_S \phi_0)^3 + \frac{\lambda}{4!} (g_S \phi_0)^4 + \frac{\zeta}{8} (g_V V_0)^4 \\
&+ \frac{1}{2} m_V^2 V_0^2 + \frac{1}{2} m_b^2 b_0^2 + 3\Lambda_V (g_V V_0)^2 (g_b b_0)^2.
\end{aligned} \tag{2.26}$$

where, $(f_{s,t},\ \overline{f}_{s,t})$ are the spin and isospin dependent Fermi distribution functions for the nucleon and anti-nucleon respectively. As already stated, $(\phi_0,\ b_0,\ V_0)$ are the ground state expectation values of the auxiliary fields. The expectation value ϕ_0 is obtained by solving

$$\begin{aligned}
&\left(\frac{m_S}{g_S}\right)^2 (g_S\phi_0) + \frac{\kappa}{2}(g_S\phi_0)^2 + \frac{\lambda}{6}(g_S\phi_0)^3 \\
&= \sum_{s,t} \int \frac{d^3k}{(2\pi)^3} \frac{M_t - g_S\phi_0}{\sqrt{k^2 + (M_t - g_S\phi_0)^2}} (f_{s,t} + \overline{f}_{s,t}),
\end{aligned} \tag{2.27}$$

and the vector ground state expectation values are obtained by solving a pair of coupled equations:

$$\begin{aligned}
n_p + n_n &= \left(\frac{m_V}{g_V}\right)^2 (g_V V_0) + 2\Lambda_V (g_b b_0)^2 (g_V V_0) \\
&+ \frac{\zeta}{6} (g_V V_0)^3 \\
n_p - n_n &= \left(\frac{m_b}{g_b}\right)^2 (g_b b_0) + 2\Lambda_V (g_V V_0)^2 (g_b b_0).
\end{aligned} \tag{2.28}$$

For a detailed description of the main features and how they match to supernovae and neutron star observations see Ref. [170]. The RMF models we focus on in this paper are the most commonly used in astrophysical calculations: FSUgold [171, 172], IUFSU [173], TM1 [174], TMA [175], DD2 [176], SFHx [177], SFHo[177]. Similar to the work on Skyrme models, in Ref. [178] a full analysis of 263 different RMF parametrizations have been carried out with the same set of 11 infinite matter constraints, and only the Z271v5 and Z271v6 [179] parametrizations were found to meet the criteria. Hence, we also include them in our analysis.

2.3.3 Zero Temperature

As the purpose of this work is to gradually select among the many available mean field models those that can be used to understand the thermodynamic evolution of a binary merger or core collapse supernova and are consistent with our current knowledge of baryonic matter, we proceed as follows:

In figures 2.6 and 2.7 we select among relativistic and skyrme models respectively based on our findings from previous sections by comparing to the chiral N^3LO 414 interaction with NN and 3NF forces. We have compared our constraints with [135] and have found that our values are well within the bands in that work. For the remaining models, we employ constraints from Dutra et al. [88], and since the refitted Skyrme parametrizations selected in Ref. [135] are essentially new parametrizations, they need to be tested for validity.

We observe in Fig. 2.6 that phenomenological models have wide variations, even down to very low densities, in contrast to the microscopic predictions shown in Fig. 2.1. This model dependence can be traced to the weak correlation between the low-density neutron matter equation of state and the observables used to constrain the phenomenological models. Among the relativistic models only Z271v6 agrees with the uncertainty bands from microscopic calculations and therefore is the only parametrization considered any further in this analysis. We notice however that both the DD2 and SFHx parametrizations are very close to fulfilling the low-density constraints, and therefore we will test them against the set of constraints from Dutra et al. [88] in the following. For the non-relativistic models all the UNEDF parametrizations fail the low density constraints. We note however that it should be possible to include low density neutron matter calculations as done in Ref. [135] to achieve a better agreement. Although the low-density regime is not important for some neutron star properties, for instance the mass-radius relation, it is essential for analyzing electron neutrino transport during core-collapse supernovae.

In Fig. 2.7 we show the chiral equation of state and low-density uncertainty estimates together with the various Skyrme models that satisfy also the infinite matter constraints. The uncertainty band for neutron matter at $n = 0.02$ fm^{-3} excludes parametrizations SKT1-1.0, SKT2-1.0, SKT3-1.0, Ska35s20-1.0, Sv-sym32-1.0. However, the Ska35s20-1.0 Skyrme interaction just misses the low-density constraint, and we choose to consider it in further analyses as the best representative of the models with $m^*/m = 1.0$.

In the high-density regime the differences between mean field models and the chiral equation of state increase. For instance, at saturation density the variations in Skyrme parametrizations are between 5% and 10% more repulsive than the perturbative prediction, while RMF models can differ by up to 40%. At these densities and beyond, theoretical error bands on the perturbative calculation increase due to the approximate treatment of three-body forces in the two-body normal-ordering approximation [180, 181, 182, 183] at second-order in perturbation theory, whose uncertainties have not been evaluated in the present work (but see Ref. [184] for an initial study). We therefore do not place strong constraints on the mean field models from χEFT beyond low densities. We note however that given the results obtained at low densities a 5% error is to be expected and we can therefore assume that the parametrizations SKT1-0.9, SKT2-0.9, SKT3-0.9, Ska35s20-0.9 and Ska35s20-1.0 are in very good agreement with the results obtained from chiral interactions.

For the symmetric nuclear matter equations of state shown in Fig. 2.8 the predictions of different models are very similar, reflecting the fact that the parametrizations have been predominantly fitted to properties of

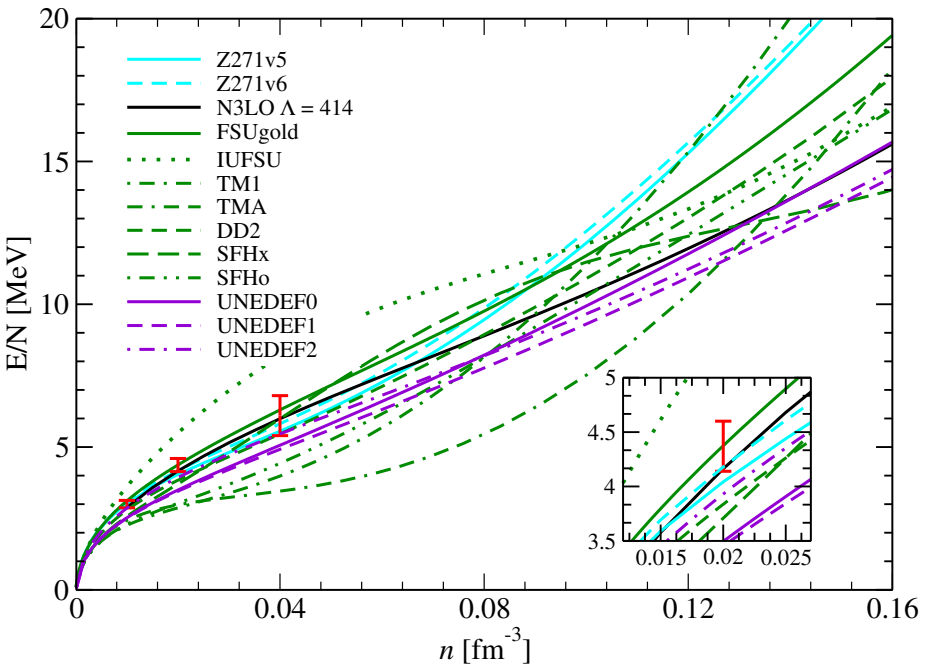

Figure 2.6: Energy per particle for neutron matter at $T = 0$, where the red bars show the constraints derived in the previous sections. In the inset we show a close-up of the low-density ($n \simeq 0.02$ fm^{-3}) regime.

infinite matter around and below the saturation density. As discussed in Section 2.2, in this case we do not have a tight constraint on the perturbation theory uncertainties, and considering an average error of $\Delta E/E \approx 10\%$, all parametrizations in Fig. 2.8 are compatible with the perturbative results. As a further check we compare the predictions for the saturation point and find that all parametrizations are able to reproduce the empirical result within the 5% box shown in Fig. 2.8. We therefore cannot use the $T = 0$ SNM equation of state to further eliminate mean field models.

In Table 2.1 we summarize the numerical infinite matter constraints from Ref. [88]. In particular, the observables listed are the symmetric matter incompressibility

$$K_m = 9 \left.\frac{\partial P}{\partial n}\right|_{n_0} \tag{2.29}$$

at saturation density, where $P = n^2 \frac{\partial (E/N)}{\partial n}$ is the pressure; the derivative of the incompressibility with respect to density (the so-called skewness parameter)

$$K' = -27 n_0^3 \left.\frac{\partial^3 (E/N)}{\partial n^3}\right|_{n_0} ; \tag{2.30}$$

the symmetry energy

$$J = S(n_0) = \left.\frac{\partial (E/N)}{\partial \delta_{np}^2}\right|_{n_0} , \tag{2.31}$$

where $\delta_{np} = \frac{n_n - n_p}{n_n + n_p}$ is the isospin asymmetry; the symmetry energy slope

$$L = 3 n_0 \left.\frac{\partial S}{\partial n}\right|_{n_0} ; \tag{2.32}$$

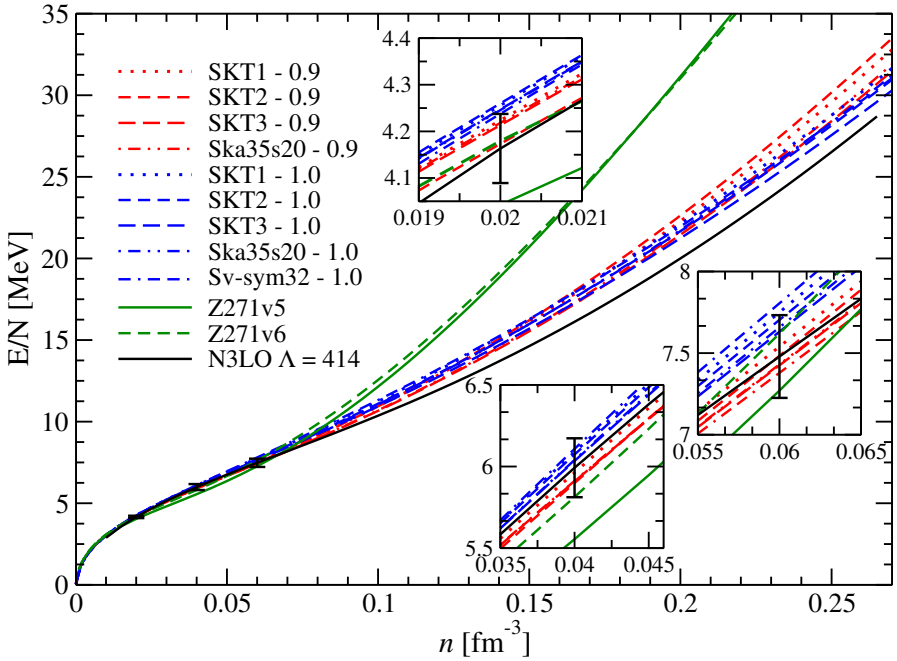

Figure 2.7: Equation of state for pure neutron matter. The insets show the uncertainty bands from neglected correlations in the perturbative treatment from Section 2.2.

the isospin incompressibility

$$K_{\tau,v} = K_{\rm sym} - L\left(6 + \frac{K'}{K_m}\right), \tag{2.33}$$

where $K_{\rm sym} = 9n_0^2 \left.\frac{\partial^2 S}{\partial n^2}\right|_{n_0}$; the ratio between the symmetry energy at half saturation density and its value at n_0; and finally the quantity $3P_{PNM}/Ln_0$, where P_{PNM} is the pressure in PNM at saturation density. In addition, there are four "band constraints" on the symmetric nuclear matter and pure neutron matter equations of state in specific density regimes below and above nuclear saturation:

1. $P_{\rm SNM}$ for $1.2 < \frac{n}{n_0} < 2.2$
2. $P_{\rm SNM}$ for $2 < \frac{n}{n_0} < 4.6$
3. $P_{\rm PNM}$ for $2 < \frac{n}{n_0} < 4.6$
4. $(E/N)_{\rm PNM}$ for $0.014 < \frac{n}{n_0} < 0.106$.

First we note that the two RMF parametrizations that were close to reproduce low–density neutron matter constraints, DD2 and SFHx, do not satisfy the constraints. In particular DD2 has a skewness parameter K' with the wrong sign ($K' = -168.7$ MeV) while SFHx has too low a value for the slope L of the symmetry energy ($L = 23.18$ MeV). Furthermore, as can be seen from Table 2.1, some of the new parametrizations are inconsistent with the empirical constraints in Ref. [88]. Specifically, Ska25s20-0.9, Ska25s20-1.0 and Sv-sym32-0.9 fail to meet the constraint for isospin incompressibility.

We note that the discrepancies between our results for the symmetry energy and the ones reported in Table I from Ref. [135] are due to different definitions. In our case we follow Ref. [88] and start with the generic expression at arbitrary isospin asymmetry $\delta_{np} = \frac{n_n - n_p}{n} = 1 - 2y_p$ and define S as the second derivative of the

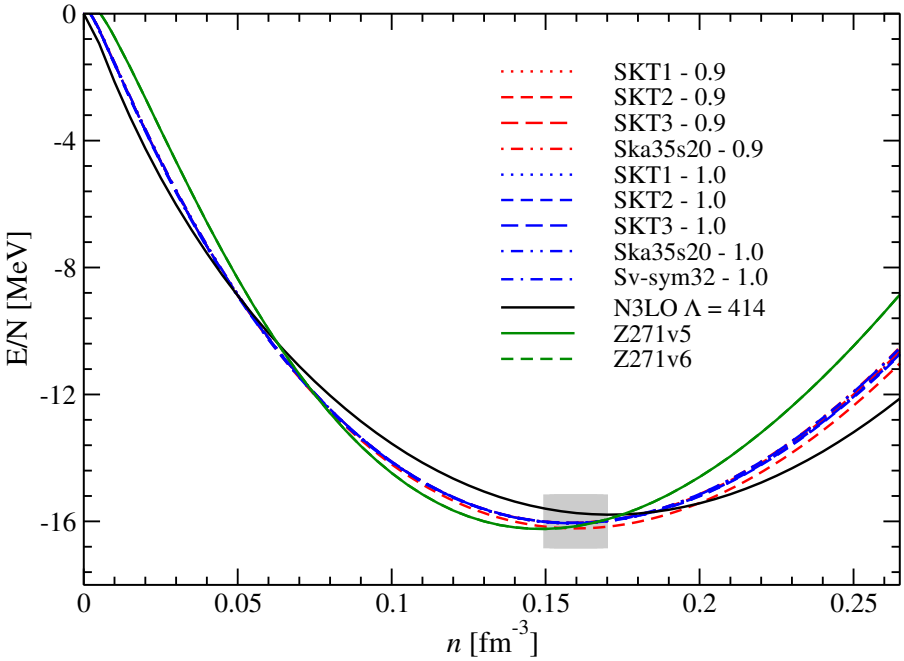

Figure 2.8: Same as Fig. 2.7 but for symmetric nuclear matter. The grey box shows a 5% tolerance at nuclear matter saturation density.

energy per particle with respect to y_p, as shown previously, while in Ref. [135] S is obtained as the difference between the PNM and the SNM equations of state at a given density. For microscopic approaches (like MBPT) these two definitions of S give very similar values (see e.g., [185, 186]).

As mentioned above the chiral 414 MeV interaction is used at second order in many-body perturbation theory with two- and three-body forces. Results using the potential with a cutoff of 450 MeV are very close to those from the N^{3}LO 414 potential. We see that in all cases the microscopic calculations of the equation of state with this potential are consistent with the empirical infinite matter constraints considered in Ref. [88]. We note that all models considered meet the band constraints.

2.3.4 Finite Temperature

In this section we focus on the nuclear thermodynamic equation of state of homogeneous matter from the mean field models that were found in the last section to be compatible with the zero-temperature equation of state from low-momentum χEFT and analyze the conditions necessary for consistency at finite temperature. We therefore focus on only the parametrizations SKT1-0.9, SKT2-0.9, SKT3-0.9, Ska35s20-1.0, Ska35s20-0.9 and Z271v6. Since there are no nonpertubative microscopic calculations available, we cannot assign uncertainty bands at specific densities as in the zero-temperature analysis. However, one would not expect the many-body perturbation expansion to change dramatically by including finite-temperature effects, and therefore we use the chiral interaction N3LO414 together with 3NF forces to be a qualitative guiding tool for low-density thermodynamical properties. The aim is to identify mean field models that quantitatively reproduce chiral nuclear thermodynamics at low to moderate densities and temperatures. The coefficients for the refitted Skyrme parametrizations that meet our selection criteria so far are given in Table 2.2.

The mean field models we are considering are fit to nuclei and infinite matter at $T = 0$ and contain no empirical input at finite temperature. The nucleon effective mass however controls the density of states and

therefore aspects of thermal excitations. We anticipate that the single-particle properties of nucleons in mean field models will control whether the associated thermodynamic equations of state will be consistent with those from perturbative chiral interactions. We choose low- and high-temperature representative values $T = 5, 25\,\mathrm{MeV}$.

The formalism employed in this section is self-consistent Hartree-Fock theory which treats the density matrix as effectively of one-body type. The problem of treating interactions properly is cast into an energy density functional for which a corresponding local density is found by minimization of the energy. The Skyrme and RMF models fall into this category. In the thermodynamic limit an ensemble equivalence is guaranteed, and the canonical or grand-canonical potential can be minimized. As we opt to have temperature T and density n as external fixed parameters, we work in the canonical ensemble. The set of self-consistent equations to be satisfied at Hartree-Fock level is given by Eqs. (2.34) and (2.35) below. For a given momentum-dependent nucleon single-particle spectrum $\epsilon_{s,t}(k)$, where s and t are the spin and isospin quantum numbers, the energy density and entropy density can be calculated from

$$\begin{aligned} f_{s,t}(k) &= \left[1 + e^{\left(\epsilon_{s,t}(k)-\mu\right)/T}\right]^{-1}, \\ n &= \sum_{s,t} \int \frac{d^3k}{(2\pi)^3} f_{s,t}(k), \\ \tau &= \sum_{s,t} \int \frac{d^3k}{(2\pi)^3} k^2 f_{s,t}(k), \\ S/V &= -\sum_{s,t} \int \frac{d^3k}{(2\pi)^3} \big[f_{s,t} \ln f_{s,t} + (1 - f_{s,t}) \ln(1 - f_{s,t}) \big], \end{aligned} \tag{2.34}$$

where a sum over all discrete quantum numbers is performed (spin and isospin). The chemical potential can be found by inverting the expression for the density. From the energy density functionals described in detail in the previous section, an effective mass and mean field shift can be extracted:

$$\begin{aligned} M_t^\star &= \frac{1}{2} \left(\frac{\delta \mathcal{E}}{\delta \tau_t} \right)^{-1} \\ U_t &= \frac{\delta \mathcal{E}}{\delta n_t}, \end{aligned} \tag{2.35}$$

which gives a single-particle spectrum of the form

$$\epsilon_t(k) = k^2/2M_t^\star + U_t. \tag{2.36}$$

Indeed, since at finite temperature the single particle properties are needed for the Fermi distributions which give rise to the energy density, and are derived themselves by the energy density, a set of coupled equations arises and needs to be solved consistently. The full glory of the details has already been described by the seminal work of Lattimer and Schwesty [187].

In Figs. 2.9 and 2.10 we plot the free energy per particle of neutron matter and isospin-symmetric nuclear matter for the microscopic and mean field models under consideration. We employ the Matsubara finite-temperature formalism up to second order in perturbation theory to compute the free energy per particle from the chiral two- and three-body potentials. Since the formalism was already described in chapter 1, we will refer the interested reader for additional details in [133, 134]. At $T = 5\,\mathrm{MeV}$ the PNM free energy is similar to that at zero temperature, where the mean field equations of state are consistently less attractive than that from chiral low-momentum interactions. However, at $T = 25\,\mathrm{MeV}$ the Skyrme mean field models exhibit larger

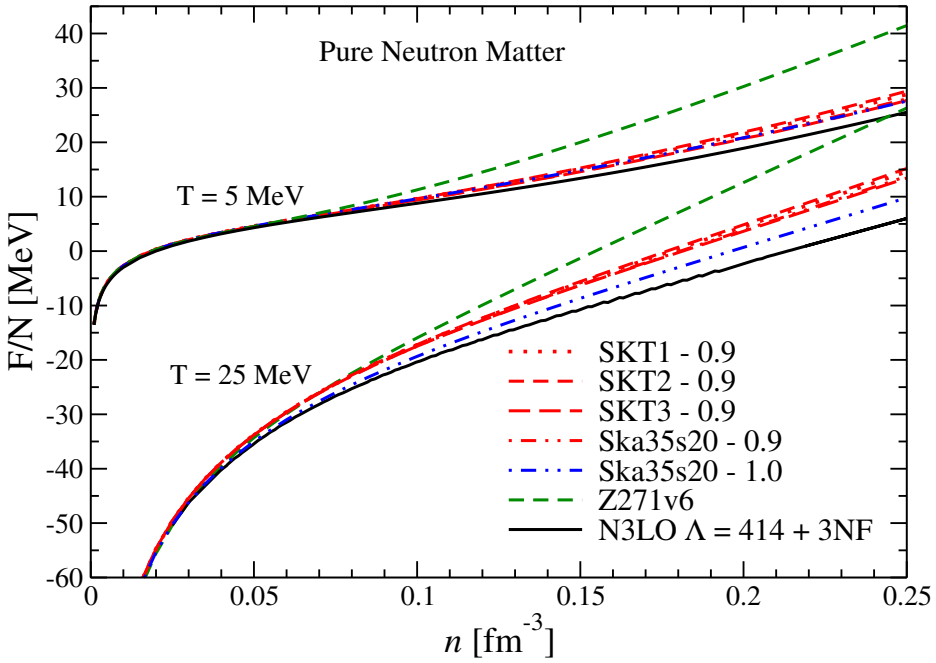

Figure 2.9: Free energy per nucleon in pure neutron matter at temperatures $T = 5, 25\,\mathrm{MeV}$ for the 414 MeV chiral nuclear potential and mean field models.

variations in the free energy. In particular smaller values of the effective mass result in a larger kinetic energy contribution and a small entropy term, both of which reduce the attraction at high temperatures. In symmetric nuclear matter at low temperatures there is consistency between all mean field models considered and the chiral equation of state. At the largest temperature considered ($T = 25\,\mathrm{MeV}$) the Skyrme models remain in good agreement with each other, owing to the very similar values of the effective masses, but deviate by about 5 MeV from the χEFT prediction. This pattern is different than that in the neutron matter equation of state, and it suggests that the average effective nucleon mass in symmetric nuclear matter is smaller than that in the Skyrme mean field models.

To explain the difference more carefully, we study the single-particle spectrum. The relativistic and non-relativistic models treat this quantity (as well as the chemical potential) differently. We first compare the non-relativistic reduction of the single-particle spectrum in RMF models to that in the Skyrme models:

$$\begin{aligned} e_{t\mathrm{Skyrme}}(k) =& \epsilon_t(k) - \mu_t = \frac{k^2}{2M_t^*} + U_t - \mu_t^{\mathrm{NR}} \\ \equiv& \frac{k^2}{2M_t^*} + U_t^*, \\ e_{t\mathrm{RMF}}(k) =& \epsilon_t(k) - \mu_t = \sqrt{k^2 + M_t^{*2}} + U_t - \mu_t^{\mathrm{R}} \\ \approx& \frac{k^2}{2M_t^*} + M_t^* + U - \mu_t^{\mathrm{R}} \\ \equiv& \frac{k^2}{2M_t^*} + U_t^*. \end{aligned} \tag{2.37}$$

At the HF level, the low-energy spectrum can be accurately modeled by an effective mass and mean field shift, both density dependent. We show in Figs. 2.11 and 2.12 the effective mass and mean-field shifts in neutron

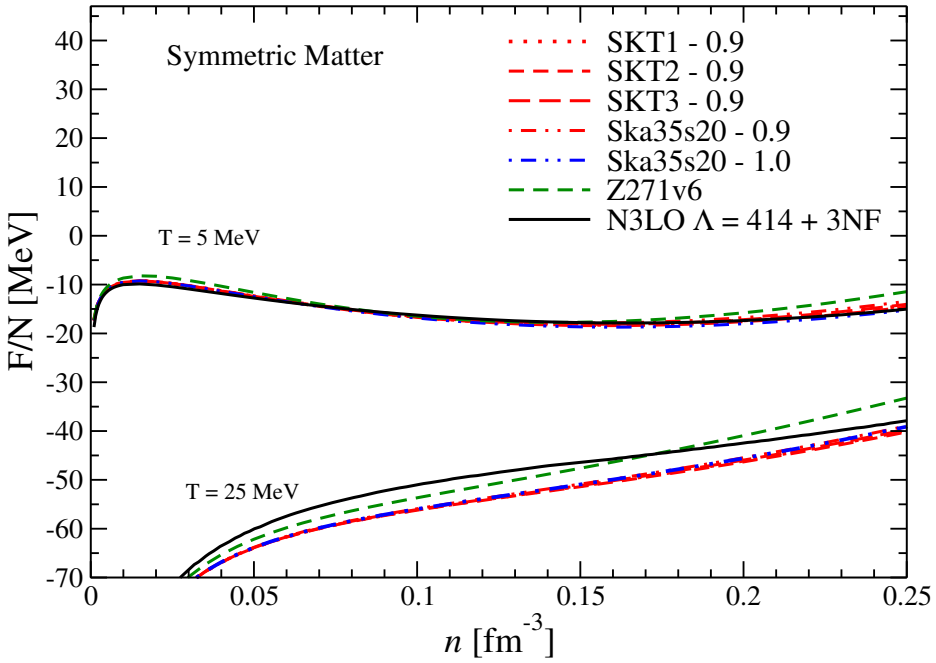

Figure 2.10: Same as Fig. 2.9 except for symmetric nuclear matter.

matter and symmetric nuclear matter for the models under consideration. In the case of SNM, the lower value of the effective mass corresponds to a higher value of the energy per baryon for Skyrme interactions, which results from a larger kinetic energy contribution to the free energy. Since the mean field shifts for the different Skyrme interactions with $M^*/M = 0.9$ in PNM at $n = 0.1\,\mathrm{fm}^{-3}$ are nearly identical, the kinetic contribution dominates the difference while the interaction contribution depends mostly on the density.

In contrast, RMF models predict smaller effective masses and larger (negative) effective mean field shifts. In the case of Z271v6 these effects balance in SNM, with the effective mass becoming more important only at higher densities (higher values of F/N). However, for PNM, Z271v6 has a very small effective mass which leads the kinetic energy to dominate over interactions as can be seen by higher values of F/N for the whole density range depicted in fig. 2.9. Despite the effective mass and energy shifts being very different between these two models, the free energies predicted are relatively similar. To understand the physical relevance of these two parameters, we have to study physical 'observables' which are specifically susceptible to them. The next section focuses on neutrino response and thermodynamic evolution, both sensitive to the single-particle spectrum, to differentiate Skyrme and RMF models.

2.3.5 Effect of Single-Particle Properties

Nuclear thermodynamics is governed by the free energy per nucleon as a function of the density and temperature. Related quantities such as pressure, entropy and chemical potential are given in terms of the free energy through standard thermodynamic relations. Dynamical phenomena in nuclear matter at finite temperature are strongly related to the single-particle properties of nucleons, and as shown in the last section the effective mass and mean field shift can be quite different between two models that nevertheless have similar equations of state. Thus, to explore a different set of consistency requirements between mean field models and microscopic nuclear dynamics we employ an analysis of the neutrino response and isentropic curves for core-collapse supernovae. We focus on Ska35s20-0.9, Ska35s20-1.0, and Z271v6, which are the "best fit" parametrizations from non-relativistic

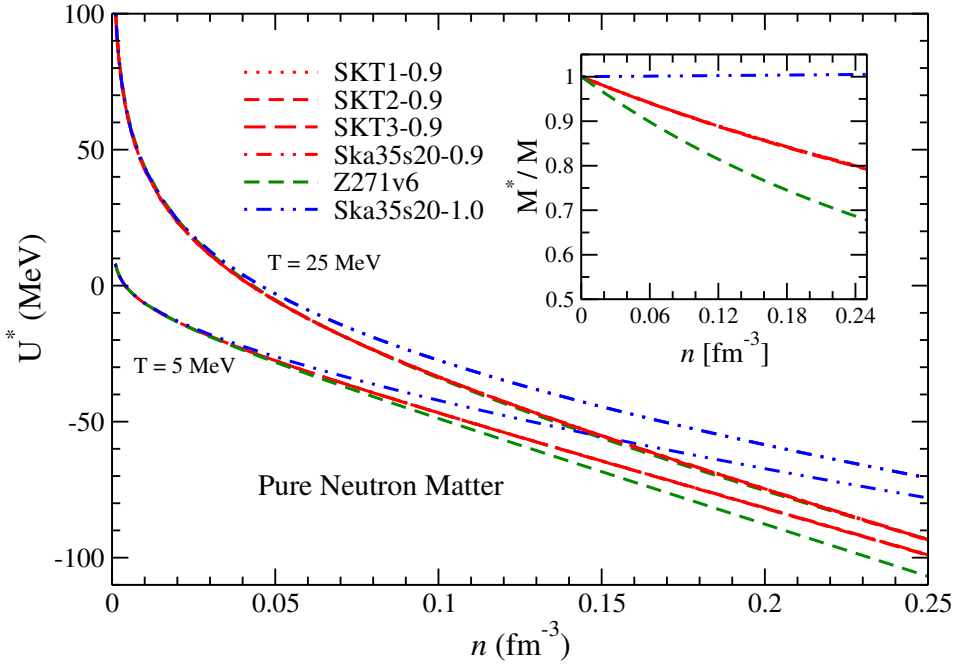

Figure 2.11: Neutron mean field shift and effective mass in pure neutron matter. Note that all "Sk...0.9" Skyrme interactions have nearly identical effective masses.

and relativistic mean field models to chiral equations of state at finite temperature.

Neutrino Response

Charged-current weak reactions were the focus of chapter 1. As already mentioned, they are primarily responsible for setting the ν_e opacity in the warm ($T = 5 - 8\,\mathrm{MeV}$) and dilute ($n = 0.001 - 0.01 n_0$) region of last scattering (the neutrino-sphere) for neutrinos diffusing from the core of a newly born PNS [188, 189, 190]. Owing to the non-degenerate conditions, the Fermi distribution functions for neutrons and protons are strongly smeared in the vicinity of the chemical potential. The proton and neutron energy shifts are primarily responsible for modifications to neutrino and anti-neutrino mean free paths, but the momentum dependence of the single-particle potential can also be relevant for low-density moderate-temperature conditions. The inverse mean free path of ν_e from the reaction $\nu_e + n \rightarrow e^- + p$ follows from Fermi's golden rule and is given by

$$\begin{aligned} \lambda_{\nu_e}^{-1} &= \frac{2}{(2\pi)^5} \int d^3p_n\, d^3p_e\, d^3p_p\, \mathcal{W}_{fi} \\ &\times \delta^{(4)}(p_{\nu_e} + p_n - p_e - p_p) f_n (1 - f_e)(1 - f_p), \end{aligned} \tag{2.38}$$

where f is the Fermi distribution function and W_{fi} is the transition probability. Both depend on the single-particle spectrum, and due to the energy-momentum conserving delta function, the phase space is also highly impacted by M^* and U^*.

We consider β-equilibrated matter at the density $n = 0.02\,\mathrm{fm}^{-3}$ and temperature $T = 8\,\mathrm{MeV}$. Table 2.3 shows the proton and neutron effective masses and energy shifts for the mean field models considered as well as for the chiral n3lo414 potential at Hartree-Fock level and the pseudo-potential which resums iterated ladder diagrams (without Pauli blocking) to all orders in perturbation theory and which is defined in terms of nucleon-nucleon scattering phase shifts (see Ref. [191] for additional details). The effective mass and mean field shift for the

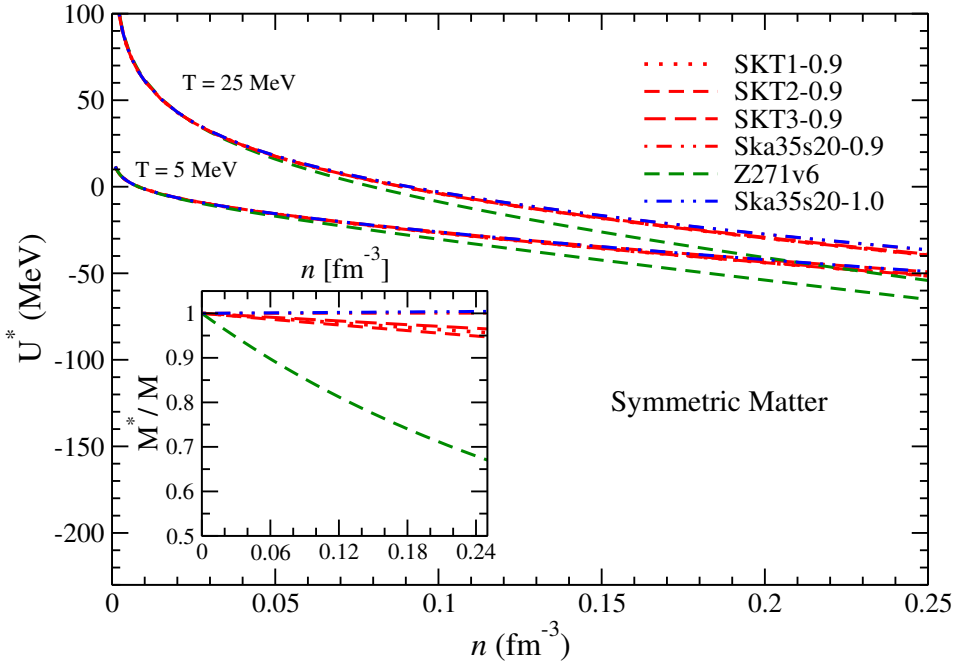

Figure 2.12: Same as in Fig. 2.11 except for symmetric nuclear matter.

chiral interactions come from a global fit of the single-particle spectrum from $k = 0$ to $k = 2k_f$. Note that for the temperature and density considered here, the two Skryme parametrizations Ska35s20-0.9 and Ska35s20-1.0 give nearly identical single-particle properties.

Given the paramount importance of charged-current absorption rates in determining the decoupling regions, and thus the energy spectra of ν_e and $\overline{\nu}_e$, Fig. 2.13 shows the opacity from two mean field equations of state. We observe that for ν_e absorption all mean field models are consistent with the lower bound provided by the chiral Hartree-Fock approximation and the upper bound set by the pseudo-potential. The Skyrme Ska35s20-0.9 mean field prediction is in good agreement with the pseudo-potential results, given that both models predict large values of $\Delta U = U_n - U_p$. Since the χEFT calculation is only at the self-consistent Hartree-Fock level, considerable attraction in the iterated tensor force channel is missing, and results much closer to those from the pseudo-potential are expected when second-order perturbative contributions are included. We plan to study these effects more carefully in future work. To completely determine the neutrino opacity, neutral current reactions are needed. Particularly for the case of $\overline{\nu}_e$ in the lower regions of the power spectrum, bremsstrahlung absorption rates dominate [192, 193, 191].

Supernova Isentropic Curves

During the core collapse of a massive star, the entropy per baryon changes from about 1 k_B to 2-3 k_B, and the adiabatic (isentropic) approximation can be used to describe the thermodynamic evolution during such a short time scale. The temperature versus density at constant entropy then provides a prediction of the temperature of the core in the initial and final stages. Since neutrinos are primarily emitted from the high-density region by neutral- and charged-current reactions, the temperature of the core plays an important role in determining their spectra [194]. At low temperatures both the density of states and entropy are expected to be proportional to the nucleon effective mass M^*. For the same entropy per baryon, a smaller effective mass at a given density therefore translates to a higher temperature.

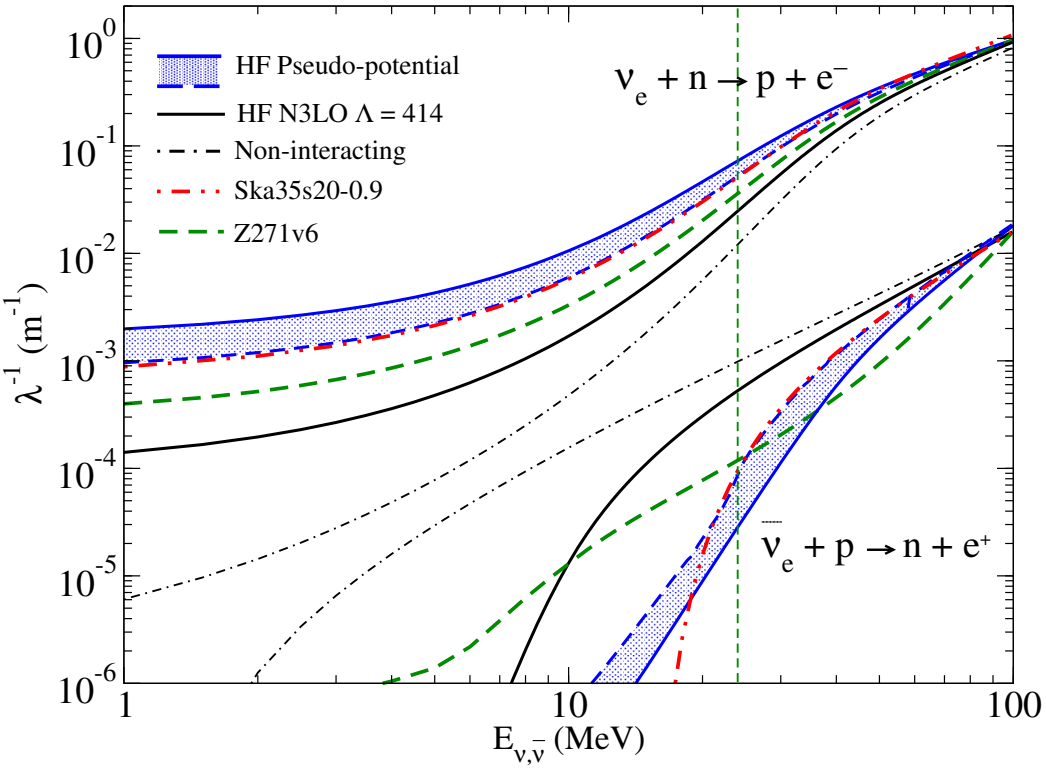

Figure 2.13: Charged-current rates at β equilibrium: T = 8 MeV, n = 0.02 fm^{-3}. The vertical dashed line indicates the 'thermal' energy, $E_{\nu_e,\overline{\nu}_e} = 3\,T$.

$$\begin{aligned} N(0) &= \sum_t \frac{M_t^* k_{f_t}}{\pi^2}, \\ S/V &= \sum_t \frac{M_t^* k_{f_t}}{3} T. \end{aligned} \tag{2.39}$$

In Fig. 2.14 we depict the Skyrme, RMF and chiral isentropic lines for pure neutron matter and isospin-symmetric matter for densities up to $4n_0$. We use the exact expression for entropy from Eq. 2.35 in this plot. For low-density neutron matter ($n < n_0/2$), the Ska35s20-1.0 Skyrme interaction gives results that are consistent with the n3lo414 chiral potential, which from Fermi liquid theory [195] predicts an effective mass $M^*/M \sim 1$. Beyond nuclear matter saturation density, the differences between the temperature of neutron matter at $S/N = 1$ can vary by up to 8 MeV for the chiral and mean field theory equations of state, while for $S/N = 2$ all models are nearly consistent. In the case of symmetric nuclear matter the two Skyrme parametrizations considered have very similar effective masses (see Fig. 2.12) and therefore the isentropic curves are nearly identical. At the highest temperatures ($T \gtrsim 20$ MeV) there are large variations in the predicted densities. In the microscopic calculation with the chiral n3lo414 potential, one may interpret this as a significant reduction of the effective mass at finite temperature due to a damping of collective modes [196], which normally lead to an enhanced effective mass. In general for temperatures less than T = 10 MeV the chiral isentropic curves are in good agreement with those from the Ska35s20-1.0 Skyrme interaction.

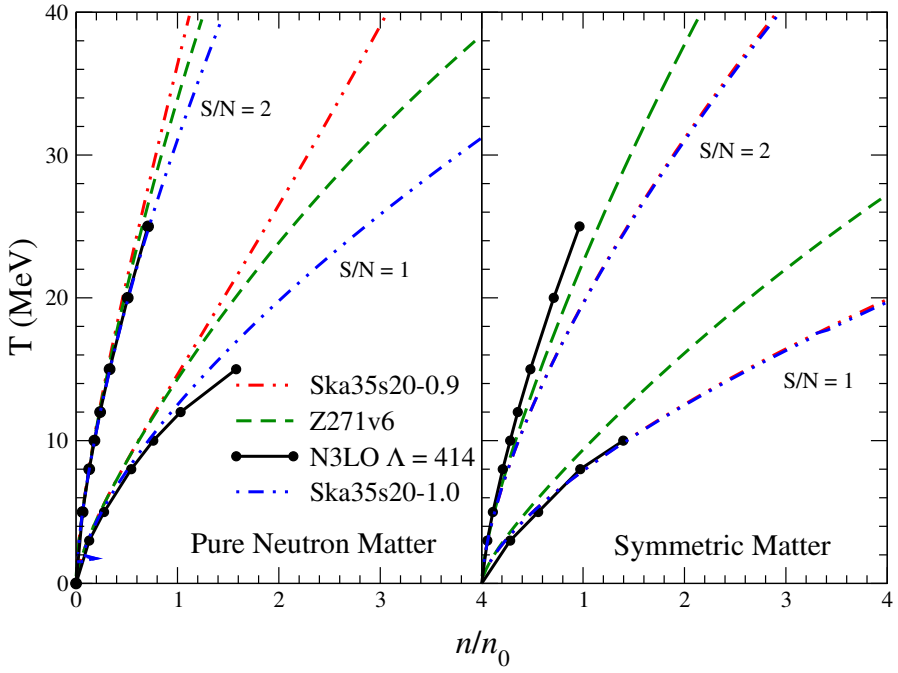

Figure 2.14: Temperature versus density isentropic lines for PNM and SNM.

Name	compatible	K_m (MeV)	K' (MeV)	J (MeV)	L (MeV)	$K_{\tau,v}$ (MeV)	$S(n/2)/J$	$3P_{PNM}/Ln_0$
Ska25s20 - 0.9	-	220	413	32.1	50.9	-345	0.66	1.0
Ska35s20 - 0.9	+	240	378	32.2	53.6	-374	0.65	1.0
SKT1 - 0.9	+	238	382	32.6	55.3	-378	0.65	1.0
SKT2 - 0.9	+	240	385	33.1	58.0	-385	0.64	1.0
SKT3 - 0.9	+	237	382	32.0	52.6	-370	0.65	1.0
Sv-sym32 - 0.9	-	234	384	31.5	49.5	-360	0.66	1.0
Ska25s20 - 1.0	-	220	415	32.0	46.4	-355	0.67	1.0
Ska35s20 - 1.0	+	240	379	32.2	50.6	-385	0.66	1.0
SKT1 - 1.0	+	237	384	32.5	51.5	-386	0.66	1.0
SKT2 - 1.0	+	236	387	32.3	50.4	-381	0.66	1.0
SKT3 - 1.0	+	237	385	33.0	48.9	-377	0.66	1.0
Sv-sym32 - 1.0	+	237	375	32.0	47.7	-387	0.66	1.1
DD2	-	243	-169	31.7	55.0	-461.7	0.66	1.0
SFHx	-	239	457	28.7	23.2	–	–	1.0
Z271v5	+	270	734	34.0	73.9	-389	0.57	1.0
Z271v6	+	270	734	33.8	70.9	-388	0.57	1.0
N3LO $\Lambda = 414$ MeV + 3NF	+	223	270	32.5	53.8	-424	0.70	1.0
Range of constraint		190-270	200-1200	30-35	40-76	-760 to -372	0.57-0.86	0.9-1.1

Table 2.1: Constraints on the properties of infinite nuclear matter from Dutra et al. [88, 178]. See text for definitions and details.

Name	α	**a** (MeV fm^5)	**b** (MeV fm^5)	$\mathbf{t_0}$ (MeV fm^3)	$\mathbf{x_0}$	$\mathbf{t_3}$ (MeV fm$^{3(1+\alpha)}$)	$\mathbf{x_3}$
Ska35-0.9	0.35	-172.485	172.087	-1767.71	0.282732	12899.2	0.413266
SKT1-0.9	1/3	-112.324	142.467	-1810.72	0.28223	12863.0	0.392585
SKT2-0.9	1/3	-113.857	143.999	-1807.87	0.267778	12802.4	0.366144
SKT3-0.9	1/3	-124.432	148.492	-1812.16	0.288584	12906.6	0.416129
Ska35-1.0	0.35	-2.41114	-0.507978	-1767.92	0.247025	12910.2	0.220377

Table 2.2: Parameters for the refitted Skyrme interactions of Ref. [135].

Model	Y_p	M_n^*/M_n	M_p^*/M_p	$-U_n$	$-U_p$	ΔU
HF Pseudo-potential	4.9%	0.65	0.42	22	55	33
HF Pseudo-potential (mod)	3.8%	0.78	0.57	18	42	23
HF N3LO $\Lambda = 414$ MeV	2.2%	0.95	0.89	8	16	8
RMF: Z271v6	2.8%	0.96	0.96	9	22	13
Skyrme: Ska35s20-0.9	3.3%	0.98	1.0	9	26	17

Table 2.3: The Hartree-Fock (HF) effective masses M^* and energy shifts U (in units of MeV) for protons and neutrons in beta equilibrium at $n_B = 0.02\,\mathrm{fm}^{-3}$ and temperature $T = 8\,\mathrm{MeV}$. The difference in proton and neutron mean-field shifts is given by $\Delta U = U_n - U_p$, and the proton fraction is denoted by Y_p.

2.4 Neutron Star Mass-Radius Relationship

An important feature of the 'strong' physics of neutron stars is the interdependence of mass and radius, which is uniquely determined by the EoS and the self-gravity of these compact objects. A relatively stiff EoS at high densities is required to generate a maximal mass of $2M_{\odot}$, which is currently the highest mass of an observed neutron star [86]. However, chiral interactions have a momentum cutoff that is comparable to the Fermi momentum at about $2n_0$ in neutron matter, and central densities in neutron stars can reach values of $5n_0$ or higher. Thus, at the present, nuclear potentials derived from χEFT can not be employed to cover the entire density range needed to describe nuetron stars. The mean field models considered in the present work can therefore be used to probe the very high density regime inaccessible to chiral effective field theory with coarse-resolution potentials. Caution, however, must be taken in using mean field models at such high densities. Since, at the moment, there are no tight experimental constraints that can be used for these densities, the results that mean fields show are fiducial extrapolations at best. Indeed, the predictions obtained outside the region from which mean field models were fit should be taken as 'qualitative', subject to improvements once these models are fit to data at higher densities. In our analysis we choose to use the chiral interaction up to the limit of its validity without model-dependent extensions. RMF models by construction remain causal, but Skyrme models can become superluminal at very large densities. However, we find no evidence for this behavior in this work.

In Fig. 2.15 we plot the neutron star mass vs. radius in the absence of protons and light leptons at $T = 0$ from the mean field models consistent with the chiral n3lo414 equation of state at low to moderate densities. Recently, in Ref. [197] a similar analysis has been performed for relativistic mean field models consistent with the infinite matter constraints considered in Section 2.3. Given the low values of the proton fraction found for β-equilibrated matter, this approximation is expected to be very good. We show also in Fig. 2.15 the current observational constraints on the mass and radius [198]. For each mean field model, we plot the mass vs. radius relationship both with and without the inclusion of the PBS crust equation of state [199].

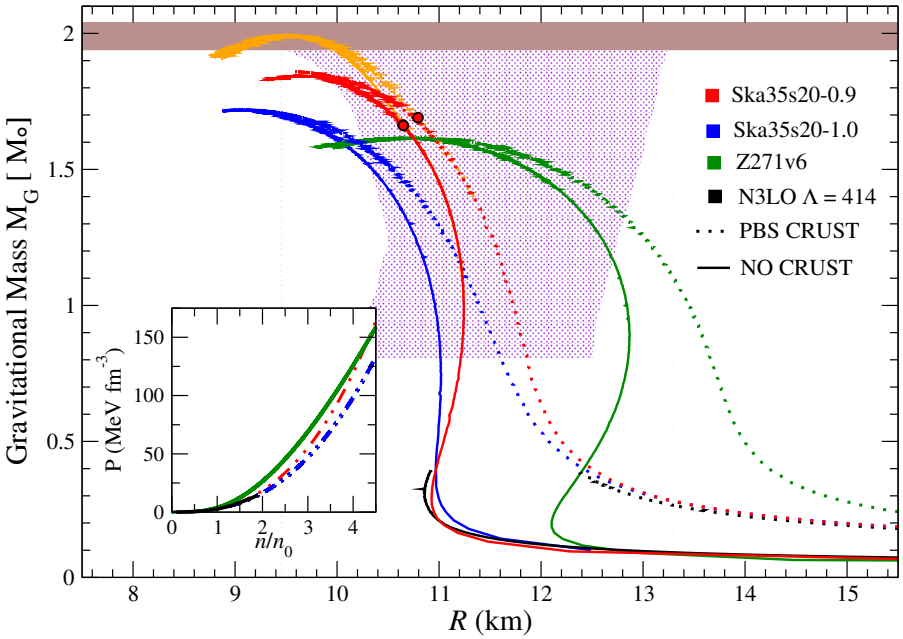

Figure 2.15: Neutron star mass as a function of radius. The mass-radius observational constraint comes from Ref. [198] and the maximum neutron star mass comes from Refs. [85, 86]. We use the BPS crust EoS [199] at low densities. The solid dots indicate the transition region to the constant speed of sound equation of state.

Skyrme models employed in our work are softer at lower densities and stiffer at higher densities, compared to the relativistic mean field model Z271v6. This results in generally smaller radii at a given mass for the Skyrme interactions and a larger maximum mass. For neutron star masses greater than about $1.3M_\odot$, all equations of state give mass-radius relations consistent with the empirical constraints from Ref. [198]. The inclusion of a crust increases the radius by about 0.5 km for a 1.4 $M_\odot$ neutron star and for the most massive neutron stars has a relatively small impact. This is, perhaps, a first indication that the crust equation of state used should be consistent with the underlying microphysics model given its impact in the size of typical neutron stars (of mass 1.4 $M_\odot$). This and other implications of the crust EoS are current subject of investigation to be published in future works.

We see that none of the models employed reaches the maximal mass value of 2 solar masses, indicating that the phenomenological interactions must be supplemented by a stiffer EoS at high densities. We identify the density above which the equation of state must be modified by employing the constant speed of sound parametrization [200] at the superluminal boundary. As a representative example, the Ska35s20.09 Skyrme interaction can generate a 2 solar-mass neutron star if the equation of state beyond $n = 4.5n_0$ is taken to be that of a liquid with constant speed of sound equal to the speed of light. The presence of the crust has only a very small effect, increasing the transition density to $n = 4.6n_0$.

However, for the high densities required for 2 solar mass neutron stars there are no other constraints on the properties of baryonic matter and our criteria is valid only for low densities. Thus, we would only like to emphasize that is feasible to reach the mass limit by modifications of the high density regime, but the proper study of matter in this range is beyond the scope of this work.

2.5 Conclusion

We have studied the use of mean field models to reproduce zero- and finite-temperature nuclear equations of state derived from microscopic many-body theory with realistic chiral two- and three-body forces. Comparing to quantum Monte Carlo simulations employing two-body forces alone, we find that the zero-temperature neutron matter equation of state is well converged in perturbation theory up to half saturation density, with uncertainties on the order of a few percent. From this density regime we select mean field models consistent with the predictions from chiral effective field theory as well as the available empirical infinite matter constraints. We then explore consistency with chiral nuclear thermodynamics and find that the free energy as a function of the temperature for mean field models are strongly correlated with the nucleon effective mass, with smaller values giving rise to larger kinetic energy contributions and smaller entropy contributions to the free energy.

In addition we studied the effects of the single-particle dispersion relation on select astrophysical phenomena, such as neutrino absorption in the proto-neutron star neutrino-sphere and the adiabatic evolution of core collapse. While the single-particle energy shift is most relevant for determining the charged-current weak reaction rates, the nucleon effective mass largely governs the isentropic temperature-density relation. For the latter quantity, significant variations are observed in the neutron matter low-entropy regime. At the largest densities considered ($n \sim 1.6n_0$), the temperature can vary by up to 50% for matter with an entropy per baryon of $S/N = 1$.

Finally, the mean field models consistent with the low-density chiral n3lo414 equation of state were used to explore the high-density regime relevant for cold neutron star matter where chiral effective field theory is expected to break down. While the mass-radius curves are consistent with present observational constraints around $M \sim 1.5M_\odot$, all maximum neutron star masses lie below $M \sim 2M_\odot$ and the constant speed of sound parametrization was used to complete the mean field models in the high-density regime above $n = 4.5n_0$.

The present work lays the foundation for future efforts to construct consistent equations of state and neutrino

response functions that are compatible with chiral effective field theory for use in numerical simulations of core-collapse supernovae and binary neutron star mergers.

Chapter 3

Electron - neutron induced interactions in Neutron Stars

3.1 Introduction

We started this journey of extremely compact objects at the 'birth' phase in hot and violent supernovae. In such conditions, weak and nuclear interactions are paramount in understanding the rapid processes that take place and their outcomes. After having spent some time exploring these fascinating interactions and the phenomenology they cause, it is time to focus on the 'child' of the core collapse, the neutron star itself. Here, the focus is on transport properties, and how previously unconsidered interactions, can shape the thermal relaxation, electric conductivity and shear viscosity of these stars.

Even before their discovery more than fifty years ago, it was anticipated on theoretical grounds that neutron stars would contain cold and dense matter where quantum effects would manifest on a macroscopic scale [201]. The interpretation of time dependent phenomena observed in x-rays continues to unravel the connection between such quantum behavior and observable phenomena [202]. In this context, transport properties of cold, dense matter play a particularly important role because coherence and correlations between particles can have a dramatic impact on the thermal and electrical conductivity, and the shear viscosity of dense matter. For example, shortly after Bell and Hewish discovered neutron stars [203], Baym, Pethick, and Pines showed that due to extreme degeneracy, matter in the neutron star core would be an excellent electrical conductor, implying that large magnetic fields could be sustained without ohmic dissipation for time scales larger than the age of the universe [204]. In the subsequent decades, several authors, including Flowers and Itoh [205], and Yakovlev and collaborators [206, 207, 208], have studied in some detail the electrical conductivity, thermal conductivity, and shear viscosity of neutron star matter. The roles of degeneracy, superfluidity, and superconductivity in the core, and crystalline phases in the lower density regions called the crust, have been studied. Yet, an important scattering mechanism between electrons and neutrons, induced by protons in the core and ions in the crust, has been overlooked.

At the high densities and relatively low temperatures characteristic of neutron stars, a rich phase structure is expected because of strong nuclear and Coulomb interactions, and in some phases, transport processes can be either greatly enhanced or suppressed. In the outer crust, matter is solid as fully pressure ionized nuclei freeze and form a lattice at low temperature due to strong Coulomb interactions. In the inner crust, where the mass density exceeds 4×10^{11} g cm^{-3}, neutrons drip out of nuclei and form a nearly uniform and degenerate Fermi gas alongside the electrons. Due to the strong and attractive s-wave interaction, dripped neutrons in the inner crust are expected to form Cooper pairs and become superfluid at low temperature. The critical temperature

for neutron superfluidity T_c^n is a strong function of density and typical values are in the range $T_c^n \approx 10^8 - 10^{10}$ K for the densities found in the crust (for a recent review on Cooper pairing of nucleons in neutron stars see [209]).

When the mass density $\rho \gtrsim 10^{14}$ g cm^{-3}, nuclei disappear, possibly through a relatively continuous transition involving non-spherical nuclear shapes, collectively called the pasta phase [210]. This transition marks the crust-core boundary, with the core containing a liquid phase with degenerate neutrons, protons, and electrons. The baryon density in the core is expected to be in the range $n = n_0/2 - 4n_0$, where $n_0 = 0.16$ nucleons fm^{-3} is the number density inside ordinary nuclei, also called the nuclear saturation density. The typical electron/proton fraction is on the order of a few percent at $n = n_0$, and increases with density. When the electron Fermi energy exceeds the mass of the muon, matter also contains an admixture of muons. This matter containing neutrons, protons, electrons, and muons in a liquid state may persist up to the highest densities $\approx 10^{15}$ g cm^{-3} at the center of the star in the absence of phase transitions to other exotic forms of matter containing hyperons, kaons, or quarks (for a recent review see [202]). At the high densities in the core the neutron Fermi momentum is large, and s-wave interactions between neutrons become repulsive. Superfluid pairing is only possible in p-waves, and p-wave pairing has been found to be fragile and model dependent, with estimates of the critical temperature $T_c^n \approx 10^8$ K [211]. In contrast, because the proton density is small, s-wave interactions remain strongly attractive for protons and s-wave proton superconductivity with a critical temperature $T_c^p \approx 10^8 - 10^{10}$ K is expected.

Throughout these different phases of matter inside the neutron star, electrons remain relativistic, degenerate, and weakly interacting. They consequently play an important role in transport phenomena that shape the thermal, magnetic field, and spin evolution of neutron stars. In this article we calculate the electron-neutron coupling, which dominantly depends on the polarizability of the medium. In earlier work electron-neutron scattering due to the intrinsic magnetic moment of the neutron was considered and found to be unimportant [205]. Here, in contrast, we find that electron-neutron scattering due to the induced coupling is important for determining the electronic transport properties in the neutron star core.

We begin with a derivation of the induced interaction in the core and in the inner crust in sections 3.2 and 3.3, respectively. In section 3.5 we derive general formulae for the the electron thermal conductivity, electrical conductivity, and shear viscosity. We present our results for these electronic transport properties, and compare them to those obtained in earlier work in section 3.6 to highlight situations in which electron-neutron scattering could be important. Our conclusions and some limitations of our study are presented in section 3.7. Throughout we use natural units, setting $\hbar = 1$, $c = 1$, and $k_B = 1$, and the electric charge $e = \sqrt{4\pi\alpha}$ where $\alpha = 1/137$ is the fine structure constant. Since the electron Fermi momentum $k_{Fe} \simeq 100$ MeV $\gg m_e$ for typical densities encountered in the neutron star inner crust and core, throughout we treat the electrons as ultra-relativistic particles with velocity $v_e = c = 1$.

3.2 Induced electron-neutron interaction in the core

In free space, and at low momenta, the electron-neutron interaction is weak as it arises due to the neutron magnetic moment. In contrast, in the dense plasma inside neutron stars, electrons can couple to neutrons due to an interaction induced by the polarizability of the charged protons. This can be understood intuitively by noting that the presence of the neutron in the medium will disturb its immediate vicinity, and affect in particular the proton density distribution. This will create either a positively or negatively charged cloud around the neutrons depending on whether the neutron-proton interaction is attractive or repulsive. At low density since the neutron-proton interaction is attractive, the neutron will acquire a net positive charge while at the high density where the interaction can be repulsive, the charge cloud surrounding the neutron will be negative.

The effective coupling between neutrons and electrons is mediated by the in-medium photon (the plasmon) and can be derived using standard techniques in quantum field theory as will be shown in this section. An effective Lagrangian for the electron-neutron coupling can be derived in analogy with the plasmon-neutrino coupling described in Refs. [212, 213]. The Feynman diagram in Fig. 3.1 shows the exchange of a plasmon which couples electrons to protons. The protons in turn couple to neutrons by the short-range strong interaction

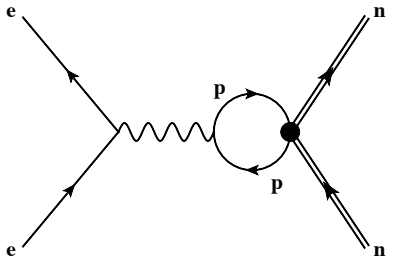

Figure 3.1: Effective interaction between electrons and neutrons induced by protons in the medium. The wavy line represents the plasmon.

depicted by a filled circle. From the diagram it follows that the plasmon-neutron coupling can be described by the effective Lagrangian

$$\mathcal{L}_{\gamma-\mathrm{n}} = -\sqrt{4\pi\alpha}\; V_{\mathrm{np}}\; \bar{n}\gamma_\mu n\; \Pi_{\mathrm{p}}^{\mu\nu} A_\nu\,, \tag{3.1}$$

where n and A_ν are the neutron and plasmon fields, V_{np} is the short-range nuclear potential, and $\Pi_{\mathrm{p}}^{\mu\nu}$ is the proton polarization correction to the photon in the plasma which can be decomposed into longitudinal and transverse components and is given by

$$\Pi_p^{\mu\nu}(\omega,q) = \Pi_p^L(\omega,q)\left(1,\frac{\omega}{q}\hat{q}\right)^\mu\left(1,\frac{\omega}{q}\hat{q}\right)^\nu + \Pi_p^T(\omega,q)\; g^{\mu i}(\delta^{ij}-\hat{q}^i\hat{q}^j)g^{j\nu}\,, \tag{3.2}$$

where i,j are spatial indices and the four-momentum $q^\mu = (\omega, q\hat{q})$ [214]. Π_p^L and Π_p^T are complex functions in general but we neglect the imaginary part in defining the plasmon-neutron coupling for the following reasons. When the protons are in the normal phase, the imaginary part corresponds to real proton excitations and leads to Landau damping of the plasmon. Its magnitude is small (proportional to $m_p^2\;\omega/q$ where m_p is proton mass) and vanishes in the static limit $\omega \to 0$ [141]. Instead if protons are superconducting, the imaginary part is zero for $\omega < 2\Delta_p$ where Δ_p is the energy gap in the proton spectrum [215]. The real part of the longitudinal polarization function is denoted as $\chi_p(\omega,q)$ and is given by

$$\chi_p(\omega,q) = \mathcal{R}e\;\Pi_p^L(\omega,q) = \mathcal{R}e\;\int dt\; e^{i\omega t}\int d\mathbf{r}\; e^{-i\mathbf{q}\cdot\mathbf{r}}\;\langle n_p(\mathbf{r},t)n_p(0,0)\rangle\,, \tag{3.3}$$

where $n_p = \bar{p}\gamma_0 p = p^\dagger p$ is the proton density operator. The real part of the transverse polarization function is related to the velocity-velocity correlation function of the proton fluid. Note that $q_\mu\Pi^{\mu\nu} = 0$ so that this effective electron-neutron coupling is manifestly gauge invariant.

Since the proton fraction in neutron stars is typically only a few percent, the proton Fermi momentum is small and protons can be treated in the non-relativistic limit. The neutrons are also only mildly relativistic in the vicinity of nuclear saturation density with a velocity $v_{\mathrm{Fn}} = k_{\mathrm{Fn}}/m_n \simeq 1/3$. This, together with the fact that scattering kinematics is restricted to the region $\omega < q$, implies that it is reasonable to neglect the spatial components in Eq. 3.1.

To illustrate how the induced interaction arises we consider the case of electron scattering from an interacting liquid of neutrons and protons at zero temperature. For simplicity, we will work in the assumptions that protons

and neutrons are non-relativistic, and only consider the Coulomb coupling of electrons to the proton density. The linear response formalism to describe scattering off the density fluctuations in a liquid in terms of the density-density correlation function $\Pi^p(\omega, q)$ is derived and discussed in Ref. [141]. Explicitly, the differential cross-section per unit volume for an electron with momentum k to scatter from density fluctuations in a proton liquid is given by

$$\frac{1}{V}\,\frac{d\sigma}{d\omega dq}(k) = -\frac{q}{2\pi^2}\left(1-\frac{q^2}{4k^2}\right)\,\mathcal{U}_{\rm ep}^2(q)\;\mathcal{I}{\rm m}\;\Pi^p(\omega,q);\quad \mathcal{U}_{\rm ep}(q) = \frac{-4\pi\alpha}{q^2+q_{\rm TF}^2}\,, \tag{3.4}$$

where ω and q are the energy and momentum transfer from the electron to the medium, $\alpha = 1/137$ is the fine structure constant, and $\mathcal{U}_{\rm ep}(q)$ is the effective interaction in the medium between electrons and protons which includes the effects of screening in the plasma through the Thomas-Fermi screening momentum, which includes the screening of electric charge due to protons, electrons, and muons, and is defined by

$$q_{\rm TF}^2 = 4\pi\alpha\sum_{\rm i=e,p,\mu}\frac{\partial n_i}{\partial\mu_i} \approx \frac{4\alpha}{\pi}\left(m_p k_{\rm Fp} + k_{\rm Fe}^2 + k_{{\rm F}\mu}\sqrt{m_\mu^2+k_{{\rm F}\mu}^2}\right). \tag{3.5}$$

A generalization of this formalism to a two component liquid is outlined in [216, 217] where it was used to study neutrino scattering off neutrons and protons. Using this generalized formalism to describe scattering of relativistic electrons off neutron and proton density fluctuations, we find that the differential cross-section per unit volume for an electron with momentum k to scatter from a neutron-proton liquid is given by

$$\frac{1}{V}\,\frac{d\sigma}{d\omega dq}(k) = -\frac{q}{2\pi^2}\left(1-\frac{q^2}{4k^2}\right)\frac{1}{(q^2+q_{\rm TF}^2)^2}\;(0,\quad 4\pi\alpha)\;\mathcal{I}{\rm m}\;\mathbf{\Pi}(\omega,q)\;\begin{pmatrix}0\\4\pi\alpha\end{pmatrix}, \tag{3.6}$$

where $\mathbf{\Pi}(\omega, q)$ is the density-density correlation function of the two component liquid which we shall define explicitly below. The coupling between the neutron and proton components of the liquid is incorporated by summing a class of particle-hole diagrams most relevant at long-wavelengths within the Random Phase Approximation (RPA) [141]. In this approximation (which satisfies current conservation), a closed form expression for the time-ordered correlation function $\mathbf{\Pi}(\omega, q)$ exists and is given by

$$\mathbf{\Pi}_{\rm RPA}(\omega,q) = (\mathbf{1}-\mathbf{V}\;\mathbf{\Pi^0})^{-1}\;\mathbf{\Pi^0}\;, \tag{3.7}$$

$$\mathbf{\Pi^0} = \begin{pmatrix}\mathbf{\Pi}_n^0 & 0\\ 0 & \mathbf{\Pi}_p^0\end{pmatrix},\quad \mathbf{V} = \begin{pmatrix}V_{nn} & V_{np}\\ V_{np} & V_{pp}\end{pmatrix}, \tag{3.8}$$

where $\mathbf{V}$ is the interaction matrix that describes the strong interactions between quasi-particles in the liquid. The neutron and proton time-ordered density-density correlation functions $\mathbf{\Pi}_n^0$ and $\mathbf{\Pi}_p^0$ are approximated by the expressions obtained for a non-interacting Fermi gas

$$\Pi_j^0(\omega,q) = -2i\;\int\frac{dk_0\;d^3k}{(2\pi)^4}\;\mathcal{G}_j(k_0+\omega,|\vec{k}+\vec{q}|)\mathcal{G}_j(k_0,k)\,, \tag{3.9}$$

where $\mathcal{G}_j(k_0, k)$ is the single particle Greens function [141].

To make explicit the real and imaginary parts, the correlation function can be written as

$$\mathbf{\Pi}_j^0 = \chi_j + i\Phi_j\,. \tag{3.10}$$

Of particular interest to our study here is the case when $\Phi_p \approx 0 \ll |\chi_p|$. As already stated, this is realized when protons are superconducting and the energy transfer ω is small compared to the gap in the excitation spectrum,

Δ_p. Further, when $|V_{nn}\chi_n| \ll 1$ and $|V_{pp}\chi_p| \ll 1$, we find that in the limit $\Phi_p \to 0$ the differential cross-section per unit volume is given by

$$\frac{1}{V}\frac{d\sigma}{d\omega dq} = -\frac{8\alpha^2 q}{(q^2+q_{TF}^2)^2}\left(1-\frac{q^2}{4k_{Fe}^2}\right)V_{pn}^2\chi_p^2\ \Phi_n\,. \tag{3.11}$$

Here, electrons excite neutron particle-hole states indirectly through the proton polarization. Comparing Eq. 3.11 with Eq. 3.4 we define the induced electron-neutron interaction

$$\mathcal{U}_{\rm enp}(\omega,q) = \frac{-4\pi\alpha\ \mathcal{C}_{\rm enp}(\omega,q)}{q^2+q_{\rm TF}^2}\,, \tag{3.12}$$

where $\mathcal{C}_{\rm enp}(\omega,q) = V_{np}\chi_p(\omega,q)$.

The effective electron-neutron interaction from this potential is, then, described by the Lagrangian

$$\mathcal{L}_{\rm e-n} = -\bar{e}\gamma_0 e\ \mathcal{U}_{\rm enp}(\omega,q)\ \bar{n}\gamma_0 n\,, \tag{3.13}$$

where e is the electron field.

We now discuss χ_p and $V_{\rm np}$, both of which are needed to calculate the effective electron-neutron coupling $\mathcal{C}_{\rm enp}(q)$, which characterizes the strength of the electron-neutron interaction relative to the Coulomb interaction between electrons and protons. First, we note that due to the strong degeneracy of electrons at low temperature, the energy transfer $\omega \approx T$ is small compared to the momentum transfer q and other relevant energy scales associated with the dense medium. For this reason, the effective coupling can be calculated in the static limit. In this limit, the susceptibility $\chi_p(q) \equiv \chi_p(\omega=0,q)$ is well known from non-relativistic many-body theory for a non-interacting Fermi gas and is given by

$$\chi_p(q) = \mathcal{R}e\ \Pi_p^0(\omega=0,q) = -\frac{m_p k_{\rm Fp}}{2\pi^2}\ \left(1+\left(\frac{1-y^2}{2y}\right)\log\left|\frac{1+y}{1-y}\right|\right)\,, \tag{3.14}$$

where the one-loop polarization function Π_p^0 is defined in Eq. 3.9 and $y = q/2k_{\rm Fp}$ [141]. In a strongly interacting system, higher order corrections to the one-loop polarization function can become relevant but are known not to change the qualitative behavior. We estimate the size of these corrections by noting that in the long-wavelength limit $\chi_p(q\to 0) = -\partial n_p/\partial\mu_p$ where n_p and μ_p are the proton number density and chemical potential, respectively. Using microscopic calculations of the dense matter equation of state (EoS) reported in Refs. [218] and [219], we have calculated this derivative to find corrections in the range 20% – 50% in the vicinity of $n = n_0$, and an enhancement by a factor of two at the highest densities ($n \simeq 0.48$ fm^{-3}) encountered in the core. In contrast, corrections to $\chi_p(q)$ due to proton superconductivity are small in the static limit for typical values of the superconducting gap $\Delta_p \simeq 1$ MeV $\ll \mu_p$ and can be safely neglected [215].

The potential $V_{\rm np}(q)$ describes the interaction between neutrons and protons in the medium and is in general a complicated function of density and momentum. However, later in section 3.5 we shall find that typical momentum transfer involved in electron collisions is in the range of a few times $q_{\rm TF}$, and this justifies a low momentum expansion of the form

$$V_{\rm np}(q) = V_{\rm np}^{(0)} + V_{\rm np}^{(2)}\ \frac{q^2}{k_{\rm Fe}^2}\,. \tag{3.15}$$

The effective interaction at zero momentum exchange can be extracted from the EoS of dense matter through the relation

$$V_{\rm np}^{(0)} = V_{\rm np}(q\to 0) = \frac{\partial^2\mathcal{E}}{\partial n_p \partial n_n}\,, \tag{3.16}$$

where $\mathcal{E}(n_n, n_p)$ is the energy density of the liquid of neutrons and protons with density n_n and n_p, respectively. We use EoS models described in Refs. [218] and [219], which are based on non-perturbative calculations using realistic two and three nucleon interactions, to calculate $\mathcal{E}(n_n, n_p)$ and the second derivative $\partial^2\mathcal{E}(n_n, n_p)/\partial n_n \partial n_p$. Numerical differences between them can be viewed as a rough error estimate and for this reason we shall present results for both EoSs. The second term in the expansion $V_{\rm np}^{(2)}$ cannot be derived from the EoS, but it is related to the $L = 1$ Fermi liquid parameters. Since we are unaware of a microscopic calculation of these parameters in neutron-rich matter, we have opted to use a range $V_{\rm np}^{(2)} = 5 \times 10^{-6} - 5 \times 10^{-5}$ MeV^{-2} as suggested by calculations in symmetric nuclear matter from Ref. [220].

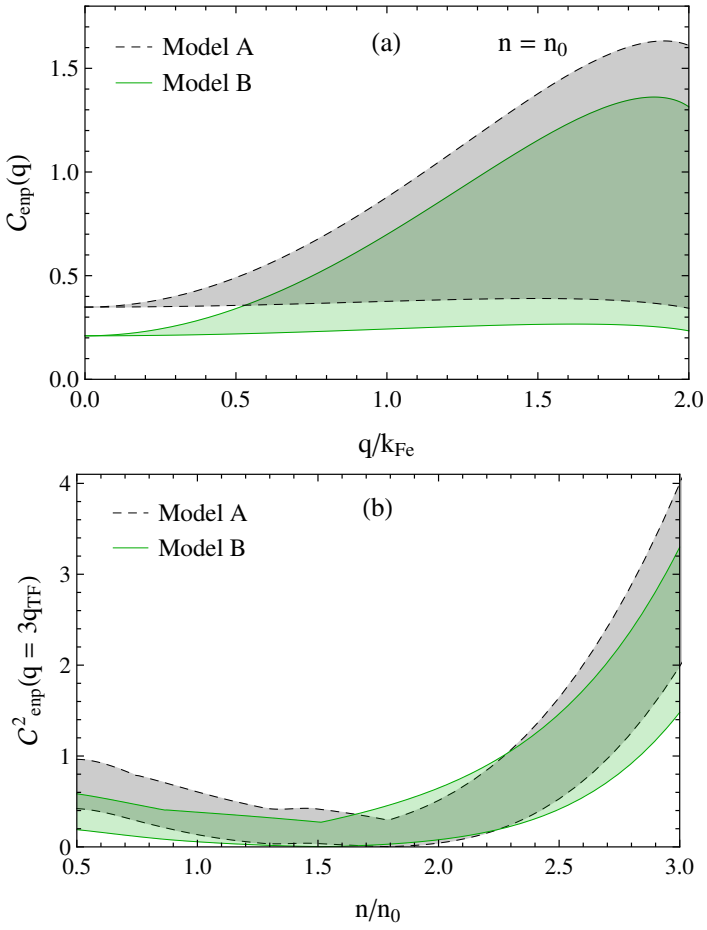

Figure 3.2: (a) The strength of the induced electron-neutron interaction defined in Eq. 3.12 as a function of q at nuclear saturation density $n_0 = 0.16$ fm^{-3}. (b) $\mathcal{C}_{\rm enp}^2(q = 3q_{\rm TF})$ as a function of density.

The momentum and density dependence of the strength of the induced coupling $\mathcal{C}_{\rm enp}$ is shown in Fig. 3.2 for the two models defined as follows. In model A, we use the EoS from Ref. [218] to obtain $V_{\rm np}^{(0)}$ and in model B, we instead use the EoS from Ref. [219]. In both cases, the band is obtained by varying $V_{\rm np}^{(2)}$ over the range mentioned above.

3.3 Electron-neutron interaction in the crust

In the inner crust, free protons are absent as they are all bound into neutron-rich ions. Here, the interaction between electrons and neutrons is induced by these ions and arises due to the nuclear interaction between the ions and the unbound neutrons. The calculation of the induced interaction proceeds along the lines described earlier, but with ions in the crust playing the role of protons in the core. We find, as before, that the induced interaction can be written in the form

$$\mathcal{U}_{\rm enI}(0,q) = \frac{-4\pi\alpha\ \mathcal{C}_{\rm enI}(q)}{q^2+q_{\rm TFe}^2};\quad \mathcal{C}_{\rm enI}(q) = V_{\rm nI}(q)\ Z\ \chi_I(q)\,, \tag{3.17}$$

where $q_{\rm TFe} = \sqrt{4\alpha/\pi}\ k_{\rm Fe}$ is the Thomas-Fermi screening momentum of the electron gas, $V_{\rm nI}(q)$ is the short-range neutron-ion interaction, Z is the charge of the ion, and

$$\chi_I(q) = \mathcal{R}e\ \int dt \int d\mathbf{r}\ e^{-i\mathbf{q}\cdot\mathbf{r}}\ \langle n_I(\mathbf{r},t) n_I(0,0)\rangle\,, \tag{3.18}$$

is the ion static density-density correlation function where $n_I(r,t)$ is the ion density operator. The strength and momentum dependence of the interaction $V_{\rm nI}(q)$ will in general depend on the nuclear structure of the extreme neutron-rich nuclei present in the crust and has not been studied in any detail. Since the typical momentum transfer $q \simeq$ a few times $q_{\rm TFe}$, and $q_{\rm TFe}$ is small compared to $k_{\rm Fe}$, a momentum expansion of the form in Eq. 3.15 can be justified. Again, the leading order term, which is independent of momentum, can be calculated from the EoS through the relation $V_{\rm nI}^{(0)} = \partial^2\mathcal{E}/\partial n_n \partial n_I$ where $\mathcal{E}$ is the energy density. We use the data from [1] for the composition and EoS of the crust to calculate $V_{\rm nI}^{(0)}$. However, as we are unaware of any calculations of $V_{\rm nI}^{(2)}$ that we can make use of here, and its calculation is beyond the scope of this study, we set $V_{\rm nI}^{(2)} = 0$ to obtain a conservative estimate of $\mathcal{C}_{\rm enI}(q)$.

$\chi_I(q)$ in the crust differs from $\chi_p(q)$ in the core because Coulomb correlations between ions are strong enough to result in crystalline structure at low temperature. To compute $\chi_I(q)$ in the crystalline state we can use the fact that the ion dynamic form factor $S_I(\omega,q)$ is dominated by phonons, and we can combine this with the fluctuation-dissipation theorem and the Kramers-Kronig relation to find that

$$\chi_I(q) = -\mathcal{P}\ \int_{-\infty}^{\infty} \frac{d\omega'}{2\pi} \frac{(1-e^{-\omega'/T}) S_I(\omega',q)}{\omega'}\,. \tag{3.19}$$

In the one-phonon approximation,

$$S_I(\omega,q) = \frac{n_I}{M_I} \sum_{\lambda,\mathbf{K},\mathbf{k}} \frac{\pi(\epsilon_\lambda(\mathbf{k})\cdot\mathbf{q})^2}{\omega_{k\lambda}} \left[\frac{\delta(\omega-\omega_{k\lambda})\delta_{\mathbf{q},\mathbf{k}+\mathbf{K}}}{1-e^{-\omega/T}} + \frac{\delta(\omega+\omega_{k\lambda})\delta_{\mathbf{q},\mathbf{k}+\mathbf{K}}}{e^{-\omega/T}-1} \right], \tag{3.20}$$

where the sum is over the reciprocal lattice vector $\mathbf{K}$, the three polarization states λ of the phonon spectrum ($\omega_{k\lambda} = v_\lambda k$) with velocity v_λ, and the vector $\mathbf{k}$ is restricted to be in the first Brillouin zone. n_I is the ion density and M_I is the ion mass. Approximating the medium of nuclei as a cubic lattice with spacing $a = n_I^{-1/3}$, we find that

$$\begin{aligned} \chi_I(q) &= -\frac{n_I}{M_I} \sum_{\lambda,\mathbf{K},\mathbf{k}} \frac{(\epsilon_\lambda(\mathbf{k})\cdot\mathbf{q})^2}{\omega_{k\lambda}^2} \delta_{\mathbf{q},\mathbf{k}+\mathbf{K}} \\ &= -\frac{n_I}{M_I} \sum_{\lambda,\mathbf{K}} \frac{(\epsilon_\lambda(\mathbf{q}-\mathbf{K})\cdot\mathbf{q})^2}{\omega_{|\mathbf{q}-\mathbf{K}|\lambda}^2} \prod_{i=x,y,z} \theta\left(\frac{\pi}{a} - |\mathbf{q}_i - \mathbf{K}_i|\right), \end{aligned} \tag{3.21}$$

where $\mathbf{q}_i$ and $\mathbf{K}_i$ are the i$^{\text{th}}$ components of the respective vectors. The corresponding ion density, mass, and charge, and the two transverse and one longitudinal phonon velocities can be calculated following [221]. The velocity of the longitudinal mode of lattice vibrations is $v_l \approx \omega_P/q_{\text{TFe}}$ where $\omega_P = \sqrt{4\pi\alpha Z^2 n_I/M_I}$ is the ion plasma frequency. The velocity of the two transverse modes is $v_t \approx 0.4\ \omega_P/q_D$ where $q_D = (6\pi^2 n_I)^{1/3}$ is the Debye wavenumber. In general, both the longitudinal and the two transverse modes contribute to the ion response. However, for $q < \pi/a$, Eq. 3.21 simplifies since only one term of the sum, which corresponds to $\mathbf{K} = 0$ with longitudinal polarization, survives and we find that

$$\chi_I(q < \pi/a) = -\frac{n_I}{M_I v_l^2}\,. \tag{3.22}$$

For $q \gg \frac{\pi}{a}$ we found that converting the sum over $\mathbf{K}$ to an integral and confining $\mathbf{q}-\mathbf{K}$ to be within a sphere of diameter π/a instead of a cube with side length π/a gave an analytic, conservative lower limit on $\chi_I(q)$ given by

$$\chi_I(q \gg \pi/a) = -\frac{n_I}{M_I v_t^2}\left(\frac{4\pi}{3}\right)^{1/3}\left(1+\frac{v_t^2}{2v_l^2}\right)\left(\frac{q}{q_D}\right)^2\,. \tag{3.23}$$

This result combined with the fact that $v_t \ll v_l$ implies that $\chi_I(q > \pi/a)$ increases rapidly with momentum.

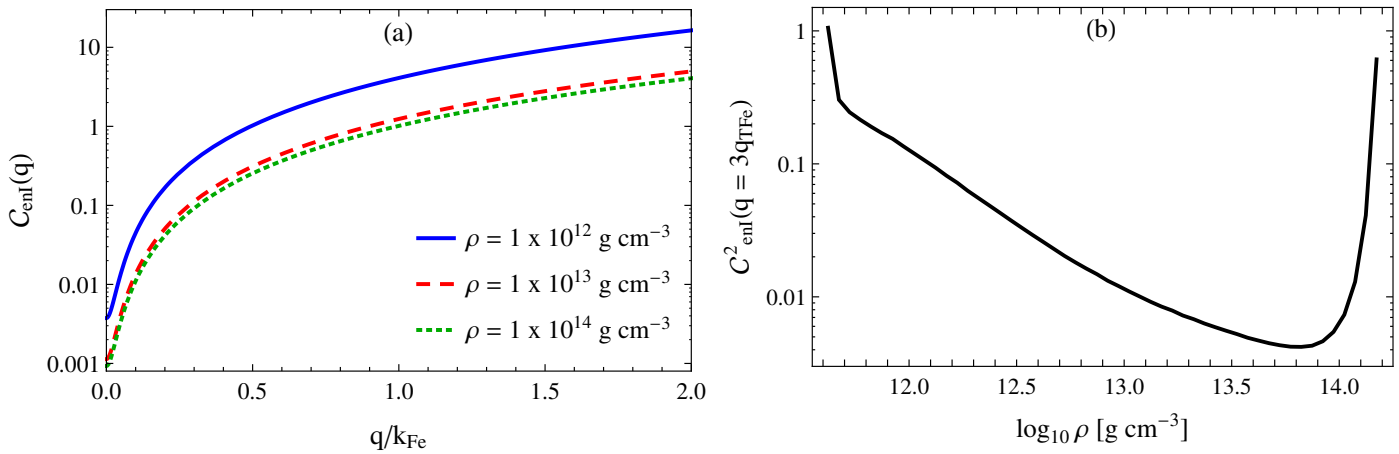

Figure 3.3: (a) The strength of the induced electron-neutron interaction in the crust as a function of q at various densities in the crust. (b) $\mathcal{C}^2_{\text{enI}}(q = 3q_{\text{TFe}})$ as a function of density.

The momentum dependence of $\mathcal{C}_{\text{enI}}(q)$ is plotted in the left panel of Fig. 3.3 for typical densities encountered in the crust and arises solely due to large momentum dependence of $\chi_I(q)$. The right panel of Fig. 3.3 shows the density dependence of $\mathcal{C}_{\text{enI}}$ evaluated at a momentum $q = 3q_{\text{TFe}}$ which is expected to be a typical scale. Here, the large density dependence is entirely due the EoS of the crust from Ref. [1]. Before discussing the implications of the electron-neutron coupling we present an alternate, perhaps simpler and more instructive, derivation of the electron-neutron interaction which follows from noting that at low momentum, the interaction is mediated by one-phonon exchange. The process is shown by the Feynman diagram in Fig. 3.4 where the single and double fermion lines represent electrons and neutrons, respectively and the exchange particle is the longitudinal phonon of the ion lattice.

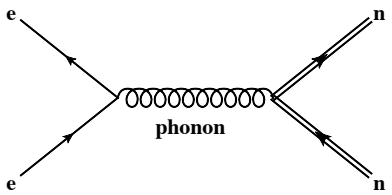

Figure 3.4: Effective interaction between electrons and neutrons induced by ion density fluctuations represented by a phonon.

The electron-phonon coupling is well known, and at small momentum it is described by the Lagrangian

$$\mathcal{L}_{\rm e-ph} = \frac{4\pi Z\alpha\ f_{\rm I}}{q^2+q_{\rm TFe}^2}\ e^\dagger e\ \nabla_i\xi_i\,, \tag{3.24}$$

where ξ_i is the canonically normalized phonon field which is related to ion density fluctuations, $\delta n_I = -f_{\rm I}\nabla_i\xi_i$, and $f_{\rm I} = \sqrt{n_I/m_I}$ [141]. Density fluctuations of the ion lattice also couple to the neutrons due to the short-range neutron-ion potential $V_{\rm nI}$. The coupling between low energy neutrons and lattice phonons is described by the Lagrangian

$$\mathcal{L}_{\rm n-ph} = -V_{\rm nI}\ f_{\rm I}\ n^\dagger n\ \nabla_i\xi_i\,. \tag{3.25}$$

The electron-neutron interaction follows from Fig. 3.4, where the phonon-electron and phonon-neutron vertices are given by Eq. 3.24 and Eq. 3.25, respectively. Using the longitudinal phonon propagator $\mathcal{D}(\omega,q) = (\omega^2-\tilde{\omega}^2(q))^{-1}$ where the phonon dispersion relation is $\tilde{\omega}^2(q) = v_l^2q^2$ and v_l is the velocity of the longitudinal mode, we find that the induced interaction is

$$\mathcal{U}_{\rm enI}(\omega,q) = \left(\frac{-4\pi Z\alpha V_{\rm nI}f_{\rm I}^2}{q^2+q_{\rm TFe}^2}\right)\ \frac{q^2}{(\omega^2-v_l^2q^2)}\,. \tag{3.26}$$

In the static limit where $\omega \ll v_l q$ this simplifies to

$$\mathcal{U}_{\rm enI}(0,q) = \frac{4\pi\alpha Z V_{\rm nI}f_{\rm I}^2}{(q^2+q_{\rm TFe}^2)v_l^2}\,, \tag{3.27}$$

which coincides with the result obtained earlier in Eq. 3.17 because $\mathcal{C}_{\rm enI}(q) = -V_{\rm nI}Zf_I^2/v_l^2$ for small $q < \pi/a$.

3.4 Transport coefficients from the variational method

In this section, we outline the procedure for deriving the transport coefficients of dense matter. While the focus will be on low temperature results, we will give a general description that can be used together with RPA to study transport phenomena in a more general setting. Most of this section is based on the seminal work of [205].

In Fermi systems, to describe all but the ground state properties, quasi particles (low lying excitations) are used extensively. Indeed, what we have referred so far to protons, neutrons, and electrons, are such excitations which retain the same quantum numbers as the respective elementary (and composite) particles. Quasi particles act similarly to a dilute gas, justifying the employment of Boltzmann equation in order to describe the flow of heat, electric charge etc. By linearizing (in terms of deviations from the equilibrium) this equation, transport coefficients are expressed in terms of irreversible entropy production rate, $\dot{S}$.

In this work we treat thermal conductivity κ, electric conductivity σ, and shear viscosity η. In terms of $\dot{S}$, they can be written as,

$$\begin{aligned}\kappa =& \frac{j_E^2}{T^2\dot{S}} \ , \\ \sigma =& \frac{j_e^2}{T\dot{S}} \ , \\ \eta =& \frac{(\Pi_{ik})^2}{2T\dot{S}} \ .\end{aligned} \tag{3.28}$$

The respective currents are given in terms of fluctuations of the Fermi distribution for the quasi particles:

$$\begin{aligned}\vec{j}_E =& \int \frac{d^3p}{(2\pi)^3}(\epsilon_p - \mu)\vec{v}\delta f(\epsilon_p) \\ \vec{j}_e =& \int \frac{d^3p}{(2\pi)^3} q\vec{v}\delta f(\epsilon_p) \\ \Pi_{ij} =& \int \frac{d^3p}{(2\pi)^3} p_i v_j \delta f(\epsilon_p) \ ,\end{aligned} \tag{3.29}$$

where $\vec{v} = \frac{\partial \epsilon_p}{\partial p}$ is the quasi particle velocity, q is the charge, and

$$\delta f(\epsilon_p) = -\phi(\vec{p})\frac{\partial f}{\partial \epsilon_p} = \phi(p) f(\epsilon_p)\frac{1 - f(\epsilon_p)}{T} \tag{3.30}$$

is the Fermi distribution fluctuation from equilibrium ($\frac{\delta f}{f} \ll 1$). The irreversible entropy is generated via inelastic particle scattering from initial momentum $\vec{p}$ to final momentum $\vec{p}'$:

$$\dot{S} = \frac{1}{2T^2}\int \frac{d^3p}{(2\pi)^3}\frac{d^3p'}{(2\pi)^3}\big[\phi(\vec{p} - \phi(\vec{p})]\big)^2 \frac{d\Gamma_{\vec{p}\to\vec{p}'}}{d^3q} \ , \tag{3.31}$$

where $\vec{q} = \vec{p} - \vec{p}'$ is the momentum exchange. The transport coefficients are functionals of the trial function(s) $\phi(\vec{p})$, and the values obtained are lower bounds, since the entropy rate is maximized. As per usual, a linear superposition of functions $\{\phi_i(\vec{p})\}$ can be chosen and the parameters chosen so as to maximize the entropy rate. However, in practice only one function is chosen; there is no need to tune parameters and the result is an upper bound. For each transport coefficient there is a specific, standard, choice of trial function, $\phi_\kappa(\vec{p}) = (\epsilon_p - \mu)\vec{p}\cdot\hat{v}$, $\phi_\sigma(\vec{p}) = \vec{p}\cdot\hat{v}$, $\phi_\eta^{ij}(\vec{p}) = p_i p_j$. At $T \approx 0$, the expressions for the currents and $\dot{S}$ simplify greatly. For instance, the electric current and respective entropy rate are given below,

$$\begin{aligned}\dot{S} =& \frac{2}{3(2\pi)^3}\frac{\epsilon_{Fe}^2}{T}\int_0^{ek_{Fe}} dq\ q^3 U_{ef}^2(\omega, q)\int_{-\infty}^{\infty}\frac{d\omega}{2\pi}\frac{\omega}{T}S(\omega, q) \ , \\ \vec{j}_e =& en_e v_{Fe}\hat{v} \ ,\end{aligned} \tag{3.32}$$

where all quantities are calculated at the Fermi surface unless integrated, U_{ef} is the effective interaction, and $S(\omega, q)$ is the dynamic structure function. In the following section, we summarize the results for the transport coefficients and proceed to calculate their values in the core and crust due to induced interactions.

3.5 Electron conductivities and shear viscosity

Both in the crust and in the core, the thermal and electrical conductivity, and the shear viscosity are given by

$$\kappa_{\rm en} = \frac{k_{\rm Fe}^2\ T}{9}\ \langle\lambda_{en}\rangle_\kappa\,, \quad \sigma_{\rm en} = \frac{k_{\rm Fe}^2\ \alpha}{3\pi^2}\ \langle\lambda_{en}\rangle_\sigma\,, \quad \eta_{\rm en} = \frac{k_{\rm Fe}^4}{15\pi^2}\ \langle\lambda_{en}\rangle_\eta\,, \tag{3.33}$$

respectively, and these expressions are written in a form familiar from kinetic theory. The relevant transport mean free paths are obtained by applying the procedure of section 3.4 for degenerate and relativistic electrons [205]. For electron-neutron scattering described by an effective interaction of the form in Eq. 3.12, the mean free paths are given by

$$\langle\lambda_{en}\rangle_\kappa^{-1} = \frac{1}{4\pi k_{\rm Fe}^2}\int_0^{2k_{\rm Fe}} dq\ q^3\frac{(4\pi\alpha)^2\mathcal{C}_{\rm en}^2(q)}{(q^2+q_{\rm TF}^2)^2}\left(1-\frac{q^2}{4k_{\rm Fe}^2}\right)\ I_\kappa(q)\,, \tag{3.34}$$

$$\langle\lambda_{en}\rangle_\sigma^{-1} = \frac{1}{4\pi k_{\rm Fe}^2}\int_0^{2k_{\rm Fe}} dq\ q^3\frac{(4\pi\alpha)^2\mathcal{C}_{\rm en}^2(q)}{(q^2+q_{\rm TF}^2)^2}\left(1-\frac{q^2}{4k_{\rm Fe}^2}\right)\ I_\sigma(q)\,, \tag{3.35}$$

$$\langle\lambda_{en}\rangle_\eta^{-1} = \frac{1}{4\pi k_{\rm Fe}^2}\int_0^{2k_{\rm Fe}} dq\ q^3\frac{(4\pi\alpha)^2\mathcal{C}_{\rm en}^2(q)}{(q^2+q_{\rm TF}^2)^2}\left(1-\frac{q^2}{4k_{\rm Fe}^2}\right)\ I_\eta(q)\,, \tag{3.36}$$

respectively. Here, the strength of the induced coupling in the general case is defined as $\mathcal{C}_{\rm en}$ which stands for $\mathcal{C}_{\rm enp}$ in the core and $\mathcal{C}_{\rm enI}$ in the crust, and

$$I_{\kappa/\sigma/\eta}(q) = \int_{-\infty}^{\infty}\frac{d\omega}{2\pi}\ \frac{\beta\omega}{e^{\beta\omega}-1}S_n(\omega,q)\ g_{\kappa/\sigma/\eta}\,, \tag{3.37}$$

where

$$g_\kappa = 1+\left(\tfrac{\beta\omega}{\pi}\right)^2\left(3\tfrac{k_{\rm Fe}^2}{q^2}-\tfrac{1}{2}\right), \quad g_\sigma = 1\,, \quad g_\eta = 3\left(1-\tfrac{q^2}{4k_{\rm Fe}^2}\right), \tag{3.38}$$

$\beta = 1/T$, and $S_n(\omega,q)$ is the dynamical structure function describing the spectrum of neutron density fluctuations. The factor of $(1-q^2/(4k_{\rm Fe}^2))$ in the mean free paths arises because helicity is conserved for ultra-relativistic particles and this suppresses the back-scattering of electrons. The dynamical structure function of the degenerate neutron gas in the normal and superfluid phases differs greatly. In the normal phase, the response is dominated by particle-hole excitations at the Fermi surface. In the superfluid phase, because particle-hole excitations are suppressed by the gap, the response is dominated by a collective mode (the Goldstone boson associated with the spontaneous breaking of the $U(1)$ symmetry in the superfluid state) called the superfluid phonon.

We will begin by first considering the dynamical structure function in the normal phase which is given by

$$S_n(\omega,q) = \frac{-2\ \mathcal{I}{\rm m}\ \Pi_n^0(\omega,q)}{1-\exp\left(-\beta\omega\right)}\ , \tag{3.39}$$

where $\Pi_n^0(\omega,q)$ is the neutron density-density correlation function defined in section 3.2. In the special case when interactions can be neglected the dynamical structure function is given by

$$S_n^{\rm FG}(\omega,q) = 2\int\frac{d^3p_1}{(2\pi)^3}\int\frac{d^3p_2}{(2\pi)^3}(2\pi)^4\delta^4(q^\mu+p_1^\mu-p_2^\mu)f(E_1)(1-f(E_2))\,, \tag{3.40}$$

where p_1 and p_2 are initial and final neutron momenta, E_1 and E_2 are initial and final neutron energies, $q^\mu = (\omega, \vec{q})$, and $f(E)$ is the Fermi-Dirac distribution function of the non-interacting neutron gas. Further, when $\omega \ll \mu_n$ and $q \ll k_{\rm Fn}$ interactions can be incorporated within the framework of Fermi liquid theory. In this case

$$S_n(\omega, q) \approx \frac{(1-e^{-\beta\omega})^{-1}}{(1+F_0)^2} \, \frac{(m_n^*)^2 \, \omega}{\pi q} \, \Theta(q v_{\rm Fn} - |\omega|) \,, \tag{3.41}$$

where $v_{\rm Fn} = k_{\rm Fn}/m_n^*$ is the neutron Fermi velocity, and the effective mass $m_n^* \simeq m_n$ and the factor $F_0 \approx -0.5 - 1$ are Fermi liquid parameters for the conditions encountered in neutron stars [222]. In the following we shall neglect these Fermi liquid corrections by setting $F_0 = 0$ and $m_n^* = m_n$ in Eq. 3.41. Using this result we can explicitly write the integral defined in Eq. 3.37 as

$$I_{\kappa/\sigma/\eta}(q) = \frac{m_n^2}{\pi^2 \beta q} \int_0^{q v_{\rm Fn}} d\omega \, \frac{(\beta\omega)^2}{(e^{\beta\omega}-1)(1-e^{-\beta\omega})} \, g_{\kappa/\sigma/\eta} \,. \tag{3.42}$$

$$\tag{3.43}$$

In the low temperature limit when $T \ll k_{\rm Fe} v_{\rm Fn}$ the integral over ω is performed by setting the upper limit to ∞ and the integral becomes independent of the neutron Fermi momentum. We find that

$$I_\kappa(q) = \frac{1}{5}\frac{m_n^2}{\beta^2 q} \left(1 + \frac{4k_{\rm Fe}^2}{q^2}\right), \quad I_\sigma(q) = \frac{1}{3}\frac{m_n^2}{\beta^2 q}, \quad I_\eta(q) = \frac{m_n^2}{\beta^2 q} \left(1 - \frac{q^2}{4k_{\rm Fe}^2}\right). \tag{3.44}$$

It is interesting to note the difference between $I_\kappa(q)$ and $I_\sigma(q)$ in the above. This difference arises solely due to the inelasticity of electron-neutron collisions since the energy transfer $\omega \simeq q v_{\rm Fn} \simeq T$ is favored and this implies that the Wiedemann-Franz law will be violated for electron-neutron scattering.

It is convenient to define the following momentum averaged effective couplings:

$$\langle \mathcal{C}_{\rm en}^2 \rangle_{\kappa/\sigma/\eta} = \frac{\int_0^{2k_{\rm Fe}} \mathcal{C}_{\rm en}^2(q) f_{\kappa/\sigma/\eta}(q)}{\int_0^{2k_{\rm Fe}} f_{\kappa/\sigma/\eta}(q)} \,, \tag{3.45}$$

where

$$f_{\kappa/\sigma/\eta}(q) = \frac{q^3}{(q^2+q_{\rm TF}^2)^2} \left(1 - \frac{q^2}{4k_{\rm Fe}^2}\right) I_{\kappa/\sigma/\eta}(q) \,. \tag{3.46}$$

From Eq. 3.44 and the momentum averages defined above we can deduce that the typical momentum transfer $q \approx$ few $\times\, q_{\rm TFe} < k_{\rm Fe}$, and that in general the typical momenta relevant for the calculation of κ are smaller than those relevant for σ and η. $\langle \mathcal{C}_{\rm enp}^2 \rangle_\kappa$ and $\langle \mathcal{C}_{\rm enp}^2 \rangle_\eta$ are plotted in Fig. 3.5 for the typical densities expected in the neutron star core. In the crust, the ion density-density correlation function $\chi_I(q)$ has a strong momentum dependence (c.f. Eq. 3.23), and consequently the stronger momentum dependence of $\mathcal{C}_{\rm enI}(q)$ implies that the differences between the momentum averaged couplings for κ, σ, and η will be more pronounced than in the core. Using the results for the crust composition and EoS used in [1] we obtain the density dependence of the momentum averaged effective couplings $\langle \mathcal{C}_{\rm enI} \rangle_{\kappa/\sigma/\eta}$ shown in Fig. 3.6.

By using the momentum averaged couplings we can factor $\mathcal{C}_{\rm en}^2(q)$ out of the q integration in Eqs. 3.34, 3.35,

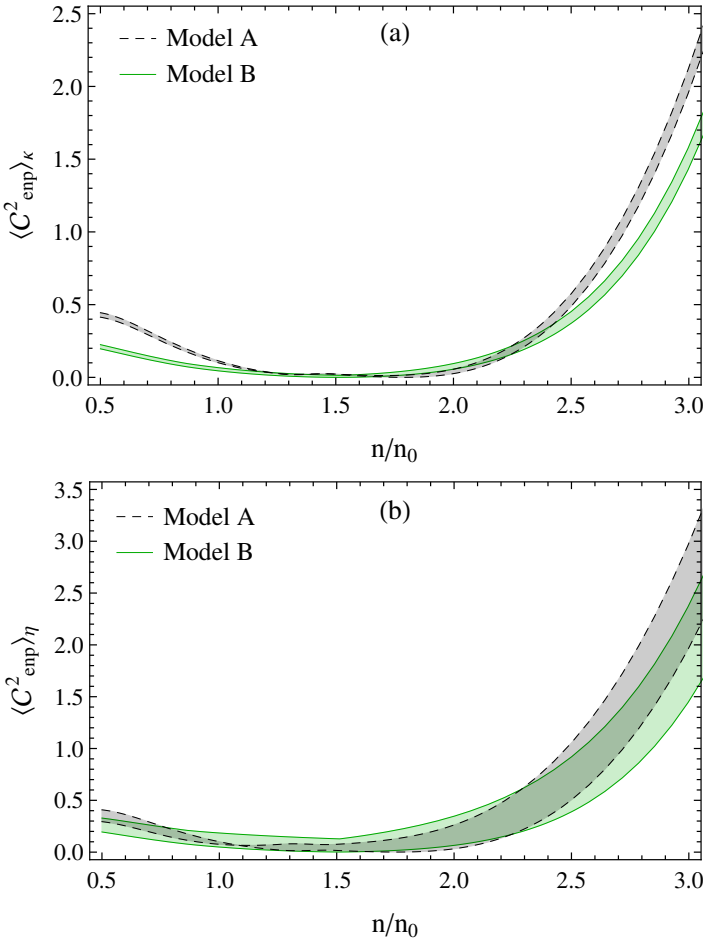

Figure 3.5: The momentum averaged couplings for (a) $\langle \mathcal{C}^2_{\rm enp}\rangle_\kappa$ and (b) $\langle \mathcal{C}^2_{\rm enp}\rangle_\eta$, for densities of relevance in the core. It is assumed that neutrons are in the normal phase and Eq. 3.45 is used to obtain the averages. Although it is not shown we remark that $\langle \mathcal{C}^2_{\rm enp}\rangle_\sigma \approx \langle \mathcal{C}^2_{\rm enp}\rangle_\eta$.

and 3.36, and we obtain analytic results for the inverse mean free paths given by

$$\langle \lambda_{en}\rangle^{-1}_\kappa = \frac{4\pi^2\alpha^2\langle \mathcal{C}^2_{\rm en}\rangle_\kappa}{5}\,\frac{m_n^2\,T^2}{q^3_{\rm TF}}\,\Phi_\kappa\left(\frac{q_{\rm TF}}{k_{\rm Fe}}\right), \tag{3.47}$$

$$\langle \lambda_{en}\rangle^{-1}_\sigma = \frac{\pi^2\alpha^2\langle \mathcal{C}^2_{\rm en}\rangle_\sigma}{3}\,\frac{m_n^2\,T^2}{k^2_{\rm Fe}q_{\rm TF}}\,\Phi_\sigma\left(\frac{q_{\rm TF}}{k_{\rm Fe}}\right), \tag{3.48}$$

$$\langle \lambda_{en}\rangle^{-1}_\eta = \pi^2\alpha^2\langle \mathcal{C}^2_{\rm en}\rangle_\eta\,\frac{m_n^2\,T^2}{k^2_{\rm Fe}q_{\rm TF}}\,\Phi_\eta\left(\frac{q_{\rm TF}}{k_{\rm Fe}}\right), \tag{3.49}$$

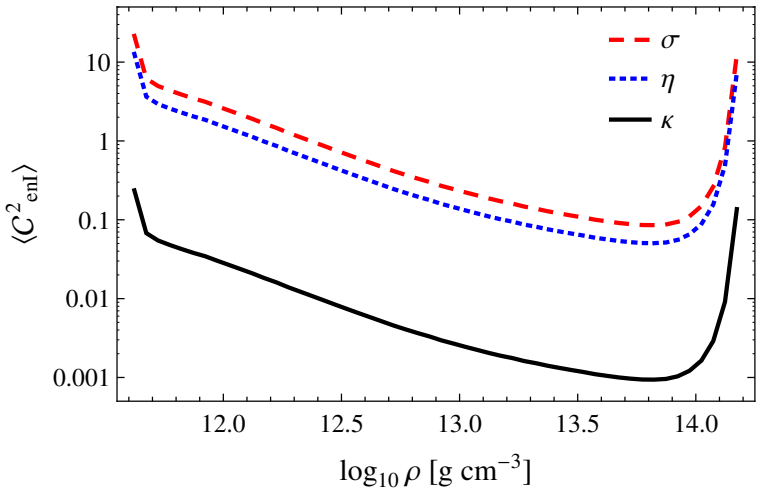

Figure 3.6: $\langle \mathcal{C}^2_{\rm enI}\rangle_{\kappa/\sigma/\eta}$ in the crust as a function of density using $V_{\rm nI}$ derived from data presented in Ref. [1]

where

$$\Phi_\kappa(x) = \left(1+\frac{3x^4}{16}\right)\frac{2}{\pi}\text{ArcTan}\left[\frac{2}{x}\right]+\frac{x}{\pi}-\frac{3x^3}{4\pi}\,, \tag{3.50}$$

$$\Phi_\sigma(x) = \left(1+\frac{3x^2}{4}\right)\frac{2}{\pi}\text{ArcTan}\left[\frac{2}{x}\right]-\frac{3x}{\pi}\,, \tag{3.51}$$

$$\Phi_\eta(x) = \frac{1}{8\pi}\left(4+x^2\right)\left(4+5x^2\right)\text{ArcTan}\left[\frac{2}{x}\right]-\frac{x}{\pi}\left(\frac{13}{3}+\frac{5x^2}{4}\right)\,, \tag{3.52}$$

are normalized so that $\Phi_{\kappa/\sigma/\eta}(0) = 1$.

The corresponding thermal and electrical conductivity, and the shear viscosity are given by the following analytic expressions

$$\kappa_{\rm en} = \frac{5}{36\pi^2\alpha^2\langle\mathcal{C}^2_{\rm en}\rangle_\kappa}\,\frac{k^2_{\rm Fe}q^3_{\rm TF}}{m_n^2\,T}\,\Phi^{-1}_\kappa\left(\frac{q_{\rm TF}}{k_{\rm Fe}}\right)\,, \tag{3.53}$$

$$\sigma_{\rm en} = \frac{1}{\pi^4\alpha\langle\mathcal{C}^2_{\rm en}\rangle_\sigma}\,\frac{k^4_{\rm Fe}q_{\rm TF}}{m_n^2\,T^2}\,\Phi^{-1}_\sigma\left(\frac{q_{\rm TF}}{k_{\rm Fe}}\right)\,, \tag{3.54}$$

$$\eta_{\rm en} = \frac{1}{15\pi^4\alpha^2\langle\mathcal{C}^2_{\rm en}\rangle_\eta}\,\frac{k^6_{\rm Fe}q_{\rm TF}}{m_n^2\,T^2}\,\Phi^{-1}_\eta\left(\frac{q_{\rm TF}}{k_{\rm Fe}}\right)\,, \tag{3.55}$$

respectively. For the fiducial values $k_{\rm Fe} = 100$ MeV, $T = 10^8$ K, and $q_{\rm TF} \approx 30$ MeV, the above formulae predict $\kappa \approx 10^{23}$ erg cm^{-1} s^{-1} K^{-1}, $\sigma \approx 10^{29}$ s^{-1} and $\eta \approx 10^{18}$ g cm^{-1} s^{-1} when we set $\langle\mathcal{C}^2_{\rm en}\rangle = 1$.

Now we will consider the case when neutrons are in the superfluid state. As already mentioned, neutrons are likely to form s-wave Cooper pairs in the crust, and p-wave Copper pairing is a possibility in the core. While s-wave superfluidity in the crust appears rather robust with critical temperatures for $^1S_0$ pairing in the range $T^{\rm n}_{\rm c} = 10^8 - 10^{10}$ K, it remains unclear if p-wave pairing occurs in the core. Recent calculations, which

account for non-central interactions and polarization effects in the medium, favor the smaller values $T_c^n < 10^8$ K indicating that p-wave pairing is fragile and may be unlikely at typical temperatures encountered in the neutron star core [211]. Nonetheless, for completeness we entertain the possibility of neutron superfluidity both in the crust and in the core. When $T \ll T_c^n$ quasi-particle excitations are suppressed by the factor $\exp(-T_c^n/T)$ and under these conditions, $S_n(\omega, q)$ is dominated by $\omega = qv_n$ corresponding to interactions with the low-energy Goldstone mode associated with the breaking of the $U(1)$ baryon number symmetry in the superfluid ground state. For a weakly coupled neutron superfluid

$$S_n(\omega, q) = \frac{\pi n_n q}{m_n v_n}\left[\frac{\delta(\omega - v_n q)}{1 - e^{-\beta\omega}} + \frac{\delta(\omega + v_n q)}{e^{-\beta\omega} - 1}\right] , \tag{3.56}$$

where n_n is the neutron density and $v_n \approx k_{\rm Fn}/(\sqrt{3}\, m_n)$ is the velocity the superfluid phonon mode [223]. The relevant frequency integrals for electron mean free paths due to electron collisions with superfluid neutrons are given by

$$I_\kappa(q) = \frac{n_n q^2 \beta(2\pi^2 + (6{k_{\rm Fe}}^2 - q^2){v_n}^2\beta^2)\mathrm{Csch}(\frac{qv_n\beta}{2})^2}{8m_n\pi^2} , \tag{3.57}$$

$$I_\sigma(q) = \frac{n_n q^2 \beta\ \mathrm{Csch}(\frac{qv_n\beta}{2})^2}{4m_n} , \tag{3.58}$$

$$I_\eta(q) = \frac{3n_n q^2 \beta(4k_{\rm Fe}^2 - q^2)\mathrm{Csch}(\frac{qv_n\beta}{2})^2}{4k_{\rm Fe}m_n} . \tag{3.59}$$

Using these expressions the conductivities can be calculated numerically.

3.6 Results and Discussion

3.6.1 Electron Transport in the Core

We find that electron-neutron scattering is most relevant in the core when neutrons are in the normal phase and protons are superconducting. This is because proton superconductivity suppresses electron scattering from the other electrons, muons, and protons. When the protons are in the normal phase, electrons interact mainly through the current-current interaction because in this case the interaction is only weakly screened by dynamical effects due to the Landau damping of transverse plasmons [224]. In the superconducting state, the transverse plasmon is massive due to the Meissner effect and the inverse screening length (proportional to Δ_p) suppresses the electron-electron, electron-muon, and electron-proton scattering. Electron-proton scattering is additionally suppressed by the factor $\simeq \exp(-T_c^p/T)$ due to the gap in the proton particle-hole spectrum. In what follows we discuss the relevance of electron-neutron scattering in the core for typical conditions and choose two fiducial values of the proton critical temperature $T_c^p = 10^9$ K and $T_c^p = 10^{10}$ K, which are taken to be independent of density.

We begin by discussing the relevance of electron-neutron scattering for the electron thermal conductivity. In the core electrons can scatter off other electrons, muons, protons, and neutrons. Hence the full electron thermal conductivity is given by

$$\kappa_e = \left(\frac{1}{\kappa_{\rm ref}} + \frac{1}{\kappa_{en}}\right)^{-1} , \tag{3.60}$$

where

$$\kappa_{\rm ref} = \left(\frac{1}{\kappa_{ee}} + \frac{1}{\kappa_{e\mu}} + \frac{1}{\kappa_{ep}}\right)^{-1} , \tag{3.61}$$

is the contribution to the electron thermal conductivity due to electron-electron, electron-muon, and electron-proton scattering considered in earlier work.

From [207] we find that the electron contribution to the thermal conductivity due to electron-electron, electron-muon and electron-proton scattering is given (in natural units) by

$$\kappa_{ei} = \frac{\pi^2 T n_e}{3 m_e^* \nu_{ei}^{\kappa}}\,, \tag{3.62}$$

where n_e is the number density of electrons, T is the temperature, $m_e^* = \mu_e \approx k_{Fe}$, and ν_{ei}^{κ} is the frequency of electron-i collisions where i stands for electrons, muons, or protons. The collision frequency is dominated by the exchange of transverse plasmons because scattering due to the exchange of longitudinal plasmons is strongly screened in the static limit. In Eq. 3.62 the coupling between the heat transport of electrons and muons is neglected and was shown to be unimportant for strongly degenerate conditions in neutron star cores [207].

In the absence of proton superconductivity, the collision frequency for thermal conductivity is given by

$$\nu_{ei}^{\kappa} = \frac{24\zeta(3)}{\pi^3}\frac{\alpha^2 T}{m_e^*}\frac{k_{\rm Fi}^2 k_{\rm Fe}}{q_{\rm t}^2}\,, \tag{3.63}$$

where $\zeta(z)$ is the Riemann zeta function, $k_{\rm Fi}$ is the Fermi momentum of particle i, and $q_{\rm t}$ is the transverse screening momentum,

$$q_{\rm t}^2 = \frac{4\alpha}{\pi}\sum_i k_{Fi}^2\,. \tag{3.64}$$

The total electron thermal conductivity is then given by

$$\kappa_{\rm ref} = \left(\frac{1}{\kappa_{ee}} + \frac{1}{\kappa_{e\mu}} + \frac{1}{\kappa_{ep}}\right)^{-1} = \frac{\pi^2}{54\zeta(3)}\frac{k_{\rm Fe}^2}{\alpha}\,, \tag{3.65}$$

only depending on $k_{\rm Fe}$ and not on the temperature—an interesting dependence that is due to the exchange of dynamically screened transverse plasmons. It is in contrast to our result of $\kappa \propto T^{-1}$ which is due to the exchange of longitudinal plasmons that remain massive in the static limit.

In the presence of proton superconductivity, the transverse plasmons become massive due to the Meissner effect and this restores the T^{-1} behavior of $\kappa_{\rm ref}$. In addition, the number of proton quasiparticles becomes exponentially suppressed. In this case, from [207] we find that the thermal conductivity

$$\kappa_{\rm ref} \to \kappa_{\rm ref}\frac{1}{R_{\rm tot}^{\kappa}(y,r)}\,, \tag{3.66}$$

where

$$R_{\rm tot}^{\kappa}(y,r) = p_1 e^{-0.14y^2} + \frac{1-p_1}{\sqrt{1+p_3 y^2}}\,, \quad p_1 = 0.48 - 0.17r\,, \quad p_3 = \left[(1-p_1)\frac{45\zeta(3)}{4\pi^2 r}\right]^2\,, \tag{3.67}$$

$$y = \sqrt{1-t}\left(1.456 - \frac{0.157}{\sqrt{t}} + \frac{1.764}{t}\right), \quad r = \frac{k_{\rm Fe}^2 + k_{\rm F\mu}^2}{k_{\rm Fp}^2}\,, \tag{3.68}$$

and $t = T/T_{\rm c}^{\rm p}$. Eq. 3.66 was used to make the plots shown in Fig. 3.7. For the case of strong proton superconductivity when $y \gg 1$, the thermal conductivity simplifies to

$$\kappa_{\rm ref}(T \ll T_{\rm c}^{\rm p}) = \frac{5}{24\alpha}\; k_{\rm Fe}^2\; \frac{\Delta_p}{T}\; f\,, \tag{3.69}$$

where the factor $f = k_{\rm Fp}^2/(k_{\rm Fe}^2 + k_{{\rm F}\mu}^2) \approx 1$ includes the correction in regions where the muon fraction is not negligible [207]. Comparing Eq. 3.69 to the result we obtained for electron-neutron scattering in Eq. 3.53, we can estimate when the latter will dominate. To obtain a simple expression we neglect $k_{{\rm F}\mu}$, and set $k_{\rm Fp} = k_{\rm Fe}$ to find that when

$$\langle \mathcal{C}_{\rm en}^2 \rangle_\kappa \gtrsim \frac{16\sqrt{\alpha}}{3\pi^{7/2}} \sqrt{\frac{k_{\rm Fe}}{m_n}}\, \frac{k_{\rm Fe}}{\Delta_p} \approx 0.27 \left(\frac{k_{\rm Fe}}{100\ {\rm MeV}}\right)^{3/2} \left(\frac{1\ {\rm MeV}}{\Delta_p}\right), \tag{3.70}$$

electron-neutron scattering dominates.

In Fig. 3.7 we show the ratio $\kappa_{\rm ref}/\kappa_{en}$ to asses the relative importance of electron-neutron scattering. $\kappa_{\rm ref}$ is calculated using the fitting formula from [207]. When $\kappa_{\rm ref}/\kappa_{en} > 1$ electron-neutron scattering is the dominant scattering mechanism and from the figure we can deduce that electron-neutron scattering is unlikely to be important when $T_{\rm c}^{\rm p}$ is small and $T \gtrsim T_{\rm c}^{\rm p}$. This is because a smaller gap $\Delta_p \simeq 1.76\ T_{\rm c}^{\rm p}$ results in weaker screening of electron-electron and electron-muon scattering, and when $T \gtrsim T_{\rm c}^{\rm p}$, electron-proton scattering becomes relevant and further reduces the electron mean free path. For the larger $T_{\rm c}^{\rm p} \simeq 10^{10}$ K, results shown in the right panel of Fig. 3.7 indicate that electron-neutron scattering can be relevant both at low density near the crust-core boundary, and at higher density deep inside the core. Here, because $T > T_{\rm c}^{\rm p}$ both $\kappa_{\rm ref}$ and κ_{en} scale as $1/T$. Thus, their ratio is independent of temperature and the bands shown in the right panel overlap.

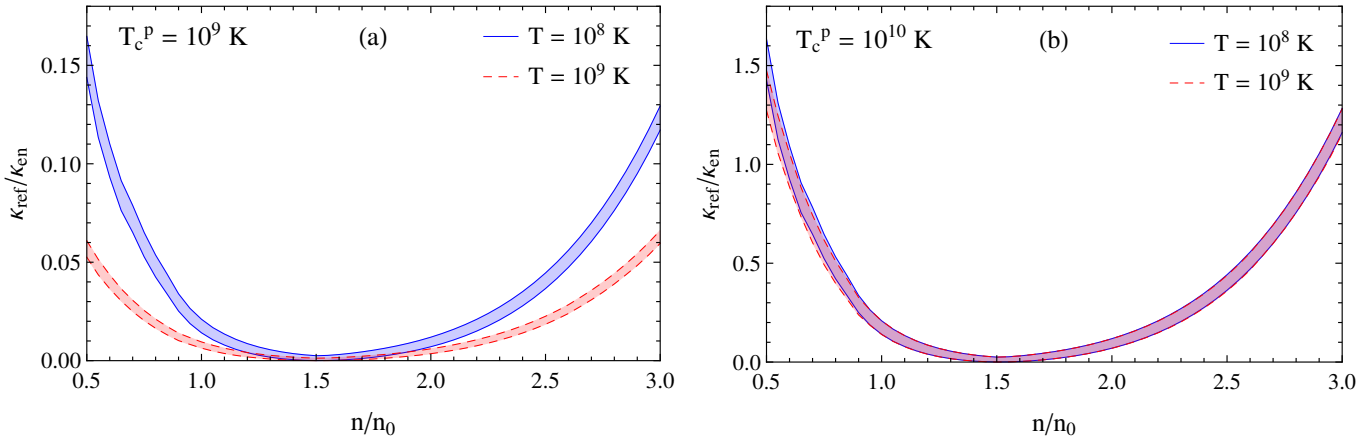

Figure 3.7: The ratio $\kappa_{\rm ref}/\kappa_{en}$ for two proton critical temperatures: (a) $T_c^p = 10^9$ K and (b) $T_c^p = 10^{10}$ K, for densities of relevance to the core. When the $\kappa_{\rm ref}/\kappa_{en} > 1$, electron-neutron scattering dominates.

Similarly, the total electron shear viscosity in the core is given by

$$\eta_{\rm e} = \left(\frac{1}{\eta_{\rm ref}} + \frac{1}{\eta_{en}}\right)^{-1}, \tag{3.71}$$

where

$$\eta_{\rm ref} = \left(\frac{1}{\eta_{ee}} + \frac{1}{\eta_{e\mu}} + \frac{1}{\eta_{ep}}\right)^{-1}, \tag{3.72}$$

is the contribution to the shear viscosity due to electron scattering off other electrons, protons, and muons considered in earlier work. For the electron contribution to the shear viscosity we used the analytic results of [208] in the same way as we used [207] for the thermal conductivity discussed above. The shear viscosity is given by

$$\eta_{ei} = \frac{n_e k_{\rm Fe}^2}{5 m_e^* \nu_{ei}^\eta}, \tag{3.73}$$

when the longitudinal plasmon exchange and the coupling between the electron and muon shear viscosity can be neglected. This is a good approximation here, though it is not as good as in the thermal conductivity case. In the absence of proton superconductivity, the collision frequencies for shear viscosity are given by

$$\nu_{ei}^{\eta} = \frac{\chi\alpha\pi}{4}\frac{q_{\rm t}^{4/3}}{k_{Fe}m_e^*}T^{5/3}\,, \tag{3.74}$$

where $\chi \approx 6.93$ and $q_{\rm t}$ is given by Eq. 3.64. Note that this expression (and subsequent expressions) in [208] is missing the factor of α.

The total electron shear viscosity is then given by

$$\eta_{\rm ref} = \left(\frac{1}{\eta_{ee}} + \frac{1}{\eta_{e\mu}} + \frac{1}{\eta_{ep}}\right)^{-1} = \frac{4}{15\chi\alpha}\frac{k_{\rm Fe}^6}{\pi^3}\left(\frac{1}{q_{\rm t}^4 T^5}\right)^{1/3}\,, \tag{3.75}$$

where the temperature dependence is due to the exchange of dynamically screened transverse plasmons and is in contrast to our result of $\eta \propto T^{-2}$ due to the exchange of massive longitudinal plasmons.

In the presence of proton superconductivity, this screening of transverse plasmons is no longer dynamical and the transverse plasmons acquire a mass (which restores the T^{-2} behavior of $\eta_{\rm ref}$), and the number of proton quasi particles becomes exponentially suppressed. Allowing for proton superconductivity, the shear viscosity becomes

$$\eta_{\rm ref} \to \eta_{\rm ref}\frac{1}{R_{\rm tot}^{\eta}(y,r)}\,, \tag{3.76}$$

where

$$R_{\rm tot}^{\eta} = \frac{1-g_1}{(1+g_3 y^3)^{1/9}} + (g_1+g_2){\rm Exp}\left[0.145 - \sqrt{0.145^2+y^2}\right]\,, \tag{3.77}$$

$$g_1 = 0.87 - 0.314r\,,\ g_2 = (0.423+0.003r)y^{1/3} + 0.0146y^2 - 0.598y^{1/3}e^{-y}\,, \tag{3.78}$$

$$g_3 = 251 r^{-9}(r+1)^6(1-g_1)^9\,, \tag{3.79}$$

and y, t, and r were defined earlier. Although we use Eq. 3.76 to make the plots shown in Fig. 3.8 we note that when proton superconductivity is strong ($y \gg 1$), the shear viscosity is given by the simpler expression

$$\eta_{\rm ref}(T \ll T_{\rm c}^{\rm p}) = \frac{\xi}{9\pi^4\alpha^{5/3}}\ \frac{k_{\rm Fe}^5}{T^2}\ \left(\frac{\Delta_p}{k_{\rm Fp}}\right)^{1/3}\ f'\,, \tag{3.80}$$

where $\xi \approx 1.7$, and the factor $f' = k_{\rm Fp}k_{\rm Fe}/(k_{\rm Fe}^2 + k_{{\rm F}\mu}^2) \approx 1$ includes the correction in regions where the muon fraction is not negligible [208]. Comparing Eq. 3.80 to the result we obtained for electron-neutron scattering in Eq. 3.55 we can estimate that electron-neutron scattering will dominate when the induced coupling

$$\langle \mathcal{C}_{\rm en}^2\rangle_\eta \gtrsim \frac{6\alpha^{1/6}}{5\sqrt{\pi}\xi}\left(\frac{k_{\rm Fe}}{m_n}\right)^{3/2}\left(\frac{k_{\rm Fe}}{\Delta}\right)^{1/3} \approx 0.03\ \left(\frac{k_{\rm Fe}}{100\ {\rm MeV}}\right)^{11/6}\ \left(\frac{1\ {\rm MeV}}{\Delta_p}\right)^{1/3}\,. \tag{3.81}$$

As before, in deriving the above criterion, we have neglected $k_{{\rm F}\mu}$ and set $k_{\rm Fp} = k_{\rm Fe}$.

In Fig. 3.8 we show the ratio $\eta_{\rm ref}/\eta_{en}$ for two values of fiducial temperature in the core $T = 10^8$ and $T = 10^9$ K, and for two representative values of the proton critical temperature to asses the relative importance of electron-neutron scattering. As before, in regions where $\eta_{\rm ref}/\eta_{en} > 1$, electron-neutron scattering is the dominant scattering mechanism for electrons. The results in the figure indicate that electron-neutron scattering is relevant

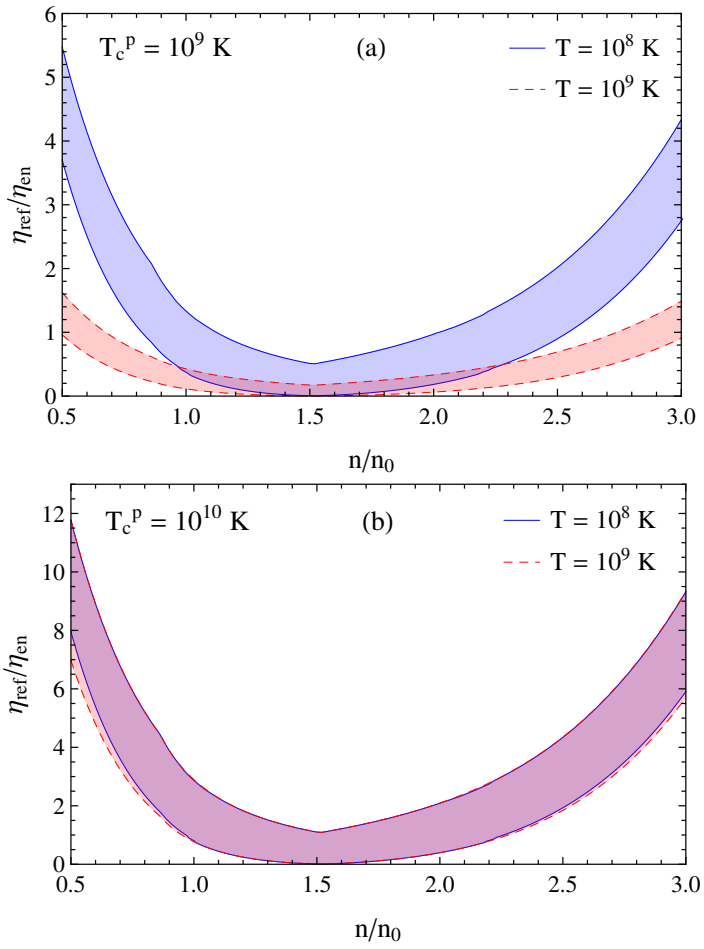

Figure 3.8: The ratio $\eta_{\rm ref}/\eta_{en}$ for two proton critical temperatures: (a) $T_c^p = 10^9$ K and (b) $T_c^p = 10^{10}$ K, for densities in the core.

everywhere in the core. Further, because $\eta_{\rm ref}$ is a weaker function of the superconducting gap compared to $\kappa_{\rm ref}$, we find that $\eta_{\rm ref}/\eta_{en} > 1$ even when $T \simeq T_{\rm c}^{\rm p}$.

The general trend that the electron-neutron contribution is more relevant for η rather than κ, and that it remains relevant for η even when proton superconductivity is weak or absent, can be understood by noting that screening is more important for κ than it is for η. This is because low momentum scattering with energy transfer $\omega \simeq T$ can make an important contribution to κ. This is reflected by the fact that $\kappa \propto \Lambda^3$ where Λ is the momentum transfer scale set by the physics of screening, while $\eta \propto \Lambda$ (c.f. the dependence on $q_{\rm TF}$ in Eqs. 3.53 and 3.55). In the case of the density-density interaction that we have considered between electrons and neutrons $\Lambda = q_{\rm TF} \approx (4\alpha m_p k_{\rm Fp}/\pi)^{1/2}$, while for the current-current interaction between electrons considered in [207, 208] the relevant scale of the screening momentum is $\Lambda \approx (\pi\alpha k_{\rm Fp}^2 \Delta_p)^{1/3}$ when protons are superconducting, and $\Lambda \approx (2\alpha T k_{\rm Fp}^2)^{1/3}$ when protons are normal.

We have calculated both κ_{en} and η_{en} for the case when neutrons are superfluid and found them to be too large compared to $\kappa_{\rm ref}$ and $\eta_{\rm ref}$ to be relevant. Here, electron scattering occurs either by absorption or emission of the superfluid phonon with energy $\omega = qv_n$. Since large energy transfer is exponentially suppressed due to degeneracy and typical $\omega \simeq T$, the electron-phonon scattering is highly peaked in the forward direction and contributes little to the electron transport properties. Superfluid phonons could contribute to the shear

viscosity [225] and to the thermal conductivity [226] when phonon-phonon scattering is assumed to limit the phonon mean free paths. However, recent work in Ref. [227] suggests that the absorption process phonon + electron → electron dominates and greatly reduces the phonon mean free paths. This is the inverse of the process in which an electron scattered by absorption or emission of superfluid phonons considered here. Thus we conclude that phonon diffusion is unlikely to be relevant for transport. Instead phonons are likely dragged along with the electrons, and this could have a modest effect on transport properties. This aspect warrants further investigation when neutrons in the core are superfluid.

Finally, we note that the electrical conductivity is only relevant when protons are normal, and in this case we find that electron-neutron scattering can be as relevant as electron-proton scattering when $\langle \mathcal{C}^2_{\rm enp} \rangle \gtrsim 1$. However, this warrants a careful study of the induced interaction between the electron and neutron currents mediated by transverse plasmons in the normal state, and is beyond the scope of this study.

3.6.2 Electron Transport in the Crust

In the inner crust, ions form a crystal and electron-ion scattering is suppressed due to correlations for $T < T_P$ where $T_P = \hbar\omega_P/k_B$ is the ion plasma temperature and $\omega_P = \sqrt{4\pi\alpha Z^2 n_I/M_I}$ is the plasma frequency of ions with charge Z, mass M_I, and number density n_I. The dominant electron scattering processes considered in earlier work were due to electron-phonon and electron-impurity interactions. When the impurity concentration is negligible, the electron contribution to κ, σ, and η at low temperature is limited by the emission or absorption of lattice phonons by electrons and has been studied in earlier work [205, 228, 229, 230]. The importance of Umklapp scattering was realized early in Ref. [205] because this allows the electron momentum to change by a large amount, $\mathbf{K} = (2\pi/a)(n_x\hat{\mathbf{x}} + n_y\hat{\mathbf{y}} + n_z\hat{\mathbf{z}})$, where n_i are integers, even for relatively small energy transfer $\omega \simeq T \ll |\mathbf{K}|$. For this reason, electron-ion scattering remains very effective down to low temperatures until the Umklapp processes are frozen out by the small band gap in the electron spectrum. This occurs when $T < T_{\rm um}$ where $T_{\rm um} \approx (\alpha/9\pi)Z^{1/3}T_P$ is called the Umklapp temperature. In the inner crust where $Z \approx 40$, $T_{\rm um} \approx 10^{-3}T_P$.

By comparing our results in the inner crust to those obtained from only considering electron-phonon Umklapp scattering from Ref. [230], we find that our values for κ and σ are much too large (typically by a factor of about 100 or more) to be relevant for temperatures in the range $10^7 - 10^9$ K. A similar comparison between our results for η with those presented in Ref. [231] shows that electron-neutron scattering is also too weak to be relevant in this case. At very low temperature when $T \lesssim 10^6$ K the Umklapp process is frozen out, and in this case electron-neutron scattering can become relevant if neutrons are in the normal phase and the impurity concentration can be neglected. However, since neither of these conditions seem likely in the crust we do not present a detailed comparison.

3.7 Conclusions

In this work, a new mechanism for electron scattering off neutrons induced by protons in the core and ions in the crust has been identified. Using simple models of the neutron-proton interaction in the core and the neutron-ion interaction in the crust, the strength of this induced interaction was estimated. In calculating the electron thermal conductivity, shear viscosity, and electrical conductivity, the coupling was characterized by a density-dependent, dimensionless parameter $\langle \mathcal{C}^2_{\rm enp} \rangle$ in the core, and $\langle \mathcal{C}^2_{\rm enI} \rangle$ in the crust. The main findings are:

- When protons are superconducting with $T_{\rm c}^{\rm p} \gtrsim 10^9$ K, electron-neutron scattering is a relevant process that limits the electron mean free paths and determines the electron thermal conductivity and shear viscosity in the neutron star core. Our calculations indicate the shear viscosity in the vicinity of the crust-core transition can be $5 - 10$ times larger than earlier estimates. This enhancement may be relevant in the

context of damping hydrodynamic modes and r-modes, and could have implications for neutron star spin evolution and gravitational wave instabilities (e.g. see [232, 233]). In contrast, changes to the thermal conductivity are relatively small and given current uncertainties in their calculation these changes are unlikely to be of much interest for neutron star phenomenology.

- In the crust, electron-neutron scattering is unlikely to be relevant because (i) electron Umklapp scattering off the ion lattice is efficient for typical temperatures of interest, (ii) at low temperature when Umklapp scattering is suppressed, electron-impurity scattering will likely dominate, and (iii) neutrons are likely to be in the superfluid state in the crust and in this case electron-neutron scattering is highly suppressed.

The results presented are sensitive to the momentum dependent electron-neutron couplings $\mathcal{C}_{\rm enp}(q)$ and $\mathcal{C}_{\rm enI}(q)$. Although these coupling were well determined at low momentum because they were directly related to the EoS, the finite momentum component warrants further study. Calculations of the Fermi liquid parameters and effective interactions in asymmetric matter are being pursued using realistic nucleon-nucleon potentials and will be reported in future work.

Finally, we note that in the crust, Bragg scattering of unbound neutrons from the ion lattice will result in a distorted Fermi surface and band structure for the neutrons. This implies that Umklapp processes involving neutrons can become important. Since such processes enable large momentum transfer they warrant further study before we can discount the relevance of electron-neutron processes in the crust.

3.8 Caveats

We have only considered the electron coupling to neutron density fluctuations and have ignored (3-vector) the current-current coupling. We argued that the current-current interaction would be subdominant because protons, and to a lesser extent neutrons, can be treated as non-relativistic particles and the current-current coupling is proportional to the nucleon speed which is expected to be a small parameter. However, when protons in the core are in the normal phase, the current-current interaction is stronger because it is only weakly screened by Landau damping. This may well compensate for the smaller proton velocity and warrants further investigation, especially to ascertain if electron-neutron scattering could be relevant in the absence of proton superconductivity in the core. We note that the formalism to incorporate the electron coupling to the density and current of a multi-component interacting medium exists and has been used in the context of studying neutrino scattering in hot and dense matter in Ref. [216, 217]. This formalism can be adapted to study cold matter with pairing correlations and will be fully explored in future work. However, for neutrons in normal phase, we can already describe this procedure, which will be numerically implemented using the EoS from chapter 2 in the near future.

3.8.1 Relationship between the 'dressed' photon propagator and RPA polarization tensor

The 'dressed' photon propagator, obtained by the re-summation of a subset of diagrams with one loop polarization tensor, and the RPA polarization tensor can related to each other. Diagrammatically, the photon propagator be expanded as depicted in Fig. 3.9. In index free notation, the diagram can be written as follows:

$$\mathcal{D} = \mathcal{D}^{(0)} + \mathcal{D}\Pi^{(0)}\mathcal{D}^{(0)} \ . \tag{3.82}$$

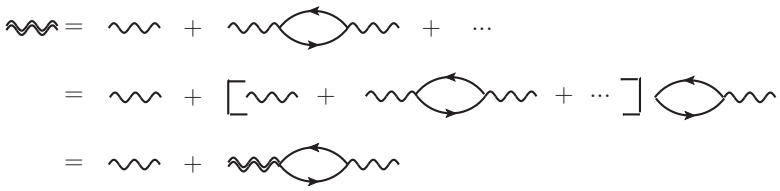

Figure 3.9: Dressed photon propagator

The closed form solution, that will be needed later, is:

$$\begin{aligned}\mathcal{D} =&\left[I - \mathcal{D}^{(0)}\Pi^{(0)}\right]^{-1}\mathcal{D}^{(0)}\\ =&\mathcal{D}^{(0)}\left[I - \Pi^{(0)}\mathcal{D}^{0}\right]^{-1} \ .\end{aligned} \tag{3.83}$$

And, similarly, the diagrammatic representation of the polarization tensor is shown in Fig.3.10.

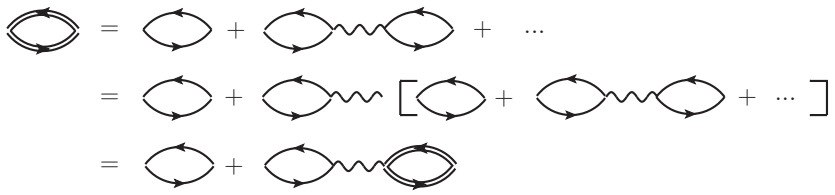

Figure 3.10: RPA polarization tensor

The respective equation:

$$\begin{aligned}\Pi =&\Pi^{0} + \Pi^{(0)}\mathcal{D}^{(0)}\Pi\\ =&\Pi^{0} + \Pi\mathcal{D}^{(0)}\Pi^{(0)} \ ,\end{aligned} \tag{3.84}$$

with solution,

$$\begin{aligned}\Pi =&\left[I - \Pi^{(0)}\mathcal{D}^{(0)}\right]^{-1}\Pi^{(0)}\\ =&\Pi^{(0)}\left[I - \mathcal{D}^{0}\Pi^{(0)}\right]^{-1} \ .\end{aligned} \tag{3.85}$$

Now, the two expressions can be finally related:

$$\mathcal{D} =\mathcal{D}^{(0)} + \mathcal{D}^{(0)}\Pi\mathcal{D}^{(0)} \ , \tag{3.86}$$

which can easily be proven by combining Eq.3.83 and Eq.3.85:

$$\begin{aligned}\mathcal{D}^{(0)} + \mathcal{D}^{(0)}\Pi\mathcal{D}^{(0)} =&\mathcal{D}^{(0)} + \mathcal{D}^{(0)}\left[I - \Pi^{(0)}\mathcal{D}^{(0)}\right]^{-1}\Pi^{(0)}\mathcal{D}^{(0)}\\ =&\mathcal{D}^{(0)} + \mathcal{D}\Pi^{(0)}\mathcal{D}^{(0)}\\ =&\mathcal{D}\end{aligned} \tag{3.87}$$

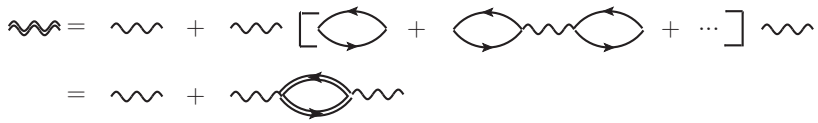

(a) Dressed photon propagator in terms of the RPA polarization tensor

3.8.2 Implications for the decay rate

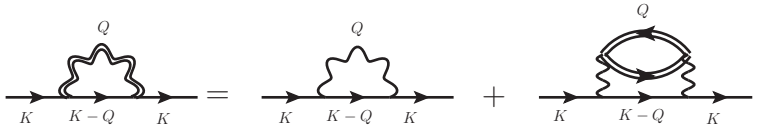

Figure 3.12: Electron self energy from the dressed photon propagator, using the RPA polarization tensor

Since the electron is the most important carrier for the transport properties under investigation, we can include the many body nuclear effects by studying their impact on its relaxation rate (scattering rate). Practically, this is given by the imaginary part of the electron self energy. Note that, only the second diagram in fig. 3.12 has imaginary contributions, the first diagram is just a correction to the field strength. The electron self energy at one loop, based on fig. 3.12:

$$\mathrm{Im}[\Sigma(K)] = \int \frac{d^4q}{(2\pi)^4}\gamma^\mu S_F^>(K-Q)\gamma^\nu \frac{1}{(Q^2)^2}\mathrm{Im}[\Pi_{\mu\nu}(Q)] \ , \tag{3.88}$$

where,

$$S_F^>(P) = 2\pi[1-f_f(p_0)](\not{P}+m)\theta(p_0)\delta(P^2-m^2) \ . \tag{3.89}$$

The notation used here is based on chapter 8 in [234]. Due to the optical theorem, this is the total scattering cross section. And the decay width is given by

$$\Gamma(K) = \frac{1}{4k_0}\mathrm{Tr}\big[(\not{K}+m)\mathrm{Im}[\Sigma(K)]\big] \tag{3.90}$$

For the transport coefficients, the rate is:

$$\begin{aligned}\frac{d\Gamma}{d^3q} =& \frac{1}{4k_0}\mathrm{Tr}\big[(\not{K}+m)\frac{d\mathrm{Im}[\Sigma]}{d^3q}\big] \\ =& \frac{1}{[(k_0-\epsilon_P)^2-q^2]^2}\frac{[1-f_f(\epsilon_P)][1+f_b(k_0-\epsilon_P)]}{2k_0(2\pi)^3(k_0-\epsilon_P)}\Big\{(k_0^2+k_0\epsilon_P-\frac{1}{2}(q^2+k^2-p^2))\mathrm{Im}[\tilde{\Pi}^L(k_0-\epsilon_P,q)] \\ &+\ 2(k_0^2+k_0\epsilon_P+k^2-\frac{(k^2-p^2)^2}{4q^2}+\frac{q^2}{4})\mathrm{Im}[\tilde{\Pi}^T(k_0-\epsilon_P,q)]\Big\} \ ,\end{aligned} \tag{3.91}$$

where, $P = K - Q$ is the 4-momentum of the final state of the electron and K is the 4-momentum of the initial state. The single particle energy is $\epsilon_P = \sqrt{p^2+m^2}$, and,

$$\tilde{\Pi}^{L,T} \equiv (\tilde{\Pi}^{L,T}_{ee}+\tilde{\Pi}^{L,T}_{pp}) - (\tilde{\Pi}^{L,T}_{ep}+\tilde{\Pi}^{L,T}_{pe}) \ , \tag{3.92}$$

This expression is to be used in calculating the entropy production rate, Eq. 3.31. The polarization tensor modes, transverse and longitudinal, are given by the RPA calculation. In order to incorporate both interactions together only $\tilde{\Pi}_p \equiv (0\ 1) \cdot \mathbf{\Pi}_{\mathrm{RPA}}(\omega, q)$ from Eq. 3.8 is needed and the combined RPA polarization tensor is:

$$\begin{aligned}
\tilde{\Pi} =& (I - \tilde{\Pi}^{(0)} V_{el})^{-1} \tilde{\Pi}^{(0)} \\
=& \frac{1}{Q^2 - 4\pi\alpha(\Pi_e + \tilde{\Pi}_p)} \begin{pmatrix} \Pi_e(Q^2 - 4\pi\alpha\tilde{\Pi}_p) & -4\pi\alpha\Pi_e\tilde{\Pi}_p \\ -4\pi\alpha\Pi_e\tilde{\Pi}_p & (Q^2 - 4\pi\alpha\Pi_e)\tilde{\Pi}_p \end{pmatrix} \\
\equiv& \begin{pmatrix} \tilde{\Pi}_{ee} & \tilde{\Pi}_{ep} \\ \tilde{\Pi}_{pp} & \tilde{\Pi}_{pe} \end{pmatrix} .
\end{aligned} \tag{3.93}$$

Chapter 4

Dark Matter Constraint from Supernova Mechanism and Neutron Star Evolution

4.1 Introduction

The detection of about 20 neutrinos over about 10 seconds from supernova SN1987A confirmed in broad-brush the paradigm for core-collapse supernova in which the neutrinos carry away the bulk of the gravitational binding energy $\simeq 3-5\times10^{53}$ ergs of the neutron star. The time scale associated with this intense neutrino emission is determined by neutrino diffusion in the hot and dense core of the newly born neutron star called the proto-neutron star[235]. During this phase, the emission of other weakly interacting particles, were they to exist, could carry energy away from the core and reduce the number and time scale over which neutrinos would be detectable. This allows one to extract useful constraints on the coupling of these hypothetical particles for masses up to about 200 MeV from the neutrino signal observed from SN1987A. Now widely referred to as the supernova cooling constraint [236], it has provided stringent constraints on the properties of QCD axions [237], the size of large gravity-only extra-dimensions into which light Kaluza-Klein gravitons could be radiated [238, 239], light supersymmetric particles such as neutralinos [240], and more recently on the properties of dark photons [4, 241, 242].

Observations of galaxy rotation curves, the motion of galaxies in clusters, gravitational lensing, and the remarkable success of the ΛCDM model of the early universe (see Ref. [243] for a pedagogic review), combined with the direct empirical evidence from the bullet cluster [244] indicates the existence of dark matter (DM) which interacts with ordinary matter through gravitational interactions. This has spurred much recent research in particle physics and a plethora of DM models have been proposed that also naturally predict non-gravitational interactions. In a class of these models, DM is part of neutral hidden sector which interacts with standard model (SM) particles through the exchange of light vector bosons (LVBs) that couple to SM conserved currents [245, 246, 247, 248]. Here, DM is charged under a local $U(1)$ and it is convenient from a phenomenological perspective to consider two possibilities. One in which the mediator couples to the SM electric charge Q, and is described by the spin-one field A'_μ called the dark photon γ_Q . The other is often referred to as the leptophobic gauge boson γ_B and is described by the field B_μ which couples only to baryon number.

At low energy it suffices to consider minimal coupling of the LVBs to charge and baryon number described by the Lagrangian

$$\mathcal{L} \supset g_Q A'_\mu J^{\mathrm{EM}}_\mu + g_B B_\mu J^{\mathrm{B}}_\mu - \frac{1}{2}m^2_{\gamma_Q} A'_\mu A'^\mu - \frac{1}{2}m^2_{\gamma_B} B_\mu B^\mu \,, \tag{4.1}$$

which also includes mass terms for the gauge bosons. Of the two LVBs, the dark photon has been studied

extensively and is usually motivated as arising from kinetic mixing of a dark sector gauge boson with the photon [249, 250]. This mixing is described by the term $\epsilon_Q F'_{\mu\nu} F^{\mu\nu}$ in the low energy Lagrangian where $F^{\mu\nu}$ and $F'_{\mu\nu}$ are the field tensors associated with the ordinary photon field and dark photon field, respectively. The Yukawa coupling in Eq. 4.1 $g_Q = \epsilon_Q e$ where $e = \sqrt{4\pi\alpha_{\rm em}}$ is the electric charge. To simplify notation, and for later convenience, we shall also introduce the parameter ϵ_B such that Yukawa coupling of leptophobic gauge boson is $g_B = \epsilon_B e$.

When the mass of the LVBs is less than or comparable to few times $T_{\rm SN} \simeq 30$ MeV, the temperature encountered in the supernova core, they can be produced copiously through nucleon-nucleon bremsstrahlung and electron-position pair-annihilation reactions. For both types of LVB, the bremsstrahlung production rate is expected to the major rate of production (with respect to pair-annihilation) given the abundance of nucleons and the strong nature of nuclear interactions. In this work this rate is calcualted using the soft-radiation theorem and a model independent estimate is obtained, related directly to the nucleon-nucleon elastic scattering data. A similar method was used in earlier work in [238] to estimate low energy neutrino and axion production and in [251] to estimate the rate of production of Kaluza-Klein gravitons and dilatons from nucleon-nucleon bremsstrahlung. Here we present for the first time a calculation of the rate of emission of the LVB γ_B which couples to baryon number from nucleon-nucleon bremsstrahlung. Our calculation of the bremsstrahlung production of dark photons predicts a rate that is about a factor 10 smaller than that predicted in Ref. [4]. We trace this difference to an overly simplified treatment of the nucleon-nucleon interaction based on one-pion-exchange, and the use of the Born approximation for strong interactions.

In section 4.2, we review the well known result for soft bremsstrahlung radiation and outline the calculation for the emissivity of LVBs from the supernova core in this limit. The elastic neutron-neutron, proton-proton and neutron-proton cross-sections are discussed and experimental data is used to compute the emissivities in section 4.3. In section 4.4 astrophysical constraints on ϵ_B are derived for the first time, and earlier constraints on ϵ_Q are revised. Sources of opacity for LVBs that can suppress cooling arising from inverse bremsstrahlung process, Compton scattering, and decay into electron–positron pairs are considered, as well.

4.2 Nucleon-nucleon bremsstrahlung in the soft limit

We begin by briefly reviewing nucleon-nucleon bremsstrahlung in the soft limit where the energy radiated is small compared to the energy associated with nucleon-nucleon interaction. It is well known that the amplitude for bremsstrahlung production of particles can be related to the elastic scattering cross-section when expanded in powers of the energy ω, carried away by the radiated particles[252, 253]. The amplitude for a generic bremsstrahlung process $XY \to XY\gamma$ can be written as

$$\mathcal{M}_{XY\to XY\gamma} = \frac{A(E_{\rm cm})}{\omega} + B(E_{\rm cm}) + \mathcal{O}(\omega)\,, \tag{4.2}$$

where $A(E_{\rm cm})$ and $B(E_{\rm cm})$ are related directly to the elastic $XY \to XY$ cross-section without radiation in the final state. This result, called Low's soft-photon theorem for bremsstrahlung, was first derived by F. E. Low [254]. It has been used to study neutron-proton and proton-proton bremsstrahlung reactions since the pioneering work of [255, 256] and calculations which only retain on-shell elastic amplitudes $A(E_{\rm cm})$ and $B(E_{\rm cm})$ are referred to as the soft-photon approximation or the soft radiation approximation (SRA).

The Feynman diagrams that contribute in the SRA are shown in Fig. 4.1. Here, nucleons are represented by solid lines, the LVB as the wavy-photon lines, and the shaded circle represents the nucleon-nucleon interaction which contains both the long-distance pion-exchange component and all the shorter-distance components that contribute to nucleon-nucleon scattering. The amplitude for the reaction $pp \to pp\gamma$ is obtained by summing diagrams $(a), (b), (c)$ and (d), while for the reaction $np \to np\gamma$ only two of these diagrams contribute in which

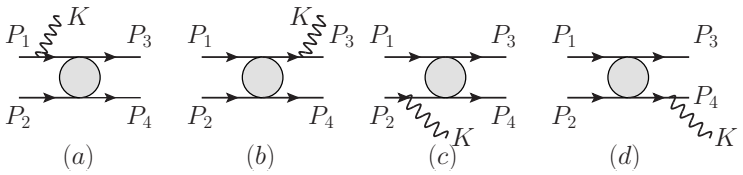

Figure 4.1: Diagrams in which radiation denoted by the wavy-line attaches to the external nucleon legs (solid lines) dominates in the low energy limit. Grey blob represents anti-symmetrized nucleon-nucleon potential and contains both the direct and exchange contributions.

the photon couples only to the proton at leading order in this expansion. The four momenta of the initial state nucleons is denoted P_1 and P_2, and by P_3 and P_4 in the final state. $K = (\omega, \vec{k})$ is the four momentum of the radiated quanta and ϵ_μ is its polarization. These diagrams dominate at small ω because the intermediate nucleon is close to being on-shell and makes a contribution to the bremsstrahlung amplitude at order ω^{-1}. In this limit, when the energy radiated is small compared to $E_{\rm cm}$ of the nucleon pair, the unpolarized differential cross-sections for bremsstrahlung radiation of LVBs are given by

$$d\sigma_{pp\to pp\gamma_i} = -4\pi\alpha_{\rm em}\epsilon_i^2 \frac{d^3k}{2\omega}(\epsilon^\mu J_\mu^{(4)})^2 \, d\sigma_{pp\to pp}\,, \tag{4.3}$$

$$d\sigma_{np\to np\gamma_Q} = -4\pi\alpha_{\rm em}\epsilon_Q^2 \frac{d^3k}{2\omega}(\epsilon^\mu J_\mu^{(2)})^2 \, d\sigma_{np\to np}\,, \tag{4.4}$$

$$d\sigma_{np\to np\gamma_B} = -4\pi\alpha_{\rm em}\epsilon_B^2 \frac{d^3k}{2\omega}(\epsilon^\mu J_\mu^{(4)})^2 \, d\sigma_{np\to np}\,, \tag{4.5}$$

where

$$J_\mu^{(2)} = \left(\frac{P_1}{P_1\cdot K} - \frac{P_3}{P_3\cdot K}\right)_\mu\,, \tag{4.6}$$

$$J_\mu^{(4)} = \left(\frac{P_1}{P_1\cdot K} + \frac{P_2}{P_2\cdot K} - \frac{P_3}{P_3\cdot K} - \frac{P_4}{P_4\cdot K}\right)_\mu\,, \tag{4.7}$$

are the currents associated with dipole and quadrupole radiation, respectively [252, 255]. The unpolarized elastic differential cross-sections for pp and np and given by $d\sigma_{pp\to pp}$ and $d\sigma_{np\to np}$, respectively. These results are valid to leading order (LO) in an expansion in powers of $\chi = \omega/E_{\rm cm}$ where $E_{\rm cm} = (\vec{p}_1 - \vec{p}_2)^2/4M$ is the non-relativistic center of mass (cm) energy. When it is appropriate to only retain terms at order χ^{-2} the elastic cross-section $d\sigma$ is calculated at the $E_{\rm cm}$ and is determined by the incoming nucleon energies. Next-to-leading order corrections at order χ^{-1} and χ^0 arise and are proportional to the $d\sigma/dE_{\rm cm}$ and can be come important when $E_{\rm cm} \lesssim 10$ MeV where $d\sigma$ varies rapidly. However, for ambient conditions in the supernova core $E_{\rm cm} \approx 100$ MeV and for these energies $d\log\sigma/d\log E_{\rm cm} \ll 1$ and these corrections can be expected to be small.

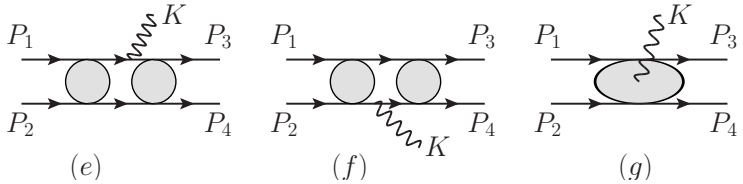

Figure 4.2: Neglected diagrams (e) and (f) in which radiation attaches to internal nucleon lines, and (g) in which it couples to short-distance two-body currents represented by the grey blob.

Diagrams shown in Fig. 4.2 contribute to bremsstrahlung radiation at order χ^1 in the low energy expansion. Here, the separation between the contributions from diagrams labeled (e) and (f), and the two-body current shown in the diagram labeled (g) is model and scale dependent and it is inconsistent to selectively include any subset of these contributions. We also note, once again, that the grey blobs should include both the pion exchanges and short-distance contributions and latter being especially important. Comparisons between model calculations which include order χ contributions with those obtained in the SRA, and nucleon-nucleon bremsstrahlung data find that the SRA provides as good a description of the data as do the potential models with their prescribed 2-body currents[257]. For this reasons we will neglect the contributions from the diagrams in Fig. 4.2 and use Eqns. 4.3, 4.4 & 4.5 to calculate the emission rates. A comparison between the photon bremsstrahlung data measured in the laboratory, and predictions of the rate in SRA provides an estimate of the associated error. For collisions with $E_{\rm cm} \approx 100$ MeV these comparisons show that the SRA provides a good description of the data for $\omega << E_{\rm cm}$, and for $\omega \simeq E_{\rm cm}$ underestimates the cross-sections by about a factor of about 2 [257, 258, 259]. For these reasons we consider the leading order SRA better suited to calculate emission and scattering rates of LVB rather than models which include corrections arising from a sub-class diagrams in Fig. 4.2 in perturbation theory.

The emissivity, which is the rate of emission of energy in LVBs per unit volume, can be calculated in the SRA using Eqns. 4.3, 4.4, and 4.5. For the process $np \to np\gamma_Q$ and $np \to np\gamma_B$ they are given by

$$\dot{\epsilon}_{np\to np\gamma_Q} = -4\pi\alpha_{\rm em}\epsilon_Q^2 \int \frac{d^3k}{2\omega(2\pi)^3}\omega \int \frac{d^3p_1 f_n(E_1)}{(2E_1)(2\pi)^3} \int \frac{d^3p_2 f_p(E_2)}{(2E_2)(2\pi)^3} \int d\Pi (\epsilon^\mu J_\mu^{(2)})^2 \; 32\pi E_{\rm cm}^2 v_{rel} \; \frac{d\sigma_{\rm np}(E_{\rm cm},\theta)}{d\theta_{\rm cm}} \tag{4.8}$$

$$\dot{\epsilon}_{np\to np\gamma_B} = -4\pi\alpha_{\rm em}\epsilon_B^2 \int \frac{d^3k}{2\omega(2\pi)^3}\omega \int \frac{d^3p_1 f_n(E_1)}{(2E_1)(2\pi)^3} \int \frac{d^3p_2 f_p(E_2)}{(2E_2)(2\pi)^3} \int d\Pi (\epsilon^\mu J_\mu^{(4)})^2 \; 32\pi E_{\rm cm}^2 \; v_{rel} \; \frac{d\sigma_{\rm np}(E_{\rm cm},\theta)}{d\theta_{\rm cm}} \tag{4.9}$$

where

$$d\Pi = (2\pi)^4 \; \delta^4(P_1 + P_2 - P_3 - P_4 - k)(1 - f_n(E_3))(1 - f_p(E_4)) \frac{d^3p_3}{2E_3(2\pi)^3} \frac{d^3p_4}{2E_4(2\pi)^3} \,, \tag{4.10}$$

is the final state phase space of the nucleons, $d\sigma_{\rm np}/d\theta$ is the differential elastic np scattering cross-section, $v_{rel} = |\vec{p}_1 - \vec{p}_2|/M$ is the relative speed, and $\theta_{\rm cm}$ is the scattering angle. $f_i(E) = 1/(1 + \exp((E - \mu_i)/T))$ is the Fermi distributions functions for neutrons and protons. Eq. 4.10 includes Pauli blocking factors for the final state nucleons and is important under degenerate conditions. However, in the supernova core matter is partially degenerate with $\mu_{(n/p)}/T \simeq 1$ and suppression due to Pauli blocking is small. The emission rates due to the reactions $nn \to nn\gamma_B$ and $pp \to pp\gamma_B$ are obtained by replacing $d\sigma_{\rm np}$ in Eq. 4.9 by $d\sigma_{\rm nn}$ and $d\sigma_{\rm pp}$, respectively and introduce the relevant distribution functions. Similarly, to obtain the contribution for $pp \to pp\gamma_Q$ we replace $d\sigma_{\rm np}$ in Eq. 4.8 by $d\sigma_{\rm pp}$ and f_n by f_p. In section 4.3 we discuss our calculations of the elastic nucleon-nucleon cross-sections and find that since $d\sigma_{\rm np}$ is larger at the energies of interest and because γ_Q radiation occurs at dipole order in the np reaction, the quadrupole order contribution from the $pp \to pp\gamma_Q$ reaction is small.

Despite the high density and temperature in the supernova core, the typical nucleon velocity $v \lesssim 1/3$ and it is useful to expand in powers of v as this leads to simplifications that allows us to do the phase space integrals needed to calculate the emissivities. We find that under non-degenerate conditions the emissivities are given by

$$\dot{\epsilon}_{np\to np\gamma_Q} = \frac{\alpha_{\rm em}\epsilon_Q^2}{\pi^{3/2}} \frac{n_n n_p}{(MT)^{3/2}} \int_{m_{\gamma_Q}}^{\infty} dE_{\rm cm} \; e^{-\frac{E_{\rm cm}}{T}} \; E_{\rm cm}^3 \; \mathcal{I}^{(2)}(\frac{m_{\gamma_Q}}{E_{\rm cm}}) \; \sigma_{np}^{(2)}(E_{\rm cm}) \tag{4.11}$$

$$\dot{\epsilon}_{pp\to pp\gamma_Q} = \frac{\alpha_{\rm em}\epsilon_Q^2}{\pi^{3/2}} \frac{n_p n_p}{(MT)^{3/2}} \int_{m_{\gamma_Q}}^{\infty} dE_{\rm cm} \; e^{-\frac{E_{\rm cm}}{T}} \; \frac{E_{\rm cm}^4}{M} \; \mathcal{I}^{(4)}(\frac{m_{\gamma_Q}}{E_{\rm cm}}) \; \sigma_{pp}^{(4)}(E_{\rm cm}) \tag{4.12}$$

$$\dot{\epsilon}_{ij\to ij\gamma_B} = \frac{\alpha_{\rm em}\epsilon_B^2}{\pi^{3/2}} \frac{n_i n_j}{(MT)^{3/2}} \int_{m_{\gamma_B}}^{\infty} dE_{\rm cm} \; e^{-\frac{E_{\rm cm}}{T}} \; \frac{E_{\rm cm}^4}{M} \; \mathcal{I}^{(4)}(\frac{m_{\gamma_B}}{E_{\rm cm}}) \; \sigma_{ij}^{(4)}(E_{\rm cm}) \tag{4.13}$$

where

$$\mathcal{I}^{(2)}(x) = \frac{4}{3}\left(\sqrt{1-x^2}(1-\frac{x^2}{4}) - \frac{3x}{4}\arctan\left(\frac{\sqrt{1-x^2}}{x}\right)\right), \tag{4.14}$$

$$\mathcal{I}^{(4)}(x) = \frac{8}{5}\left(\sqrt{1-x^2}(1+\frac{x^2}{12}+\frac{x^4}{6}) - \frac{5x}{4}\arctan\left(\frac{\sqrt{1-x^2}}{x}\right)\right), \tag{4.15}$$

and

$$\sigma^{(2)}_{ij} = \int d\cos\theta_{\rm cm}\frac{d\sigma_{n_in_j\to n_in_j}}{d\theta_{\rm cm}}(1-\cos\theta_{\rm cm}), \tag{4.16}$$

$$\sigma^{(4)}_{ij} = \int d\cos\theta_{\rm cm}\frac{d\sigma_{n_in_j\to n_in_j}}{d\theta_{\rm cm}}(1-\cos^2\theta_{\rm cm}). \tag{4.17}$$

The derivation of these results is discussed in Appendix C. Albeit cumbersome, numerical calculations of the emissivity including relativistic dispersion relations for the nucleons and corrections due to matter degeneracy can be performed directly using Eqs. 4.8 and 4.9. At $T = 30$ MeV and nucleon number density $n \simeq n_0 = 0.16$ fm^{-3} we have estimated these corrections to be small $\simeq 30\%$ compared to order χ corrections neglected in the SRA, which could be about factor of 2 as mentioned earlier.

4.3 Elastic cross-sections and LVB emissivity

Any realistic nucleon-nucleon potential constructed to reproduce the nucleon-nucleon phase shifts can be used to calculate the elastic differential cross-sections appearing in Eqs. 4.16 and 4.17. It is, however, simpler to obtain these cross-sections directly from the measured phase shifts and this calculation is outlined in Appendix D. The differential cross section is expanded in the spherical wave basis with definite orbital angular momentum L and the angular dependence is given by associated Legendre polynomials $P_l^m(\cos\theta_{\rm cm})$ and the energy dependence is encoded in the phase shifts [260]. This expansion converges rather rapidly as can be seen from Fig. 4.3 where we present our calculation of the total $n-p$ cross-section including individual contributions from phase shifts with angular momentum from $L = 0$ to $L = 5$. With the inclusion of phase shifts $L = 0, 1, \&, 2$ one finds good agreement between theory and the high quality data shown by the dashed curve. To better resolve the angular dependencies needed to determine $\sigma^{(2)}_{ij}$ and $\sigma^{(4)}_{ij}$ we retain terms up to $L = 5$.

In Fig. 4.3 we also show the np cross-section calculated in the Born approximation using the one pion exchange potential (OPEP). A comparison reveals large differences in the magnitude and energy dependence of the cross-section and implies that earlier work in Ref. [4] where bremsstrahlung was calculated using the one pion exchange potential will also be similarly discrepant. We can deduce that at small values of the $E_{\rm cm}$ one pion exchange model grossly underestimates the scattering rate, while for $E_{\rm cm} > 50$ MeV it overestimates it by about a factor of 6. We find a similar trend for the nn and pp cross-sections. In the supernova where $T \simeq 30$ MeV the relevant $E_{\rm cm} \simeq 100$ MeV, and we can anticipate that calculations based on the OPEP will overestimates the bremsstrahlung rate by a similar factor. As we shall see shortly this is borne out by the comparison between our results for the dark photon production with those presented in [4].

In the left panel of Fig. 4.4 we plot the function

$$\Phi^{(2)}_{np}(E_{\rm cm}) = \exp\left(-\frac{E_{\rm cm}}{T}\right) E^3_{\rm cm}\ \mathcal{I}^{(2)}(0)\ \sigma^{(2)}_{np}(E_{\rm cm}) \tag{4.18}$$

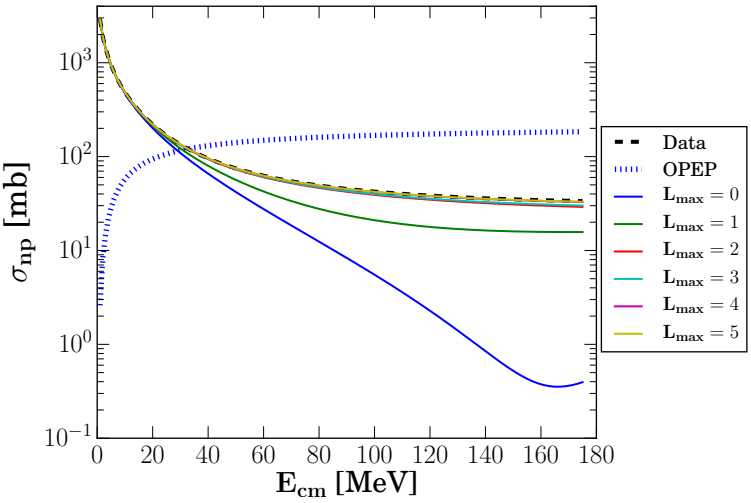

Figure 4.3: The np scattering cross section reconstructed from the phase shifts is compared with data and the predictions of the OPEP. The change in the total cross-section as more partial waves are included is shown and is accordance with the expectation about its rapid convergence. In contrast, the Born cross-sections in the OPEP fail to reproduce both the qualitative and quantitative features seen in the data.

which appears as the integrand on the RHS of Eq.4.11, and in the right panel we show the function

$$\Phi_{ij}^{(4)}(E_{\rm cm}) = \exp\left(-\frac{E_{\rm cm}}{T}\right) \frac{E_{\rm cm}^4}{M}\, \mathcal{I}^{(4)}(0)\, \sigma_{ij}^{(4)}(E_{\rm cm}) \tag{4.19}$$

which appears as the integrand on the RHS of Eq.4.13 with $m = 0$. These plots show the distribution of center of mass energies of nucleons in the initial state that contribute to the bremsstrahlung process when the mass of the LVB is negligible. The $np \to np\gamma_Q$ process shown in the left panel is stronger because this occurs at dipole order, while the processes that occur at quadrupole order $pp \to pp\gamma_Q$, $np \to np\gamma_B$, $nn \to nn\gamma_B$ and $pp \to pp\gamma_B$ are shown in the right panel are suppressed by $E_{\rm cm}/M \propto v^2$ where v is nucleon velocity in the initial state. The emissivity is proportional to the area under these curves and difference between the curves obtained in the SRA and the OPEP is striking and the trends follow from the comparison between the cross sections seen in Fig. 4.3. For soft dipole radiation these curves suggest that OPEP would overestimate the rate by about a factor 2, while for quadrupole radiation it would overestimate the rate by about a factor 10. In these plots $T = T_{SN} = 30$ MeV and under these conditions we see that bremsstrahlung production of dark photons peaks at $E_{\rm cm} \simeq 100$ MeV and production of leptophobic LVB peaks at $E_{\rm cm} \simeq 150$ MeV. The spectrum of LVBs emitted will be approximately thermal with $\omega \approx T - 3T$ suggesting that expansion parameter for the SRA, $\chi \simeq 1/5 - 1$.

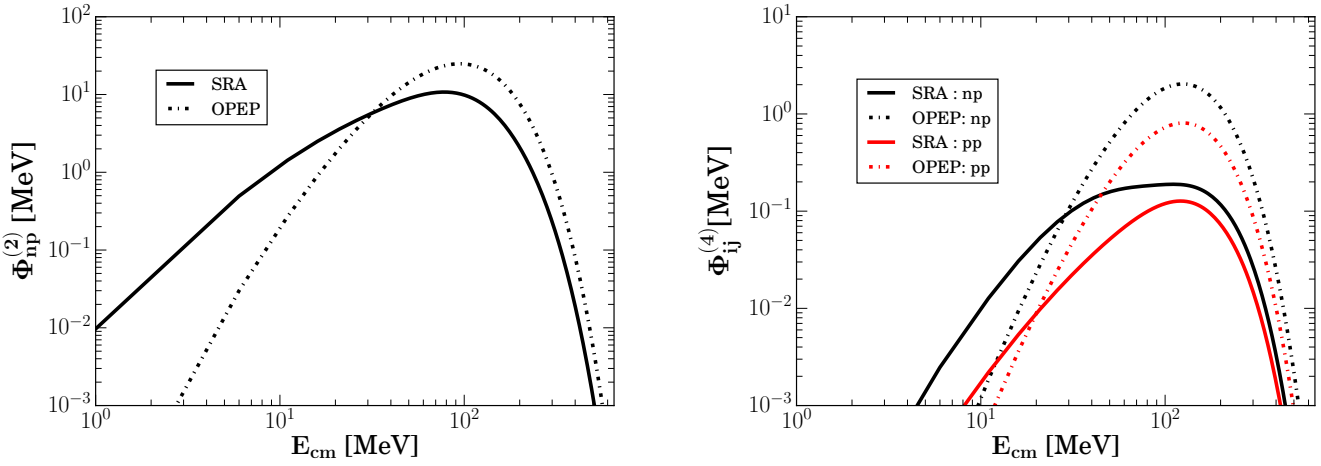

Figure 4.4: Dipole (left) and quadrupole (right) contributions to the emissivity integral defined in Eqs. 4.18 and 4.19, respectively. The solid lines were obtained using experimentally measured differential cross sections and the dotted lines are obtained from the OPEP model. Fiducial values $T = 30$ MeV and $m = 0$ are used in these plots.

4.4 New and Revised Constraints

In earlier work Raffelt found empirically that when the energy loss rate per gram due to the radiation of free streaming particles in the supernova core at a fiducial density $\rho = 3 \times 10^{14}$ g/cm^3 and temperature $T = 30$ MeV exceeds

$$\dot{E}_{\rm Raffelt} = 10^{19} \ \frac{\rm erg}{\rm g \ s} \tag{4.20}$$

the duration of the SN neutrino burst is approximately reduced by half [236]. Detailed simulations of neutrino transport in the protoneutron star and its predictions for the neutrino events in Kamioka and IMB which were the neutrino detectors at the time of SN1987A validate Raffelt's approximate local criterion [236, 239] and in what follows we shall employ it to constrain ϵ_Q and ϵ_B. We note that Raffelt's criterion approximately corresponds to limiting the energy loss due to LVBs to total luminosity of $L < \dot{E}_{\rm Raffelt} \times M_{\rm core} \simeq 2 \times 10^{52} \ (M_{\rm core}/M_\odot)$ ergs/s.

First, we determine the SN1987A constraints on γ_B, which is the leptophobic LVB that couples to baryon number. The total energy loss rate per gram due to γ_B radiation is

$$\dot{E}_B(\rho, T, Y_p) = (\dot{\epsilon}_{np\to np\gamma_B} + \dot{\epsilon}_{nn\to nn\gamma_B} + \dot{\epsilon}_{pp\to pp\gamma_B})/\rho \, , \tag{4.21}$$

where ρ is the matter mass density, T is the temperature and $Y_p = n_p/(n_n + n_p)$ is the fraction of protons. As already noted, we choose $\rho = 3 \times 10^{14}$ g/cm^3, $T = T_{\rm SN} = 30$ MeV and we set the proton fraction $Y_p = 0.3$ to reflect typical conditions encountered in proto-neutron star simulations[261, 262].

In Fig. 4.5 we show the constraint on the coupling strength defined as $\alpha_B = \epsilon_B^2 \alpha_{\rm em}$ where $\alpha_{\rm em} = 1/137$ is the fine structure constant. We have opted to work with α_B rather ϵ_B because this is widely used in the context of discussing LVBs that couple to baryon number. The solid blue curve is obtained by setting $\dot{E}_B(\rho = 3 \times 10^{14} \ {\rm g/cm^3}, T = 30 \ {\rm MeV}, Y_p = 0.3) = 10^{19}$ erg/g/s and solving for ϵ_B for a range of LVB masses $m_B = 1$ eV – 200 MeV. For value of α_B larger than those defined by the blue curve the supernova would cool too rapidly to produce the neutrino events detected from SN1987A. For lighter masses when $m_B \ll 1$ eV the

exchange of the LVB leads to macroscopic forces, collectively referred as fifth forces, and have been probed by a host experiments (for a review see Ref. [263]). These have strongly constrained α_B to values that are several orders of magnitude smaller than can be accessed by the SN cooling constraint. At intermediate values in the range $m_B \simeq$ few eV – MeV neutron scattering and neutron optics provide the strongest experimental constraints [2, 3] and these are also shown in Fig. 4.5.

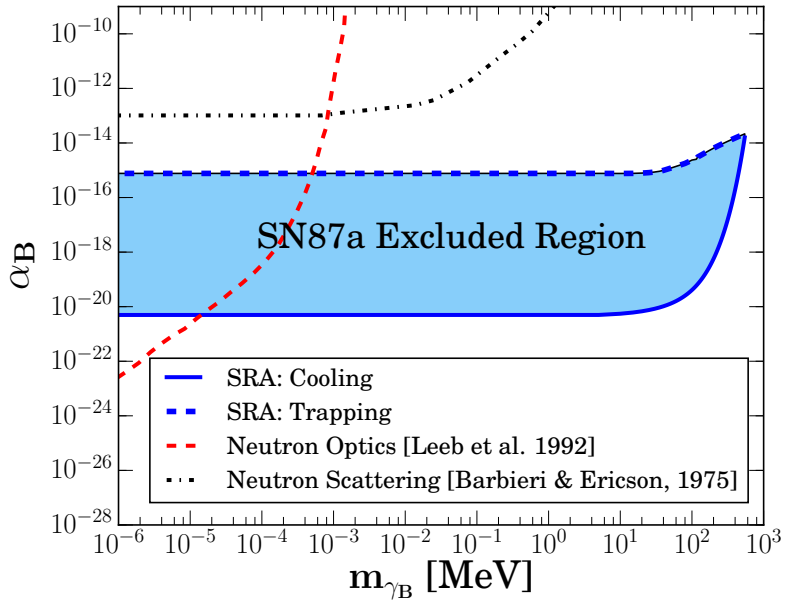

Figure 4.5: Cooling and trapping constraints in the parameter space of the LVB that couples to baryon number. The solid blue line is the lower limit set by cooling, and the dashed blue line is the upper limit set by trapping. Experimental constraints derived from neutron scattering from Ref. [2] (black dot-dashed curve) and from neutron optics from Ref. [3] (red dashed curve) are also shown.

While it is remarkable that the SN cooling constraint in Fig. 4.5 is several orders of magnitude more stringent than the experimental constraints it relies on the assumption that once produced the LVBs can free stream out of the proto-neutron star. Clearly this will not be true for large values of the coupling α_B. At these larger values of α_B LVBs will be trapped in the core and will be emitted as black-body radiation with a luminosity

$$L_s \simeq \frac{\pi^3}{30} g^*(\eta)\ R_s^2 T_s^4 \tag{4.22}$$

where $\eta = m/T_s$, R_s and T_s are the radius and temperature at which LVBs decouple. The effective spin-degeneracy factor

$$g^*(\eta) = \frac{45}{\pi^4} \int_0^\infty dy\ \frac{y^2\sqrt{\eta^2+y^2}}{\exp\left(\sqrt{\eta^2+y^2}\right)-1} \tag{4.23}$$

includes corrections due to the finite mass of LVBs and the contribution from the additional longitudinal modes. When $L_s > 3\times10^{52}$ ergs/s the neutrino signal is discernibly altered and neutrino events from SN1987A provide an upper bound on the coupling of LVBs [236].

An accurate description of the decoupling process will rely on computer simulations of proto-neutron star evolution which include energy transport due to both neutrinos and LVBs and is beyond the scope of this study. In what follows we shall adopt a simple criterion to estimate the upper bound on our constraint. For LVB radiation from the decoupling surface to discernibly reduce the neutrino luminosity, a large fraction of this radiation originating at R_s should propagate to regions beyond the radii at which neutrinos decouple from matter. Otherwise, the energy radiated in LVBs will be reabsorbed by matter and transferred back to neutrinos. To enforce this we define an effective optical depth in the vicinity of R_s

$$\tau(R_s) = \int_{R_s}^{R_m} \frac{dr}{\langle\lambda(r)\rangle}\,, \tag{4.24}$$

where

$$\langle\lambda(r)\rangle = \frac{\int_\eta^\infty\ dx\ \frac{x^2\sqrt{x^2-\eta^2}}{(e^x-1)}\ \lambda_r(\omega = xT_s)}{\int_\eta^\infty\ dx\ \frac{x^2\sqrt{x^2-\eta^2}}{(e^x-1)}} \tag{4.25}$$

is a simple energy weighted spectral average of the mean free path $\lambda_r(\omega)$ of LVBs, $\eta = m/T_s$ and R_m is the radius at which the temperature has dropped to $T = T_\nu/2 \approx 3$ MeV, and require that $\tau(R_s) < 3$. The choice of R_m and $\tau(R_s)$ are well motivated but the associated errors are difficult to asses because they are compounded by the fact that the ambient conditions in the vicinity of R_s change with time and in analysis here we use static profiles of density and temperature. Near the surface of the newly born neutron star density and temperature can be modeled using simple power laws given by $\rho(r) = \rho(R_s)(R_s/r)^n$ and $T(r) = T_s(R_s/r)^{n/3}$. The index n is varied over the range 3–7 it is possible to mimic representative profiles found from supernova and proto-neutron star simulations at a characteristic time of 1–2 seconds after bounce from Ref. [261, 262]. However, when the LVB mass is larger than the temperature in the outer regions, the decoupling surface will be pushed to higher temperature region in the core. To describe decoupling of these heavier LVBs we smoothly connect the steep density and temperature profiles in the surface regions to the core density profiles with $\rho_{\rm core} \simeq 3\times10^{14}$ g/cm^3 and a core temperature $T_{\rm core} \simeq 30$ MeV.

For densities and temperatures of interest, inverse bremsstrahlung reactions $\gamma_B np \to np$, $\gamma_B nn \to nn$ and $\gamma_B pp \to pp$ are more important than the Compton scattering process $\gamma_B p \to p\gamma$ (interestingly, due to plasma effects, Compton scattering off electrons $\gamma_B e^- \to e^-\gamma$ and pair production of electron-positron pairs $\gamma_B \to e^+e^-$ is induced through in-medium mixing with the photon due a proton-hole loop but was found to be small compared to the bremsstrahlung processes). The mean free path due to the inverse bremsstrahlung process can be calculated in the soft radiation approximation. Using the transition matrix element calculated for bremsstrahlung and making appropriate changes to the phase space integrals (see Appendix E for details) we find the mean free path for the process $\gamma_B ij \to ij$

$$\frac{1}{\lambda^{ij}_{\gamma_B}(\omega)} = \frac{2496}{135\pi}\ \alpha_B\ n_i n_j\ \left(\frac{\pi T}{M}\right)^{5/2}\ \frac{1}{\omega^3}\sqrt{1-\xi^2}(1+\frac{2}{13}\xi^2)\ \langle\sigma^{(4)}_{ij}(T)\rangle \tag{4.26}$$

where n_i, n_j and number densities of the nucleons involved, T is the ambient temperature, $\xi = m_B/\omega$, and the thermal cross-section

$$\langle\sigma^{(4)}_{ij}(T)\rangle = \frac{1}{6}\int_0^\infty dx\ e^{-x}x^3\ \sigma^{(4)}_{ij}(E_{\rm cm} = xT)\,, \tag{4.27}$$

$$\sigma^{(4)}_{ij}(E_{\rm cm}) = \int_{-1}^{1} d\cos\theta_{\rm cm}\ (1-\cos^2\theta_{\rm cm})\ \frac{d\sigma_{ij}(E_{\rm cm})}{d\theta_{\rm cm}}\,. \tag{4.28}$$

Here, as before $d\sigma_{ij}(E_{\rm cm})$ is the differential cross-section for elastic nucleon-nucleon scattering process $ij \to ij$ and $E_{\rm cm}$ is the center of mass energy of the nucleon pair in the initial state. In Fig. 4.6 the variation of the

thermal cross sections with temperature is shown and the large increase at low temperature arises because the nucleon-nucleon cross sections at low energy increase rapidly, as can be seen in Fig. 4.3.

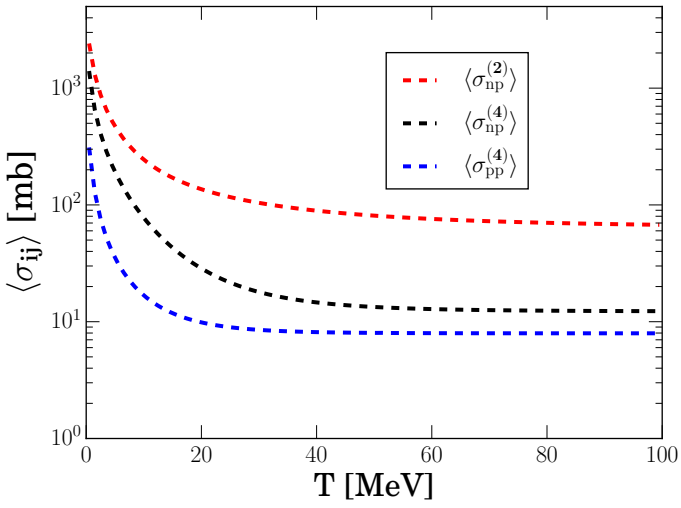

Figure 4.6: The temperature dependence of the thermally averaged nuclear cross sections needed for the calculation of the bremsstrahlung absorption contributions to the mean free path of LVBs.

We note that the one pion exchange model for nuclear interactions would have predicted the opposite behavior. The thermal cross section which will be relevant when we discuss the opacity of dark photons later

$$\langle\sigma_{np}^{(2)}(T)\rangle = \frac{1}{2}\int_0^\infty dx\; e^{-x}x^2\;\sigma_{np}^{(2)}(E_{\rm cm}=xT)\,, \tag{4.29}$$

$$\sigma_{np}^{(2)}(E_{\rm cm}) = \int_{-1}^{1} d\cos\theta_{\rm cm}\;(1-\cos\theta_{\rm cm})\;\frac{d\sigma_{np}(E_{\rm cm})}{d\theta_{\rm cm}}\,. \tag{4.30}$$

is also shown in Fig. 4.3. It is interesting to note that $\langle\sigma_{ij}^{(4)}(T)\rangle$ relevant for LVBs that couple to baryon number is quite smaller because in this case scattering occurs only due quadrupole fluctuations of baryon charge in nucleon-nucleon collisions. Summing over the individual contributions the mean free path in Eq. 4.25 is given by $\lambda_r(\omega) = (1/\lambda_r^{np}+1/\lambda_r^{nn}+1/\lambda_r^{pp})^{-1}$ and we use it in Eq. 4.24 and employ the matter profile previously mentioned to calculate $\tau(R_s)$. The blue dashed curve in Fig. 4.5 is the obtained by solving the $\tau(R_s)=3$.

We now turn to perform a similar analysis to constrain the properties of the dark photon. In this case the total energy loss rate per gram due to the radiation of dark photons is

$$\dot{E}_Q(\rho,T,Y_p) = (\dot{\epsilon}_{np\to np\gamma_Q}+\dot{\epsilon}_{pp\to pp\gamma_Q})/\rho\,, \tag{4.31}$$

and requiring that $\dot{E}_Q(\rho=3\times10^{14}\ {\rm g/cm^3}, T=30\ {\rm MeV}, Y_p=0.3) < \dot{E}_{\rm Raffelt}$ provides a constraint on ϵ_Q that is shown by the solid blue curve in Fig. 4.7. In this case, we choose to show constraints on ϵ_Q rather than the

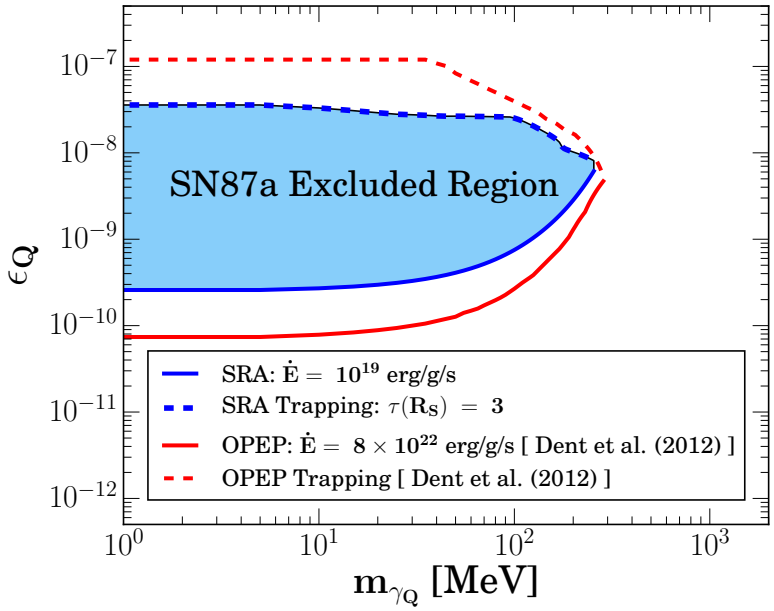

Figure 4.7: The revised excluded region in the dark photon parameter space. Blue curves show results obtained using the bremsstrahlung rates calculating in the SRA while the red curves are taken from [4] and are based on rates calculated using the OPEP (see text for details).

related quantity $\alpha_Q = \epsilon_Q^2 \alpha$ to help compare with earlier constraints obtained in Ref. [4, 242]. For reference the SN cooling constraint from Ref. [4] is also shown in Fig. 4.7 as a solid red curve. The differences between the results arise due to two unrelated factors which partially offset each–other. First, as noted earlier, the OPEP used in [4] to calculate the bremsstrahlung rate of dark photon production is expected to be larger than our predictions based on the SRA. In addition, the inclusion of a specific contribution to the the 2-body current coming from the pion-exchange current could spuriously enhance the np bremsstrahlung rate by a large factor. Secondly, in [4] the authors chose to derive the constraint by requiring that total energy loss due to dark photons produced in the central 1 km region of the SN core with a density $\rho_{\rm core} = 3 \times 10^{14}$ g/cm^3 and $T_{\rm core} = 30$ MeV be less than 10^{53} ergs/s. This corresponds to a local bound on the energy loss $\dot{E} < 8 \times 10^{22}$ ergs/g/s. Had we used this bound instead of $\dot{E} < \dot{E}_{\rm Raffelt}$, our constraint on ϵ_Q would be weaker by a factor of about 100. This suggests that the bremsstrahlung rate in [4] is larger than ours by a factor of about 500! This large difference cannot be explained by the differences we see between the data and the nucleon-nucleon cross sections predictions by the OPEP. It is also unlikely that inclusion of a specific meson-exchange contribution in [4] can account for this large enhancement.

To obtain the upper bound on ϵ_Q due to trapping we calculate the dark photon mean free path. At high density and for dark photon masses $m_Q < 100$ MeV the dominant absorption process is the inverse bremsstrahlung $\gamma_Q np \to np$ and the associated mean free path is given by

$$\frac{1}{\lambda^{np}_{\gamma_Q}(\omega)} = 8\alpha_{\rm em}\epsilon_Q^2 \; n_i n_j \; \left(\frac{\pi T}{M}\right)^{3/2} \frac{1}{\omega^3} \frac{2+\xi^2}{\sqrt{1-\xi^2}} \; \langle \sigma^{(2)}_{np}(T) \rangle \tag{4.32}$$

where as before n_n, n_p are number densities of neutrons and protons, T is the ambient temperature, $\xi = m_Q/\omega$ and thermal cross-section was defined earlier in Eq. 4.29. The reaction $\gamma_Q pp \to pp$ makes a smaller contribution

because it occurs at quadrupole order and is given by

$$\frac{1}{\lambda^{pp}_{\gamma_Q}(\omega)} = \frac{2496}{135\pi}\alpha_{\rm em}\epsilon_Q^2\ n_p^2\ \left(\frac{\pi T}{M}\right)^{5/2}\ \frac{1}{\omega^3}\sqrt{1-\xi^2}(1+\frac{2}{13}\xi^2)\ \langle\sigma^{(4)}_{pp}(T)\rangle\,, \tag{4.33}$$

where the thermal cross section $\langle\sigma^{(4)}_{pp}(T)\rangle$ was defined earlier in Eq. 4.27. The direct decay of the dark photon to electron-positron pairs $\gamma_Q \to e^+ + e^-$ becomes relevant for larger dark photon masses. In the supernova core Pauli blocking of the final state electrons due to their high chemical potentials $\mu_e \simeq 100$ MeV suppresses this decay rate and the mean free path is given by

$$\begin{aligned}\frac{1}{\lambda^{e^+e^-}_{\gamma_Q}(\omega)} =& \frac{\alpha\epsilon^2}{3}\frac{m_Q^2+2m_e^2}{\omega^2-m_Q^2}\int_{E^-}^{E^+} dE\ (1-f_{e^-}(E))\\ =& \frac{\alpha\epsilon^2}{3}\frac{m_Q^2+2m_e^2}{\omega^2-m_Q^2}\Big[2(E^+-E^-)-T\log(\frac{e^{E^+/T}-e^{\mu_e/T}}{e^{E^-/T}-e^{\mu_e/T}})\Big]\end{aligned} \tag{4.34}$$

where,

$$E^\pm = \Big[m_Q^2+\omega^2\Big(\sqrt{1-4\frac{m_e^2}{m_Q^2}}\pm\frac{1}{2}\sqrt{1-\frac{m_Q^2}{\omega^2}}\Big)^2\Big]^{1/2}\,, \tag{4.35}$$

and $\omega = \sqrt{k^2+m_Q^2}$ is the energy of the dark photon in the rest frame of the dense plasma. Including inverse bremsstrahlung and decay contributions the mean free path of the dark photon $\lambda_r(\omega) = (1/\lambda^{e^+e^-}_{\gamma_Q}(\omega)+1/\lambda^{pp}_{\gamma_Q}(\omega)+1/\lambda^{np}_{\gamma_Q}(\omega))^{-1}$. We use this to calculate the optical depth defined in Eq. 4.24 and obtain the trapping upper bound on the constraint. As discussed earlier for larger values of ϵ_Q dark photons are reabsorbed in the region in the vicinity of the neutrino sphere and the neutrino emission will not be altered significantly.

4.5 Conclusions

We have calculated, for the first time, the energy loss rate due to dark gauge bosons that couple to baryon number from the supernova core and used it to constrain its properties. We find that for gauge boson masses in the range $m_B = 10^{-4} - 10^2$ MeV the SN provides the most stringent constraint to date on the effective baryon number fine structure constant α_B which is about 7 orders of magnitude smaller than earlier constraints based on neutron scattering data. Our calculation is based on the SRA which is valid in the limit when the energy carried by the radiation is small compared to the energy of nucleons involved in the reaction. In this limit, the bremsstrahlung rate can be related to the nucleon-nucleon elastic scattering cross-sections and provides a benchmark that is independent of the potential used to model the nucleon-nucleon interaction. Using the SRA we have also calculated the emissivity of dark photons and compared our predictions to those obtained in [4] which were based on the one pion exchange potential of nucleon-nucleon interactions. We find significant differences because one-pion exchange is a poor approximation to the nucleon-nucleon interaction. The revised SN cooling constraint for the dark photons is about one order of magnitude weaker.

The LVB mean free paths in the SRA was calcualted to estimate the upper bound on the coupling, and the inverse bremsstrahlung reactions were found to dominate the opacity. At the relevant densities and temperatures the SRA predicts an enhancement of these rates in the outer regions of the supernova when compared to the results obtained in the one pion exchange model because the latter underestimates the nucleon-nucleon elastic cross-section at low energy.

While the SRA is a significant improvement over simple models of the nucleon-nucleon interaction treated in the Born approximation, its strictly valid for low energy processes where the expansion parameter $\chi = \omega/E_{\rm cm} \ll 1$. In our calculations we used the SRA for values of $\chi \simeq 1/5 - 1$ and the contribution of higher order terms in this expansions cannot be ignored. Nonetheless, as noted earlier comparisons between the predictions of SRA and experimental data in the context of photon bremsstrahlung from nucleon-nucleon collisions have shown that the agreement between SRA predictions and data for photon energies $\lesssim 100$ MeV is typically better than expected, differing by about a factor of 2 at the higher energies. For these larger energies two-body currents and re-scattering diagrams contribute and their inclusion relies on a model of the nucleon-nucleon interaction and the associated 2-body currents. χEFT NN potentials are well suited for this purpose, and it would be desirable to first perform bremsstrahlung calculations in this framework, benchmark them with available data from pp and np bremsstrahlung experiments, and then employ them to predict the emissivities of LVBs in the supernova context. In addition, other corrections of $\mathcal{O}(1)$ arising from many-body effects in the dense core also need to be studied. If these corrections can suppress the emissivities in the core then the ability of supernovae to constrain LVBs will be further diminished.

Further work is warranted before we can draw firm conclusions about the extent of the LVB parameter space excluded by SN1987A. The rapid increase in NN cross-sections at low energy implies that the opacity due to the inverse bremsstrahlung processes in the outer cooler regions of the star is larger, while in contrast the smaller cross section at high energy imply a smaller emissivity in the high temperature core. Together, this indicates that the inclusion of realistic nuclear physics acts to reduce the region of parameter space that can be constrained. This underscores the need to further improve the nuclear physics of bremsstrahlung processes by going beyond the SRA, and to incorporate them self-consistently into supernova simulations. Corrections to the SRA would be especially relevant for LVB masses greater than about 100 MeV so our constraints in the region of parameter space must be viewed as preliminary. Interestingly, for the dark photon masses in the MeV - GeV range and for coupling ϵ_Q in the range $10^{-7} - 10^{-9}$, recent work suggests dark mater annihilations in the earth's core can lead to detectable signatures in terrestrial detectors [264]. Since this has significant overlap with the region constrained by SN1987A it would be worthwhile to refine these constraints. As a first step, the contribution of LVBs is being included in the energy transport of 1-d models of core-collapse supernova simulations using the formulae for the emissivities and opacities derived in this study, and which will be reported in future work.

Appendices

Appendix A

Configuration Interaction Monte Carlo Method

A.1 Sign Problem

As explained in Section 2.2.2 the main systematic bias in the CIMC calculations come from imposing a fixed-node approximation in order to deal with the sign problem. In this section we discuss additional details and estimate the impact of this approximation. First we recall that within the fixed-node approach one defines a family of *sign-problem-free* Hamiltonians H_γ (see e.g., Ref. [265]). If we introduce the sign function

$$\mathfrak{s}(\mathbf{m},\mathbf{n}) = sign\left(\frac{\langle\Phi_G|\mathbf{m}\rangle}{\langle\mathbf{n}|\Phi_G\rangle}\langle\mathbf{m}|H|\mathbf{n}\rangle\right), \tag{A.1}$$

where Φ_G is the wavefunction used for the fixed node procedure, we can define the off-diagonal matrix elements ($\mathbf{n} \neq \mathbf{m}$) of the sign-problem-free Hamiltonian H_γ as:

$$\langle\mathbf{m}|\mathcal{H}_\gamma|\mathbf{n}\rangle = \begin{cases} -\gamma\frac{\langle\Phi_G|\mathbf{m}\rangle}{\langle\mathbf{n}|\Phi_G\rangle}\langle\mathbf{m}|H|\mathbf{n}\rangle & \mathfrak{s}(\mathbf{m},\mathbf{n}) > 0 \\ \frac{\langle\Phi_G|\mathbf{m}\rangle}{\langle\mathbf{n}|\Phi_G\rangle}\langle\mathbf{m}|H|\mathbf{n}\rangle & \text{otherwise} \end{cases}, \tag{A.2}$$

while the diagonal elements are:

$$\langle\mathbf{n}|\mathcal{H}_\gamma|\mathbf{n}\rangle = \langle\mathbf{n}|H|\mathbf{n}\rangle + (1+\gamma)\sum_{\substack{\mathbf{n}\neq\mathbf{m} \\ \mathfrak{s}(\mathbf{m},\mathbf{n})>0}}\frac{\langle\Phi_G|\mathbf{m}\rangle}{\langle\mathbf{n}|\Phi_G\rangle}\langle\mathbf{m}|H|\mathbf{n}\rangle \tag{A.3}$$

It can be easily seen that for $\gamma = -1$ the original Hamiltonian is recovered. Furthermore, if we label with E_γ the lowest eigenvalue of a given H_γ one can prove that any linear extrapolation from two values E_{γ_1} and E_{γ_2} at $\gamma_1, \gamma_2 \geq 0$ to $E_{-1}^{\gamma_1,\gamma_2}$ provides an upper bound on the true ground state energy E_{-1}.

In the calculations presented here this procedure has been adopted by performing linear extrapolations using values at $\gamma = 0$ and $\gamma = 1$. The variation between the eigenvalues at different γ, including the extrapolated value at $\gamma = -1$ can be used as lower bounds on the missing energy contribution coming from the fixed-node approximation. We find that this spread in the case of PNM is within the estimated error bars coming from statistical uncertainties and are usually less than 20 keV per particle. In the case of SNM, however, the values at different gamma are outside the statistical error bars for densities below $0.1 - 0.14\,\mathrm{fm}^{-3}$ but still of the order of 100 keV per particle even at the lowest densities.

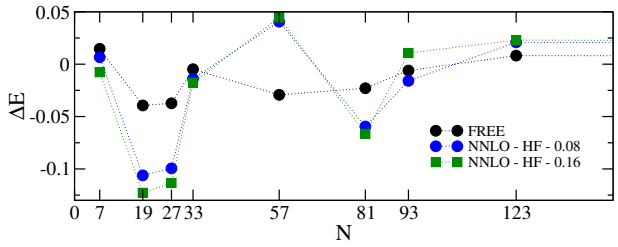

Figure A.1: Finite-size errors in the energy per particle as a function of the number of particles per spin-isospin species. The results shown are for a free gas as well as for Hartree-Fock calculations with the NNLO$_{opt}$ interaction at the two densities $\rho = \rho_0$ and $0.5\rho_0$.

This lower bound on the fixed-node error would be a good estimate provided there are no relevant contributions beyond the linear one in the γ extrapolation, a condition that cannot be checked in practice. In order to have another quantitative estimate of the systematic bias introduced by using the fixed-node approximation, we can check the sensitivity to changes in the underlying guiding wavefunction. This is analogous to the error estimates in MBPT obtained by changing the single-particle spectrum. The guiding wavefunction used in our calculations comes from the coupled-cluster double approximation with amplitudes obtained from second-order MBPT (see Ref. [145] for additional details) which clearly has zero overlap with states composed of an odd number of particle-hole excitations. In order to check the sensitivity to this choice we can set a lower bound on the overlaps of this wavefunction to any state in the Hilbert space generated by the single-particle space we have chosen. In this way we are including effectively a crude ansatz for triple and higher cluster excitations in this wavefunction that we will call CCD^*.

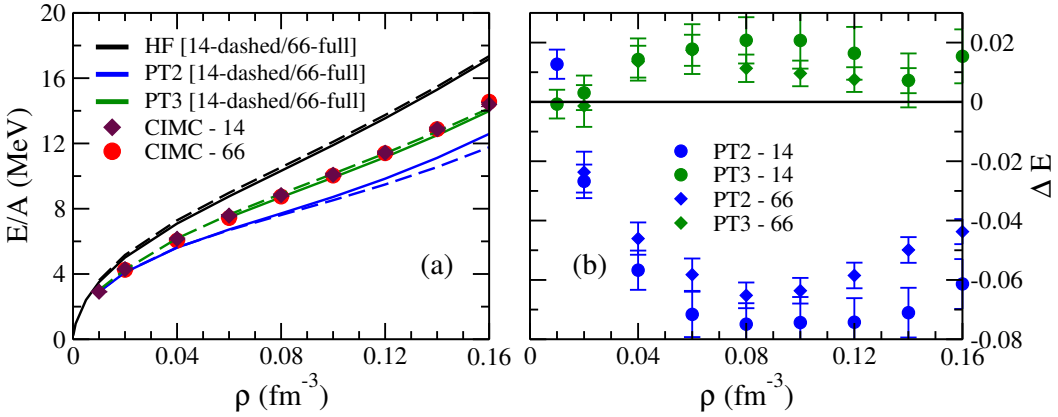

Figure A.2: (panel (a)): energy per particle in PNM computed with $N = 14$ and 66 neutrons from CIMC and MBPT using the NNLO$_{opt}$ chiral two-nucleon potential. (panel (b)): differences between the results from CIMC and MBPT at second and third order using $N = 14$ and 66.

The effect of using this as a guiding wavefunction in the case of PNM in the density range explored in this work is just to increase the statistical error on the ground state energy and no difference can be seen outside the error bars, which suggests that the CCD^* wavefunction provides a worse nodal constraint (higher statistical error) but the bias introduced by neglecting triples and higher correlations is smaller or comparable to the statistical errors in the calculation. This is also compatible with the estimates from coupled-cluster calculations using perturbative triples [128]. In the case of SNM the effect of using the CCD^* wavefunction is

much stronger: the statistical error is comparable to the one obtained using the bare CCD wavefunction but now the extrapolated eigenvalue E_{-1} shows considerably less binding, and this effect is stronger as the density is lowered (indicating that the origin is probably the appearance of clustering in the system). For instance, in the case of the N^{3}LO 414 interaction we find changes of about 1 MeV at $\rho = 0.02\,\mathrm{fm}^{-3}$ and about 0.5 MeV at $\rho = 0.08\,\mathrm{fm}^{-3}$. Since both wavefunctions provide upper bounds on the energy, estimates are always obtained with the CCD guiding wavefunction, but we can use the $CCD^\star$ results to obtain a qualitative error band. This is the procedure we employ to produce the grey band in Fig. 2.5.

A.2 Finite Size Effects

The quantum Monte Carlo calculations presented in Section 2.2 have been carried out using finite systems containing a fixed number of particles N. In order to reach the thermodynamic limit this number has to be taken as large as possible for a given density; however due to the strong dependence (N^2 for CIMC and PT2 and N^3 for part of PT3) of the computational time on the number of particles, all the results presented so far employed $N_s = 7$ for each spin/isospin species. Here we show that this is sufficient for the low densities considered in Section 2.2.

In order to avoid degenerate ground states we choose N_s such that all states up to a Fermi momentum k_F have been filled, and in our cubic lattice this restricts the allowed particle numbers to take on the values shown on the x-axis in Fig. A.1. Among these *closed-shell* configurations the ones that preserve the cubic symmetry of the underlying lattice (corresponding to $N_s = 7, 33, \dots$) have smaller deviations from the $N_s \to \infty$ limit as can be seen from Fig. A.1 and are usually selected so as to minimize finite size effects. It is remarkable that for a small system with $N_s = 7$ both the free-particle energy and the interacting Hartree-Fock energies are converged to the thermodynamic limit at the $\approx 1 - 2\%$ level, similar to the $N_s = 33$ system usually employed in similar calculations.

The left panel of Fig. A.2 shows the energy per particle in PNM for two systems composed of either $N = 14$ or $N = 66$ neutrons interacting through the NNLO$_{opt}$ interaction obtained both with CIMC and with different orders of MBPT. The differences are very small for all calculations apart from second-order perturbation theory (PT2), which for $N = 66$ shows a stronger density dependence above $\rho \approx 0.10\,\mathrm{fm}^{-3}$. The situation is similar with the other interactions used throughout this work. Since our main focus is to explore the convergence of MBPT calculations we plot in the right panel of Fig. A.2 the relative difference between CIMC and both PT2 and PT3 for the case of $N = 14$ particles (black and red dots respectively) and $N = 66$ particles (green and blue dots). The conclusions on the expected convergence errors are consistent for densities $\rho \lesssim 0.10\,\mathrm{fm}^{-3}$, a density at which three-body interactions are already important. We therefore conclude that our $N_s = 7$ particle systems are large enough for our purposes in the density region where two-body interactions are the dominant contribution.

PNM	$NNLO_{opt}$			$N^3LO-414$		
$\rho\,(fm^{-3})$	$\Delta PT2_{free}$	$\Delta PT2_{hf}$	$\Delta(PT2_{free}\text{-}PT2_{hf})$	$\Delta PT2_{free}$	$\Delta PT2_{hf}$	$\Delta(PT2_{free}\text{-}PT2_{hf})$
0.02	-0.0422(55)	-0.0268(56)	-0.015449(90)	-0.0239(46)	-0.0131(47)	-0.010774(51)
0.04	-0.0863(64)	-0.0567(66)	-0.02961(21)	-0.0408(48)	-0.0253(48)	-0.015511(77)
0.06	-0.1175(73)	-0.0716(76)	-0.04590(38)	-0.0473(51)	-0.0287(52)	-0.018634(99)
0.08	-0.1381(71)	-0.0749(71)	-0.06320(48)	-0.0490(52)	-0.0282(54)	-0.02079(11)
SNM	$NNLO_{opt}$			$N^3LO-414$		
$\rho\,(fm^{-3})$	$\Delta PT2_{free}$	$\Delta PT2_{hf}$	$\Delta(PT2_{free}\text{-}PT2_{hf})$	$\Delta PT2_{free}$	$\Delta PT2_{hf}$	$\Delta(PT2_{free}\text{-}PT2_{hf})$
0.04	0.1711(15)	0.0217(13)	0.14940(19)	0.166(12)	0.040(11)	0.1264(14)
0.06	0.2829(12)	0.0946(10)	0.18832(17)	0.1965(67)	0.0540(59)	0.14250(80)
0.08	0.31699(81)	0.10439(68)	0.21260(13)	0.2185(81)	0.0662(71)	0.1523(10)

Table A.1: Deviations from CIMC energies of 2nd order MBPT calculations for both PNM (top part) and SNM (bottom part) for two of the interactions used in this work. $\Delta PT2_{free}$ is the relative difference with respect to MBPT2 with a free spectrum in the propagators, $\Delta PT2_{hf}$ instead uses a Hartree-Fock dispersion while $\Delta(PT2_{free}\text{-}PT2_{hf})$ simply states the variation coming from changes in the single-particle spectrum. Errors in parenthesis are statistical errors coming from the CIMC result.

A.3 Effects of the Single Particle Spectrum

For all calculations presented the Hartree-Fock spectrum has been used in the single particle propagators (see e.g., Ref. [146] for details). We find that this choice yields a considerable improvement in the convergence pattern of the perturbative calculations. As can be seen from the results in Table A.1 for instance, the errors at second order are approximately twice as large using a free spectrum as the ones employing self-energy corrections at the Hartree-Fock level. For nuclear matter this factor can be even larger, and it does not seem connected to the perturbativeness of the interaction as can be deduced from the increased difference in going from the harder $NNLO_{opt}$ to the softer N^3LO 414 potential.

We conclude by pointing out that using the difference in energies obtained by varying the single-particle dispersion relation gives a qualitative understanding of the convergence of the perturbative calculations, with N^3LO 414 variations being smaller than the $NNLO_{opt}$ ones and with a substantial increase in going from PNM to SNM. It has to be noted, however, that these variations cannot be used to give a quantitative estimate of the errors in the many-body calculation, which is evident from the SNM results where $\Delta(PT2_{free}\text{-}PT2_{hf})$ overestimates the error by a factor of $\approx 2-3$. This is however not conclusive, since in SNM the CIMC calculation is not fully under control. In PNM where the difference with CIMC is a more reliable check of convergence, the errors are consistently underestimated by employing $\Delta(PT2_{free}\text{-}PT2_{hf})$.

Appendix B

Skyrme Phenomenology

B.1 Energy density from the potential matrix element

The most general form of the interaction matrix is given by,

$$
\begin{aligned}
V_{ij} =& t_0(1+x_0P_\sigma)\delta(\mathbf{r}_{ij}) + \frac{1}{2}t_1(1+x_1P_\sigma)\frac{1}{\hbar^2}[\overleftarrow{p^\dagger}^2_{ij}\delta(\mathbf{r}_{ij}) + \delta(\mathbf{r}_{ij})\overrightarrow{p}^2_{ij}] \\
&+ t_2(1+x_2P_\sigma)\frac{1}{\hbar^2}\overleftarrow{\mathbf{p}^\dagger}_{ij}\cdot\delta(\mathbf{r}_{ij})\overrightarrow{\mathbf{p}}_{ij} + \frac{1}{6}t_3(1+x_3P_\sigma)\rho^\alpha(\mathbf{r})\delta(\mathbf{r}_{ij}) \\
&+ \frac{i}{\hbar^2}W_0(\sigma_i+\sigma_j)\cdot\overleftarrow{\mathbf{p}^\dagger}_{ij}\times\delta(\mathbf{r}_{ij})\overrightarrow{\mathbf{p}}_{ij} \\
&+ \frac{1}{4}t_4(1+x_4P_\sigma)\frac{1}{\hbar^2}[\overleftarrow{p^\dagger}^2_{ij}\rho^\beta(\mathbf{r})\delta(\mathbf{r}_{ij}) + \delta(\mathbf{r}_{ij})\rho^\beta(\mathbf{r})\overrightarrow{p}^2_{ij}] \\
&+ t_5(1+x_5P_\sigma)\frac{1}{\hbar^2}\overleftarrow{\mathbf{p}}_{ij}\cdot\rho^\gamma(\mathbf{r})\delta(\mathbf{r}_{ij})\overrightarrow{\mathbf{p}}_{ij}
\end{aligned}
\tag{B.1}
$$

where, $\mathbf{r}_{ij} = \frac{\mathbf{r}_i-\mathbf{r}_j}{2}$, $\mathbf{r} = \frac{\mathbf{r}_i+\mathbf{r}_j}{2}$, $P_\sigma = \frac{1}{2}(1+\sigma_1\cdot\sigma_2)$, $\mathbf{p}_{ij} = -i\hbar\frac{\nabla_i-\nabla_j}{2}$, $\rho(\mathbf{r}) = \rho_p(\mathbf{r}) + \rho_n(\mathbf{r})$ and the arrows show the direction on which the momentum operators act.

Assume time reversal invariance. The Energy of the ground state can be written as integration over an

energy density functional, $E_{HFB} = \int d^r \varepsilon_{HFB}$

$$
\begin{aligned}
\varepsilon_{HFB} = & \sum_{t=n,p} \frac{\hbar^2}{2M_q}\tau_q + \frac{1}{2}t_0\Big[(1+\frac{1}{2}x_0)\rho^2 - (\frac{1}{2}+x_0)\sum_{q=n,p}\rho_q^2\Big] \\
& + \frac{1}{4}t_1\Big[(1+\frac{1}{2}x_1)(\rho\tau + \frac{3}{4}(\nabla\rho)^2) - (\frac{1}{2}+x_1)\sum_{q=n,p}(\rho_q\tau_q + \frac{3}{4}(\nabla\rho_q)^2)\Big] \\
& + \frac{1}{4}t_2\Big[(1+\frac{1}{2}x_2)(\rho\tau + \frac{3}{4}(\nabla\rho)^2) + (\frac{1}{2}+x_2)\sum_{q=n,p}(\rho_q\tau_q - \frac{1}{4}(\nabla\rho_q)^2)\Big] \\
& + \frac{1}{12}t_3\rho^\alpha\Big[(1+\frac{1}{2}x_3)\rho^2 - (\frac{1}{2}+x_3)\sum_{q=n,p}\rho_q^2\Big] \\
& + \frac{1}{4}t_4\Big[(1+\frac{1}{2}x_4)(\rho\tau + \frac{3}{4}(\nabla\rho)^2) - (\frac{1}{2}+x_4)\sum_{q=n,p}(\rho_q\tau_q + \frac{3}{4}(\nabla\rho_q)^2)\Big]\rho^\beta \\
& + \frac{\beta}{8}t_4\Big[(1+\frac{1}{2}x_4)\rho(\nabla\rho)^2 - (\frac{1}{2}+x_4)\nabla\rho\cdot\sum_{q=n,p}\rho_q\nabla\rho_q\Big]\rho^{\beta-1} \\
& + \frac{1}{4}t_5\Big[(1+\frac{1}{2}x_5)(\rho\tau + \frac{3}{4}(\nabla\rho)^2) + (\frac{1}{2}+x_5)\sum_{q=n,p}(\rho_q\tau_q - \frac{1}{4}(\nabla\rho_q)^2)\Big]\rho^\gamma \\
& - \frac{1}{16}(t_1x_1 + t_2x_2)J^2 + \frac{1}{16}(t_1 - t_2)\sum_{q=n,p}J_q^2 \\
& - \frac{1}{16}(t_4x_4\rho^\beta + t_5x_5\rho^\gamma)J^2 + \frac{1}{16}(t_4\rho^\beta - t_5\rho^\beta)\sum_{q=n,p}J_q^2 \\
& + \frac{1}{2}W_0(\mathbf{J}\cdot\nabla\rho + \sum_{q=n,p}\mathbf{J}_q\cdot\nabla\rho_q)
\end{aligned}
\tag{B.2}
$$

where,

$$
\begin{aligned}
\rho &= 2\int \frac{d^3k}{(2\pi\hbar)^3}n(k) \\
\tau &= 2\int \frac{d^3k}{(2\pi\hbar)^3}k^2 n(k) \\
\mathbf{J} &= \int \frac{d^3k}{(2\pi\hbar)^3}\mathbf{k}\times\sum_{s,s'}\langle s|\boldsymbol{\sigma}|s'\rangle\ n(k)
\end{aligned}
\tag{B.3}
$$

The different terms can be grouped together in simpler notation:

$$
\begin{aligned}
\varepsilon = & \sum_{t=n,p} \frac{\hbar^2}{2M_q}\tau_q + \frac{1}{4}t_0\Big[(2+x_0)\rho^2 - (1+2x_0)\sum_{q=n,p}\rho_q^2\Big] \\
& + \frac{1}{8}\Big[a(\rho\tau + \frac{3}{4}(\nabla\rho)^2) + 2b\sum_{q=n,p}(\rho_q\tau_q + \frac{3}{4}(\nabla\rho_q)^2)\Big] \\
& + \frac{1}{24}t_3\rho^\alpha\Big[(2+x_3)\rho^2 - (1+2x_3)\sum_{q=n,p}\rho_q^2\Big] \\
& + \frac{1}{8}t_4\Big[(2+x_4)(\rho\tau + \frac{3}{4}(\nabla\rho)^2) - (1+2x_4)\sum_{q=n,p}(\rho_q\tau_q + \frac{3}{4}(\nabla\rho_q)^2)\Big]\rho^\beta \\
& + \frac{\beta}{16}t_4\Big[(2+x_4)\rho(\nabla\rho)^2 - (1+2x_4)\nabla\rho\cdot\sum_{q=n,p}\rho_q\nabla\rho_q\Big]\rho^{\beta-1} \\
& + \frac{1}{8}t_5\Big[(2+x_5)(\rho\tau + \frac{3}{4}(\nabla\rho)^2) + (1+2x_5)\sum_{q=n,p}(\rho_q\tau_q - \frac{1}{4}(\nabla\rho_q)^2)\Big]\rho^\gamma \\
& - \frac{1}{16}(t_1x_1 + t_2x_2)J^2 + \frac{1}{16}(t_1 - t_2)\sum_{q=n,p}J_q^2 \\
& - \frac{1}{16}(t_4x_4\rho^\beta + t_5x_5\rho^\gamma)J^2 + \frac{1}{16}(t_4\rho^\beta - t_5\rho^\beta)\sum_{q=n,p}J_q^2 \\
& + \frac{1}{2}W_0(\mathbf{J}\cdot\nabla\rho + \sum_{q=n,p}\mathbf{J}_q\cdot\nabla\rho_q)
\end{aligned}
\tag{B.4}
$$

where, $a = t_1(x_1+2) + t_2(x_2+2)$, $b = \frac{1}{2}[t_2(2x_2+1) - t_1(2x_1+1)]$.

In uniform matter $\nabla\rho = 0$:

$$
\begin{aligned}
\varepsilon = & \sum_{t=n,p} \frac{\hbar^2}{2M_q}\tau_q + \frac{1}{4}t_0\Big[(2+x_0)\rho^2 - (1+2x_0)\sum_{q=n,p}\rho_q^2\Big] \\
& + \frac{1}{8}\Big[a\rho\tau + 2b\sum_{q=n,p}\rho_q\tau_q\Big] \\
& + \frac{1}{24}t_3\rho^\alpha\Big[(2+x_3)\rho^2 - (1+2x_3)\sum_{q=n,p}\rho_q^2\Big] \\
& + \frac{1}{8}t_4\Big[(2+x_4)\rho\tau - (1+2x_4)\sum_{q=n,p}\rho_q\tau_q\Big]\rho^\beta \\
& + \frac{1}{8}t_5\Big[(2+x_5)\rho\tau + (1+2x_5)\sum_{q=n,p}\rho_q\tau_q\Big]\rho^\gamma \\
& - \frac{1}{16}(t_1x_1 + t_2x_2)J^2 + \frac{1}{16}(t_1 - t_2)\sum_{q=n,p}J_q^2 \\
& - \frac{1}{16}(t_4x_4\rho^\beta + t_5x_5\rho^\gamma)J^2 + \frac{1}{16}(t_4\rho^\beta - t_5\rho^\beta)\sum_{q=n,p}J_q^2
\end{aligned}
\tag{B.5}
$$

In unpolarized matter, $\mathbf{J} = 0$:

$$\begin{aligned}
\varepsilon = & \sum_{t=n,p} \frac{\hbar^2}{2M_q}\tau_q + \frac{1}{4}t_0\Big[(2+x_0)\rho^2 - (1+2x_0)\sum_{q=n,p}\rho_q^2\Big] \\
& + \frac{1}{8}\Big[a\rho\tau + 2b\sum_{q=n,p}\rho_q\tau_q\Big] \\
& + \frac{1}{24}t_3\rho^\alpha\Big[(2+x_3)\rho^2 - (1+2x_3)\sum_{q=n,p}\rho_q^2\Big] \\
& + \frac{1}{8}t_4\Big[(2+x_4)\rho\tau - (1+2x_4)\sum_{q=n,p}\rho_q\tau_q\Big]\rho^\beta \\
& + \frac{1}{8}t_5\Big[(2+x_5)\rho\tau + (1+2x_5)\sum_{q=n,p}\rho_q\tau_q\Big]\rho^\gamma
\end{aligned} \tag{B.6}$$

Energy per baryon, $\mathcal{E} \equiv \varepsilon/\rho$:

$$\begin{aligned}
\mathcal{E} = & \sum_{t=n,p} \frac{\hbar^2}{2M_q}\frac{\tau_q}{\rho} + \frac{1}{4}t_0\Big[(2+x_0)\rho - (1+2x_0)\sum_{q=n,p}\frac{\rho_q^2}{\rho}\Big] \\
& + \frac{1}{8}\Big[a\tau + 2b\sum_{q=n,p}\frac{\rho_q\tau_q}{\rho}\Big] \\
& + \frac{1}{24}t_3\rho^\alpha\Big[(2+x_3)\rho - (1+2x_3)\sum_{q=n,p}\frac{\rho_q^2}{\rho}\Big] \\
& + \frac{1}{8}t_4\Big[(2+x_4)\tau - (1+2x_4)\sum_{q=n,p}\frac{\rho_q\tau_q}{\rho}\Big]\rho^\beta \\
& + \frac{1}{8}t_5\Big[(2+x_5)\tau + (1+2x_5)\sum_{q=n,p}\frac{\rho_q\tau_q}{\rho}\Big]\rho^\gamma
\end{aligned} \tag{B.7}$$

In terms of proton fraction, $y = \frac{\rho_p}{\rho_p+\rho_n}$:

$$\begin{aligned}
\mathcal{E} = & \sum_{t=n,p} \frac{\hbar^2}{2M_q}\frac{\tau_q}{\rho} + \frac{1}{4}t_0\Big[(2+x_0) - (1+2x_0)[y^2 + (1-y)^2]\Big]\rho \\
& + \frac{1}{8}\Big[a\tau + 2b[y\tau_p + (1-y)\tau_n]\Big] \\
& + \frac{1}{24}t_3\rho^{\alpha+1}\Big[(2+x_3) - (1+2x_3)[y^2 + (1-y)^2]\Big] \\
& + \frac{1}{8}t_4\Big[(2+x_4)\tau - (1+2x_4)[y\tau_p + (1-y)\tau_n]\Big]\rho^\beta \\
& + \frac{1}{8}t_5\Big[(2+x_5)\tau + (1+2x_5)[y\tau_p + (1-y)\tau_n]\Big]\rho^\gamma
\end{aligned} \tag{B.8}$$

B.2 Single particle properties

From the energy density the single particle spectrum can be derived. By performing functional variation of the energy density with respect to the single particle wavefunction, a modified Schrodinger equation can be

derived:

$$\delta\varepsilon_i = \Big[\frac{\delta\varepsilon_i}{\delta\tau_i} + \frac{\delta\varepsilon_i}{\delta\rho_i}\Big]\delta\phi_i = \epsilon_i\delta\phi_i \tag{B.9}$$

Since the Skyrme potential is at mostly quadratic in momenta with nonlinear density dependence, its effect is exactly included by effective mass and mean field shift(residual interaction), both density dependent:

$$\begin{aligned} \epsilon_i(k) &= \frac{\hbar^2 k^2}{2M_i^*} + U_i \\ \frac{\hbar^2}{2M_q^*} &\equiv \frac{\partial\varepsilon}{\partial\tau_q} \\ U_i &\equiv \frac{\partial\varepsilon}{\partial\rho_i} \end{aligned} \tag{B.10}$$

From eq. B.6 the effective baryon masses:

$$\begin{aligned} M_p^*/M &= \Big\{1 + \frac{M\ \rho}{4\hbar^2}\Big[a + 2\ y\ b + t_4[(2+x_4) - (1+2x_4)\ y]\rho^\beta + t_5[2 + x_5 + (1+2x_5)\ y]\rho^\gamma\Big]\Big\}^{-1} \\ M_n^*/M &= \Big\{1 + \frac{M\ \rho}{4\hbar^2}\Big[a + 2\ (1-y)\ b + t_4[(2+x_4) - (1+2x_4)\ (1-y)]\rho^\beta + t_5[2 + x_5 + (1+2x_5)\ (1-y)]\rho^\gamma\Big]\Big\}^{-1} \end{aligned} \tag{B.11}$$

and the residual potentials:

$$\begin{aligned} U_p &= \frac{1}{8}(2b\ \tau_p + a\ \tau) + \frac{1}{2}t_0[(2+x_0) - (1+2x_0)\ y]\rho \\ &\quad + \frac{1}{24}t_3\Big[4 + \alpha - 2y(1-(1-y)\alpha) + x_3(1-2y)[2-(1-2y)\alpha]\Big]\rho^{\alpha+1} \\ U_n &= \frac{1}{8}(2b\ \tau_n + a\ \tau) + \frac{1}{2}t_0[(1-x_0) + (1+2x_0)y]\rho \\ &\quad + \frac{1}{24}t_3\Big[2 + \alpha + 2y(1+\alpha-y\alpha) - x_3(1-2y)[2+(1-2y)\alpha]\Big]\rho^{\alpha+1} \end{aligned} \tag{B.12}$$

Appendix C

LVB Emissivity

The non-relativistic limit of the current products $(J^{(2)^\mu} J^{(2)}{}_\mu,\ J^{(4)^\mu} J^{(4)}{}_\mu)$, from 4.15, is quadratic and quartic respectively in baryon velocity. The difference is due to an anomaly in the scenario where all baryons can radiate, as the center of charge is also the center of mass and the dipole radiation vanishes and the leading term is quadrupole radiation. Another consequence of this difference is the dependence on $\theta_{\rm cm}$ as is shown here.

Due to the boson being massive, the 4-vector product differs from the usual expression for photons:

$$\begin{aligned}(\epsilon_\mu \tilde{J}^\mu)^2 &= -(g_{\mu\nu} - \frac{k_\mu k_\nu}{m_A^2})\tilde{J}^\mu \tilde{J}^\nu \\ &= -\tilde{J}_\mu \tilde{J}^\mu + (k_\mu \tilde{J}^\mu)^2/m_A^2\end{aligned} \tag{C.1}$$

where m_A is the mass of LVB.

The term proportional to the currents:

$$\begin{aligned}J^{(2)}_\mu J^{(2)\mu} &= -\Big[\frac{M^2}{(\mathbf{p}_1\cdot\mathbf{k})^2} + \frac{M^2}{(\mathbf{p}_3\cdot\mathbf{k})^2} - 2\frac{(\mathbf{p}_1\cdot\mathbf{p}_3)}{(\mathbf{p}_1\cdot\mathbf{k})(\mathbf{p}_3\cdot\mathbf{k})}\Big]\,, \\ J^{(4)}_\mu J^{(4)\mu} &= -\Big[\sum_{i=1}^{4}\frac{M^2}{(\mathbf{p}_i\cdot\mathbf{k})^2} + \frac{(\mathbf{p}_1\cdot\mathbf{p}_2)}{(\mathbf{p}_1\cdot\mathbf{k})(\mathbf{p}_2\cdot\mathbf{k})} + \frac{(\mathbf{p}_3\cdot\mathbf{p}_4)}{(\mathbf{p}_3\cdot\mathbf{k})(\mathbf{p}_4\cdot\mathbf{k})} - \sum_{i=1}^{2}\sum_{j=3}^{4}\frac{(\mathbf{p}_i\cdot\mathbf{p}_j)}{(\mathbf{p}_i\cdot\mathbf{k})(\mathbf{p}_j\cdot\mathbf{k})}\Big]\,,\end{aligned} \tag{C.2}$$

where, $M = 938.918$ MeV is the average baryon mass. Due to SRA, the scattering is almost elastic, and the mass dependent term does not contribute:

$$\begin{aligned}J^{(2)np}_\mu k^\mu &= \Big[\frac{\mathbf{p}_1\cdot\mathbf{k}}{\mathbf{p}_1\cdot\mathbf{k}} - \frac{\mathbf{p}_3\cdot\mathbf{k}}{\mathbf{p}_3\cdot\mathbf{k}}\Big] = 0\,, \\ J^{(4)np}_\mu k^\mu &= \Big[\frac{\mathbf{p}_1\cdot\mathbf{k}}{\mathbf{p}_1\cdot\mathbf{k}} + \frac{\mathbf{p}_2\cdot\mathbf{k}}{\mathbf{p}_2\cdot\mathbf{k}} - \frac{\mathbf{p}_3\cdot\mathbf{k}}{\mathbf{p}_3\cdot\mathbf{k}} - \frac{\mathbf{p}_4\cdot\mathbf{k}}{\mathbf{p}_4\cdot\mathbf{k}}\Big] = 0\,.\end{aligned} \tag{C.3}$$

In the non-relativistic limit, the velocities are defined as $\vec{v}_i = \vec{p}_i/M$ and energies are $E_i = M\sqrt{1+v_i^2} \approx M(1+v_i^2/2)$. The expansion of Eq. C.2 to leading order in velocities depends on the relative momentum of the incoming and

outgoing nucleons:

$$
\begin{aligned}
J^{(2)}_{\mu} J^{(2)\mu} &= \frac{1}{\omega^2}\Big\{\frac{(\vec{p}-\vec{p}\,')^2}{M^2} - \Big[\frac{(\vec{p}-\vec{p}\,')}{M}\cdot\frac{\vec{k}}{\omega}\Big]^2\Big\}, \\
J^{(4)}_{\mu} J^{(4)\mu} &= \frac{4}{\omega^2}\Big\{(\frac{\vec{p}\,'}{M}\cdot\frac{\vec{k}}{\omega})^2[\frac{p'^2}{M^2} + 2(\frac{\vec{p}}{M}\cdot\frac{\vec{k}}{\omega})^2] + \frac{p^2}{M^2}(\frac{\vec{p}}{M}\cdot\frac{\vec{k}}{\omega})^2 \\
&\qquad - \Big[\frac{(\vec{p}+\vec{p}\,')}{M}\cdot\frac{\vec{k}}{\omega}\Big]^4 - 2\frac{(\vec{p}\cdot\vec{p}\,')}{M^2}(\frac{\vec{p}}{M}\cdot\frac{\vec{k}}{\omega})(\frac{\vec{p}\,'}{M}\cdot\frac{\vec{k}}{\omega})\Big\},
\end{aligned}
\tag{C.4}
$$

where, $\vec{p} = \frac{1}{2}(\vec{p}_1 - \vec{p}_2)$, $\vec{p}\,' = \frac{1}{2}(\vec{p}_3 - \vec{p}_4)$, are the usual relative momenta in the center-of-mass frame.

In the soft limit $p = p'$. Performing the integration of the relative angles between the emitted LVB and the nucleons confirms the dipole and quadrupole radiation statement made earlier as can be seen in Eq. C.5.

$$
\begin{aligned}
\frac{\omega^2}{4\pi}\int d\Omega_{\omega} J^{(2)}_{\mu} J^{(2)\mu} &= 2\frac{E_{\rm CM}}{M}(1 - \frac{k^2}{3\omega^2})(1 - \cos\theta_{\rm CM}) \ , \\
\frac{\omega^2}{4\pi}\int d\Omega_{\omega} J^{(2)}_{\mu} J^{(4)\mu} &= \frac{8}{15}(\frac{E_{\rm CM}}{M})^2\frac{k^2}{3\omega^2}(5 - 2\frac{k^2}{3\omega^2})(1 - \cos^2\theta_{\rm CM}) \ .
\end{aligned}
\tag{C.5}
$$

Since in the $n-p$ scattering cross section only protons radiate (considering just the dark photon for now), it is dipole radiation, and its contribution is dominant in determining the rate of emission of dark photons. This rather simple feature has important consequences, as for LVBs cupled only to baryon number, there is only quadrupole radiation. The suppression of emission from quadrupole radiation provides weaker constraints on this type of LVBs with respect to the same ambient conditions, in comparison with for LVB coupled to electric charge. The final expressions in Eq. 4.15 are obtained by integrating Eq. C.5 over the radiated energy ω.

Appendix D

Unpolarized differential cross-section

The scattering amplitude in the helicity basis, $M^{s',s}_{m'_s,m_s}$, is described in detail in Ref. [260]. $\mathcal{T}$ is the Fourier transform of the T-matrix, which can be decomposed by spherical waves in the center-of-mass frame of reference:

$$\langle p|\mathcal{T}|p'\rangle = -\frac{4\pi\hbar^2}{(2\pi)^3 2M} f(p,p') = -\frac{\hbar^2}{(2\pi)^2 M} f(p,p') \tag{D.1}$$

For spin – 1/2 particles scattering, the wave function of the 2 particles system in center-of-mass frame is given in a similar fashion to that of spinless particles scattering:

$$\begin{aligned}
&\Psi^s_m(\vec{r}) \sim e^{ikz}\xi^s_m + \frac{e^{ikr}}{r}\sum_{s',m'_s}\xi^{s'}_{m'_s} M^{s',s'}_{m_s,m_s}(\theta,\phi)\\
&M^{s',s}_{m'_s,m_s}(\theta,\phi) = \sum_{l,J,l'}\sqrt{4\pi(2l+1)}Y^{l'}_{m_s-m'_s}(\theta,\phi)C^{l'\ s'\ J}_{m_s-m'_s\ \ m'_s\ \ m_s} C^{l\ \ s\ \ J}_{0\ \ m_s\ \ m_s}\frac{\langle l',s'|S^J-1|l,s\rangle}{2ip}\\
&S^J_{s=s'=1} = \begin{pmatrix} e^{2i\delta_1}\cos 2\epsilon_J & ie^{i(\delta_1+\delta_2)}\sin 2\epsilon_J \\ ie^{i(\delta_1+\delta_2)}\sin 2\epsilon_J & e^{2i\delta_1}\cos 2\epsilon_J \end{pmatrix},\ \delta_1 \equiv \delta_{l=l'=J-1,J}, \delta_2 \equiv \delta_{l=l'=J+1,J}\\
&S'^J_{s\neq s} = \begin{pmatrix} e^{2i\delta_l}\cos 2\gamma_l & ie^{i(\delta_l+\delta_{l,l})}\sin 2\gamma_l \\ ie^{i(\delta_l+\delta_{l,l})}\sin 2\gamma_l & e^{2i\delta_{l,l}}\cos 2\gamma_l \end{pmatrix},\ \delta_l \equiv \delta_{l=l'=J,s=0}, \delta_{l,l} \equiv \delta_{l=l'=J,s=1}\\
&= \begin{pmatrix} e^{2i\delta_l} & 0 \\ 0 & e^{2i\delta_{l,l}} \end{pmatrix}.
\end{aligned} \tag{D.2}$$

Here, we relate it to the unpolarized differential cross section needed for our calculations:

$$\frac{d\sigma^{el,un}}{d\Omega} = \frac{1}{4}\mathrm{Tr} M M^\dagger \tag{D.3}$$

From time-reversal invariance:

$$M^{1,1}_{1,1} = M^{1,1}_{-1,-1},\ M^{1,1}_{1,1} = M^{1,-1}_{-1,1},\ M^{1,1}_{0,1} = -M^{1,1}_{-1,0},\ M^{1,1}_{1,0} = -M^{1,1}_{0,-1}\ , \tag{D.4}$$

$$\frac{d\sigma}{d\Omega} = \frac{1}{4}\left\{2|M^{1,1}_{1,1}|^2 + |M^{1,1}_{0,0}|^2 + |M^{0,0}_{0,0}|^2 + 2|M^{1,1}_{1,0}|^2 + 2|M^{1,1}_{0,1}|^2 + 2|M^{1,1}_{1,-1}|^2\right\}\ . \tag{D.5}$$

Each matrix element can be expanded in partial wave basis as follows,

$$
\begin{aligned}
M^{0,0}_{0,0} =&(ip)^{-1}\sum_L P_L(\frac{L+1}{2})\alpha_{L,L}\ ,\\
M^{1,1}_{0,0} =&(ip)^{-1}\sum_L P_L\Big[(\frac{L+1}{2})\alpha_{L,L+1}+(\frac{L}{2})\alpha_{L,L-1}+\frac{\sqrt{(L+1)(l+2)}}{2}\alpha^{l+1}+\frac{\sqrt{L(L-1)}}{2}\alpha^{L-1}\Big]\ ,\\
M^{1,1}_{0,1} =&-(ip)^{-1}e^{i\phi}\sum_L P^1_L\Big[\frac{\sqrt{2}}{4}(\frac{2L+1}{L(L+1)})\alpha_{L,L}+\frac{\sqrt{2}}{4}(\frac{L-1}{L})\alpha_{L,L-1}-\frac{\sqrt{2}}{4}(\frac{L+2}{L+1})\alpha_{L,L+1}+\frac{\sqrt{2}}{4}\sqrt{\frac{L+2}{L+1}}\alpha^{L+1}\ ,\\
M^{1,1}_{1,0} =&-(ip)^{-1}e^{-i\phi}\sum_L P^1_L\Big[\frac{\sqrt{2}}{4}\alpha_{L,L+1}-\frac{\sqrt{2}}{4}\alpha_{L,L-1}+\frac{\sqrt{2}}{4}\sqrt{\frac{L+2}{L+1}}\alpha^{L+1}-\frac{\sqrt{2}}{4}\alpha^{L-1}\Big]\ ,\\
M^{1,1}_{1,-1} =&(ip)^{-1}e^{-2i\phi}\sum_L P^2_L\Big[\frac{\alpha_{L,L+1}}{4(L+1)}-\frac{2L+1}{4L(L+1)}\alpha_{L,L}+\frac{\alpha_{L,L-1}}{4L}-\frac{\alpha^{L+1}}{4\sqrt{(L+1)(L+2)}}-\frac{\alpha^{L-1}}{4\sqrt{L(L+1)}}\Big]\ .
\end{aligned}
\tag{D.6}
$$

The dependence on the phase shifts ($\delta^{S,L,J}$) is given below:

$$
\begin{aligned}
&\alpha_{J,J}=e^{2i\delta^{1,J,J}}-1\ ,\\
&\alpha_{J\pm1,J}=\cos(2\epsilon_J)e^{2i\delta^{1,\pm J,J}}-1\ ,\\
&\alpha^J=i\sin(2\epsilon_J)e^{i(\delta^{1,J+1,J}+\delta^{1,J-1,J})}\ ,\\
&\alpha_J=e^{2i\delta^{0,J,J}}-1\ .
\end{aligned}
\tag{D.7}
$$

For the p-p channel, the total matrix elements have to be antisymmetrized. This means that the spatial component has to be symmetrized for spin-singlet and anti-symmetrized for spin-triplet. So, the matrix elements squared and evaluated at $\phi=0$:

n-p channel:

$$
\begin{aligned}
|M^{0,0}_{0,0}|^2 =&p^{-2}\Big[\sum_L P^2_L(\eta)|\alpha^{0,L}_{0,0}|^2+2\sum_{L_1<L_2}P_{L_1}(\eta)P_{L_2}(\eta)\mathrm{Re}[\alpha^{0,L_1}_{0,0}\alpha^{*0,L_2}_{0,0}]\Big]\ ,\\
|M^{1,1}_{r,s}|^2 =&p^{-2}\Big[\sum_L P^2_L(\eta)|\alpha^{1,L}_{r,s}|^2+2\sum_{L_1<L_2}P_{L_1}(\eta)P_{L_2}(\eta)\mathrm{Re}[\alpha^{1,L_1}_{r,s}\alpha^{*1,L_2}_{r,s}]\Big]\ ,
\end{aligned}
\tag{D.8}
$$

p-p channel:

$$
\begin{aligned}
|M^{0,0}_{0,0}|^2 =&4p^{-2}\Big[\sum_{\mathrm{even},L} P^2_L(\eta)|\alpha^{0,L}_{0,0}|^2+2\sum_{\mathrm{even},L_1<L_2}P_{L_1}(\eta)P_{L_2}(\eta)\mathrm{Re}[\alpha^{0,L_1}_{0,0}\alpha^{*0,L_2}_{0,0}]\Big]\ ,\\
|M^{1,1}_{r,s}|^2 =&4p^{-2}\Big[\sum_{\mathrm{odd},L} P^2_L(\eta)|\alpha^{1,L}_{r,s}|^2+2\sum_{\mathrm{odd},L_1<L_2}P_{L_1}(\eta)P_{L_2}(\eta)\mathrm{Re}[\alpha^{1,L_1}_{r,s}\alpha^{*1,L_2}_{r,s}]\Big]\ ,
\end{aligned}
\tag{D.9}
$$

The complete expansion of the differential cross section in partial wave basis:

$$
\begin{aligned}
p^2\frac{d\sigma^{pp}}{d\Omega} =& \sum_{\text{even},L}(P_L^0)^2|\alpha_{0,0}^{0,L}|^2 + 2\sum_{\text{even},L_1<L_2} P_{L_1}^0 P_{L_2}^0 \mathrm{Re}[\alpha_{0,0}^{0,L_1}\alpha^{*0,L_2}_{0,0}] \\
&+ \sum_{\text{odd},L}\left[2(P_L^0)^2|\alpha_{1,1}^{1,L}|^2 + (P_L^0)^2|\alpha_{0,0}^{1,L}|^2 + 2(P_L^1)^2|\alpha_{0,1}^{1,L}|^2 + 2(P_L^1)^2|\alpha_{1,0}^{1,L}|^2 + 2(P_L^2)^2|\alpha_{1,-1}^{1,L}|^2\right] \\
&+ 2\sum_{\text{odd},L_1<L_2} 2P_{L_1}P_{L_2}\mathrm{Re}\left[\alpha_{1,1}^{1,L_1}\alpha^{*1,L_2}_{1,1}\right] + 2P_{L_1}^1P_{L_2}^1\mathrm{Re}\left[\alpha_{0,1}^{1,L_1}\alpha^{*1,L_2}_{0,1}\right] \\
&+ 2P_{L_1}^1P_{L_2}^1\mathrm{Re}\left[\alpha_{1,0}^{1,L_1}\alpha^{*1,L_2}_{1,0}\right] + P_{L_1}P_{L_2}\mathrm{Re}\left[\alpha_{0,0}^{1,L_1}\alpha^{*1,L_2}_{0,0}\right] + 2P_{L_1}^2P_{L_2}^2\mathrm{Re}\left[\alpha_{1,-1}^{1,L_1}\alpha^{*1,L_2}_{1,-1}\right] , \\
4p^2\frac{d\sigma^{np}}{d\Omega} =& \sum_{L}(P_L^0)^2|\alpha_{0,0}^{0,L}|^2 + 2\sum_{L_1<L_2} P_{L_1}^0 P_{L_2}^0 \mathrm{Re}[\alpha_{0,0}^{0,L_1}\alpha^{*0,L_2}_{0,0}] \\
&+ \sum_{L}\left[2(P_L^0)^2|\alpha_{1,1}^{1,L}|^2 + (P_L^0)^2|\alpha_{0,0}^{1,L}|^2 + 2(P_L^1)^2|\alpha_{0,1}^{1,L}|^2 + 2(P_L^1)^2|\alpha_{1,0}^{1,L}|^2 + 2(P_L^2)^2|\alpha_{1,-1}^{1,L}|^2\right] \\
&+ 2\sum_{L_1<L_2} 2P_{L_1}P_{L_2}\mathrm{Re}\left[\alpha_{1,1}^{1,L_1}\alpha^{*1,L_2}_{1,1}\right] + 2P_{L_1}^1P_{L_2}^1\mathrm{Re}\left[\alpha_{0,1}^{1,L_1}\alpha^{*1,L_2}_{0,1}\right] \\
&+ 2P_{L_1}^1P_{L_2}^1\mathrm{Re}\left[\alpha_{1,0}^{1,L_1}\alpha^{*1,L_2}_{1,0}\right] + P_{L_1}P_{L_2}\mathrm{Re}\left[\alpha_{0,0}^{1,L_1}\alpha^{*1,L_2}_{0,0}\right] + 2P_{L_1}^2P_{L_2}^2\mathrm{Re}\left[\alpha_{1,-1}^{1,L_1}\alpha^{*1,L_2}_{1,-1}\right] .
\end{aligned}
\tag{D.10}
$$

When performing angular integration, the following integral needs to be evaluated analytically:

$$
I_{l_1,\,l_2,\,l_3}^{m_1,m_2,m_3} \equiv \frac{1}{2}\int_{-1}^{1} P_{l_1}^{m_1}(x)P_{l_2}^{m_2}(x)P_{l_3}^{m_3}(x)dx \ . \tag{D.11}
$$

In our specific case, we need expression for $I_{l_1\ l_2\ l_3}^{m\ m\ 0}$, and $l_3 = \{0,1,2\}, (l_1+l_2)\mid 2$, and we provide the identities needed,

$$
\begin{aligned}
I_{l_1\ l_2\ 0}^{m\ m\ 0} =& \frac{(l_1+m)!}{(2l+1)(l_1-m)!}\delta_{l_1,l_2} \ , \\
I_{l_1\ l_2\ 1}^{m\ m\ 0}\Big|_{|l_1-l_2|\le 1} =& \frac{(-1)^{(l_1-l_2+1)/2}(l_2+m)!(l_1+l_2-1)!((l_1+l_2+1)/2)!}{(l_2-m)!((l_2-l_1+1)/2)!((l_1-l_2+1)/2)!((l_2+l_1-1)/2)!(l_2+l_1+2)!} \\
&\times \sum_{t=\mathrm{Max}(0,1-m-l_2)}^{\mathrm{Min}(1+l_2-m,l_1-m,1)} \frac{(-1)^t(l_1+t+m)!(l_2+1-m-t)!}{t!(l_1-m-t)!(l_2-1+m+t)!(1-t)!} \ , \\
I_{l_1\ l_2\ 1}^{m\ m\ 0}\Big|_{|l_1-l_2|>1} =& 0 \ , \\
I_{l_1\ l_2\ 2}^{m\ m\ 0}\Big|_{|l_1-l_2|\le 2} =& \frac{2(-1)^{(l_1-l_2)/2+1}(l_2+m)!(l_1+l_2-2)!((l_1+l_2)/2+1)!}{(l_2-m)!((l_2-l_1)/2+1)!((l_1-l_2)/2+1)!((l_2+l_1)/2-1)!(l_2+l_1+3)!} \\
&\times \sum_{t=\mathrm{Max}(0,2-m-l_2)}^{\mathrm{Min}(2+l_2-m,l_1-m,2)} \frac{(-1)^t(l_1+t+m)!(l_2+2-m-t)!}{t!(l_1-m-t)!(l_2-2+m+t)!(2-t)!} \ , \\
I_{l_1\ l_2\ 2}^{m\ m\ 0}\Big|_{|l_1-l_2|>2} =& 0 \ .
\end{aligned}
\tag{D.12}
$$

Appendix E

Dark photon Mean Free Path

The derivation of the mean free path is similar to the emissivity, with two main differences; there is no integration of the radiated energy, and the focus is on particle absorption and not energy loss (there is a factor of energy missing in comparison with Eqs. 4.8, 4.9. In the following equations we show the decay rate ($\Gamma = v_{\tilde{\gamma}}/\lambda$):

$$\Gamma_{np\to np\gamma_Q} = -\frac{2\pi}{\omega}\alpha_{\rm em}\epsilon_Q^2 \int \frac{d^3p_1}{(2E_1)(2\pi)^3} f_n(E_1) \int \frac{d^3p_2}{(2E_2)(2\pi)^3} f_p(E_2) \int d\Pi (\epsilon^\mu J_\mu^{(2)})^2 \; 32\pi E_{\rm cm}^2 \; v_{rel} \; \frac{d\sigma_{\rm np}(E_{\rm cm},\theta)}{d\theta_{\rm cm}} ,$$
$$\Gamma_{np\to np\gamma_B} = -\frac{2\pi}{\omega}\alpha_{\rm em}\epsilon_B^2 \int \frac{d^3p_1}{(2E_1)(2\pi)^3} f_n(E_1) \int \frac{d^3p_2}{(2E_2)(2\pi)^3} f_p(E_2) \int d\Pi (\epsilon^\mu J_\mu^{(4)})^2 \; 32\pi E_{\rm cm}^2 \; v_{rel} \; \frac{d\sigma_{\rm np}(E_{\rm cm},\theta)}{d\theta_{\rm cm}} .$$

The non-relativistic expansion of the currents to leading order in the expansion in powers of the radiated energy of the LVB, ω, has been performed in Appendix C, and after integrating over the angle between the center-of-mass momentum of one of the incoming nucleons and the momentum of the outgoing LVB we find

$$\begin{aligned} \frac{1}{4\pi}\int d\Omega \; L_\mu L^\mu \equiv & \frac{E_{\rm cm}}{M}\frac{\mathcal{J}^{(2)}}{\omega^2}(1-\cos\theta_{\rm cm}) , \\ \frac{1}{4\pi}\int d\Omega \; J_\mu J^\mu \equiv & \frac{E_{\rm cm}}{M}\frac{\mathcal{J}^{(4)}}{\omega^2}(1-\cos^2\theta_{\rm cm}) , \end{aligned} \tag{E.1}$$

where

$$\begin{aligned} \mathcal{J}^{(2)} = & 2(1-\frac{k^2}{3\omega^2}) , \\ \mathcal{J}^{(4)} = & \frac{8}{45}\;\frac{E_{\rm CM}}{M}\;\frac{k^2}{\omega^2}(5-\frac{2k^2}{3\omega^2} . \end{aligned} \tag{E.2}$$

The integration over initial states of the nucleons can be simplified when they are non-degenerate and we find that

$$\int \frac{d^3p_1}{(2\pi)^3}\int \frac{d^3p_2}{(2\pi)^3} \; f_i(E_1) f_j(E_2) = \frac{n_i n_j}{2\sqrt{\pi}\; T^{3/2}} \int dE_{\rm cm} \; e^{-E_{\rm cm}/T}\sqrt{E_{\rm cm}} . \tag{E.3}$$

Putting all these expressions back into expressions for the decay rate, the mean free paths in our work can be easily derived.

Bibliography

[1] D. Kobyakov and C. Pethick, "Dynamics of the inner crust of neutron stars: Hydrodynamics, elasticity, and collective modes," *Physical Review C*, vol. 87, no. 5, p. 055803, 2013. [Online]. Available: http://journals.aps.org/prc/abstract/10.1103/PhysRevC.87.055803

[2] R. Barbieri and T. E. O. Ericson, "Evidence Against the Existence of a Low Mass Scalar Boson from Neutron-Nucleus Scattering," *Phys. Lett.*, vol. B57, p. 270, 1975. [Online]. Available: http://dx.doi.org/10.1016/0370-2693(75)90073-8

[3] H. Leeb and J. Schmiedmayer, "Constraint on hypothetical light interacting bosons from low-energy neutron experiments," *Phys. Rev. Lett.*, vol. 68, pp. 1472–1475, 1992. [Online]. Available: http://dx.doi.org/10.1103/PhysRevLett.68.1472

[4] J. B. Dent, F. Ferrer, and L. M. Krauss, "Constraints on Light Hidden Sector Gauge Bosons from Supernova Cooling," 2012. [Online]. Available: https://arxiv.org/abs/1201.2683

[5] C. X. ray Center, "Stellar evolution poster," 2013. [Online]. Available: http://chandra.harvard.edu/edu/formal/stellar_ev/poster_horiz_med2.jpg

[6] H. C. Webster, "Possible existence of a neutron," *Nature*, vol. 129, pp. 402–402, March 1932. [Online]. Available: http://www.nature.com/nature/journal/v129/n3254/abs/129402b0.html

[7] H. Yukawa, "On the interaction of elementary particles. i," *Progress of Theoretical Physics Supplement*, vol. 1, pp. 1–10, 1955. [Online]. Available: http://ptps.oxfordjournals.org/content/1/1.1.short

[8] G. Cleaver, "Universe and multiverse, part 3," April 2012. [Online]. Available: http://biologos.org/blogs/archive/universe-and-multiverse-part-3

[9] H. D. Politzer, "Asymptotic freedom: An approach to strong interactions," *Physics Reports*, vol. 14, no. 4, pp. 129 – 180, 1974. [Online]. Available: http://www.sciencedirect.com/science/article/pii/0370157374900143

[10] P. Hohenberg and W. Kohn, "Inhomogeneous electron gas," *Phys. Rev.*, vol. 136, pp. B864–B871, Nov 1964. [Online]. Available: http://link.aps.org/doi/10.1103/PhysRev.136.B864

[11] H. A. Bethe, "Supernova mechanisms," *Rev. Mod. Phys.*, vol. 62, pp. 801–866, Oct 1990. [Online]. Available: http://link.aps.org/doi/10.1103/RevModPhys.62.801

[12] H. T. Janka, K. Langanke, A. Marek, G. Martínez-Pinedo, and B. Müller, "Theory of core-collapse supernovae," *Physics Reports*, vol. 442, no. 1–6, pp. 38 – 74, 2007, the Hans Bethe Centennial Volume 1906-2006. [Online]. Available: http://www.sciencedirect.com/science/article/pii/S0370157307000439

[13] B. Müller, H.-T. J., and A. Marek, "A new multi-dimensional general relativistic neutrino hydrodynamics code for core-collapse supernovae. ii. relativistic explosion models of core-collapse supernovae," *The Astrophysical Journal*, vol. 756, no. 1, p. 84, 2012. [Online]. Available: http://stacks.iop.org/0004-637X/756/i=1/a=84

[14] R. C. Duncan, S. L. Shapiro, and I. Wasserman, "Neutrino-driven winds from young, hot neutron stars," *ApJ* , vol. 309, pp. 141–160, oct 1986. [Online]. Available: http://adsabs.harvard.edu/abs/1986ApJ...309..141D

[15] A. Arcones and T. F. K., "Neutrino-driven wind simulations and nucleosynthesis of heavy elements," *Journal of Physics G: Nuclear and Particle Physics*, vol. 40, no. 1, p. 013201, 2013. [Online]. Available: http://stacks.iop.org/0954-3899/40/i=1/a=013201

[16] Y. Z. Qian and S. E. Woosley, "Nucleosynthesis in neutrino-driven winds. i. the physical conditions," *The Astrophysical Journal*, vol. 471, no. 1, p. 331, 1996. [Online]. Available: http://stacks.iop.org/0004-637X/471/i=1/a=331

[17] R. D. Hoffman, S. E. Woosley, and Y. Z. Qian, "Nucleosynthesis in neutrino-driven winds. ii. implications for heavy element synthesis," *The Astrophysical Journal*, vol. 482, no. 2, p. 951, 1997. [Online]. Available: http://stacks.iop.org/0004-637X/482/i=2/a=951

[18] K. Otsuki, H. Tagoshi, and T. W. S. Kajino, "General relativistic effects on neutrino-driven winds from young, hot neutron stars and r-process nucleosynthesis," *The Astrophysical Journal*, vol. 533, no. 1, p. 424, 2000. [Online]. Available: http://stacks.iop.org/0004-637X/533/i=1/a=424

[19] T. A. Thompson, A. Burrows, and B. S. Meyer, "The physics of protoneutron star winds: implications for r-process nucleosynthesis," *Astrophys. J.*, vol. 562, p. 887, 2001. [Online]. Available: http://iopscience.iop.org/article/10.1086/323861/meta;jsessionid=CC0B1CC55669499322C7CDA60012B547.c2.iopscience.cld.iop.org

[20] Arcones, A., Janka, H.-Th., and Scheck, L., "Nucleosynthesis-relevant conditions in neutrino-driven supernova outflows," *A&A*, vol. 467, no. 3, pp. 1227–1248, 2007. [Online]. Available: http://www.aanda.org/articles/aa/abs/2007/21/aa6983-06/aa6983-06.html

[21] K. Kuroda, T.and Wanajo S.and Nomoto, "The r-process in supersonic neutrino-driven winds: The role of the wind termination shock," *The Astrophysical Journal*, vol. 672, no. 2, p. 1068, 2008. [Online]. Available: http://stacks.iop.org/0004-637X/672/i=2/a=1068

[22] R. L. F., S. E. Woosley, and R. D. Hoffman, "Integrated nucleosynthesis in neutrino-driven winds," *The Astrophysical Journal*, vol. 722, no. 1, p. 954, 2010. [Online]. Available: http://stacks.iop.org/0004-637X/722/i=1/a=954

[23] F. Arcones, A.and Montes, "Production of light-element primary process nuclei in neutrino-driven winds," *The Astrophysical Journal*, vol. 731, no. 1, p. 5, 2011. [Online]. Available: http://stacks.iop.org/0004-637X/731/i=1/a=5

[24] M. T. Keil, G. G. Raffelt, and H.-T. Janka, "Monte carlo study of supernova neutrino spectra formation," *The Astrophysical Journal*, vol. 590, no. 2, p. 971, 2003. [Online]. Available: http://stacks.iop.org/0004-637X/590/i=2/a=971

[25] C. Fröhlich, P. Hauser, M. Liebendörfer, G. Martinez-Pinedo, F.-K. Thielemann, E. Bravo, N. T. Zinner, W. R. Hix, K. Langanke, A. Mezzacappa, and K. Nomoto, "Composition of the innermost core-collapse supernova ejecta," *The Astrophysical Journal*, vol. 637, no. 1, p. 415, 2006. [Online]. Available: http://stacks.iop.org/0004-637X/637/i=1/a=415

[26] G. Maartinez-Pinedo, "Selected topics in nuclear astrophysics," *The European Physical Special Topics*, vol. 156, no. 1, pp. 123–149, 2008. [Online]. Available: http://link.springer.com/article/10.1140%2Fepjst%2Fe2008-00611-5

[27] G. Martínez-Pinedo, T. Fischer, A. Lohs, and L. Huther, "Charged-current weak interaction processes in hot and dense matter and its impact on the spectra of neutrinos emitted from protoneutron star cooling," *Phys. Rev. Lett.*, vol. 109, p. 251104, Dec 2012. [Online]. Available: http://link.aps.org/doi/10.1103/PhysRevLett.109.251104

[28] L. F. Roberts, "A new code for proto-neutron star evolution," *The Astrophysical Journal*, vol. 755, no. 2, p. 126, 2012. [Online]. Available: http://stacks.iop.org/0004-637X/755/i=2/a=126

[29] L. F. Roberts, S. Reddy, and G. Shen, "Medium modification of the charged-current neutrino opacity and its implications," *Phys. Rev. C*, vol. 86, p. 065803, Dec 2012. [Online]. Available: http://link.aps.org/doi/10.1103/PhysRevC.86.065803

[30] S. Reddy, M. Prakash, and J. M. Lattimer, "Neutrino interactions in hot and dense matter," *Phys. Rev. D*, vol. 58, p. 013009, May 1998. [Online]. Available: http://link.aps.org/doi/10.1103/PhysRevD.58.013009

[31] A. Burrows and R. F. Sawyer, "Effects of correlations on neutrino opacities in nuclear matter," *Phys. Rev. C*, vol. 58, pp. 554–571, Jul 1998. [Online]. Available: http://link.aps.org/doi/10.1103/PhysRevC.58.554

[32] ——, "Many-body corrections to charged-current neutrino absorption rates in nuclear matter," *Phys. Rev. C*, vol. 59, pp. 510–514, Jan 1999. [Online]. Available: http://link.aps.org/doi/10.1103/PhysRevC.59.510

[33] S. Reddy, M. Prakash, J. M. Lattimer, and J. A. Pons, "Effects of strong and electromagnetic correlations on neutrino interactions in dense matter," *Phys. Rev. C*, vol. 59, pp. 2888–2918, May 1999. [Online]. Available: http://link.aps.org/doi/10.1103/PhysRevC.59.2888

[34] L. F. Roberts, G. Shen, V. Cirigliano, J. A. Pons, S. Reddy, and S. E. Woosley, "Protoneutron star cooling with convection: The effect of the symmetry energy," *Phys. Rev. Lett.*, vol. 108, p. 061103, Feb 2012. [Online]. Available: http://link.aps.org/doi/10.1103/PhysRevLett.108.061103

[35] L. Hüdepohl, B. Müller, H.-T. Janka, A. Marek, and G. G. Raffelt, "Neutrino signal of electron-capture supernovae from core collapse to cooling," *Phys. Rev. Lett.*, vol. 104, p. 251101, Jun 2010. [Online]. Available: http://link.aps.org/doi/10.1103/PhysRevLett.104.251101

[36] M. Sanjay, R.and Prakash, J. M. Lattimer, and J. A. Pons, "Effects of strong and electromagnetic correlations on neutrino interactions in dense matter," *Phys. Rev. C*, vol. 59, pp. 2888–2918, 1999. [Online]. Available: http://adsabs.harvard.edu/abs/1999PhRvC..59.2888R

[37] J. A. Pons, M. Reddy, S.and Prakash, and J. A. Lattimer, J. M.and Miralles, "Evolution of proto-neutron stars," *The Astrophysical Journal*, vol. 513, no. 2, p. 780, 1999. [Online]. Available: http://stacks.iop.org/0004-637X/513/i=2/a=780

[38] H. Duan, G. M. Fuller, J. Carlson, and Y.-Z. Qian, "Simulation of coherent nonlinear neutrino flavor transformation in the supernova environment: Correlated neutrino trajectories," *Phys. Rev. D*, vol. 74, p. 105014, Nov 2006. [Online]. Available: http://link.aps.org/doi/10.1103/PhysRevD.74.105014

[39] H. Duan and A. Friedland, "Self-induced suppression of collective neutrino oscillations in a supernova," *Phys. Rev. Lett.*, vol. 106, p. 091101, Mar 2011. [Online]. Available: http://link.aps.org/doi/10.1103/PhysRevLett.106.091101

[40] S. Weinberg, "Phenomenological lagrangians," *Physica A Statistical Mechanics and its Applications*, vol. 96, pp. 327–340, apr 1979. [Online]. Available: http://adsabs.harvard.edu/abs/1979PhyA...96..327W

[41] H. Georgi, *Lie algebras in particle physics. From isosipn to unified theories.*, 1982, vol. 54.

[42] K. Nakamura and et al., "The review of particle physics," *J. Phys. G*, vol. 37, 2010. [Online]. Available: http://iopscience.iop.org/article/10.1088/0954-3899/37/7A/075021/meta

[43] S. Scherer and M. R. Schindler, "A chiral perturbation theory primer," 2005. [Online]. Available: http://arxiv.org/abs/hep-ph/0505265

[44] S. Coleman, J. Wess, and B. Zumino, "Structure of phenomenological lagrangians. i," *Phys. Rev.*, vol. 177, pp. 2239–2247, Jan 1969. [Online]. Available: http://link.aps.org/doi/10.1103/PhysRev.177.2239

[45] C. G. Callan, S. Coleman, J. Wess, and B. Zumino, "Structure of phenomenological lagrangians. ii," *Phys. Rev.*, vol. 177, pp. 2247–2250, Jan 1969. [Online]. Available: http://link.aps.org/doi/10.1103/PhysRev.177.2247

[46] J. Gasser, S. M.E., and A. Švarc, "Nucleons with chiral loops," *Nuclear Physics B*, vol. 307, no. 4, pp. 779 – 853, 1988. [Online]. Available: http://www.sciencedirect.com/science/article/pii/0550321388901083

[47] V. Bernard, N. Kaiser, J. Kambor, and U. Meißner, "Chiral structure of the nucleon," *Nuclear Physics B*, vol. 388, no. 2, pp. 315–345, 1992. [Online]. Available: http://www.sciencedirect.com/science/article/pii/055032139290615I

[48] V. Bernard, N. Kaiser, and U. Meissner, "Chiral dynamics in nucleons and nuclei," *International Journal of Modern Physics E*, vol. 4, no. 02, pp. 193–344, 1995. [Online]. Available: http://www.worldscientific.com/doi/abs/10.1142/S0218301395000092

[49] E. Jenkins and A. V. Manohar, "Chiral corrections to the baryon axial currents," *Physics Letters B*, vol. 259, no. 3, pp. 353 – 358, 1991. [Online]. Available: http://www.sciencedirect.com/science/article/pii/037026939190840M

[50] H. Georgi, "An effective field theory for heavy quarks at low-energies," *Phys. Lett.*, vol. B240, pp. 447–450, 1990. [Online]. Available: http://www.sciencedirect.com/science/article/pii/037026939091128X

[51] S. Weinberg, "Nuclear forces from chiral lagrangians."

[52] ——, "Effective chiral lagrangians for nucleon-pion interactions and nuclear forces," *Phys. Lett. B*, vol. 363, p. 3, 1991. [Online]. Available: http://www.sciencedirect.com/science/article/pii/055032139190231L

[53] S. Weinberg, "Three-body interactions among nucleons and pions," *Phys. Lett. B*, vol. 295, p. 114, 1992. [Online]. Available: http://www.sciencedirect.com/science/article/pii/037026939290099P

[54] E. Epelbaum, "Nuclear forces from chiral effective field theory: A primer," 2010. [Online]. Available: http://inspirehep.net/record/843247/files/arXiv:1001.3229.pdf

[55] R. Machleidt and D. R. Entem, "Chiral effective field theory and nuclear forces," *Phys. Rept.*, vol. 503, pp. 1–75, 2011. [Online]. Available: http://www.sciencedirect.com/science/article/pii/S0370157311000457

[56] D. B. Kaplan, M. J. Savage, and M. B. Wise, "A new expansion for nucleon-nucleon interactions," *Physics Letters B*, vol. 424, no. 3, pp. 390–396, 1998. [Online]. Available: http://www.sciencedirect.com/science/article/pii/S037026939800210X

[57] ——, "Two-nucleon systems from effective field theory," *Nuclear Physics B*, vol. 534, no. 1, pp. 329–355, 1998. [Online]. Available: http://www.sciencedirect.com/science/article/pii/S0550321398004404

[58] B. A. Lippmann and J. Schwinger, "Variational principles for scattering processes. i," *Phys. Rev.*, vol. 79, pp. 469–480, Aug 1950. [Online]. Available: http://link.aps.org/doi/10.1103/PhysRev.79.469

[59] T. D. Cohen and J. M. Hansen, "Low energy theorems for nucleon-nucleon scattering," *Phys. Rev. C*, vol. 59, pp. 13–20, Jan 1999. [Online]. Available: http://link.aps.org/doi/10.1103/PhysRevC.59.13

[60] ——, "Testing low energy theorems in nucleon-nucleon scattering," *Phys. Rev. C*, vol. 59, pp. 3047–3051, Jun 1999. [Online]. Available: http://link.aps.org/doi/10.1103/PhysRevC.59.3047

[61] T. Fleming, S.and Mehen and I. W. Stewart, "Nnlo corrections to nucleon–nucleon scattering and perturbative pions," *Nuclear Physics A*, vol. 677, no. 1, pp. 313 – 366, 2000. [Online]. Available: http://www.sciencedirect.com/science/article/pii/S0375947400002219

[62] D. R. Entem and R. Machleidt, "Accurate charge-dependent nucleon-nucleon potential at fourth order of chiral perturbation theory," *Phys. Rev. C*, vol. 68, no. 4, p. 041001, oct 2003. [Online]. Available: http://journals.aps.org/prc/abstract/10.1103/PhysRevC.68.041001

[63] G. D. Mahan, *Many-Particle Physics*, 2nd ed. New York, N.Y.: Plenum, 1993.

[64] C. J. Horowitz and A. Schwenk, "Cluster formation and the virial equation of state of low-density nuclear matter," *Nucl. Phys. A*, vol. 776, pp. 55–79, 2006. [Online]. Available: http://www.sciencedirect.com/science/article/pii/S0375947406002132

[65] ——, "The Virial equation of state of low-density neutron matter," *Phys. Lett. B*, vol. 638, pp. 153–159, 2006. [Online]. Available: http://www.sciencedirect.com/science/article/pii/S0370269306006599

[66] N. Fukuda and R. G. Newton, "Energy level shifts in a large enclosure."

[67] W. B. Riesenfeld and K. M. Watson, "Energy of a many-particle system," *Phys. Rev.*, vol. 104, p. 492, 1956. [Online]. Available: http://journals.aps.org/pr/abstract/10.1103/PhysRev.104.492

[68] G. Röpke, "Light nuclei quasiparticle energy shifts in hot and dense nuclear matter," *Phys. Rev. C*, vol. 79, p. 014002, Jan 2009. [Online]. Available: http://link.aps.org/doi/10.1103/PhysRevC.79.014002

[69] S. Typel, G. Röpke, T. Klähn, D. Blaschke, and H. H. Wolter, "Composition and thermodynamics of nuclear matter with light clusters," *Phys. Rev. C*, vol. 81, p. 015803, Jan 2010. [Online]. Available: http://link.aps.org/doi/10.1103/PhysRevC.81.015803

[70] M. Hempel, J. Schaffner-Bielich, S. Typel, and G. Röpke, "Light Clusters in Nuclear Matter: Excluded Volume versus Quantum Many-Body Approaches," *Phys. Rev. C*, vol. 84, p. 055804, 2011. [Online]. Available: http://journals.aps.org/prc/abstract/10.1103/PhysRevC.84.055804

[71] V. G. J. Stoks, R. A. M. Klomp, M. C. M. Rentmeester, and J. J. de Swart, *Phys. Rev. C*, vol. 48, p. 792, 1993. [Online]. Available: http://nn-online.org

[72] L. F. Roberts, S. Reddy, and G. Shen, "Medium modification of the charged-current neutrino opacity and its implications," *Phys. Rev. C*, vol. 86, no. 6, p. 065803, dec 2012. [Online]. Available: http://adsabs.harvard.edu/abs/2012PhRvC..86f5803R

[73] G. Martínez-Pinedo, T. Fischer, A. Lohs, and L. Huther, "Charged-Current Weak Interaction Processes in Hot and Dense Matter and its Impact on the Spectra of Neutrinos Emitted from Protoneutron Star Cooling," *Phys. Rev. Lett.*, vol. 109, no. 25, p. 251104, dec 2012. [Online]. Available: http://adsabs.harvard.edu/abs/2012PhRvL.109y1104M

[74] N. K. Glendenning and S. A. Moszkowski, "Reconciliation of neutron-star masses and binding of the lambda in hypernuclei," *Phys. Rev. Lett.*, vol. 67, pp. 2414–1417, 1991. [Online]. Available: http://adsabs.harvard.edu/abs/1991PhRvL..67.2414G

[75] F. J. Fattoyev, C. J. Horowitz, J. Piekarewicz, and G. Shen, "Relativistic effective interaction for nuclei, giant resonances, and neutron stars," *Phys. Rev. C*, vol. 82, no. 5, pp. 055 803–+, 2010. [Online]. Available: http://adsabs.harvard.edu/abs/2010PhRvC..82e5803F

[76] G. Martínez-Pinedo, T. Fischer, and L. Huther, "Supernova neutrinos and nucleosynthesis," *J. Phys. G.*, vol. 41, no. 4, p. 044008, 2014. [Online]. Available: http://iopscience.iop.org/article/10.1088/0954-3899/41/4/044008

[77] A. Burrows and R. F. Sawyer, "Many-body corrections to charged-current neutrino absorption rates in nuclear matter," *Phys. Rev. C*, vol. 59, pp. 510–514, jan 1999. [Online]. Available: http://adsabs.harvard.edu/abs/1999PhRvC..59..510B

[78] C. J. Horowitz, "Weak magnetism for antineutrinos in supernovae," *Phys. Rev. D*, vol. 65, no. 4, p. 043001, feb 2002. [Online]. Available: http://adsabs.harvard.edu/abs/2002PhRvD..65d3001H

[79] C. J. Horowitz and G. Li, "Charge-conjugation violating neutrino interactions in supernovae," *Phys. Rev. D*, vol. 61, no. 6, p. 063002, Feb 2000. [Online]. Available: http://journals.aps.org/prd/abstract/10.1103/PhysRevD.61.063002

[80] S. Hannestad and G. Raffelt, "Supernova Neutrino Opacity from Nucleon-Nucleon Bremsstrahlung and Related Processes," *Astrophys. J.*, vol. 507, pp. 339–352, nov 1998. [Online]. Available: http://adsabs.harvard.edu/abs/1998ApJ...507..339H

[81] A. Bartl, C. Pethick, and A. Schwenk, "Supernova matter at subnuclear densities as a resonant Fermi gas: Enhancement of neutrino rates," *Phys. Rev. Lett.*, vol. 113, p. 081101, 2014. [Online]. Available: http://journals.aps.org/prl/abstract/10.1103/PhysRevLett.113.081101

[82] J. M. Lattimer and M. Prakash, "The physics of neutron stars," *Science*, vol. 304, no. 5670, pp. 536–542, 2004. [Online]. Available: http://science.sciencemag.org/content/304/5670/536

[83] A. Steiner, L. J. M., and E. F. Brown, "The neutron star mass-radius relation and the equation of state of dense matter," *Astrophy. J.*, vol. 765, no. 1, p. L5, 2013. [Online]. Available: http://stacks.iop.org/2041-8205/765/i=1/a=L5

[84] F. Özel, "Surface emission from neutron stars and implications for the physics of their interiors," *Rept. Prog. Phys.*, vol. 76, no. 1, p. 016901, 2013. [Online]. Available: http://stacks.iop.org/0034-4885/76/i=1/a=016901

[85] P. B. Demorest, T. Pennucci, S. M. Ransom, M. S. E. Roberts, and J. W. T. Hessels, "A two-solar-mass neutron star measured using Shapiro delay," *Nature*, vol. 467, p. 1081, Oct 2010. [Online]. Available: http://www.nature.com/nature/journal/v467/n7319/abs/nature09466.html

[86] J. Antoniadis and et al, "A massive pulsar in a compact relativistic binary," *Science*, vol. 340, p. 6131, 2013. [Online]. Available: http://science.sciencemag.org/content/340/6131/1233232

[87] P. Danielewicz, R. Lacey, and W. Lynch, "Determination of the equation of state of dense matter," *Science*, vol. 298, p. 1592, 2002. [Online]. Available: http://science.sciencemag.org/content/298/5598/1592

[88] M. Dutra, O. Lourenço, J. S. Sá Martins, A. Delfino, J. R. Stone, and P. D. Stevenson, "Skyrme interaction and nuclear matter constraints," *Phys. Rev. C*, vol. 85, p. 035201, Mar 2012. [Online]. Available: http://link.aps.org/doi/10.1103/PhysRevC.85.035201

[89] K. Hebeler, J. M. Lattimer, C. J. Pethick, and A. Schwenk, "Constraints on Neutron Star Radii Based on Chiral Effective Field Theory Interactions," *Phys. Rev. Lett.*, vol. 105, no. 16, p. 161102, oct 2010. [Online]. Available: http://adsabs.harvard.edu/abs/2010PhRvL.105p1102H

[90] S. Gandolfi, J. Carlson, and S. Reddy, "Maximum mass and radius of neutron stars, and the nuclear symmetry energy," *Phys. Rev. C*, vol. 85, p. 032801, Mar 2012. [Online]. Available: http://link.aps.org/doi/10.1103/PhysRevC.85.032801

[91] T. Krüger, I. Tews, K. Hebeler, and A. Schwenk, "Neutron matter from chiral effective field theory interactions," *Phys. Rev. C*, vol. 88, p. 025802, 2013. [Online]. Available: http://journals.aps.org/prc/abstract/10.1103/PhysRevC.88.025802

[92] A. Roggero, A. Mukherjee, and F. Pederiva, "Quantum Monte Carlo Calculations of Neutron Matter with Nonlocal Chiral Interactions," *Phys. Rev. Lett.*, vol. 112, p. 221103, Jun 2014. [Online]. Available: http://link.aps.org/doi/10.1103/PhysRevLett.112.221103

[93] G. Wlazłowski, J. W. Holt, A. Moroz, S.and Bulgac, and K. Roche, "Auxiliary-field quantum monte carlo simulations of neutron matter in chiral effective field theory," *Phys. Rev. Lett.*, vol. 113, p. 182503, 2014. [Online]. Available: http://journals.aps.org/prl/abstract/10.1103/PhysRevLett.113.182503

[94] I. Tews, S. Gandolfi, A. Gezerlis, and S. A., "Quantum monte carlo calculations of neutron matter with chiral three-body forces," *Phy. Rev. C*, 2015. [Online]. Available: http://journals.aps.org/prc/abstract/10.1103/PhysRevC.93.024305

[95] J. Lattimer and D. Swesty, "A generalized equation of state for hot, dense matter."

[96] H. Shen, H. Toki, and K. Oyamatsu, K.and Sumiyoshi, "Relativistic equation of state of nuclear matter for supernova explosion," *Nucl. Phys.*, vol. A637, p. 435, 1998. [Online]. Available: http://ptp.oxfordjournals.org/content/100/5/1013.short

[97] T. S.-B. J. Hempel, M.and Fischer and M. Liebendorfer, "New equations of state in simulations of core-collapse supernovae," *Astrophys. J.*, vol. 748, p. 70, 2012. [Online]. Available: http://adsabs.harvard.edu/abs/2011arXiv1108.0848H

[98] M. Lüscher, "Volume dependence of the energy spectrum in massive quantum field theories. ii. scattering states," *Comm. Math. Phys.*, vol. 105, no. 2, pp. 153–188, 1986. [Online]. Available: http://projecteuclid.org/euclid.cmp/1104115329

[99] L. Maiani and M. Testa, "Final state interactions from euclidean correlation functions," *Physics Letters B*, vol. 245, no. 3, pp. 585 – 590, 1990. [Online]. Available: http://www.sciencedirect.com/science/article/pii/0370269390906953

[100] M. Lüscher, "Two-particle states on a torus and their relation to the scattering matrix," *Nuclear Physics B*, vol. 354, no. 2, pp. 531 – 578, 1991. [Online]. Available: http://www.sciencedirect.com/science/article/pii/0550321391903666

[101] M. Fukugita, Y. Kuramashi, M. Okawa, H. Mino, and A. Ukawa, "Hadron scattering lengths in lattice qcd," *Phys. Rev. D*, vol. 52, pp. 3003–3023, Sep 1995. [Online]. Available: http://link.aps.org/doi/10.1103/PhysRevD.52.3003

[102] S. R. Beane, P. F. Bedaque, K. Orginos, and M. J. Savage, "Nucleon-nucleon scattering from fully dynamical lattice qcd," *Phys. Rev. Lett.*, vol. 97, p. 012001, Jul 2006. [Online]. Available: http://link.aps.org/doi/10.1103/PhysRevLett.97.012001

[103] S. R. Beane and NPLQCD collaboration, "Evidence for a bound h-dibaryon from lattice qcd," *Phys. Rev. Lett.*, vol. 106, p. 162001, 2011. [Online]. Available: http://journals.aps.org/prl/abstract/10.1103/PhysRevLett.106.162001

[104] T. Yamazaki, Y. Kuramashi, and A. Ukawa, "Helium nuclei in quenched lattice qcd," *Phys. Rev. D*, vol. 81, p. 111504, Jun 2010. [Online]. Available: http://link.aps.org/doi/10.1103/PhysRevD.81.111504

[105] S. Aoki, "Hadron interactions in lattice QCD," *Prog. Part. Nucl. Phys.*, vol. 66, pp. 687–726, Oct. 2011. [Online]. Available: http://adsabs.harvard.edu/abs/2011PrPNP..66..687A

[106] I. Takashi and HAL QCD collaboration, "Bound h dibaryon in flavor su(3) limit of lattice qcd," *Phys. Rev. Lett.*, vol. 106, p. 162002, Apr 2011. [Online]. Available: http://link.aps.org/doi/10.1103/PhysRevLett.106.162002

[107] S. Aoki, "Nucleon-nucleon interactions via Lattice QCD: Methodology. HAL QCD approach to extract hadronic interactions in lattice QCD," *Eur. Phys. J. A*, vol. 49, p. 81, Jul. 2013. [Online]. Available: http://adsabs.harvard.edu/abs/2013EPJA...49...81A

[108] M. J. Savage, "Nuclear physics from lattice QCD," *Prog. Part. Nucl. Phys.*, vol. 67, pp. 140–152, Apr. 2012. [Online]. Available: http://adsabs.harvard.edu/abs/2012PrPNP..67..140S

[109] I. Takashi and HAL QCD collaboration, "Equation of State for Nucleonic Matter and its Quark Mass Dependence from the Nuclear Force in Lattice QCD," *Phys. Rev. Lett.*, vol. 111, p. 112503, Sep 2013. [Online]. Available: http://link.aps.org/doi/10.1103/PhysRevLett.111.112503

[110] E. Epelbaum, H.-W. Hammer, and U.-G. Meißner, "Modern theory of nuclear forces," *Rev. Mod. Phys.*, vol. 81, pp. 1773–1825, Oct. 2009. [Online]. Available: http://adsabs.harvard.edu/abs/2009RvMP...81.1773E

[111] N. Kalantar-Nayestanaki, E. Epelbaum, J. G. Messchendorp, and A. Nogga, "Signatures of three-nucleon interactions in few-nucleon systems," *Rep. Prog. Phys.*, vol. 75, no. 1, p. 016301, 2012. [Online]. Available: http://stacks.iop.org/0034-4885/75/i=1/a=016301

[112] B. R. Barrett, P. Navrátil, and J. P. Vary, "Ab initio no core shell model," *Prog. Part. Nucl. Phys.*, vol. 69, no. 0, pp. 131–181, 2013. [Online]. Available: http://www.sciencedirect.com/science/article/pii/S0146641012001184

[113] R. Roth, J. Langhammer, A. Calci, S. Binder, and P. Navrátil, "Similarity-Transformed Chiral NN+3N Interactions for the Ab Initio Description of C12 and O16," *Phys. Rev. Lett.*, vol. 107, no. 7, p. 072501, Aug. 2011. [Online]. Available: http://adsabs.harvard.edu/abs/2011PhRvL.107g2501R

[114] H. Hergert, S. K. Bogner, S. Binder, A. Calci, J. Langhammer, R. Roth, and A. Schwenk, "In-medium similarity renormalization group with chiral two- plus three-nucleon interactions," *Phys. Rev. C*, vol. 87, no. 3, p. 034307, mar 2013. [Online]. Available: http://adsabs.harvard.edu/abs/2013PhRvC..87c4307H

[115] G. Hagen, M. Hjorth-Jensen, G. R. Jansen, R. Machleidt, and T. Papenbrock, "Evolution of Shell Structure in Neutron-Rich Calcium Isotopes," *Phys. Rev. Lett.*, vol. 109, no. 3, p. 032502, Jul. 2012. [Online]. Available: http://adsabs.harvard.edu/abs/2012PhRvL.109c2502H

[116] T. Otsuka, T. Suzuki, J. D. Holt, A. Schwenk, and Y. Akaishi, "Three-Body Forces and the Limit of Oxygen Isotopes," *Phys. Rev. Lett.*, vol. 105, no. 3, p. 032501, Jul. 2010. [Online]. Available: http://adsabs.harvard.edu/abs/2010PhRvL.105c2501O

[117] J. D. Holt, T. Otsuka, A. Schwenk, and T. Suzuki, "Three-body forces and shell structure in calcium isotopes," *J. Phys. G*, vol. 39, no. 8, p. 085111, Aug. 2012. [Online]. Available: http://adsabs.harvard.edu/abs/2012JPhG...39h5111H

[118] V. Somà, C. Barbieri, and T. Duguet, "Ab initio Gorkov-Green's function calculations of open-shell nuclei," *Phys. Rev. C*, vol. 87, no. 1, p. 011303, Jan. 2013. [Online]. Available: http://adsabs.harvard.edu/abs/2013PhRvC..87a1303S

[119] F. Wienholtz, D. Beck, K. Blaum, C. Borgmann, M. Breitenfeldt, R. Cakirli, S. George, F. Herfurth, J. Holt, M. Kowalska *et al.*, "Masses of exotic calcium isotopes pin down nuclear forces," *Nature*, vol. 498, no. 7454, pp. 346–349, 2013. [Online]. Available: http://www.nature.com/nature/journal/v498/n7454/full/nature12226.html

[120] A. Ekström, G. R. Jansen, K. A. Wendt, G. Hagen, T. Papenbrock, B. D. Carlsson, C. Forssén, M. Hjorth-Jensen, P. Navrátil, and W. Nazarewicz, "Accurate nuclear radii and binding energies from a chiral interaction," *Phys. Rev. C*, vol. 91, p. 051301, May 2015. [Online]. Available: http://link.aps.org/doi/10.1103/PhysRevC.91.051301

[121] N. Kaiser, S. Fritsch, and W. Weise, "Chiral dynamics and nuclear matter," *Nucl. Phys. A*, vol. 697, pp. 255–276, jan 2002. [Online]. Available: http://adsabs.harvard.edu/abs/2002NuPhA.697..255K

[122] J. W. Holt, N. Kaiser, and W. Weise, "Quasiparticle interaction in nuclear matter with chiral three-nucleon forces," *Nucl. Phys.*, vol. A876, p. 61, 2012. [Online]. Available: http://www.sciencedirect.com/science/article/pii/S0375947411006701

[123] J. W. Holt, N. Kaiser, and W. Weise, "Chiral Fermi liquid approach to neutron matter," *Phys. Rev. C*, vol. 87, no. 1, p. 014338, Jan. 2013. [Online]. Available: http://adsabs.harvard.edu/abs/2013PhRvC..87a4338H

[124] A. Gezerlis, I. Tews, E. Epelbaum, S. Gandolfi, K. Hebeler, A. Nogga, and A. Schwenk, "Quantum Monte Carlo Calculations with Chiral Effective Field Theory Interactions," *Phys. Rev. Lett.*, vol. 111, p. 032501, 2013. [Online]. Available: http://journals.aps.org/prl/abstract/10.1103/PhysRevLett.111.032501

[125] L. Coraggio, J. W. Holt, N. Itaco, R. Machleidt, and F. Sammarruca, "Reduced regulator dependence of neutron-matter predictions with perturbative chiral interactions," *Phys. Rev. C*, vol. 87, p. 014322, 2013. [Online]. Available: http://journals.aps.org/prc/abstract/10.1103/PhysRevC.87.014322

[126] I. Tews, T. Krüger, K. Hebeler, and A. Schwenk, "Neutron Matter at Next-to-Next-to-Next-to-Leading Order in Chiral Effective Field Theory," *Phys. Rev. Lett.*, vol. 110, no. 3, p. 032504, Jan. 2013. [Online]. Available: http://adsabs.harvard.edu/abs/2013PhRvL.110c2504T

[127] G. Baardsen, A. Ekström, G. Hagen, and M. Hjorth-Jensen, "Coupled-cluster studies of infinite nuclear matter," *Phys. Rev. C*, vol. 88, p. 054312, Nov 2013. [Online]. Available: http://link.aps.org/doi/10.1103/PhysRevC.88.054312

[128] G. Hagen, T. Papenbrock, A. Ekström, K. A. Wendt, G. Baardsen, S. Gandolfi, M. Hjorth-Jensen, and C. J. Horowitz, "Coupled-cluster calculations of nucleonic matter," *Phys. Rev. C*, vol. 89, p. 014319, Jan 2014. [Online]. Available: http://link.aps.org/doi/10.1103/PhysRevC.89.014319

[129] A. Roggero, A. Mukherjee, and F. Pederiva, "Constraining the nuclear energy density functional with quantum Monte Carlo calculations," *Phys. Rev. C*, vol. 92, p. 054303, 2014. [Online]. Available: http://journals.aps.org/prc/abstract/10.1103/PhysRevC.92.054303

[130] L. Tolos, B. Friman, and A. Schwenk, "Neutron matter at finite temperature," *Nucl. Phys. A*, vol. A806, p. 105, 2008. [Online]. Available: http://www.sciencedirect.com/science/article/pii/S0375947408004077

[131] S. Fiorilla, N. Kaiser, and W. Weise, "Chiral thermodynamics of nuclear matter," *Nucl. Phys.*, vol. A880, p. 65, 2012. [Online]. Available: http://www.sciencedirect.com/science/article/pii/S037594741200005X

[132] J. W. Holt, N. Kaiser, and W. Weise, "Nuclear chiral dynamics and thermodynamics," *Prog. Part. Nucl. Phys.*, vol. 73, p. 35, 2013. [Online]. Available: http://www.sciencedirect.com/science/article/pii/S0146641013000756

[133] C. Wellenhofer, J. W. Holt, N. Kaiser, and W. Weise, "Nuclear thermodynamics from chiral low-momentum interactions," *Phys. Rev. C*, vol. 89, p. 064009, Jun 2014. [Online]. Available: http://link.aps.org/doi/10.1103/PhysRevC.89.064009

[134] C. Wellenhofer, J. W. Holt, and N. Kaiser, "Thermodynamics of isospin-asymmetric nuclear matter from chiral effective field theory," *Phys. Rev. C*, vol. 92, p. 015801, 2015. [Online]. Available: http://journals.aps.org/prc/abstract/10.1103/PhysRevC.92.015801

[135] A. B. Brown and A. Schwenk, "Constraints on Skyrme equations of state from properties of doubly magic nuclei and *ab initio* calculations of low-density neutron matter," *Phys. Rev. C*, vol. 89, p. 011307, Jan 2014. [Online]. Available: http://link.aps.org/doi/10.1103/PhysRevC.89.011307

[136] D. Davesne, J. Navarro, and R. M.-J. P. A. Becker, P.and Jodon, "Extended skyrme pseudopotential deduced from infinite nuclear matter properties," *Phys. Rev. C*, vol. 91, p. 064303, 2015. [Online]. Available: http://journals.aps.org/prc/abstract/10.1103/PhysRevC.91.064303

[137] A. Bulgac, M. M. Forbes, and S. Jin, "Nuclear energy density functionals: What do we really know?" *arXiv:1506.09195*, 2015. [Online]. Available: http://arxiv.org/abs/1506.09195

[138] L. Coraggio, J. W. Holt, N. Itaco, R. Machleidt, L. E. Marcucci, and F. Sammarruca, "Nuclear-matter equation of state with consistent two- and three-body perturbative chiral interactions," *Phys. Rev. C*, vol. 89, p. 044321, Apr 2014. [Online]. Available: http://link.aps.org/doi/10.1103/PhysRevC.89.044321

[139] M. Gell-Mann and F. Low, "Bound states in quantum field theory," *Phys. Rev.*, vol. 84, pp. 350–354, Oct 1951. [Online]. Available: http://link.aps.org/doi/10.1103/PhysRev.84.350

[140] G. C. Wick, "The evaluation of the collision matrix," *Phys. Rev.*, vol. 80, pp. 268–272, Oct 1950. [Online]. Available: http://link.aps.org/doi/10.1103/PhysRev.80.268

[141] A. L. Fetter and J. D. Walecka, *Quantum Theory of Many-Particle Systems*. Dover Publications, 2003.

[142] W. Kohn and J. M. Luttinger, "Ground-state energy of a many-fermion system," *Phys. Rev.*, vol. 118, pp. 41–45, Apr 1960. [Online]. Available: http://link.aps.org/doi/10.1103/PhysRev.118.41

[143] J. M. Luttinger and J. C. Ward, "Ground-state energy of a many-fermion system. ii," *Phys. Rev.*, vol. 118, pp. 1417–1427, Jun 1960. [Online]. Available: http://link.aps.org/doi/10.1103/PhysRev.118.1417

[144] A. Mukherjee and Y. Alhassid, "Configuration-interaction Monte Carlo method and its application to the trapped unitary Fermi gas," *Phys. Rev. A*, vol. 88, p. 053622, Nov 2013. [Online]. Available: http://link.aps.org/doi/10.1103/PhysRevA.88.053622

[145] A. Roggero, A. Mukherjee, and F. Pederiva, "Quantum Monte Carlo with coupled-cluster wave functions," *Phys. Rev. B*, vol. 88, p. 115138, Sep 2013. [Online]. Available: http://link.aps.org/doi/10.1103/PhysRevB.88.115138

[146] I. Shavitt and R. J. Bartlett, *Many-Body Methods in Chemistry and Physics: MBPT and Coupled-Cluster Theory*, ser. Cambridge Molecular Science. Cambridge University Press, 2009.

[147] G. Booth, A. Thom, and A. Alavi, "Fermion Monte Carlo without fixed nodes: A Game of Life, death and annihilation in Slater Determinant space," *J. Chem. Phys.*, vol. 131, p. 054106, 2009. [Online]. Available: http://scitation.aip.org/content/aip/journal/jcp/131/5/10.1063/1.3193710

[148] F. R. Petruzielo, A. A. Holmes, H. J. Changlani, M. P. Nightingale, and C. J. Umrigar, "Semistochastic Projector Monte Carlo Method," *Phys. Rev. Lett.*, vol. 109, p. 230201, 2012. [Online]. Available: http://journals.aps.org/prl/abstract/10.1103/PhysRevLett.109.230201

[149] M. Kolodrubetz and B. K. Clark, "Partial node configuration-interaction Monte Carlo as applied to the Fermi polaron," *Phys. Rev. B*, vol. 86, p. 075109, 2012. [Online]. Available: http://journals.aps.org/prb/abstract/10.1103/PhysRevB.86.075109

[150] A. Ekström, G. Baardsen, C. Forssén, G. Hagen, M. Hjorth-Jensen, G. R. Jansen, R. Machleidt, W. Nazarewicz, T. Papenbrock, J. Sarich, and S. M. Wild, "Optimized Chiral Nucleon-Nucleon Interaction at Next-to-Next-to-Leading Order," *Phys. Rev. Lett.*, vol. 110, p. 192502, May 2013. [Online]. Available: http://link.aps.org/doi/10.1103/PhysRevLett.110.192502

[151] E. Epelbaum, H. Krebs, and U.-G. Meißner, "Improved chiral nucleon-nucleon potential up to next-to-next-to-next-to-leading order," *Eur. Phys. J. A*, vol. 51, 2015. [Online]. Available: http://link.springer.com/article/10.1140%2Fepja%2Fi2015-15053-8

[152] F. Sammarruca, L. Coraggio, J. W. Holt, N. Itaco, R. Machleidt, and L. E. Marcucci, "Toward order-by-order calculations of the nuclear and neutron matter equations of state in chiral effective field theory," *Phys. Rev. C*, vol. 91, p. 054311, 2015. [Online]. Available: http://journals.aps.org/prc/abstract/10.1103/PhysRevC.91.054311

[153] F. Olver, *Asymptotics and special functions*, ser. Computer science and applied mathematics. Academic Press, 1974. [Online]. Available: https://books.google.com/books?id=3jvvAAAAMAAJ

[154] T. Skyrme, "The effective nuclear potential," *Nuclear Physics*, vol. 9, no. 4, pp. 615 – 634, 1958–1959. [Online]. Available: http://www.sciencedirect.com/science/article/pii/0029558258903456

[155] D. Vautherin and D. M. Brink, "Hartree-fock calculations with skyrme's interaction," *Physics Letters B*, vol. 32, no. 3, pp. 149 – 153, 1970. [Online]. Available: http://www.sciencedirect.com/science/article/pii/0370269370904582

[156] ——, "Hartree-fock calculations with skyrme's interaction. i. spherical nuclei," *Phys. Rev. C*, vol. 5, pp. 626–647, Mar 1972. [Online]. Available: http://link.aps.org/doi/10.1103/PhysRevC.5.626

[157] R. Dreizler and E. Gross, *Desnity Fucntional Theory, An advanced course.* Springer, Berlin, Heidelberg, New York.

[158] T. Melson and et al, "Neutrino-driven explosion of a 20 solar-mass star in three dimensions enabled by strange-quark contributions to neutrino-nucleon scattering," *arXiv:1504.07631*, 2015. [Online]. Available: http://iopscience.iop.org/article/10.1088/2041-8205/808/2/L42/meta

[159] A. B. Brown, "Constraints on the Skyrme Equations of State from Properties of Doubly Magic Nuclei," *Phys. Rev. Lett.*, vol. 111, p. 232502, Dec 2013. [Online]. Available: http://link.aps.org/doi/10.1103/PhysRevLett.111.232502

[160] P. Klüpfel, P.-G. Reinhard, T. J. Bürvenich, and J. A. Maruhn, "Variations on a theme by skyrme: A systematic study of adjustments of model parameters," *Phys. Rev. C*, vol. 79, p. 034310, Mar 2009. [Online]. Available: http://link.aps.org/doi/10.1103/PhysRevC.79.034310

[161] J. Dobaczewski, W. Nazarewicz, and P.-G. Reinhard, "Error estimates of theoretical models: a guide," *J. Phys. G*, vol. 41, no. 7, p. 074001, 2014. [Online]. Available: http://stacks.iop.org/0954-3899/41/i=7/a=074001

[162] M. Kortelainen, "Propagation of uncertainties in the nuclear dft models," *J. Phys. G*, vol. 42, p. 034021, 2015. [Online]. Available: http://iopscience.iop.org/article/10.1088/0954-3899/42/3/034021/meta

[163] M. Kortelainen, T. Lesinski, J. Moré, W. Nazarewicz, J. Sarich, N. Schunck, M. V. Stoitsov, and S. Wild, "Nuclear energy density optimization," *Phys. Rev. C*, vol. 82, p. 024313, Aug 2010. [Online]. Available: http://link.aps.org/doi/10.1103/PhysRevC.82.024313

[164] M. Kortelainen, J. McDonnell, W. Nazarewicz, P.-G. Reinhard, J. Sarich, N. Schunck, M. V. Stoitsov, and S. M. Wild, "Nuclear energy density optimization: Large deformations," *Phys. Rev. C*, vol. 85, p. 024304, Feb 2012. [Online]. Available: http://link.aps.org/doi/10.1103/PhysRevC.85.024304

[165] M. Kortelainen, J. McDonnell, W. Nazarewicz, E. Olsen, P.-G. Reinhard, J. Sarich, N. Schunck, S. M. Wild, D. Davesne, J. Erler, and A. Pastore, "Nuclear energy density optimization: Shell structure," *Phys. Rev. C*, vol. 89, p. 054314, May 2014. [Online]. Available: http://link.aps.org/doi/10.1103/PhysRevC.89.054314

[166] B. Serot and J. Walecka, "The relativistic nuclear many-body problem," *Adv. Nuc. Phys.*, vol. 16, p. 1, 1986. [Online]. Available: http://link.springer.com/chapter/10.1007%2F978-1-4684-5179-5_8

[167] F. Serr and J. Walecka, "A relativistic quantum field theory of finite nuclei," *Physics Letters B*, vol. 79, no. 1, pp. 10 – 14, 1978. [Online]. Available: http://www.sciencedirect.com/science/article/pii/0370269378904239

[168] G. A. Lalazissis, J. König, and P. Ring, "New parametrization for the lagrangian density of relativistic mean field theory," *Phys. Rev. C*, vol. 55, pp. 540–543, Jan 1997. [Online]. Available: http://link.aps.org/doi/10.1103/PhysRevC.55.540

[169] B. G. Todd-Rutel and J. Piekarewicz, "Neutron-rich nuclei and neutron stars: A new accurately calibrated interaction for the study of neutron-rich matter," *Phys. Rev. Lett.*, vol. 95, p. 122501, Sep 2005. [Online]. Available: http://link.aps.org/doi/10.1103/PhysRevLett.95.122501

[170] A. W. Steiner and T. Hempel, M.and Fischer, "Core-collapse supernova equations of state based on neutron star observations," *Astrophys. J.*, vol. 774, no. 1, p. 17, 2013. [Online]. Available: http://stacks.iop.org/0004-637X/774/i=1/a=17

[171] B. G. Todd-Rutel and J. Piekarewicz, "Neutron-Rich Nuclei and Neutron Stars: A New Accurately Calibrated Interaction for the Study of Neutron-Rich Matter," *Phys. Rev. Lett.*, vol. 95, p. 122501, Sep 2005. [Online]. Available: http://link.aps.org/doi/10.1103/PhysRevLett.95.122501

[172] G. Shen, C. J. Horowitz, and S. Teige, "New equation of state for astrophysical simulations," *Phys. Rev. C*, vol. 83, p. 035802, Mar 2011. [Online]. Available: http://link.aps.org/doi/10.1103/PhysRevC.83.035802

[173] F. J. Fattoyev, C. J. Horowitz, J. Piekarewicz, and G. Shen, "Relativistic effective interaction for nuclei, giant resonances, and neutron stars," *Phys. Rev. C*, vol. 82, p. 055803, Nov 2010. [Online]. Available: http://link.aps.org/doi/10.1103/PhysRevC.82.055803

[174] Y. Sugahara and H. Toki, "Relativistic mean-field theory for unstable nuclei with non-linear σ and ω terms," *Nuclear Physics A*, vol. 579, no. 3–4, pp. 557–572, 1994. [Online]. Available: http://www.sciencedirect.com/science/article/pii/0375947494909237

[175] H. Toki, D. Hirata, Y. Sugahara, K. Sumiyoshi, and I. Tanihata, "Relativistic many body approach for unstable nuclei and supernova," *Nuclear Physics A*, vol. 588, no. 1, pp. c357–c363, 1995, proceedings of the Fifth International Symposium on Physics of Unstable Nuclei. [Online]. Available: http://www.sciencedirect.com/science/article/pii/037594749500161S

[176] S. Typel, G. Röpke, T. Klähn, D. Blaschke, and H. H. Wolter, "Composition and thermodynamics of nuclear matter with light clusters," *Phys. Rev. C*, vol. 81, p. 015803, Jan 2010. [Online]. Available: http://link.aps.org/doi/10.1103/PhysRevC.81.015803

[177] A. W. Steiner, M. Hempel, and T. Fischer, "Core-collapse Supernova Equations of State Based on Neutron Star Observations," *Astrophys. J.*, vol. 774, no. 1, p. 17, 2013. [Online]. Available: http://stacks.iop.org/0004-637X/774/i=1/a=17

[178] M. Dutra, O. Lourenço, S. S. Avancini, B. V. Carlson, A. Delfino, D. P. Menezes, C. Providência, S. Typel, and J. R. Stone, "Relativistic mean-field hadronic models under nuclear matter constraints," *Phys. Rev. C*, vol. 90, p. 055203, Nov 2014. [Online]. Available: http://link.aps.org/doi/10.1103/PhysRevC.90.055203

[179] C. J. Horowitz and J. Piekarewicz, "Constraining URCA cooling of neutron stars from the neutron radius of ^{208}Pb," *Phys. Rev. C*, vol. 66, p. 055803, Nov 2002. [Online]. Available: http://link.aps.org/doi/10.1103/PhysRevC.66.055803

[180] S. Bogner, A. Schwenk, R. Furnstahl, and A. Nogga, "Is nuclear matter perturbative with low-momentum interactions?" *Nucl. Phys.*, vol. A763, p. 59, 2005. [Online]. Available: http://www.sciencedirect.com/science/article/pii/S0375947405010651

[181] J. W. Holt, N. Kaiser, and W. Weise, "Chiral three-nucleon interaction and the 14c-dating beta decay," *Phys. Rev. C*, vol. 79, p. 054331, 2009. [Online]. Available: http://journals.aps.org/prc/abstract/10.1103/PhysRevC.79.054331

[182] ——, "Density-dependent effective nucleon-nucleon interaction from chiral three-nucleon forces," *Phys. Rev. C*, vol. 81, p. 024002, 2010. [Online]. Available: http://journals.aps.org/prc/abstract/10.1103/PhysRevC.81.024002

[183] K. Hebeler and A. Schwenk, "Chiral three-nucleon forces and neutron matter," *Phys. Rev. C*, vol. 82, p. 014314, 2010. [Online]. Available: http://journals.aps.org/prc/abstract/10.1103/PhysRevC.82.014314

[184] N. Kaiser, "Chiral four-body interactions in nuclear matter," *Eur. J. Phys. A*, vol. 48, p. 58, 2012. [Online]. Available: http://link.springer.com/article/10.1140/epja/i2012-12135-1

[185] C. Drischler, V. Somà, and A. Schwenk, "Microscopic calculations and energy expansions for neutron-rich matter," *Phys. Rev. C*, vol. 89, p. 025806, Feb 2014. [Online]. Available: http://link.aps.org/doi/10.1103/PhysRevC.89.025806

[186] S. Gandolfi, A. Lovato, J. Carlson, and K. E. Schmidt, "From the lightest nuclei to the equation of state of asymmetric nuclear matter with realistic nuclear interactions," *Phys. Rev. C*, vol. 90, p. 061306, Dec 2014. [Online]. Available: http://link.aps.org/doi/10.1103/PhysRevC.90.061306

[187] J. M. Lattimer and F. D. Swesty, "A generalized equation of state for hot, dense matter," *Nuclear Physics A*, vol. 535, no. 2, pp. 331–376, 1991. [Online]. Available: http://www.sciencedirect.com/science/article/pii/037594749190452C

[188] G. Martínez-Pinedo, T. Fischer, A. Lohs, and L. Huther, "Charged-current weak interaction processes in hot and dense matter and its impact on the spectra of neutrinos emitted from protoneutron star cooling," *Phys. Rev. Lett.*, vol. 109, p. 251104, 2012. [Online]. Available: http://journals.aps.org/prl/abstract/10.1103/PhysRevLett.109.251104

[189] L. F. Roberts, S. Reddy, and G. Shen, "Medium modification of the charged-current neutrino opacity and its implications," *Phys. Rev. C*, vol. 86, p. 065803, 2012. [Online]. Available: http://journals.aps.org/prc/abstract/10.1103/PhysRevC.86.065803

[190] L. F. Roberts, "A new code for proto-neutron star evolution," *Astrophys. J.*, vol. 755, no. 2, p. 126, 2012. [Online]. Available: http://stacks.iop.org/0004-637X/755/i=2/a=126

[191] E. Rrapaj, J. W. Holt, A. Bartl, S. Reddy, and A. Schwenk, "Charged-current reactions in the supernova neutrino-sphere," *Phys. Rev. C*, vol. 91, p. 035806, Mar 2015. [Online]. Available: http://link.aps.org/doi/10.1103/PhysRevC.91.035806

[192] G. Martínez-Pinedo, T. Fischer, and L. Huther, "Supernova neutrinos and nucleosynthesis," *J. Phys. G*, vol. 41, p. 044008, 2014. [Online]. Available: http://iopscience.iop.org/article/10.1088/0954-3899/41/4/044008/meta

[193] A. Bartl, C. J. Pethick, and A. Schwenk, "Supernova matter at subnuclear densities as a resonant fermi gas: Enhancement of neutrino rates," *Phys. Rev. Lett.*, vol. 113, p. 081101, 2014. [Online]. Available: http://journals.aps.org/prl/abstract/10.1103/PhysRevLett.113.081101

[194] E. O'Connor and C. D. Ott, "The progenitor dependence of the pre-explosion neutrino emission in core-collapse supernovae," *Astrophys. J.*, vol. 762, no. 2, p. 126, 2013. [Online]. Available: http://iopscience.iop.org/article/10.1088/0004-637X/762/2/126/meta

[195] D. Davesne, J. W. Holt, A. Pastore, and J. Navarro, "Effect of three-body forces on response functions in infinite neutron matter," *Phys. Rev. C*, vol. 91, p. 014323, 2015. [Online]. Available: http://journals.aps.org/prc/abstract/10.1103/PhysRevC.91.014323

[196] P. Donati, P. M. Pizzochero, P. F. Bortignon, and R. A. Broglia, "Temperature dependence of the nucleon effective mass and the physics of stellar collapse," *Phys. Rev. Lett.*, vol. 72, p. 2835, 1994. [Online]. Available: http://journals.aps.org/prl/abstract/10.1103/PhysRevLett.72.2835

[197] M. Dutra, O. Lourenço, and D. Menezes, "Stellar properties and nuclear matter constraints," *arXiv:1510.02060*, 2015. [Online]. Available: http://journals.aps.org/prc/abstract/10.1103/PhysRevC.93.025806

[198] A. W. Steiner, J. M. Lattimer, and E. F. Brown, "The Neutron Star Mass-Radius Relation and the Equation of State of Dense Matter," *Astrophys. J.*, vol. 765, p. L5, 2013. [Online]. Available: http://iopscience.iop.org/article/10.1088/2041-8205/765/1/L5/meta

[199] C. Gordon, B.and Pethick and P. Sutherland, "The ground state of matter at high densities: Equation of state and stellar models," *Astrophys. J.*, vol. 170, pp. 299–317, 1971. [Online]. Available: http://adsabs.harvard.edu/full/1971ApJ...170..299B

[200] M. G. Alford, G. F. Burgio, S. Han, and D. Taranto, G.and Zappalá, "Constraining and applying a generic high-density equation of state," *arXiv:1501.07902*, 2015. [Online]. Available: http://journals.aps.org/prd/abstract/10.1103/PhysRevD.92.083002

[201] A. B. Migdal, *Soviet Physics, JETP*, vol. 10, p. 176, 1960. [Online]. Available: http://www.jetp.ac.ru/cgi-bin/e/index/e/10/1/p176?a=list

[202] D. Page and S. Reddy, "Dense Matter in Compact Stars: Theoretical Developments and Observational Constraints," *Annual Review of Nuclear and Particle Science*, vol. 56, pp. 327–374, Nov. 2006. [Online]. Available: http://adsabs.harvard.edu/abs/2006ARNPS..56..327P

[203] A. Hewish, S. J. Bell, J. D. H. Pilkington, P. F. Scott, and R. A. Collins, "Observation of a Rapidly Pulsating Radio Source," *Nature* , vol. 217, pp. 709–713, Feb. 1968. [Online]. Available: http://adsabs.harvard.edu/abs/1968Natur.217..709H

[204] G. Baym, C. Pethick, and D. Pines, "Electrical conductivity of neutron star matter," *Nature* , vol. 224, pp. 674–675, Nov. 1969. [Online]. Available: http://dx.doi.org/10.1038/224673a0

[205] E. Flowers and N. Itoh, "Transport properties of dense matter," *ApJ* , vol. 206, pp. 218–242, May 1976. [Online]. Available: http://adsabs.harvard.edu/abs/1976ApJ...206..218F

[206] D. G. Yakovlev and V. A. Urpin, "Thermal and Electrical Conductivity in White Dwarfs and Neutron Stars," *Soviet Astronomy*, vol. 24, p. 303, Jun. 1980. [Online]. Available: http://adsabs.harvard.edu/abs/1980SvA....24..303Y

[207] P. Shternin and D. Yakovlev, "Electron-muon heat conduction in neutron star cores via the exchange of transverse plasmons," *Phys.Rev.*, vol. D75, p. 103004, 2007. [Online]. Available: http://dx.doi.org/10.1103/PhysRevD.75.103004

[208] ——, "Shear viscosity in neutron star cores," *Phys.Rev.*, vol. D78, p. 063006, 2008. [Online]. Available: http://dx.doi.org/10.1103/PhysRevD.78.063006

[209] A. Gezerlis, C. Pethick, and A. Schwenk, *Pairing and superfluidity of nucleons in neutron stars*, K. H. Bennemann and J. B. Ketterson, Eds. Oxford University Press, 2014. [Online]. Available: https://arxiv.org/abs/1406.6109

[210] C. J. Pethick and D. G. Ravenhall, "Matter at large neutron excess and the physics of neutron-star crusts," *Annual Review of Nuclear and Particle Science*, vol. 45, pp. 429–484, 1995. [Online]. Available: http://adsabs.harvard.edu/abs/1995ARNPS..45..429P

[211] A. Schwenk and B. Friman, "Polarization Contributions to the Spin Dependence of the Effective Interaction in Neutron Matter," *Physical Review Letters*, vol. 92, no. 8, p. 082501, Feb. 2004. [Online]. Available: http://adsabs.harvard.edu/abs/2004PhRvL..92h2501S

[212] E. Braaten and D. Segel, "Neutrino energy loss from the plasma process at all temperatures and densities," *Phys.Rev.*, vol. D48, pp. 1478–1491, 1993. [Online]. Available: http://dx.doi.org/10.1103/PhysRevD.48.1478

[213] T. Altherr and P. Salati, "The electric charge of neutrinos and plasmon decay," *Nuclear Physics B*, vol. 421, pp. 662–682, Jun. 1994. [Online]. Available: http://adsabs.harvard.edu/abs/1994NuPhB.421..662A

[214] J. I. Kapusta and C. Gale, *Finite-Temperature Field Theory Principles and Applications*. Cambridge University Press, 2006.

[215] J. R. Schrieffer, *Theory of Superconductivity*, ser. Frontiers in Physics. Perseus Books, 1964, no. ISBN 0-08053-8501-0.

[216] C. Horowitz and K. Wehrberger, "Neutrino neutral current interactions in nuclear matter," *Nucl.Phys.*, vol. A531, pp. 665–684, 1991. [Online]. Available: http://dx.doi.org/10.1016/0375-9474(91)90745-R

[217] S. Reddy, M. Prakash, J. M. Lattimer, and J. A. Pons, "Effects of strong and electromagnetic correlations on neutrino interactions in dense matter," *Phys.Rev.*, vol. C59, pp. 2888–2918, 1999. [Online]. Available: http://dx.doi.org/10.1103/PhysRevC.59.2888

[218] A. Akmal, V. Pandharipande, and D. Ravenhall, "The Equation of state of nucleon matter and neutron star structure," *Phys.Rev.*, vol. C58, pp. 1804–1828, 1998. [Online]. Available: http://dx.doi.org/10.1103/PhysRevC.58.1804

[219] S. Gandolfi, A. Y. Illarionov, S. Fantoni, J. Miller, F. Pederiva, and K. E. Schmidt, "Microscopic calculation of the equation of state of nuclear matter and neutron star structure," *Mon.Not.Roy.Astron.Soc.*, vol. 404, pp. L35–L39, 2010. [Online]. Available: http://mnrasl.oxfordjournals.org/content/404/1/L35

[220] J. Holt, N. Kaiser, and W. Weise, "Quasiparticle interaction in nuclear matter with chiral three-nucleon forces," *Nucl.Phys.*, vol. A876, pp. 61–76, 2012. [Online]. Available: http://dx.doi.org/10.1016/j.nuclphysa.2011.12.001

[221] N. Chamel, D. Page, and S. Reddy, "Low-energy collective excitations in the neutron star inner crust," *Phys. Rev. C*, vol. 87, p. 035803, Mar 2013. [Online]. Available: http://link.aps.org/doi/10.1103/PhysRevC.87.035803

[222] N. Iwamoto and C. J. Pethick, "Effects of nucleon-nucleon interactions on scattering of neutrinos in neutron matter," *Phys. Rev. D*, vol. 25, pp. 313–329, Jan. 1982. [Online]. Available: http://adsabs.harvard.edu/abs/1982PhRvD..25..313I

[223] D. Son and M. Wingate, "General coordinate invariance and conformal invariance in nonrelativistic physics: Unitary Fermi gas," *Annals of Physics*, vol. 321, no. 1, pp. 197–224, 2006. [Online]. Available: http://www.sciencedirect.com/science/article/pii/S0003491605001958

[224] H. Heiselberg and C. Pethick, "Transport and relaxation in degenerate quark plasmas," *Phys.Rev.*, vol. D48, pp. 2916–2928, 1993. [Online]. Available: http://dx.doi.org/10.1103/PhysRevD.48.2916

[225] C. Manuel and L. Tolos, "Shear viscosity due to phonons in superfluid neutron stars," *Phys.Rev.*, vol. D84, p. 123007, 2011. [Online]. Available: http://journals.aps.org/prd/abstract/10.1103/PhysRevD.84.123007

[226] C. Manuel, S. Sarkar, and L. Tolos, "Thermal conductivity due to phonons in the core of superfluid neutron stars," 2014. [Online]. Available: http://journals.aps.org/prc/abstract/10.1103/PhysRevC.90.055803

[227] P. F. Bedaque and S. Reddy, "Goldstone modes in the neutron star core," *Phys.Lett.*, vol. B735, pp. 340–343, 2014. [Online]. Available: http://www.sciencedirect.com/science/article/pii/S0370269314004389

[228] D. G. Yakovlev and V. A. Urpin, "Thermal and Electrical Conductivity in White Dwarfs and Neutron Stars," *Sov. Astron.*, vol. 24, p. 303, Jun. 1980. [Online]. Available: http://adsabs.harvard.edu/abs/1980SvA....24..303Y

[229] N. Itoh, Y. Kohyama, N. Matsumoto, and M. Seki, "Electrical and thermal conductivities of dense matter in the crystalline lattice phase," *ApJ* , vol. 285, pp. 758–765, Oct. 1984. [Online]. Available: http://adsabs.harvard.edu/abs/1984ApJ...285..758I

[230] D. A. Baiko and D. G. Yakovlev, "Thermal and electric conductivities of Coulomb crystals in the inner crust of a neutron star," *Astronomy Letters*, vol. 22, pp. 708–714, Sep. 1996. [Online]. Available: http://adsabs.harvard.edu/abs/1996AstL...22..708B

[231] A. Chugunov and D. Yakovlev, "Shear viscosity and oscillations of neutron star crust," *Astronomy Reports*, vol. 49, no. 9, pp. 724–738, 2005. [Online]. Available: http://dx.doi.org/10.1134/1.2045323

[232] C. Cutler and L. Lindblom, "Effect of viscosity on neutron star oscillations," *ApJ* , vol. 314, pp. 234–241, 1987. [Online]. Available: http://adsabs.harvard.edu/full/1987ApJ...314..234C

[233] N. Andersson, "A New class of unstable modes of rotating relativistic stars," *Astrophys.J.*, vol. 502, pp. 708–713, 1998. [Online]. Available: http://dx.doi.org/10.1086/305919

[234] M. L. Bellac, *Thermal Field Theory.* Cambridge: Cambridge University Press, 1996.

[235] A. Burrows and J. M. Lattimer, "The birth of neutron stars," *Astrophys. J.*, vol. 307, pp. 178–196, 1986. [Online]. Available: http://dx.doi.org/10.1086/164405

[236] G. G. Raffelt, *Stars as laboratories for fundamental physics: The astrophysics of neutrinos, axions, and other weakly interacting particles.* University of Chicago Press, 1996, iSBN 0-226-70272-3.

[237] A. Burrows, M. S. Turner, and R. P. Brinkmann, "Axions and SN 1987a," *Phys. Rev.*, vol. D39, p. 1020, 1989. [Online]. Available: http://dx.doi.org/10.1103/PhysRevD.39.1020

[238] C. Hanhart, D. R. Phillips, and S. Reddy, "Neutrino and axion emissivities of neutron stars from nucleon-nucleon scattering data," *Phys. Lett.*, vol. B499, pp. 9–15, 2001. [Online]. Available: http://dx.doi.org/10.1016/S0370-2693(00)01382-4

[239] C. Hanhart, J. A. Pons, D. R. Phillips, and S. Reddy, "The Likelihood of GODs' existence: Improving the SN1987a constraint on the size of large compact dimensions," *Phys. Lett.*, vol. B509, pp. 1–9, 2001. [Online]. Available: http://dx.doi.org/10.1016/S0370-2693(01)00544-5

[240] H. K. Dreiner, C. Hanhart, U. Langenfeld, and D. R. Phillips, "Supernovae and light neutralinos: SN1987A bounds on supersymmetry revisited," *Phys. Rev.*, vol. D68, p. 055004, 2003. [Online]. Available: http://dx.doi.org/10.1103/PhysRevD.68.055004

[241] H. K. Dreiner, J.-F. Fortin, C. Hanhart, and L. Ubaldi, "Supernova constraints on MeV dark sectors from e^+e^- annihilations," *Phys. Rev.*, vol. D89, no. 10, p. 105015, 2014. [Online]. Available: http://dx.doi.org/10.1103/PhysRevD.89.105015

[242] D. Kazanas, R. N. Mohapatra, S. Nussinov, V. L. Teplitz, and Y. Zhang, "Supernova Bounds on the Dark Photon Using its Electromagnetic Decay," *Nucl. Phys.*, vol. B890, pp. 17–29, 2014. [Online]. Available: http://dx.doi.org/10.1016/j.nuclphysb.2014.11.009

[243] K. A. Olive, "TASI lectures on dark matter," in *Particle physics and cosmology: The quest for physics beyond the standard model(s). Proceedings, Theoretical Advanced Study Institute, TASI 2002, Boulder, USA, June 3-28, 2002*, 2003, pp. 797–851. [Online]. Available: https://arxiv.org/abs/1502.01320

[244] D. Clowe and and et al, "A direct empirical proof of the existence of dark matter," *Astrophys. J.*, vol. 648, pp. L109–L113, 2006. [Online]. Available: http://dx.doi.org/10.1086/508162

[245] B. Holdom, *Physics Letters B*, vol. 166, no. 2, pp. 196 – 198, 1986. [Online]. Available: http://www.sciencedirect.com/science/article/pii/0370269386913778

[246] S. Rajpoot, "Electroweak interactions with gauged baryon and lepton numbers," *Phys. Rev. D*, vol. 40, pp. 2421–2424, Oct 1989. [Online]. Available: http://link.aps.org/doi/10.1103/PhysRevD.40.2421

[247] A. E. Nelson and N. Tetradis, "Constraints on a new vector boson coupled to baryons," *Phys. Lett.*, vol. B221, p. 80, 1989. [Online]. Available: http://dx.doi.org/10.1016/0370-2693(89)90196-2

[248] B. Batell, P. deNiverville, D. McKeen, M. Pospelov, and A. Ritz, "Leptophobic Dark Matter at Neutrino Factories," *Phys. Rev.*, vol. D90, no. 11, p. 115014, 2014. [Online]. Available: http://dx.doi.org/10.1103/PhysRevD.90.115014

[249] B. Holdom, "Two u(1)'s and ϵ charge shifts," *Physics Letters B*, vol. 166, no. 2, pp. 196 – 198, 1986. [Online]. Available: http://www.sciencedirect.com/science/article/pii/0370269386913778

[250] J. Jaeckel and A. Ringwald, "The Low-Energy Frontier of Particle Physics," *Ann. Rev. Nucl. Part. Sci.*, vol. 60, pp. 405–437, 2010. [Online]. Available: http://dx.doi.org/10.1146/annurev.nucl.012809.104433

[251] C. Hanhart, D. R. Phillips, S. Reddy, and M. J. Savage, "Extra dimensions, SN1987a, and nucleon-nucleon scattering data," *Nucl. Phys.*, vol. B595, pp. 335–359, 2001. [Online]. Available: http://dx.doi.org/10.1016/S0550-3213(00)00667-2

[252] J. Bjorken and S. Drell, *Relativistic quantum mechanics*, ser. International series in pure and applied physics. McGraw-Hill, 1964. [Online]. Available: https://books.google.com/books?id=pAdRAAAAMAAJ

[253] S. Weinberg, *Quantum Theory of Fields*, ser. Frontiers in Physics. University of Cambridge, 1995, vol. 1, no. ISBN 0-521-55001-7.

[254] F. E. Low, "Bremsstrahlung of very low-energy quanta in elementary particle collisions," *Physical Review*, vol. 110, p. 974, 1958. [Online]. Available: http://journals.aps.org/pr/abstract/10.1103/PhysRev.110.974

[255] E. M. Nyman, "Soft-photon theory of nucleon-nucleon bremsstrahlung," *Physical Review*, vol. 170, no. 5, p. 1628, 1968. [Online]. Available: http://journals.aps.org/pr/abstract/10.1103/PhysRev.170.1628

[256] L. Heller, "Soft-photon theorem for bremsstrahlung in a potential model," *Phys. Rev.*, vol. 174, pp. 1580–1587, Oct 1968. [Online]. Available: http://link.aps.org/doi/10.1103/PhysRev.174.1580

[257] H. Huisman, J. C. S. Bacelar, M. J. van Goethem, M. N. Harakeh, M. Hoefman, N. Kalantar-Nayestanaki, H. Löhner, J. G. Messchendorp, R. W. Ostendorf, S. Schadmand, O. Scholten, R. G. E. Timmermans, R. Turrisi, M. Volkerts, H. W. Wilschut, R. S. Simon, A. Kugler, and V. Wagner, "High-precision proton-proton bremsstrahlung measurements below the pion-production threshold," *Phys. Rev. Lett.*, vol. 83, pp. 4017–4020, Nov 1999. [Online]. Available: http://link.aps.org/doi/10.1103/PhysRevLett.83.4017

[258] H. Huisman and et al, "Probing few-body systems with bremsstrahlung," *Nuclear Physics A*, vol. 654, no. 1, Supplement 1, pp. 949c – 954c, 1999. [Online]. Available: http://www.sciencedirect.com/science/article/pii/S0375947400885796

[259] Y. Safkan, T. Akdogan, W. A. Franklin, J. L. Matthews, W. M. Schmitt, V. V. Zelevinsky, P. A. M. Gram, T. N. Taddeucci, S. A. Wender, and S. F. Pate, "Differential cross-section for neutron-proton bremsstrahlung," *Phys. Rev.*, vol. C75, p. 031001, 2007. [Online]. Available: http://dx.doi.org/10.1103/PhysRevC.75.031001

[260] V. G. J. Stoks, R. A. M. Klomp, M. C. M. Rentmeester, and J. J. de Swart, "Partial-wave analysis of all nucleon-nucleon scattering data below 350 mev," *Phys. Rev. C*, vol. 48, pp. 792–815, Aug 1993. [Online]. Available: http://link.aps.org/doi/10.1103/PhysRevC.48.792

[261] W. Keil, H. T. Janka, and G. Raffelt, "Reduced neutrino opacities and the SN1987A signal," *Phys. Rev.*, vol. D51, pp. 6635–6646, 1995. [Online]. Available: http://dx.doi.org/10.1103/PhysRevD.51.6635

[262] J. A. Pons, S. Reddy, M. Prakash, J. M. Lattimer, and J. A. Miralles, "Evolution of protoneutron stars," *Astrophys. J.*, vol. 513, p. 780, 1999. [Online]. Available: http://dx.doi.org/10.1086/306889

[263] E. G. Adelberger, B. R. Heckel, C. W. Stubbs, and W. F. Rogers, "Searches for new macroscopic forces," *Annual Review of Nuclear and Particle Science*, vol. 41, pp. 269–320, 1991. [Online]. Available: http://adsabs.harvard.edu/abs/1991ARNPS..41..269A

[264] J. L. Feng, J. Smolinsky, and P. Tanedo, "Dark Photons from the Center of the Earth: Smoking-Gun Signals of Dark Matter," 2015. [Online]. Available: http://journals.aps.org/prd/abstract/10.1103/PhysRevD.93.015014

[265] D. F. B. ten Haaf, H. J. M. van Bemmel, J. M. J. van Leeuwen, W. van Saarloos, and D. M. Ceperley, "Proof for an upper bound in fixed-node monte carlo for lattice fermions," *Phys. Rev. B*, vol. 51, pp. 13 039–13 045, May 1995. [Online]. Available: http://link.aps.org/doi/10.1103/PhysRevB.51.13039

Acknowledgements

I would like to express my deep gratitude to my supervisor Sanjay Reddy for his patient guidance, the long discussions from various topics in nuclear astrophysics to the tiniest details on how to perform calculations. In this field, there are so many factors to consider when trying to link theory to observations, and is pretty easy to not see the forest for the trees. His expertise and willingness to share it with me has proven to be crucial in my academic work so far.

I would like now to thank all the nice people I have met and collaborated with, for by working together I have learnt so much on the dedication and discipline needed. Jeremy W. Holt, with whom I have collaborated on two projects in this dissertation, has been very helpful in understanding Ch-PT and many-body calculations. My discussions with Alessandro Roggero on what new techniques to develop for non-perturbative calculations, while talking a nice cup of espresso are something I will surely miss in the future. A special thank goes to Luke Roberts, with whom I hope to finally incorporate the modified neutrino rates in numerical simulations. He has been the to-go to astrophysicist for me during these years. I would like to thank Alexander Bartl and Achim Schwenk for the work done together on neutrino opacities.

Not forgetting, the faculty at the University of Washington, has been instrumental in my education and discovery. In addition, I would like to include the acknowledgements that I and my collaborators have for each specific project:

Neutrino Opacities

We thank Kai Hebeler, Andreas Lohs, Luke Roberts, and Gang Shen for useful correspondence, and George Bertsch, Charles Horowitz and Gabriel Martínez-Pinedo for useful discussions. The work of E. R. and S. R. was supported in part by grants from NUCLEI SciDAC program and by the DOE Grant No. DE-FG02-00ER41132, J. W. H. acknowledges support from DOE Grant No. DE-FG02-97ER41014, and the work of A. B. and A. S. was supported by a grant from BMBF ARCHES, the ERC Grant No. 307986 STRONGINT, the Helmholtz Alliance HA216/EMMI, and the Studienstiftung des deutschen Volkes. A. S. thanks the Institute for Nuclear Theory at the University of Washington for its hospitality and the DOE for partial support during the completion of this work. This work was also facilitated through the use of advanced computational, storage, and networking infrastructure provided by the Hyak supercomputer system, supported in part by the University of Washington eScience Institute.

Equation of State

We thank A. Bulgac and S. Reddy for useful discussions, A. Brown for sharing the parameters of the Skyrme models used in this work, and C. Wellenhofer for providing us with the temperature- and density-dependent entropy from chiral nuclear forces. The work of J. W. Holt was supported by US DOE Grant No. DE-FG02-97ER41014. The work of A. Roggero was supported by NSF Grant No. AST-1333607. The work of E. Rrapaj

was supported by US DOE Grant No. DE-SC0008489. Some of the most intensive computations have been performed at NERSC thank to a Startup allocation.

Transport Coefficients

We thank Charles Horowitz, David Kaplan, Dany Page, Chris Pethick, Martin Savage and Dima Yakovlev for useful discussions and Andrew Steiner for reading the manuscript. S. R. thanks the International Space Science Institute in Bern, Switzerland for their hospitality and the members of the ISSI team *Probing Deep into the Neutron Star Crust with Transient Neutron- Star Low-Mass X-Ray Binaries* led by Dany Page for useful discussions. The work of S. R. and B. B. was supported by the DOE Grant No. DE-FG02-00ER41132 and by the Topical Collaboration to study *Neutrinos and nucleosynthesis in hot and dense matter*. The work of S. R. and E. R. was also supported by the NUCLEI SciDAC program.

Dark photons in supernovae

We would like to thank Michael Graesser, David Kaplan, Ann Nelson, Maxim Pospelov, Rob Timmermans and Martin Savage for useful discussions. The work of E. R. and S. R.was supported by the DOE Grant No. DE-FG02-00ER41132 and by the NUCLEI SciDAC program.